

# **University of Alberta**

Response of RADAR Backscatter at Multiple Frequencies and Polarizations to Changing  
Snow and Ice Properties on a Temperate Saline Lake

by

**Justin Francis Beckers**

A thesis submitted to the Faculty of Graduate Studies and Research  
in partial fulfillment of the requirements for the degree of

**Master of Science**

Department of Earth and Atmospheric Sciences

©Justin Francis Beckers  
Spring 2012  
Edmonton, Alberta

Permission is hereby granted to the University of Alberta Libraries to reproduce single copies of this thesis and to lend or sell such copies for private, scholarly or scientific research purposes only. Where the thesis is converted to, or otherwise made available in digital form, the University of Alberta will advise potential users of the thesis of these terms.

The author reserves all other publication and other rights in association with the copyright in the thesis and, except as herein before provided, neither the thesis nor any substantial portion thereof may be printed or otherwise reproduced in any material form whatsoever without the author's prior written permission.

## **Abstract**

Currently there is a lack of knowledge regarding the distribution of the mass of snow, or snow water equivalence, over land and ice. The proposed CoReH2O satellite mission aims to address this by launching the first coincident dual-frequency, dual-polarized Ku- and X- band Synthetic Aperture Radar. In the winters of 2008/09 and 2009/10, C-, X-, and Ku-band imagery retrieved from Envisat ASAR, TerraSAR-X and QuikSCAT were compared with repeated in-situ and autonomous measurements of snow and ice properties over Miquelon Lake, a saline lake in Alberta. Ku- and X-band backscatter increased with snow depth and SWE. Ku-band backscatter decreased with increasing snow wetness and brine volume. C- and X-band backscatter increased with snow wetness, brine volume and snow-ice formation but exhibited an unclear response to ice thickness. The co-varying snow and ice properties hampered interpretation of observed backscatter changes and will continue to complicate the retrieval of these properties.

## Acknowledgements

I wish to thank my supervisor, Dr. Christian Haas, for the many opportunities given to me. Thank you for introducing me to the amazing world of sea ice. Your guidance and support have been invaluable over these past few years. I also want to thank the numerous people who have provided guidance, mentoring and field research assistance on Miquelon Lake and the many other projects I have been involved with. I want to thank my main field research assistants, fellow graduate students Ben Lange and Anna Bramucci for their assistance collecting the data. I want to thank Jeremy Wilkinson and Keith Jackson at the Scottish Association for Marine Sciences for letting me test one of their ice-mass balance buoys on the lake in 2009. Thanks to Peter Carlson and the Department of Earth and Atmospheric Sciences for providing snow sampling equipment. I also want to thank the numerous other people who assisted in the field at one time or another.

Many thanks to my family and friends for their love and support over the course of my entire academic career. To my mother and father, thank you for providing me with the opportunity to attend University and to discover my passion. To my wife, thank you for your limitless support, patience and love.

To Jeff Kavanaugh, my undergraduate thesis supervisor, thanks for taking a chance and hiring me as an undergraduate research assistant and introducing me to the world of ice and snow and scientific field research.

This research was supported by the Queen Elizabeth II Graduate Student Scholarship, Alberta Graduate Student Scholarship, Profiling Alberta's Graduate Students Award, the Steve and Elaine Antoniuk Graduate Scholarship in Arctic Research, and the Institute for Geophysical Research Roy G. Hibbs Memorial Scholarship and Student Travel Grant. Research in Miquelon Lake was conducted with permission from Alberta Tourism Parks and Recreation under Research Permits RC08EC007 and 09-062. All Envisat ASAR data was provided by the European Space Agency under the research project AOCRY.1241. All TerraSAR-X data was provided by DLR, the German Aerospace Center, under the SOAR Project ID:5060/COA0976.

# Table of Contents

ABSTRACT

ACKNOWLEDGEMENTS

TABLE OF CONTENTS

LIST OF TABLES

LIST OF FIGURES

LIST OF SYMBOLS AND ABBREVIATIONS

<b>CHAPTER 1. INTRODUCTION .....</b>	<b>1</b>
1.1 STUDY CONTEXT .....	1
1.2 STUDY OBJECTIVES.....	5
1.3 THESIS STRUCTURE.....	5
<b>CHAPTER 2. BACKGROUND AND LITERATURE REVIEW.....</b>	<b>6</b>
2.1 SEA ICE .....	6
2.2 SNOW .....	12
2.3 RADAR.....	18
2.4 MULTI-POLARIZATION AND MULTI-FREQUENCY OBSERVATIONS OF SNOW AND SEA ICE .....	25
<b>CHAPTER 3. STUDY SITE, DATA, AND METHODS .....</b>	<b>32</b>
3.1 STUDY SITE.....	32
3.2 DATA SOURCES AND METHODS .....	36
3.3 METHODS .....	41
<b>CHAPTER 4. RESULTS AND DISCUSSION .....</b>	<b>47</b>
4.1 SEASONAL EVOLUTION OF ICE, SNOW, AND ENVIRONMENTAL PROPERTIES .....	47
4.2 TEMPORAL EVOLUTION OF RADAR BACKSCATTER .....	61
4.3 CO-VARIABILITY OF RADAR BACKSCATTER AND SNOW PROPERTIES.....	74
4.4 CO-VARIABILITY OF RADAR BACKSCATTER AND ICE PROPERTIES.....	86
<b>CHAPTER 5. SUMMARY AND CONCLUSIONS .....</b>	<b>94</b>
5.1 STUDY LIMITATIONS .....	95
5.2 SUITABILITY OF STUDY SITE FOR FUTURE WORK .....	97
5.3 FUTURE WORK.....	98
<b>BIBLIOGRAPHY .....</b>	<b>102</b>
<b>APPENDIX A. IMAGE ACQUISITION INFORMATION .....</b>	<b>115</b>
<b>APPENDIX B. SYNTHETIC APERTURE RADAR IMAGES.....</b>	<b>118</b>

## List of Tables

Table 2.1.1: Coefficients for functions $F_i(T)$ for different temperature intervals. Adapted from [Cox and Weeks, 1983; Leppäranta and Manninen, 1988; Petrich and Eicken, 2010]	12
Table 2.3.1: Radar Band Designations with nominal frequency range and corresponding wavelength. Furthermore table shows widely used satellite sensors for certain bands. Table created using data from [IEEE, 2003].	20
Table 3.1.1: Physical Characteristics of Miquelon Lake, AB. Values for elevation and maximum depth are estimated from GPS data and SRTM elevation [Swanson and Zurawell, 2006]. Surface area for 2009 was determined using image analysis of a TerraSAR image.	34
Table 4.3.1: Regression statistics between QuikSCAT Ku band backscatter and AMSR-E derived SWE. $\alpha$ value of 0.05 used.	85

## List of Figures

Figure 1.1.1: Contribution of accumulated annual snowfall to annual runoff. Black lines indicate regions where water availability is predominantly influenced by snowmelt generated upstream. Reprinted by permission from Macmillan Publishers, Ltd: [Nature]. Barnett, T. P., J. C. Adam, and D. P. Lettenmaier (2005), Potential impacts of a warming climate on water availability in snow-dominated regions Nature, 438(7066), 303-309. Copyright 2005.....	3
Figure 2.1.1: Radar penetration depth into sea ice [Hallikainen and Winebrenner, 1992]. Adapted with permission from [Petrich and Eicken, 2010].....	9
Figure 2.1.2: Dielectric constant and loss factors for sea ice at 4 and 10 GHz on left and right respectively [Hallikainen and Winebrenner, 1992].....	10
Figure 2.1.3: Brine salinity as a function of temperature. Adapted using Equation 12 from [Petrich and Eicken, 2010]. .....	11
Figure 2.2.1: Left: Snow profile over Miquelon Lake from March 10, 2010. Right: Depth hoar snow crystals observed in the snowpack on Miquelon Lake. Background grid is 3mm. Image acquired on March 10, 2010.....	14
Figure 2.2.2: Penetration depth of C, X, Ku radar waves into wet snow. Adapted from [Hallikainen et al., 1986; Tiuri et al., 1984; Ulaby et al., 1984].....	18
Figure 2.3.1: Atmospheric Transmission of the Electromagnetic Spectrum. Image Courtesy of [NASA Earth Observatory, 2011].....	19
Figure 2.3.2: Left: SAR image formation. Right: Typical SAR system geometry. Figure from [Canada Centre for Remote Sensing, Natural Resources Canada, 2001]. A represents the flight direction, B the nadir point directly below the platform, C the Swath width of the scene, D the Range direction and E the azimuth direction.....	21
Figure 2.3.3: Illustration of radar layover. Energy emitted by the sensor reaches the top (B) of the topographic feature before the base (A), and thus is laid over the base (A') in the slant range image (at B'). Figure from [Canada Centre for Remote Sensing, Natural Resources Canada, 2001].....	22
Figure 2.3.4: Example of vertically polarized EM wave. M represents the magnetic field and E the electric field. The direction of travel is to the right. Figure reproduced with permission from the European Space Agency - ESA [E.S.A., 2007a]. .....	24

Figure 2.4.1: Characteristic seasonal evolution of C-band microwave backscatter from Arctic sea ice. Ponding onset (PO) is indicated for thick and thin snow covers. Copyright (2007) Wiley. Used with permission from Yackel, J. J., Barber, D. G., Papakyriakou, T. N. and Breneman, C. (2007), First-year sea ice spring melt transitions in the Canadian Arctic Archipelago from time-series synthetic aperture radar data, 1992–2002. <i>Hydrological Processes</i> , John Wiley and Sons. ....	26
Figure 3.1.1: Envisat ASAR image showing location of Miquelon Lake, Alberta (lower right corner). One can also note Edmonton, Alberta (top left) and the Edmonton International Airport (YEG) at N 5910000, E 330000. Image is projected in UTM Zone 12N.....	33
Figure 3.1.2: Miquelon Lake Bathymetry and shore line overlain on geo-referenced TerraSAR-X Spotlight mode SAR image. Map created using data the Alberta Geological Survey Digital Datasets Archive [Alberta Environment et al., 2008]. .....	35
Figure 3.1.3: Evolution of the salinity of Miquelon Lake. Data in light grey (small diamond markers) were collected from previous studies which occurred during summer months. Values in dark grey (square-markers) were collected as part of the sampling program of this study and present winter values. Data sourced from [Bierhuizen and Prepas, 1985; Marino et al., 1990; Evans and Prepas, 1997; Swanson and Zurawell, 2006] and in-situ measurements collected during this study.....	36
Figure 3.2.1: MetOcean/CRREL and SAMS Ice Mass Balance Buoys deployed on Miquelon Lake on December 3, 2009. Photo Courtesy of Dr. Marcel Nicolaus. ....	38
Figure 3.2.2: SAR Image Footprints from Envisat ASAR and TerraSAR-X Imagery Acquired for this study. Yellow marker is located in Miquelon Lake. Top Left: Envisat ASAR APP. Top Right: TerraSAR-X MGD_RE_D. Bottom Left: TerraSAR-X SSC_SL_D. Bottom Right: TerraSAR-X SSC_SM_D.....	40
Flow Chart 3.1: Full set of SAR processing performed on TerraSAR-X SSC_SL_D imagery. All SLC imagery was run through each possible process illustrated above. ....	42
Figure 3.3.1: Location of regions of interest (ROIS) for which backscatter statistics were extracted and analyzed. The QuikSCAT pixel over Miquelon Lake is the red ROI, the blue ROI defines the region of in-situ measurements and is referred to as the Lake ROI. The white/black and green ROIs represent land and forest regions TerraSAR-X image ©DLR 2009.. ....	45
Figure 3.3.2: TerraSAR-X SL results from the Lake ROI for four selected processing chains. ....	46
Flow Chart 3.2: Flow chart outlining the processing steps used for each type of SAR image acquired for the study and used in the statistical analysis. ....	46

Figure 4.1.1: Left: Evolution of water salinity of Miquelon Lake from 2008-2010. Right: Correlation between ice thickness and water salinity.....	47
Figure 4.1.2: Skeletal (lamellar) ice layer at the bottom of an ice core extracted from Miquelon Lake on January 20, 2009. Bottom of the ice core is at the bottom of the photograph. Skeletal layer consists of vertically oriented lamellar dendritic crystals formed as salts are rejected from the ice.....	48
Figure 4.1.3: Left: Brine drainage channels and skeletal ice layer (faint lines) in ice core acquired on Miquelon Lake on March 21, 2010. Right: Skeletal ice layer in ice core from Miquelon Lake. ....	49
Figure 4.1.4: Snow-ice (black box) at the top of a 0.525m long ice core acquired from Miquelon Lake on March 21, 2010. ....	49
Figure 4.1.5: Seasonal evolution of ice salinity on Miquelon Lake in the winter of 2008/2009. Note the decrease in salinity over the course of the winter.....	50
Figure 4.1.6: Seasonal evolution of ice salinity on Miquelon Lake in the winter of 2009/10.....	51
Figure 4.1.7: In-situ measurements of ice freeboard on Miquelon Lake. Left and Right present the data for the winters of 2008/09 and 2009/10 respectively.....	52
Figure 4.1.8: Comparison of the seasonal evolution of bulk ice salinity on Miquelon Lake. ....	52
Figure 4.1.9: Inter-annual comparison of seasonal evolution of ice thickness on Miquelon Lake. ....	53
Figure 4.1.10: Ice thermal conductivity parameterization from the SAMS IMB deployed on Miquelon Lake in 2009/10. Heat is applied to the temperature sensors. The temperature increase observed is inversely proportional to the thermal conductivity of the medium surrounding the sensor. The data shown is the ratio of the amount of heating after 60s and after 15s. The plot shows the in-situ and autonomous snow and ice thickness data where Z represents thickness.....	54
Figure 4.1.11: Ice ridge that developed on Miquelon Lake in 2008/09.....	54
Figure 4.1.12: Inter-annual comparison of seasonal evolution of snow depth on Miquelon Lake. Histograms of snow thickness are presented in Figure 4.1.12a. Buoy derived snow depths are presented in Figure 4.1.12b. ....	55

Figure 4.1.13: Visual correlation between short-term variability in snow depth and wind speed. Wind speed data acquired from the Camrose, AB weather station and snow depth is from the CRREL IMB surface sonic ranger. Grey lines are wind speeds in km/hr while the black line is the snow depth in cm. Arrows indicate times of high winds and sudden changes in snow depth. Note that negative snow depths are indicated by the sonic ranger in late April. ....	56
Figure 4.1.14: Inter-annual comparison of the evolution of snow density on Miquelon Lake. ....	56
Figure 4.1.15: Comparison of mean daily air temperatures on Miquelon Lake for the winters of 2008/09 and 2009/10. Black dots indicate days where SAR images were acquired. ....	57
Figure 4.1.16: Comparison of cumulative positive and negative degree days for Dec. to May, 2008/09 and 2009/10. Degree days were calculated using the IMB on Miquelon Lake. ....	58
Figure 4.1.17: Snow thickness across the transition from lake surface to near shore environment. Survey was performed on March 03, 2009. Snow depths on the lake are representative for the day. ....	59
Figure 4.1.18: Comparison of SWE measurements from AMSR-E and in-situ measurements on Miquelon Lake in 2008/09 and 2009/10 presented on left and right, respectively. ....	60
Figure 4.2.1: Seasonal evolution of Envisat ASAR C-band backscatter over Miquelon Lake in 2008/09. Figure 4.2.1a on the left presents the results from Swath IS4 which has an incidence angle range of 30-36°. Figure 4.2.1b on the right presents the results from Swath IS6 which has an incidence angle range of 39-42°. $\theta_i$ is the incidence angle of the image measured at the study site on the lake. The NESZ is the noise estimated sigma zero (see Section 3.3.1). ....	62
Figure 4.2.2: Evolution of Envisat ASAR C-band backscatter over Miquelon Lake in 2009/10. Figure 4.2.2a(left) presents results from Swath IS2 which has an incidence angle range of 20°-26°. Figure 4.2.2b (right) presents results from Swath IS6 which has an incidence angle range of 39°-43°. Black box indicates the period of snow melt. Red box indicates the disappearance of the ice. ....	64
Figure 4.2.3: TerraSAR-X MGD RE image acquired on March 18, 2009. Red box outlines feature that is suggested to be grounded ice.....	66

Figure 4.2.4: Seasonal Evolution of X-band backscatter over Miquelon Lake in a) 2008/09. Figure 4.2.4a on the left presents results from one swath Track 144 ( $\theta_i = 32^\circ$ ). Figure 4.2.4b on the right presents results from Track 68, ( $\theta_i = 43^\circ$ ). Incidence angles given are from over the Lake. The black boxes indicates the period of snow melt where backscatter increases sharply in early April and decreases in mid-April.....	67
Figure 4.2.5: Seasonal Evolution of X-band backscatter over Miquelon Lake from TerraSAR-X spotlight mode complex images acquired in 2009 (Spot 71, $\theta_i = 46^\circ$ ). Spotlight mode images were acquired at HH and VV polarizations. TerraSAR-X image ©DLR 2009.....	68
Figure 4.2.6: TerraSAR-X spotlight mode image from April 18, 2009 over Miquelon Lake. North is up. Image is a false color composite composed from R=HH, G=HH, B=VV. Blue indicates high backscatter from VV polarized radar waves. Dark regions indicate absorption of radar waves by open water, wet snow or a flooded ice surface. ....	69
Figure 4.2.7: Full X-band Time Series over Miquelon Lake for 2008/09. Images are incidence angle corrected and are normalized to the conditions found in mid winter (February). Values below the NESZ have been removed from the plot on the right. Red boxes indicates the period of snow melt. Data after snow melt believed to result from ice covered by melt ponds.....	70
Figure 4.2.8: Seasonal Evolution of X-band backscatter over Miquelon Lake in 2009/10. Figure 4.2.8a on the left presents results from one swath (Track 144, $\theta_i = 32^\circ$ ). Figure 4.2.8b on the right presents results from Track 68 ( $\theta_i=43^\circ$ ). Red boxes indicates the period of snow melt.....	70
Figure 4.2.9: Temporal evolution of Ku-band backscatter over Miquelon Lake from the QuikSCAT sensor. The first box (red outline) indicates the period of ice onset, The second box (blue) indicates the initial deposition of snow, the third box (black) indicates the period of snow melt and the four box (shaded dark grey) indicates period of complete ice melt. ....	72
Figure 4.2.10: Semi-hourly air temperature measurements over Miquelon Lake in April 2009 acquired by the CRREL IMB. Note the daily freeze thaw cycles. ....	72
Figure 4.2.11: Left: Landsat 7TM image showing ice present on Miquelon Lake on May 1, 2009. Right: Landsat 5TM image showing no ice on Miquelon Lake on May 9, 2009. Landsat images courtesy of the U.S. Geological Survey [US Geological Survey, 2011]....	73
Figure 4.3.1: Envisat ASAR C-band backscatter response to changing snow depth over the study region in 2008/09 and 2009/10.....	75
Figure 4.3.2: Comparison of X-band backscatter with snow depth over the study site in 2009/10.....	76

Figure 4.3.3: Comparison of X-band lake backscatter with snow depth measurements in the winter of 2009/10 over Miquelon Lake.....	77
Figure 4.3.4: Evolution of Ku-band radar backscatter (db) and CRREL IMB Snow Depth (m) on Miquelon Lake, AB in winter 2008/09. The black box show the period of ice onset and the grey filled box shows ice off period. Negative snow depth indicates melt of the ice surface.....	78
Figure 4.3.5: Scatter plot of Ku-band backscatter versus snow depth measured by the CRREL IMB. Values from after snow melt have been removed in this figure. Red line presents the linear regression fit to the data. ....	79
Figure 4.3.6: Envisat ASAR C-band backscatter response to SWE over different surfaces in 2008/09. SWE was taken from the measurements performed over the lake.....	80
Figure 4.3.7: Envisat ASAR C-band backscatter response to SWE over different surfaces in 2009/10. SWE was taken from the measurements performed over the lake.....	81
Figure 4.3.8: Comparison of X-band backscatter with AMSR-E derived SWE in 2008/09. Symbols indicate different incidence angles. ....	82
Figure 4.3.9: Comparison of X-band backscatter with AMSR-E derived SWE in 2009/10. Symbols indicate different incidence angles. ....	83
Figure 4.3.10: Comparison of QuikSCAT backscatter with AMSR-E and in-situ measurements of SWE over Miquelon Lake, AB in 2008/09.....	84
Figure 4.4.1: Comparison of C-band backscatter and ice thickness of Miquelon Lake, AB. ....	87
Figure 4.4.2: Response of TerraSAR-X backscatter with ice thickness over the Lake in 2008/09.....	88
Figure 4.4.3: Response of TerraSAR-X backscatter with ice thickness over Miquelon Lake in 2009/10. Black symbols denote ice thickness values from interpolated averaged in-situ measurements. Grey symbols are used for ice thicknesses derived from the CRREL IMB.....	89
Figure 4.4.4: Ku-band backscatter correlation with ice thickness over Miquelon Lake. Red (larger) markers indicate values from after the onset of snow melt. ....	90
Figure 4.4.5: Comparison of Envisat ASAR C-band backscatter with ice surface temperature. Temperatures acquired from the CRREL and SAMS IMB in 2008/09 and 2009/10 respectively. Temperatures were taken from the nearest hour to the SAR acquisition.....	91

Figure 4.4.6: X-band backscatter response to changes in the temperature at the snow/ice-interface in 2009/10. ..... 92

Figure 4.4.7: Ku-band backscatter comparison with changes in the snow and ice interface temperature. ..... 93

## List of Symbols, Nomenclature, and Abbreviations

$\sigma^0$	radar backscatter coefficient, or sigma nought.
ASAR	Advanced Synthetic Aperture Radar
$B_{air}$	radar bandwidth in air
$\beta$	thermal diffusivity
dB	Decibels
$c_s$	TerraSAR-X calibration constant variable
co-pol	co-polarization, VV or HH
CoReH2O	Cold Regions Hydrology High-resolution Observatory; a proposed European Space Agency Synthetic Aperture Radar satellite.
cross-pol	cross-polarization, HV or VH
CRREL	Cold Regions Research Engineering Laboratory
DN	Digital Number
DLR	Deutschen Zentrums für Luft- und Raumfahrt, German Aerospace Center
EM	Electromagnetic
$\epsilon'$	Dielectric constant
$\epsilon''$	Dielectric loss
ESA	European Space Agency
$f$	frequency
FDD	freezing degree day(s)
FYI	First-year sea ice
$\gamma$	angle of depression
GHz	Giga-hertz ( $10^9$ hertz)
$h$	height
HH	Horizontal Transmit and Receive polarization, co-polarization
HV	Horizontal Transmit, Vertical Receive polarization, cross-polarization
IMB	Ice Mass Balance buoy
K	Kelvin
$k_0$	Free space wave number
km	kilometers
Ku	Microwave radar waves with frequency between 12 and 18 gigahertz
L	antenna length
$\lambda$	Wavelength
m	Meters
$m_v$	volumetric water volume
MGD	Multi-Looked Ground Range Detected Image (TerraSAR-X)
MYI	Multi-year sea ice
N	number of image looks
NEBN	Noise Estimated Beta Naught
NESZ	Noise Estimated Sigma Zero
NSIDC	National Snow and Ice Data Center
P	depth of penetration
PDD	positive degree day(s)
pol	polarization, polarized
ppt	Parts Per Thousand
psu	Practical Salinity Units

$\rho$	Density
RE	Radiometrically Enhanced (TerraSAR-X)
$R_s$	slant-range
S	Salinity
$\sigma^o$	radar backscatter coefficient
SIR	Shuttle Imaging Radar
SAMS	Scottish Association for Marine Sciences
SAR	Synthetic Aperture Radar
SL	Spot Light
SLC	Single Look Complex
SM	Strip Map
SWE	Snow Water Equivalence
T	Temperature
$\tau$	thermal conductivity
$\theta_i$	angle of incidence
ULS	Upwards looking sonar
V	Volume
VH	Vertical Transmit, Horizontal Receive polarization, cross-polarization
VV	Vertical Transmit and Receive polarization, co-polarization
W	Watts
Z	thickness

## Chapter 1. Introduction

While our ability to monitor snow and ice properties has improved dramatically since the beginning of the satellite era, numerous important parameters remain inadequately measured. New remote sensing platforms and methods are being proposed to address knowledge gaps or improve the parameterization of the state and dynamics of properties of Earth's snow and ice fields. However, data from these new platforms require validation of the mission concept, theory, and applicability. One such mission is the Cold Regions Hydrology High-Resolution Observatory (CoReH<sub>2</sub>O), a proposed European Space Agency (ESA) satellite to improve our knowledge of the state of and changes in Earth's snow and ice fields by using coincident dual-polarization Ku and X-band synthetic aperture radar (SAR) images. In addition to its primary objective of providing improved measurements of snow water equivalence (SWE), the volume of water locked in a snow pack, the mission aims to retrieve other snow and sea ice properties such as the thickness of thin ice in refrozen leads and polynyas and near the marginal ice zone.

### 1.1 Study Context

Seasonally covering  $18 \times 10^6 \text{ km}^2$  in the Antarctic and approximately  $15 \times 10^6 \text{ km}^2$  in the Arctic, sea ice plays a crucial role in the interactions between physical, biological, and chemical processes and systems of this planet [Dieckmann and Hellmer, 2010]. In addition to the vast extent of sea ice, the very properties of sea ice cause it to influence the fluxes of heat, gases, electromagnetic radiation, and momentum between the ocean and atmosphere in the polar regions [Dieckmann and Hellmer, 2010]. The degree of modification to the aforementioned fluxes is strongly influenced by properties of the sea ice from the micro through macro scales [Petrich and Eicken, 2010].

Arguably, one of the most important properties of sea ice is that it is less dense than sea water and thus floats and can cover the polar oceans. As sea ice extent increases and the ice thickens, the heat flux between the ocean and atmosphere is reduced as a result of the insulating effect of sea ice with respect to open water. Additionally, sea ice has an albedo, or reflectivity, that is an order of magnitude greater than that of open water, 0.5 - 0.7 vs. 0.06-0.10, respectively [Perovich, 1996]. Where sea ice forms, its high albedo causes less incoming solar radiation to enter and warm the ocean, resulting in the maintenance of cool temperatures and allows more sea ice to form which reflects more radiation and so forth. This positive feedback loop is called the ice-albedo feedback loop. However, its current negative state, decreasing sea ice extent causing increased solar radiation input to the oceans that induces warming that leads to a further decrease in sea ice extent, is often described (c.f. [Wadhams, 2000]).

Furthermore when sea ice forms and thickens, salts are expelled from the ice during crystal growth and through gravity drainage and brine cell migration lead to the formation of cold, dense saline water in the upper ocean which then sinks and is distributed across the globe [Carsey et al., 1992]. When the relatively low salinity sea ice melts, freshwater is contributed to the upper ocean and can be redistributed altering the ocean buoyancy forcing [Lemke et al., 2007],

At its annual peak extent sea ice covers approximately seven percent of the surface of the Earth, forming an immense biome [Wadhams, 2000]. Sea ice serves as a habitat for a wide variety of organisms from bacteria, viruses, algae and diatoms to various heterotrophic protists to fish, seals, and polar bears [Arrigo et al., 2010; Caron and Gast, 2010; Deming, 2010; Bluhm et al., 2010; Tynan et al., 2010]. Furthermore, sea ice plays an important role in the traditional lifestyles of northern residents as a platform for hunting seals, whales and polar bears and for travel between communities. The presence of sea ice influences shipping and mineral and resource exploitation in the Arctic and is a major hazard to marine activities throughout the Arctic Ocean [Kubat et al., 2003].

Like sea ice, snow is extremely important to our planet and its inhabitants. Snow cover is spatially and temporally extensive with strong seasonal variations. Snow cover extent on land varies from a maximum of  $40 \times 10^6 \text{ km}^2$  in January-February to a minimum extent of  $4 \times 10^6 \text{ km}^2$  in August (including Greenland; [Frei and Robinson, 1999]). As snow cover in the Arctic Ocean requires sea ice as a platform for deposition, the extent of snow on sea ice closely follows seasonal changes in sea ice extent. Snow has an even greater albedo than sea ice (0.7 - 0.9), and a lower thermal conductivity, further modifying the exchange of radiation, heat, and gases between the ocean/land and atmosphere [Perovich, 1996]. The properties of snow influence and the timing of snow deposition influence the aforementioned fluxes, as well as the thermodynamic growth/melt of sea ice. The weight of the snowpack can submerge the ice below the water level. This can affect the biological growth associated with the sea ice and satellite estimates of sea ice thickness. The low thermal conductivity of snow protects plants and animals such as young fir trees, seals and polar bears from the cold atmosphere and from predation [Sturm and Massom, 2010]. The low thermal conductivity of snow also insulates the ice from warm (cold) air temperatures in the spring (fall) and can delay the melt (growth) of the ice.

Snow also has significant hydrological importance, as it contributes to the freshwater budget of the oceans, rivers, lakes and groundwater reservoirs [Lemke et al., 2007; Sturm and Massom, 2010; Rott et al., 2010]. As Figure 1.1.1 reveals, large regions of the world are highly dependent on snow melt as a source of fresh water.

In numerous countries snow cover is crucial to the public utilities sector; for example, in Canada hydroelectric systems supply two-thirds of electrical power generated [NRCan, 2009]. In the Canadian prairies, accurate forecasts of annual runoff are important to maintaining the apportioned limit of water flow between Alberta and Saskatchewan and Saskatchewan and Manitoba as set out in the 1969 Master Agreement on Apportionment and By-Laws, Rules and Procedures [Prairie Provinces Water Board (Canada), 1992]. Snow melt supplies drinking water, water for irrigation and contributes to ground water recharge. SWE, the snow water equivalence of a snow pack represents the mass or depth of water stored in the snow. Knowledge of SWE is important to hydrological forecasters for both water use and power generation management. Unfortunately current snow process models show high uncertainty in the retrieval of parameters such as SWE [Rott et al., 2010].

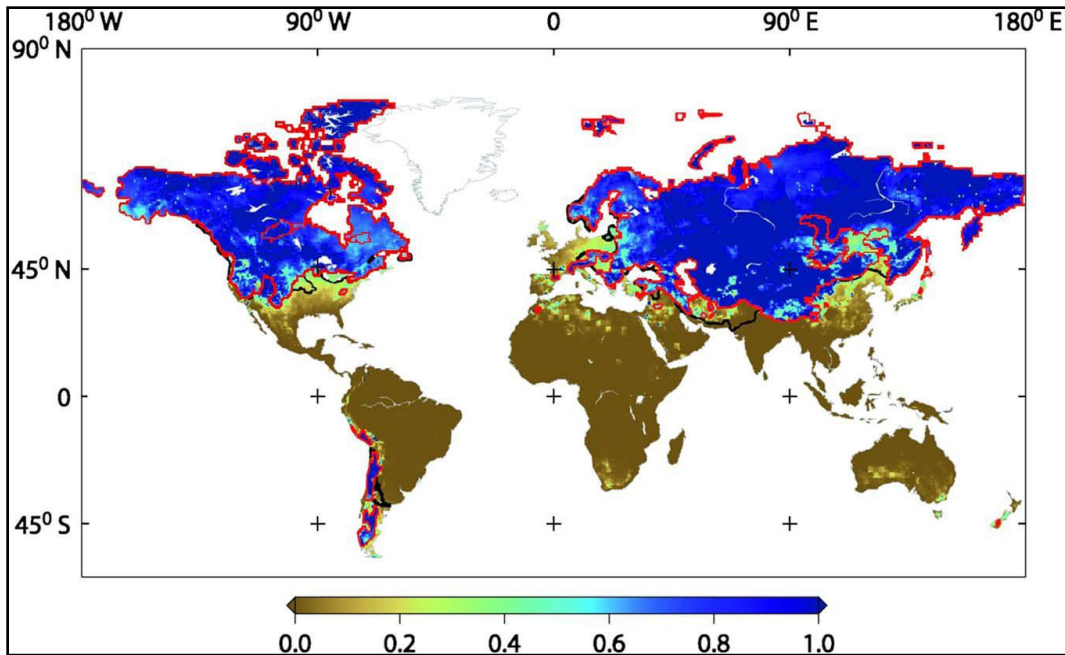


**Figure 1.1.1: Contribution of accumulated annual snowfall to annual runoff.** Black lines indicate regions where water availability is predominantly influenced by snowmelt generated upstream. Reprinted by permission from Macmillan Publishers, Ltd: [Nature]. Barnett, T. P., J. C. Adam, and D. P. Lettenmaier (2005), Potential impacts of a warming climate on water availability in snow-dominated regions Nature, 438(7066), 303-309. Copyright 2005.

Both remote sensing and in-situ measurements have shown that the average sea ice extent and thickness have been decreasing over the past few decades; sea ice extent summer and winter extent have declined at approximately 12%/decade and 3%/decade, respectively [Serreze, 2011; NSIDC, 2011]. Estimates of sea ice thickness from laser altimetry and underwater upward looking sonar (ULS) have revealed that the mean thickness of Arctic sea ice has decreased by 1.6 m over the past 50 years [Kwok and Rothrock, 2009]. Markus et al. (2009) have shown that the length of the sea ice melt season has increased by approximately six days per decade since 1979 [Markus et al., 2009]. Similar decreases in the extent and duration of seasonal snow cover have also been observed (c.f. [Lemke et al., 2007; Brown et al., 2010]). However, decreases in the extent of sea ice and increases in global temperature in the coming decades may result in increased precipitation and therefore increased snow extent and SWE in some regions, including sectors of the Arctic [Barry et al., 2007; Ghatak et al., 2010].

While the role of snow and sea ice in the physical and biogeochemical systems of the planet has been well studied, Earth's cryosphere is experiencing dramatic changes and our ability to retrieve all the parameters of interest and importance for modellers and stakeholders remains incomplete. Properties such as the extent, melt/freeze up of snow and sea ice can be readily obtained at sufficient spatial and temporal resolutions and scales via remote sensing, while the retrieval of other snow and ice properties, such as SWE, thickness/depth, and the discrimination of thin ice is only possible at relatively coarse spatial resolution and uncertainty or are currently not retrievable. For example, SWE is currently retrieved using passive microwave sensors with low spatial resolution [Clissold, 2009; Derksen, 2008]. Furthermore, significant uncertainties exist in the

retrieval of SWE in areas with forest cover, in the arctic tundra, and over sea ice using current methods [Derkzen, 2008; Langlois et al., 2010; Langlois and Barber, 2008; Pulliainen and Hallikainen, 2001; Langlois et al., 2008]. These uncertainties are strongly influenced by the large spatial variability in the physical properties of the region such as surface roughness or canopy coverage, in the dielectric properties of the surface, and the physical and dielectric properties of the snow itself.

Due to the vast scale of sea ice and snow and the large spatial and temporal variability exhibited in their properties, remote sensing is an important tool for the monitoring and measurement of sea ice and snow. Although in-situ measurements are very accurate and precise, logistical and financial constraints limit their spatial and temporal extent. At the cost of some precision, accuracy, and spatial resolution, remote sensing can provide high temporal resolution information over large regions. However, remote sensing methods require validation to ensure the quality, accuracy and precision of the output products are sufficient for the desired usage. Currently, most remote sensing methods for the retrieval of sea ice and snow properties, especially SWE, are based on coarse spatial resolution passive microwave measurements.

### **1.1.1 Cold Regions Hydrology High-Resolution Observatory**

The proposed Cold Regions Hydrology High-Resolution Observatory (CoReH<sub>2</sub>O) satellite mission, will utilize dual polarization X and Ku band radar measurements to provide high spatial and temporal resolution estimates of SWE and other snow and ice properties in order to improve our understanding of their state and variability in space and time as well as our ability to model and forecast these parameters. Current estimates of SWE and other snow and ice properties are largely based on coarse spatial resolution passive microwave sensors, or temporally and spatially sparse in-situ measurements that are extremely expensive to conduct. The scarcity of in-situ measurements of SWE and the coarse spatial resolution passive microwave estimates of SWE fail to sufficiently account for the large observed spatial and temporal variability of SWE and the underlying ground cover. The algorithms for SWE retrieval are strongly affected by sub-pixel land cover mixtures such as the Arctic tundra and in forests [Derkzen, 2008]. CoReH<sub>2</sub>O also aims to improve the retrieval and discrimination of thin sea ice and improve the parameterization of snow on sea ice, both of which are currently deficient. Thin sea ice found in leads, polynyas, and marginal ice zones play an important role in the interactions between the ocean and atmosphere. Polynyas are regions of persistently open water within the ice pack in which large amounts of sea ice are formed. As a result of brine rejection during sea ice formation, polynyas contribute to the formation of dense water [Wadhams, 2000]. Furthermore, up to one half of the total heat exchange between the ocean and atmosphere in the Arctic occurs in polynyas [Wadhams, 2000]. The Ku and X bands sensors proposed for CoReH<sub>2</sub>O have a shorter wavelength than the traditionally used C band SAR systems and should be more sensitive to thin ice and snow properties [Clissold, 2009]. Furthermore, if SWE can be retrieved over sea ice, information on snow loading, snow depth, and the influence of snow on ice mass balance could be assessed at broader spatial scales and at finer resolution than ever before.

### **1.1.2 Saline Lakes and Seas**

Although saline and brackish lakes represent one fifth of Earth's lake area, few studies have been conducted on the development of their snow, ice, and radar backscatter properties [Meybeck, 1995]. Most information has been published for the Baltic Sea, the salinity of which varies between 1 and 9 parts per thousand (ppt; [Leppäranta and Myrberg, 2009; Makynen et al., 2007a; Makynen et al., 2007b; Saloranta, 2000]). However, saline lakes occur throughout the world, with salinities varying from 0.1 to several hundred parts per thousand [Meybeck, 1995]. Saline lakes are common in British Columbia, Alberta, and Saskatchewan [Hammer, 1978; Hammer and Haynes, 1978]. The Baltic Sea, the Sea of Azov in the northern part of the Black Sea, and the Caspian Sea are all brackish water bodies with significant seasonal ice formation [Granskog et al., 2010]. Duarte and others suggested that saline lakes contribute up to half of CO<sub>2</sub> emissions from lakes to the atmosphere [Duarte et al., 2008] due to chemically enhanced emission. Saline lakes and seas have the potential to act as logically accessible and affordable analogues for studying snow on sea-ice and as an alternative to ice tanks which are too small for validation of space-borne sensors.

## **1.2 Study Objectives**

The three main objectives of this study were to:

- 1) Use space-borne radar sensors to validate the core concepts behind the CoReH<sub>2</sub>O satellite mission, including the retrieval of SWE for snow on sea ice, and additional snow and sea ice properties such as the thickness of thin ice. In addition to the proposed Ku and X-band frequencies to be used by CoReH<sub>2</sub>O, C-band imagery will also be examined as it is currently the most widely used and available SAR frequency,
- 2) Study the co-evolution of radar backscatter at multiple frequencies and polarizations and the changing snow and sea ice properties of Miquelon Lake, a saline lake in Alberta.
- 3) Assess the applicability of saline lake ice studies to other brackish water ice regions such as the Baltic Sea. The suitability of Miquelon Lake to serve as a validation and calibration site for sea ice and snow remote sensing projects will also be discussed.

## **1.3 Thesis Structure**

Chapter 2 provides background information regarding the physical and electromagnetic properties of sea ice and snow in the context of microwave remote sensing. Furthermore, a review of multi-polarization and multi-frequency SAR observations of snow on sea ice and sea ice in the context of the frequencies and polarizations utilized in this study is provided. Chapter 3 introduces the study site, data sources and methodology employed in the study. Chapter 4 presents the results and key findings of the analysis with respect to the study objectives. Chapter 5 provides a summary of the results and implications and limitations of the study and finally a discussion of future work.

## Chapter 2. Background and Literature Review

The influence of sea ice on physical, chemical, and biological systems is dependent on its properties at microscopic and macroscopic scales [Petrich and Eicken, 2010]. In order to assess the suitability of Miquelon Lake ice as a proxy for sea ice, an understanding of the properties that govern the role sea ice plays in the environment is necessary. Furthermore, the relevant sea ice and snow properties for satellite radar remote sensing and the retrieval of snow and ice properties from multi-frequency, multi-polarization SAR will be discussed. Additionally, an introduction to RADAR remote sensing and a literature review of important studies that examined snow and ice properties with SAR at C, X, and Ku bands are presented.

### 2.1 Sea Ice

In this section, the formation, growth and melt of sea ice will be discussed along with a discussion of its thermal, physical and dielectric properties. The effect of these properties on radar backscatter is also discussed.

#### 2.1.1 Sea Ice Formation, Growth and Melt

Ice formation is initiated when the temperature of the surface water reaches the freezing point of the water. In the case of sea water with salinity of 34 practical salinity units (psu; or parts per thousand, ppt) the freezing point is -1.86°C [Petrich and Eicken, 2010]. Because the temperature of maximum density disappears when the salinity of the water exceeds 24.7 psu, ice formation in the ocean cannot begin until the surface layer down to the pycnocline is cooled to the freezing point by convection [Wadhams, 2000]. In contrast, in brackish waters such as the Baltic Sea and Miquelon Lake, the maximum density is reached before the freezing temperature, thus as water is cooled towards the freezing point, it sinks and is replaced by warmer water from below that cools rapidly [Wadhams, 2000]. Eventually the cooled water at the surface passes the temperature of maximum density and becomes less dense than the surrounding water and stays at the surface, freezing rapidly [Wadhams, 2000]. Ice formation in less saline waters can therefore occur earlier in the season and more rapidly [Wadhams, 2000]. Ice formation in sea water begins with the formation of ice crystals suspended in the cooled surface layer. These ice crystals are referred to as frazil or grease ice. In calm conditions the frazil ice freezes together to form continuous sheets called nilas. In rough seas, the frazil ice forms pancake ice so called because of their rounded shape and raised edges of the ice pans which form from frazil that is splashed onto the edges of the pancake and freezes. The pancake ice continues to grow from the accretion of frazil ice and pancakes freezing together horizontally or when rafted onto one another. Ice growth continues beneath the ice as congelation ice is added layer upon layer to the bottom [Petrich and Eicken, 2010]. The congelation ice has a columnar crystal structure with vertically elongated crystals, resulting from geometric selection [Petrich and Eicken, 2010; Tucker III et al., 1992]. Salts are rejected to the ice crystal boundaries during ice formation. Brine is also trapped between the vertically elongated crystals in the columnar "skeleton" ice layer, forming brine pockets. Ice can also grow by frazil growth where the frazil crystals and platelets accumulate to the bottom of the ice, or freeze in gaps between rafted pancakes. Thermodynamic ice growth slows over time as the insulating effect of the ice increases with thickness. Dynamic growth, which occurs through the

convergence of pancakes or floes can cause ice thicknesses much greater than the thermodynamically grown ice. These dynamic processes are referred to as rafting and ridging. In rafting, one floe of ice is pushed onto another floe; whereas in ridging, floes are pushed upwards and downwards in an incoherent pattern. Ridging and rafting influence wind and ocean circulation forcing on the ice floe, and in turn the distribution of snow. Furthermore, ridges provide shelter for seals and thus hunting grounds for polar bears, and provide a major obstacle for travel on and through the ice for ships [Tynan et al., 2010; Kubat et al., 2003].

As soon as sea ice is formed, desalinization of the ice begins and the salinity of the ice decreases. Under freezing conditions salinity decreases primarily through gravity drainage of the brine that is trapped in the ice during freeze-up [Wadhams, 2000]. Because ice is less dense than water, the ice surface sits at some height above the water. This height creates a downward pressure gradient that drives the brine out of the ice [Wadhams, 2000]. Furthermore, because the ocean water is relatively warm compared to the atmosphere, the brine salinity and density in the upper ice are higher than in the ice below creating a gradient in density and salinity [Petrich and Eicken, 2010]. The desalinization of the ice requires some interconnectivity between the brine cells, called brine channels (see Figure 4.1.3).

Sea ice melt begins when the ice temperature is raised to the melting point. While the snow cover insulates the ice from warming temperatures for some time, eventually the snow melts away and ice melt begins. The melt from snow and the ice can pool in depressions. Melt ponds and wet snow have a much lower albedo and thus absorb more solar radiation, causing localized increases in ice melt. Ice melt also occurs on the underside of ice floes as energy enters the ocean in leads between the floes warming the water. Recently, Perovich et al. (2011) highlighted the important role of solar heat input to the oceans and bottom melt of sea ice to the changing sea ice mass balance [Perovich et al., 2011]. Their results show a stronger correlation between the input of heat to the ocean and the heat used in bottom melt than the heat input to the ice and heat used in surface melt which is also affected by latent and sensible heat flux and longwave radiation [Perovich et al., 2011]. As the ice and snow melt, some melt water is flushed out through the ice, further reducing the salinity of the ice. A layer of cold freshwater can form below the ice and even be trapped in the bottom topography [Notz et al., 2003]. The interaction of this freshwater with the saline water below it is one of the only mechanisms for summer sea ice growth and can also influence summer-time sea ice thickness measurements by electromagnetic (EM) induction and sonic ranging methods [Notz et al., 2003].

### 2.1.2 Thermal and Electromagnetic Properties of Sea Ice

Sea ice is a heterogeneous mixture of ice, air, and liquid brine with each component influencing the thermal and electromagnetic properties of the mixture. Furthermore the physical properties of the sea ice influence the thermal properties, which in turn can influence the electromagnetic properties.

Sea ice growth is the result of a heat flux from the warm sea water to the cool atmosphere, causing a cooling of the sea water to just below the freezing point. The ability to exchange heat is governed by the thermal conductivity of the medium, and the

temperature gradient across it. Once sea ice has formed, the heat flux between the ocean and atmosphere is strongly influenced by the thermal conductivity of the ice and the brine it contains.

The thermal conductivity of pure ice is given by Equation 1; the conductivity of brine by Equation 2 and the conductivity of sea ice by Equation 3. Equation 3 is based on accurate field measurements but requires knowledge of ice density. Another parameterization, Equation 4, based on salinity and temperature and introduced by Maykut and Untersteiner has been used in numerous major models including the Canadian Ice Service Community Ice-Ocean Model [Maykut and Untersteiner, 1971; Pringle et al., 2007]. In Equation 1 - Equation 4 below,  $\tau$  is the thermal conductivity in Watts per meter per Kelvin ( $W m^{-1} K^{-1}$ ), T is the temperature of the ice in degrees Celsius,  $S_{si}$  is the salinity of the sea ice in parts per thousand (ppt), and  $\rho$  denotes density. The subscripts i, b, si denote pure ice, brine, and sea ice, respectively.

$$\tau_i = 1.16 (1.91 - 8.66 \times 10^{-3} T + 2.97 \times 10^{-5} T^2)$$

**Equation 1: Thermal conductivity of pure ice [Petrich and Eicken, 2010].**

$$\tau_b = 0.4184 (1.25 - 3.0 \times 10^{-2} T + 1.4 \times 10^{-4} T^2) W m^{-1} K^{-1}$$

**Equation 2: Thermal conductivity of brine [Petrich and Eicken, 2010].**

$$\tau_b = \frac{\rho_{si}}{\rho_i} \left( 2.11 - 1.1 \times 10^{-2} T + 0.09 \frac{S_{si}}{T} - \frac{\rho_{si} - \rho_i}{1000} \right) W m^{-1} K^{-1}$$

**Equation 3: Thermal conductivity of brine [Pringle et al., 2007].**

$$\tau_{si} = 2.03 + 0.117 \left( \frac{S_{si}}{T} \right) W m^{-1} K^{-1}$$

**Equation 4: Thermal conductivity of sea ice from [Maykut and Untersteiner, 1971].**

From Equation 1 - Equation 4 one can see that the thermal conductivity of brine is approximately 25% that of pure ice. Therefore, as brine is removed from the ice through gravity drainage in the winter or via melt water flushing in the summer, the thermal conductivity of the ice increases. The brine reduces the thermal conductivity of saline ice with respect to freshwater ice. The thermal conductivity of ice and brine are primarily dependent on temperature and as temperature increases towards the melting point, the thermal conductivity decreases [Wadhams, 2000].

### 2.1.3 Dielectric Properties of Sea Ice

The dielectric properties of particular importance to this study are the dielectric constant, the dielectric loss, and the penetration depth. The relative permittivity,  $\epsilon$ , given in Equation 5 characterizes the electrical properties of a medium that absorbs electromagnetic radiation [Petrich and Eicken, 2010].

$$\epsilon = \epsilon' - j\epsilon''$$

**Equation 5: Relative Permittivity of a medium [Hallikainen and Winebrenner, 1992].**

The real part of the relative permittivity,  $\epsilon'$  or the dielectric constant, describes the contrast with respect to free space ( $\epsilon'_{air} = 1$ ) whereas the imaginary part,  $\epsilon''$  or the dielectric loss factor, describes the electromagnetic loss of the material and  $j = \sqrt{(-1)}$  [Hallikainen and Winebrenner, 1992]. The dielectric constant and loss factors depend

on the frequency of the EM radiation, the composition of the material, and the absorption, scattering, and transmission losses of the medium. In the case of bare sea ice, the salinity, temperature, surface roughness, bubble and brine content of the ice, as well as the temperature, salinity, volume, and orientation of the brine, all affect the relative permittivity and loss factors of the ice [Petricch and Eicken, 2010; Hallikainen and Winebrenner, 1992].

EM radiation incident upon a material can be scattered, absorbed, or transmitted. The depth of penetration or transmission into a material indicates the maximum depth of the medium that contributes to the backscatter coefficient [Hallikainen and Winebrenner, 1992]. In Equation 6, the penetration depth,  $\delta p$ , is defined as the depth where the ratio of the power transmitted at the penetration depth ( $P(\delta p)$ ) and the power transmitted just below the surface ( $P(0+)$ ) is  $1/\epsilon'$ . If one ignores scattering within the medium and assumes the absorption constant of the radiation is independent of depth into the medium, then the penetration depth can be approximated by Equation 7, where  $K_0 = 2\pi/\lambda$  and  $\lambda$  is the wavelength [Hallikainen and Winebrenner, 1992].

$$\frac{P(\delta p)}{P(0+)} = \frac{1}{\epsilon'}$$

**Equation 6: Penetration Depth of EM radiation [Hallikainen and Winebrenner, 1992].**

$$\delta p = \frac{\sqrt{\epsilon'}}{K_0 \epsilon''}; \epsilon'' \ll \epsilon'$$

**Equation 7: Penetration depth of EM radiation [Hallikainen and Winebrenner, 1992].**

Figure 2.1.1 illustrates the depth of penetration of microwave energy into first-year sea ice (FYI) and multi-year sea ice (MYI) with different salinities as a function of frequency from Hallikainen et al. (1992). As frequency increases, the depth of penetration decreases (Figure 2.1.1, Figure 2.2.2).

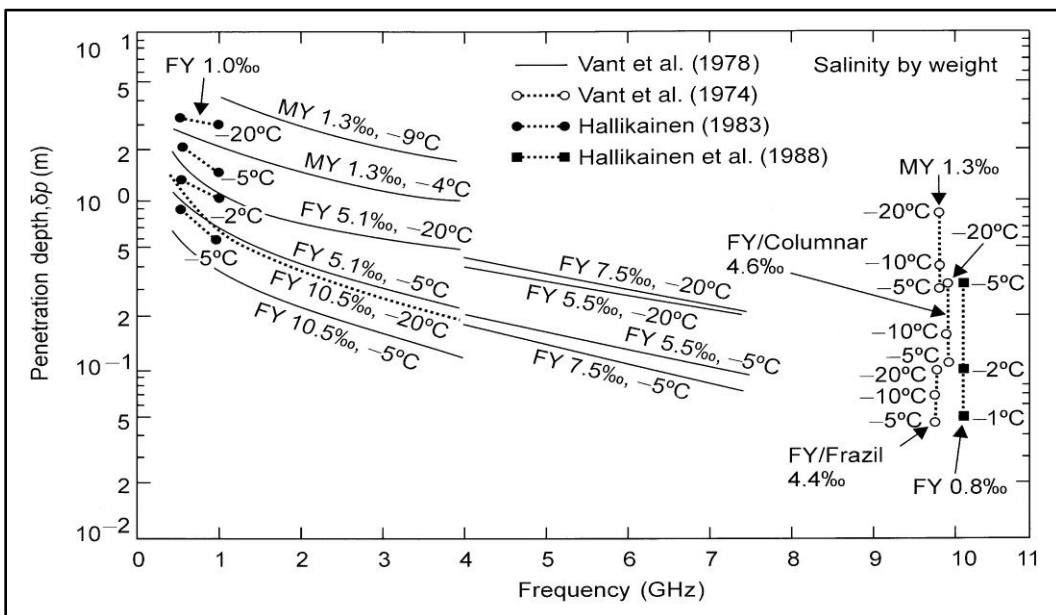


**Figure 2.1.1: Radar penetration depth into sea ice [Hallikainen and Winebrenner, 1992].**  
Adapted with permission from [Petricch and Eicken, 2010].

Figure 2.1.1 reveals that the penetration depth into FYI is limited as a result of high dielectric loss due to the higher salinity. The penetration depth in MYI is greater due to the lower salinity and brine content of the upper ice [Hallikainen and Winebrenner, 1992]. Penetration into MYI can be on the order of several tens of centimeters to over a meter, depending on the frequency [Hallikainen and Winebrenner, 1992]. As lower salinity reduces dielectric loss, the penetration depth in low salinity ice from brackish waters such as the Baltic Sea or Miquelon Lake is greater than observed for FYI in the Arctic.

Figure 2.1.2 presents values of the dielectric constant and loss factor for sea ice at 4 Gigahertz (GHz) and 10GHz as a function of temperature and salinity of the ice [Hallikainen and Winebrenner, 1992]. The figure illustrates that as temperature increases, both the dielectric constant and loss factors increase. However, the dielectric loss factor increases more rapidly. Furthermore, the dielectric constant and loss increase with increasing salinity. As salinity and temperature increase brine volume increases.

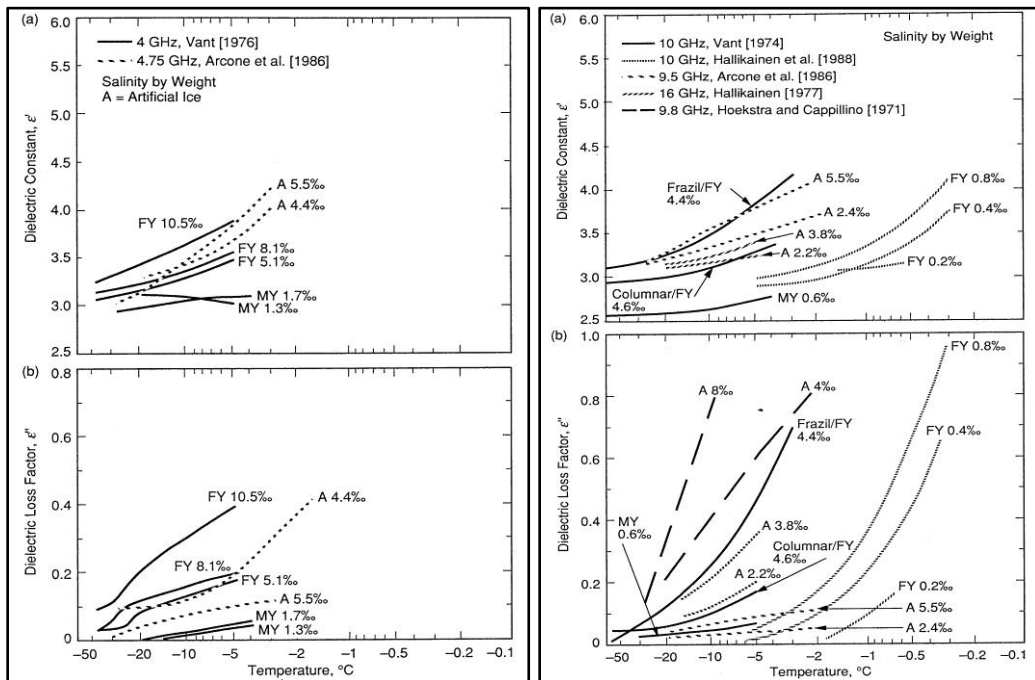


**Figure 2.1.2:** Dielectric constant and loss factors for sea ice at 4 and 10 GHz on left and right respectively [Hallikainen and Winebrenner, 1992].

Equation 8 and Equation 9 present empirical formulae for the dielectric constant and dielectric loss factor of sea ice that have been developed based on the brine volume ( $V_b$ ) of ice [Hallikainen and Winebrenner, 1992]. The brine volume is dependent on the temperature and salinity of the ice (Equation 10; [Hallikainen and Winebrenner, 1992]).

$$4\text{GHz}: \begin{cases} \varepsilon'_{si} = 3.05 + 0.0072V_b \\ \varepsilon''_{si} = 0.02 + 0.0033V_b \end{cases}$$

**Equation 8: Empirical equation for the dielectric constant and dielectric loss factor of sea ice observed at 4 GHz based on brine volume,  $V_b$  [Hallikainen and Winebrenner, 1992].**

$$10 \text{ GHz: } \begin{cases} \varepsilon'_{si} = 3.0 + 0.012V_b \\ \varepsilon''_{si} = 0.0 + 0.010V_b \end{cases}$$

**Equation 9: Empirical equation for the dielectric constant and dielectric loss factor of sea ice observed at 10GHz based on relative brine volume,  $V_b$  [Hallikainen and Winebrenner, 1992].**

### 2.1.4 Brine Inclusions

From the aforementioned dielectric equations, it is clear that brine inclusions strongly influence the dielectric properties of sea ice. The conductive salts in brine result in a higher dielectric loss factor than in pure water or ice, attenuating the incident EM radiation [Hallikainen and Winebrenner, 1992]. Brine volume and salinity can be determined empirically from sea ice temperature and bulk salinity using Equation 10 - Equation 13, and the coefficients in Table 2.1.1 developed by Cox and Weeks [Cox and Weeks, 1983] and Leppäranta and Manninen in 1988 [Leppäranta and Myrberg, 2009; Leppäranta and Manninen, 1988].  $V_b$  is the brine volume of the ice,  $V_a$  is the volume of the air pockets in the ice, and  $\rho$ ,  $S$ , and  $T$  are density in  $\text{kg m}^{-3}$ , salinity in ppt and temperature in degrees Celsius, respectively. The subscripts i, b, and si denote pure ice, brine, and sea ice, respectively.

$$\frac{V_b}{V} = \left(1 - \frac{V_a}{V}\right) \frac{\rho_i S_{si}}{F_1(T) - \rho_i S_{si} F_2(T)}, \text{ where: } F_i(T) = a_i + b_i T + c_i T^2 + d_i T^3$$

**Equation 10: Calculation of brine volume fraction of a sea ice sample [Leppäranta and Myrberg, 2009]. Coefficients for a, b, c, d are listed in Table 2.3.1.**

$$\rho_i = \frac{(917 - 0.1403 T)}{1000}$$

**Equation 11: Density of pure ice adapted from [Petrich and Eicken, 2010].**

$$S_b = \left(1 - \frac{54.11}{T}\right)^{-1} \times 1000; T \geq -23$$

**Equation 12: Brine Salinity Approximation adapted from [Petrich and Eicken, 2010].**

$$\rho_b = 1000 + 0.8S_b$$

**Equation 13: Brine Density approximation adapted from [Petrich and Eicken, 2010].**

Figure 2.1.3 presents the change in brine salinity with temperature that results from Equation 12. As temperature increases the brine salinity decreases. However, the brine volume increases with increasing temperature. Increases in the brine volume result in increased dielectric loss but also an increase in the dielectric constant.

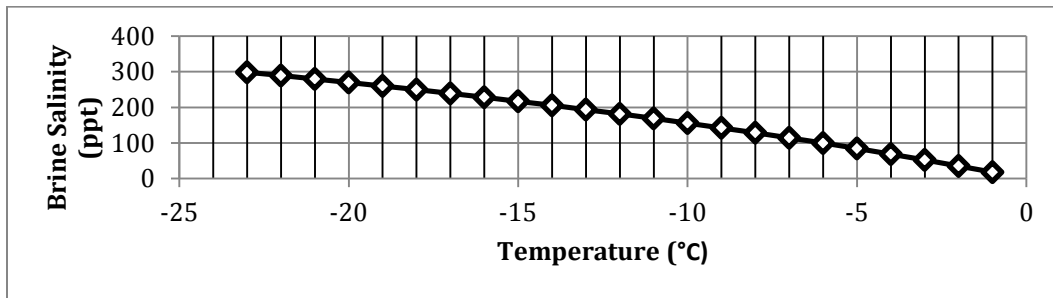


**Figure 2.1.3: Brine salinity as a function of temperature. Adapted using Equation 12 from [Petrich and Eicken, 2010].**

As one can see, the brine volume, salinity, and temperature are intricately linked to the thermal and electromagnetic properties of sea ice. Furthermore the effects are both competitive and additive with increased temperature leading to increase brine volume, which raises the dielectric constant and the dielectric loss.

**Table 2.1.1: Coefficients for functions  $F_i(T)$  for different temperature intervals. Adapted from [Cox and Weeks, 1983; Leppäranta and Manninen, 1988; Petrich and Eicken, 2010]**

T (°C)	a <sub>1</sub>	b <sub>1</sub>	c <sub>1</sub>	d <sub>1</sub>
<b>0 ≥ T &gt; -2</b>	-0.041221	-18.407	0.58402	0.21454
<b>-2 ≥ T ≥ -22.9</b>	-4.732	-22.45	-0.6397	-0.01074
<b>-22.9 &gt; T ≥ -30</b>	9899	1309	55.27	0.7160
T (°C)	a <sub>2</sub>	b <sub>2</sub>	c <sub>2</sub>	d <sub>2</sub>
<b>0 ≥ T &gt; -2</b>	0.090312	-0.016111	$1.2291 \times 10^{-4}$	$1.3603 \times 10^{-4}$
<b>-2 ≥ T ≥ -22.9</b>	0.08903	-0.01763	$-5.330 \times 10^{-4}$	$-8.801 \times 10^{-6}$
<b>-22.9 &gt; T ≥ -30</b>	8.547	1.089	0.04518	$5.819 \times 10^{-4}$

### 2.1.5 Air Bubbles

In addition to the salinity, brine content and temperature, other physical properties of the ice such as air bubbles and surface roughness also influence the backscatter from sea ice. Air bubble content increases due to desalinization as the removed brine is replaced by air. As a result, the penetration depth of EM radiation increases due to the decrease in dielectric loss. The low dielectric loss factor of air bubbles can result in multiple diffuse scattering within the volume of ice as long as the salinity is low, such as in MYI [Hallikainen and Winebrenner, 1992]. As penetration depth increases, the number of scatterers encountered within the volume of the ice pack by the EM radiation increases, and thus backscatter increases. Seasonal ice formed from brackish waters, such as Miquelon Lake should not contain significant air bubble content as a result of minimal time for brine rejection and thus volume scattering from the ice would be minimal. Furthermore, because of its low salinity and thus lower dielectric loss, the penetration depth through such ice would be greater than that for typical FYI in the Arctic.

## 2.2 Snow

In this section the physical, thermal and dielectric properties of snow are presented along with a discussion of their influence on radar backscatter. It will be shown that snow properties exhibit co-variation and a strong linkage to the sea ice.

While snow is extensive in the marine and terrestrial environments, we will focus on the properties of snow over sea ice. Sea ice is required as a platform for snow to exist in the marine system. The snow cover immediately begins to modify the interactions between the ocean, sea ice and atmosphere. Snow is a mixture of ice crystals, air, liquid water, and under certain conditions can contain brine. The parameters of main interest with regards to sea ice remote sensing and influence on sea ice properties and processes are thermal conductivity, electromagnetic properties and a host of physical properties including depth, density, grain size, and wetness. The properties of snow are highly spatially and temporally variable and intricately linked. For instance, the density of snow is typically between 10 and 500 kgm<sup>-3</sup>; however, icy layers within the snow pack can

have densities approaching  $800 \text{ kgm}^{-3}$  [Sturm and Massom, 2010]. Furthermore, the density of snow evolves over time as a result of changing crystal structure, settling and compaction, leading to changes in other properties. However, records from Russian drifting stations in the Arctic Ocean from 1954-1991 indicate that the average bulk density of snow is largely similar throughout the Arctic, increasing from  $250 \text{ kgm}^{-3}$  to  $320 \text{ kgm}^{-3}$  from September to May [Warren et al., 1999]. However local variations in snow density can be much greater due to windstorms, icy or slush layers.

The depth of snow is also highly variable in space and time. Local topography can play a large role in the distribution and redistribution of snowfall; for instance, on the windward and lee side of ridges, large snowdrifts with depths of several meters can occur. However, the average snow depth for the Arctic is approximately 0.36 m in May with some regional differences [Warren et al., 1999]. Warren et al. (1999) noted that the snow depth is usually greater off the north coast of Ellesmere Island and Greenland than over the Eurasian Arctic and that the time of maximum snow depth occurs later in Eastern Arctic Canada [Warren et al., 1999].

The mass of snow is another important property of a snow pack. Snow can press the ice surface below the water level causing flooding. This reduction in ice surface elevation adds a significant uncertainty to laser and radar altimetry retrievals of sea ice thickness. Furthermore, both the density and thickness of a snowpack are important considerations for the exchange of energy between the atmosphere, snow, sea ice and ocean. SWE, the snow water equivalent of a snowpack, provides measurements of the mass of a snowpack or the equivalent water depth that would result from the melt of the snow pack. SWE is calculated as either:

$$SWE = Z_s \times \rho_s \quad \text{or} \quad SWE = \frac{Z_s \times \rho_s}{\rho_w}$$

**Equation 14: Snow water equivalence formulas. The leftmost equation provides SWE in units of  $\text{kgm}^{-2}$  and the rightmost equation provides SWE in m depth [Colbeck et al., 1990].**

where Z is thickness, and the subscripts s and w refer to snow and water, respectively.

The snow climatology by Warren et al. gives an average SWE of  $11 \text{ gcm}^{-2}$  for the Arctic [Warren et al., 1999]. Currently, coarse spatial resolution SWE products are widely available from passive microwave sensors such as AMSR-E [Derksen, 2008]. As aforementioned, these SWE products exhibit significant uncertainty over regions with forest, in lake filled tundra regions and are not computed for sea ice.

Snow can be classified by a wide variety of variables including density, structure, crystal type, and hardness. Six types of snow are typically observed over sea ice, new snow, fine-grained snow, wind slab, faceted grain/depth hoar, icy layers, and damp/wet snow/slush [Sturm and Massom, 2010]. The last five types evolve from the deposited new snow layer. Wet snow and slush can form near the snow and ice interface as a result of brine wicking and flooding. Flooding occurs when the mass of the snow on sea ice is sufficient to lower the freeboard of the ice below the water surface. The water layer can refreeze or be wicked upwards due to the upward thermal and vapour gradients within the snow pack (see Section 2.2.1 below). The refrozen flooded snow is called snow-ice. Ice formed from melting snow or precipitation is called superimposed ice.

### 2.2.1 Thermal Modification and Evolution of Snow Properties

A snowpack begins with the deposition of new snow whose density is highly dependent on the wind conditions at the time of deposition. Under calm conditions, the snow is deposited and the original dendritic crystal structure can remain intact. However, the presence of wind causes fragmentation of these snow crystals and compaction of the deposited snow. Over time the snow becomes more dense as the snow settles under gravity, is compacted by further deposition of snow, wind acts to compress the snow by destroying grains, or through metamorphism. The density of new snow is on the order of 10 to 100  $\text{kgm}^{-3}$  with higher values associated with deposition in wind. Fine grained snow can be formed through deposition of snow in the presence of wind, the Kelvin Effect where vapour diffusion moves water from branch points to cusps, and through destructive metamorphism (i.e. equilibrium growth) in which mild temperature gradients cause water vapour to move up through the snow to be deposited on the underside of snow crystals [Sturm and Massom, 2010]. The density of fine-grained snow is up to 350  $\text{kgm}^{-3}$  [Sturm and Massom, 2010].

Wind slab forms through the action of strong winds on a snow pack leading to densification by destruction of crystal structure and compaction. The resulting rounded crystals bond together through sintering and the resulting snow layer density can be above 400  $\text{kgm}^{-3}$ .

In Error! Reference source not found. an example of a typical snow pit profile and a close up of depth hoar crystals are presented. In the profile photo, a pit has been dug behind the imaged wall to allow light to shine through. Several layers can be readily distinguished in this image. From top (air) to bottom (ice), the layers include new snow (1), windslab (2), depth hoar (3) and an icy layer (4). The depth hoar crystals on Miquelon Lake were very well developed by March 10, 2010 showing crystals up to 1 cm in diameter. The crystals exhibited the typical cusp shape of depth hoar crystals.

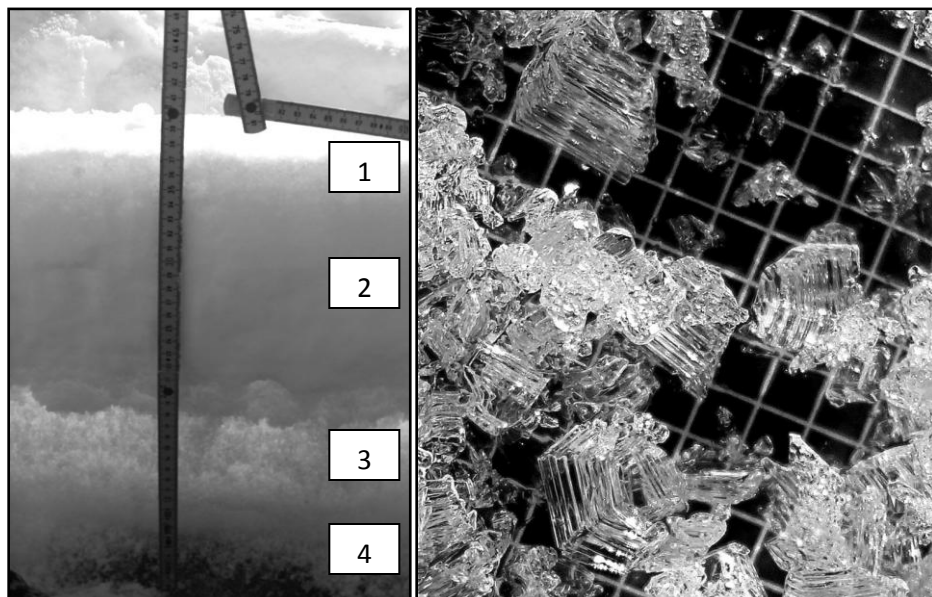


Figure 2.2.1: Left: Snow profile over Miquelon Lake from March 10, 2010. Right: Depth hoar snow crystals observed in the snowpack on Miquelon Lake. Background grid is 3mm. Image acquired on March 10, 2010.

Depth hoar results from constructive metamorphism in which large temperature gradients ( $> 25^{\circ}Cm^{-1}$ ) cause water vapour density gradients leading to the growth of faceted grains [Sturm and Massom, 2010]. The facets in the grains indicate growth is limited by crystal geometry and growth mechanisms rather than vapour supply [Sturm and Massom, 2010].

Icy layers within the snow pack form from the refreezing of liquid water. The liquid water can be derived from melting snow, rain/sleet or freezing mist, even if the temperature is below the freezing point. While ice layers represent a small fraction of a snow pack they have a large influence, dramatically altering the thermal conductivity and reducing vapour flux leading to the preferential development of depth hoar [Massom et al., 2001; Sturm et al., 2002b]. The presence of superimposed ice can also be considered an icy layer. Superimposed ice forms from melting of the snow that has already been deposited on the ice [Sturm and Massom, 2010]. While the density of the icy layers is high, these layers are often under sampled due to the difficulty of acquisition. Another important icy layer is snow-ice which forms when sea water floods the ice surface when the sea ice surface is actually below the water level due to the weight of snow on the ice [Sturm and Massom, 2010]. The sea water floods the snowpack and then refreezes. Snow-ice can represent 25-35% of the total thickness of sea ice in the Baltic Sea [Granskog et al., 2003].

Damp snow and slush result from the presence of liquid water within a snowpack. Snow packs can be classified as dry (0 %), moist (<3%), wet (3-8%), very wet (8-15%) or saturated (>15%) based on the percentage of liquid water [Colbeck et al., 1990], or as being under two distinct wetting regimes, pendular and funicular [Sturm and Massom, 2010]. The pendular regime is typically defined as snow with less than three percent liquid water by volume. Under the pendular regime, liquid water is found at the joins between snow crystals while the pore spaces remain air filled [Sturm and Massom, 2010]. Under the funicular regime, air is found as isolated bubbles and water films are continuous. The presence of liquid water strongly affects the thermal and electromagnetic properties of the snow pack.

The seasonal snowpack evolves from fresh snow to metamorphosed snow over the course of the winter through the various processes described above. On Arctic sea ice, one typically encounters a thick wind slab layer that may be overlain with recent snow if conditions have been calm. Underneath the wind slab a thick layer of depth hoar is usually observed. Finally, near the snow/ice interface one can find icy layers and snow-ice layers with extremely high density. Snow-ice is rare in the Arctic but very common in the Baltic Sea and in the Antarctic [Massom et al., 2001; Granskog et al., 2003]. Similar patterns of seasonal snow development occur over land and lake ice, as thermal gradients often exist within the snow pack.

### 2.2.2 Thermal Properties of Snow

The thermal and electromagnetic properties of a snow pack are the result of the mixed composition of snow, air, ice, liquid water and even brine and structure properties of the snowpack such as density, grain size and depth. Typical values for the effective thermal conductivity of snow range from 0.1 to  $0.6 \text{ Wm}^{-1}\text{K}^{-1}$ , or an order of magnitude smaller than that of ice [Sturm et al., 2002a; Sturm et al., 2006]. The lowest and highest

values of thermal conductivity are associated with depth hoar and wind slab, respectively [Sturm and Massom, 2010]. These two types of snow are the most prevalent on Arctic sea ice and their respective contribution to the snowpack strongly influences factors such as the growth and melt rates of sea ice [Sturm et al., 2006]. The effective conductivity of a snowpack has been empirically related to snow density ( $\rho_s$ ) as per Equation 15 below.

$$\tau_{eff} = 0.138 - 0.00101\rho_s + 3.233 \times 10^{-6}\rho_s^2$$

**Equation 15: Empirical formula for the effective conductivity of snow based on snow density.**  
Adapted from [Sturm and Massom, 2010].

In addition to the rate of heat transfer in a snow pack, the diffusion of heat through a snowpack or its thermal diffusivity ( $\beta$ ) is another important parameter and can be related to the effective thermal conductivity ( $\tau_{eff}$ ) and snow density ( $\rho_s$ ) as in Equation 16 below [Sturm and Massom, 2010].

$$\beta_s = 5.08 \times 10^{-4} \frac{\tau_{eff}}{\rho_s}$$

**Equation 16: Empirical equation for the thermal diffusivity of snow.**  
From [Sturm and Massom, 2010].

### 2.2.3 Dielectric Properties of Snow

In addition to influencing thermal exchange between the atmosphere and ice, snow also affects the dielectric properties of sea ice. When discussing the dielectric properties of snow it is important to distinguish between wet and dry snow. The dielectric loss factor increases sharply with the presence of liquid water such that even low liquid water volumes, just one to three percent by volume, can result in significant absorption of EM radiation [Hallikainen and Winebrenner, 1992]. Equation 17 below presents an empirical formula for determining the dielectric constant of dry snow ( $\epsilon'_{ds}$ ) based on snow density ( $\rho_s$ ) at frequencies between 3 and 37 GHz [Hallikainen et al., 1986].

$$\epsilon'_{ds} = \begin{cases} 1 + 1.9\rho_{ds}, & \rho_{ds} \leq 0.5 \text{ gcm}^{-3} \\ 0.51 + 2.88\rho_{ds}, & \rho_{ds} \geq 0.5 \text{ gcm}^{-3} \end{cases}$$

**Equation 17: Empirical formula for the dielectric constant of dry snow.**  
Adapted from [Hallikainen et al., 1986].

While the dielectric constant of dry snow depends only on the density of the snow, the dielectric loss factor is dependent on frequency ( $f$ ), temperature ( $T$ ), and density ( $\rho_s$ ; [Tiuri et al., 1984]; Equation 18).

$$\epsilon''_{ds} = 1.59 \times 10^6 [0.52\rho_{ds} + 0.62\rho_{ds}^2] \times [f^{-1} + 1.23 \times 10^{-14}\sqrt{f}] e^{0.036T}$$

**Equation 18: Dielectric loss factor of dry snow.** Adapted from [Tiuri et al., 1984].

The dielectric permittivity of wet snow (is dependent on frequency, temperature, water content, snow density, the shape of snow crystals and the shape of inclusions of water [Hallikainen and Winebrenner, 1992]. Since the dielectric permittivity of water is much higher than that of ice or air, the water content dominates the dielectric properties of wet snow. Equation 19 describes the calculation of the dielectric constant and loss of wet snow ( $\epsilon'_{ds}$  and  $\epsilon''_{ds}$ , respectively) for frequencies below 15 GHz where  $f$  is the

frequency of the EM radiation, T is the temperature in degrees Celsius,  $m_v$  is the liquid water content of the snow, and  $\rho_s$  is the density in  $\text{kgm}^{-3}$ .

$$\varepsilon'_{ws} = A + \frac{Bm_v^x}{1 + (f/f_0)^2} \quad (19a)$$

$$\varepsilon''_{ws} = \frac{C(f/f_0)m_v^x}{1 + (f/f_0)^2} \quad (19b)$$

$$A = 1.0 + 1.83\rho_{ds} + 0.02A_1 m_v^{1.015} + B_1 \quad (19c)$$

$$B = 0.073A_1 \quad (19d)$$

$$C = 0.073A_2 \quad (19e)$$

$$X = 1.31 \quad (19f)$$

$$f_0 = 9.07\text{GHz} \quad (19g)$$

$$A_1 = A_2 = 1.0; B_1 = 0 \quad (19h)$$

**Equation 19a-h: Dielectric Properties of Wet Snow from Debye-Like model for frequencies below 15 GHz.** Adapted from [Hallikainen et al., 1986; Hallikainen and Winebrenner, 1992].

The penetration of radar waves into a medium can be modeled following [Ulaby et al., 1984] where  $\delta p$  is the penetration depth, and  $\lambda_o$  is the wavelength in free space. For snow, the values of  $\varepsilon'$  and  $\varepsilon''$  are taken from equations 17, 18 and 19 above [Hallikainen et al., 1986; Tiuri et al., 1984].

$$\delta p = \frac{\lambda_o}{4\pi} \left\{ \frac{\varepsilon'}{2} \left[ \left( 1 + \left( \frac{\varepsilon''}{\varepsilon'} \right)^2 \right)^{1/2} - 1 \right] \right\}^{-1/2}$$

**Equation 20: Penetration depth of microwave radiation into snow from [Ulaby et al., 1984].**

As can be seen from Equations 17 - 20, snow can influence the EM radiation incident upon sea ice through its dielectric properties. As the dielectric loss factor of dry snow is very low, volume scattering can occur within the snowpack, contributing to radar backscatter values [Sturm and Massom, 2010]. When liquid water is present in the snow pack, the dielectric loss factor increases and the penetration depth is greatly reduced (Figure 2.2.2; [Hallikainen and Winebrenner, 1992; Ulaby et al., 1984]). Figure 2.2.2 illustrates the frequency and liquid water content dependence of the penetration depth of electromagnetic radiation into a medium such as wet snow. Figure 2.2.2 was generated using Equation 19 Equation 20 assuming a snow density of  $350 \text{ kgm}^{-3}$ .

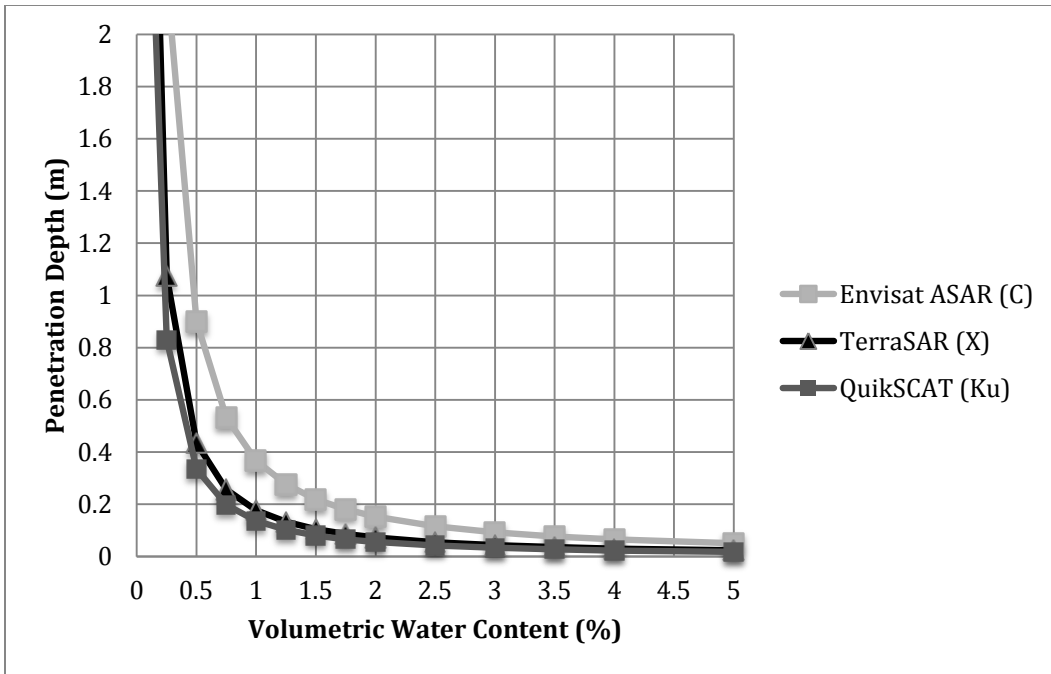


**Figure 2.2.2: Penetration depth of C, X, Ku radar waves into wet snow. Adapted from [Hallikainen et al., 1986; Tiuri et al., 1984; Ulaby et al., 1984].**

Snow can also indirectly influence the dielectric and thermal properties of the sea ice. The insulative effect of snow resulting from its low thermal conductivity leads to an increase in the snow/ice-interface temperature. As was shown in Section 2.2, warmer temperatures result in increased brine volume in the sea ice. Furthermore, brine from the surface layer of ice can be wicked into the snow via capillary suction [Perovich and Richter-Menge, 1994]. The brine layer leads to a moist snow layer but also can create a rough layer; variations in the temperature and salinity of this layer can result in large dielectric variations [Shokr and Barber, 1994].

Arslan et al. (2011) recently modelled the effects of snowpack parameters and layering on X and Ku-band backscatter and found that grain size is one of the most critical parameters for accurate SWE retrieval [Arslan et al., 2011]. Grain size was found to have a similar influence at both co- and cross-polarizations and for X and Ku-band [Arslan et al., 2011]. Furthermore, they found that the influence of snow density on backscatter has a minimal effect on the retrieval of SWE.

Snow and sea ice properties dramatically influence the global climate system through modification of the exchange of energy, gases, and radiation between the ocean, the sea ice and the atmosphere. The physical properties of snow and sea ice are exploited in the field of remote sensing for monitoring the spatial and temporal variability of snow, ice and associated features. Numerous techniques for monitoring snow and ice exist, this study and Section 2.3 highlight the use of radar remote sensing and the influence of the various snow and ice properties on radar backscatter.

### 2.3 RADAR

The large spatial and temporal range of the variability and extent in the properties of snow and ice requires a tool capable of covering large regions with high spatial and

temporal resolution. Remote sensing can meet these requirements making it a valuable tool for monitoring snow and ice. While information on sea ice and snow can be gathered throughout large parts of the electromagnetic spectrum, microwave remote sensing is particularly suited for the task. RADAR or Radio Detection And Ranging operates at the microwave portion of the electromagnetic spectrum from 0.3 to 200 GHz (1.00 m - 0.0015 m wavelengths). The atmosphere is largely transparent to radiation throughout most of the microwave spectrum as is shown in Figure 2.3.1 below. Furthermore, most microwave frequencies are relatively unaffected by clouds and precipitation. The sensitivity to clouds and precipitation increases with increasing frequency. Only very heavy precipitation events are visible in C band imagery, while at Ku-band blowing snow and light rain can influence backscatter. Finally, the complete darkness of polar winters restricts the usefulness of data in the visible portion of the spectrum while active radar sensors emit radiation and measure the amount that is returned.

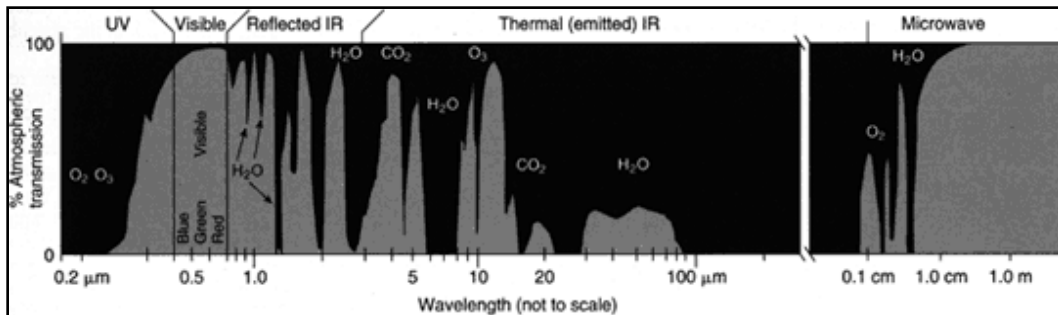


**Figure 2.3.1: Atmospheric Transmission of the Electromagnetic Spectrum. Image Courtesy of [NASA Earth Observatory, 2011].**

### 2.3.1 Introduction to Microwave Remote Sensing

In this section (2.3) the fundamentals of microwave remote sensing are introduced. The difference between active and passive systems, real and synthetic aperture systems and the basics of microwave backscatter imagery are explained. The influence of snow and sea ice properties on microwave backscatter and image interpretation are presented. Lastly a thorough literature review of polarimetric multi-frequency observations of snow and sea ice properties is presented to give background on previous work and illustrate short comings in the previous work regarding the retrieval of the properties of snow on sea ice.

### 2.3.2 Active vs. Passive Microwave Sensors

Remote sensing of electromagnetic radiation in the microwave range occurs through two main sensor systems, active and passive. Passive microwave sensors measure the amount of microwave radiation emitted by an object. However, as the amount and intensity of microwave radiation emitted by the Earth is low, passive microwave sensors require coarse spatial resolution of several kilometers to keep the signal to noise ratio great enough for meaningful data. However, high sensitivity passive microwave sensors have been developed and combined with their coarse spatial resolution and large image swaths, high temporal resolution and broad spatial coverage is achieved.

In contrast, active sensors can achieve much higher spatial resolution at the cost of spatial and temporal coverage because they actively emit electromagnetic radiation to Earth's surface and measure the strength of the returned signal which is called backscatter. Backscatter is highly dependent on the properties of the surface. Active microwave sensors typically operate at Ka to L band (40 to 0.3 GHz or 0.75 cm to 100 cm wavelengths) with imaging sensors commonly operating at C, X, or L bands. Table 2.1 below presents the frequencies and wavelengths commonly used by active microwave sensors and some of the past and current sensors that were operated at those frequencies.

**Table 2.3.1: Radar Band Designations with nominal frequency range and corresponding wavelength. Furthermore table shows widely used satellite sensors for certain bands. Table created using data from [IEEE, 2003].**

RADAR Band Designation	Frequency ( $\nu$ ) GHz	Wavelength ( $\lambda$ ) (m)	Satellite/Sensor
K <sub>a</sub>	27 – 40	0.0111 – 0.0075	
K	18 – 27	0.0167 - 0.0111	
K <sub>u</sub>	12 – 18	0.025 - 0.0167	QuikSCAT/SeaWinds
X	8 – 12	0.0375 – 0.025	TerraSAR-X; TanDEM-X
C	4 – 8	0.075 – 0.0375	ERS1/2; Envisat/ASAR; RADARSAT-1/2
S	2 – 4	0.15 – 0.075	
L	1-2	0.30 – 0.15	JERS-1; ALOS PALSAR

In a real aperture radar system, the along-track resolution is proportional to the slant-range to the object, and inversely proportional to the angular beam width (determined by the antenna length). Slant-range is the distance to the surface along the path of the radar wave, i.e. not at nadir:

$$R_{a_{RAR}} = \frac{R_s \times \lambda}{L}$$

**Equation 21: Azimuth resolution equation for a real aperture radar. Adapted from [Jensen, 2007].**  $R_{a_{RAR}}$  is azimuth resolution of a real aperture radar,  $R_s$  is the range to the object in slant-range,  $\lambda$  is the wavelength of emitted microwave pulse, and  $L$  is the length of the antenna.

In contrast, the azimuth resolution of a synthetic aperture radar system is dependent on the length of the antenna and the number of image looks:

$$R_{a_{SAR}} = N \frac{L}{2}$$

**Equation 22: Azimuth resolution equation for synthetic aperture radar systems. Adapted from [Jensen, 2007].**  $R_{a_{SAR}}$  is the azimuth resolution of a synthetic aperture radar,  $N$  is the number of image looks,  $L$  is the length of the antenna.

As Equation 22 suggests, the azimuth resolution of a SAR system is independent of the range to the target. To demonstrate the power of SAR processing, consider a high resolution TerraSAR-X Spotlight mode dual polarization image acquired over Miquelon Lake. To achieve the 3.2 m resolution of the final product, a RAR antenna length of nearly 7 kilometers would be required.

Figure 2.3.2 illustrates the formation of a SAR image of a point target. The target is sensed multiple times as the sensor passes overhead. These individual measurements are combined using the Doppler principle to form a single high-resolution signal for the target [Canada Centre for Remote Sensing, Natural Resources Canada, 2001].

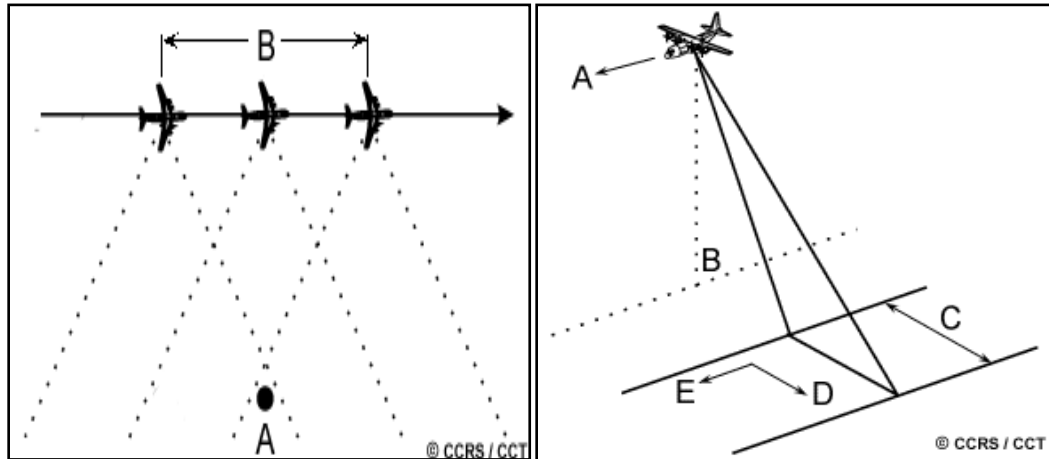


Figure 2.3.2: Left: SAR image formation. Right: Typical SAR system geometry. Figure from [Canada Centre for Remote Sensing, Natural Resources Canada, 2001]. A represents the flight direction, B the nadir point directly below the platform, C the Swath width of the scene, D the Range direction and E the azimuth direction.

### 2.3.3 RADAR Image Geometry

Unlike most optical remote sensing systems which utilize a nadir or straight down looking sensor, most SAR systems look to the left or right of the direction of motion as illustrated in Figure 2.3.2. While Figure 2.3.2 illustrates an airborne system, the same geometry is utilized in space-borne systems.

The range direction of a SAR image is perpendicular to the flight path; the azimuth direction is parallel to the flight path. The incidence angle is the angle between the incoming radiation and the direction normal to the ground surface and varies in the range direction of the image. It is important to note that radar backscatter,  $\sigma^o$ , decreases as incidence angle increases; that is, becomes more oblique. The image geometry leads to some unique features of SAR images, such as foreshortening, layover, and shadow. Other image features, such as speckle, result from SAR image processing.

Foreshortening, layover, and shadow all result from the side-look geometry of SAR platforms and surface topography, and are thus incident angle dependent. Shadow occurs on the non-illuminated side of topographic features. The radar wave front cannot sense features within the shadow and thus dark spots appear in the imagery. Shadows become more prominent as incidence angle increases. Foreshortening occurs on slopes oriented towards the radar sensor, the wave front is incident upon different parts of the slope at the same time (depending on the slope angle) resulting in compression of the feature in the image. Foreshortening in images results in a bright, foreshortened illuminated slope. Figure 2.3.3 illustrates radar layover. Layover is an extreme case of foreshortening where radar waves are reflected from the top of a topographic feature and returned to the sensor before the base. The backscatter values

from the top are thus recorded and presented before the signal from the base ([Canada Centre for Remote Sensing, Natural Resources Canada, 2001]; Figure 2.3.3).

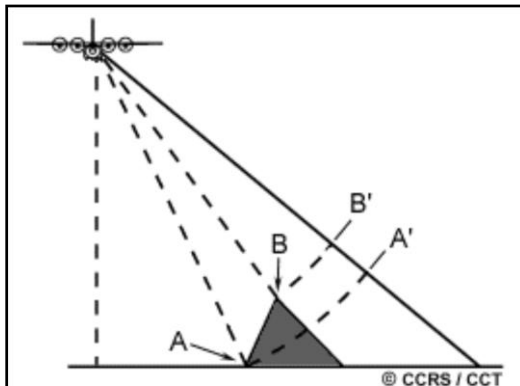


**Figure 2.3.3: Illustration of radar layover.** Energy emitted by the sensor reaches the top (B) of the topographic feature before the base (A), and thus is laid over the base (A') in the slant range image (at B'). Figure from [Canada Centre for Remote Sensing, Natural Resources Canada, 2001].

Speckle, the grainy texture visible in a SAR image, results from the SAR image formation processing. Speckle results from the constructive and destructive interference of the radar waves as they interact with the surface and return to the sensor, and during the combination of the multiple looks of the target during SAR image formation and processing. Speckle affects the ability to interpret SAR scenes and can be reduced using multi-looking, in which the scene/target is imaged multiple times as the sensor flies over head, during image formation or speckle filtering which averages pixels after the image is formed (see Section 3.3.1.1).

### 2.3.4 Backscatter

Backscatter is the amount of microwave energy that is returned to the SAR sensor after interacting with the surface. Backscatter can be generated from surfaces such as the snow to ice interface, the air to snow interface or the water surface. Backscatter can also occur from within the volume of the medium, such as from snow grains, layer boundaries, or air/brine bubbles within ice. Besides the dielectric properties of a medium, changes in the physical properties such as surface roughness, snow grain size, snow wetness, air/brine volumes within ice can lead to changes in backscatter by changing the dielectric properties of the medium and the interaction of the radar waves with the medium.

#### Surface Roughness

Surface roughness controls the direction and magnitude of the scattering of the radar wave that occurs at the interface. Surface roughness is dependent on the wavelength of the EM radiation and can be defined on a number of spatial scales. Surface roughness plays a critical role in scattering radiation back towards the sensor. In SAR systems, smooth surfaces appear dark, while rough surfaces appear bright; this is due to the fact that a rough surface scatters radiation in all directions while a smooth surface scatters radiation in one direction. In Equation 23 Equation 24,  $h$  is the height of the surface roughness,  $\lambda$  is the wavelength of the EM wave emitted by the radar sensor and  $\gamma$  is the

depression angle of the radar wave ( $90 - \theta_i$  where  $\theta_i$  is the incidence angle of the radar wave).

$$h < \frac{\lambda}{25 \sin \gamma}$$

**Equation 23: Criterion for smooth surface [Jensen, 2007].**

$$h > \frac{\lambda}{4.4 \sin \gamma}$$

**Equation 24: Criterion for a surface to be considered rough [Jensen, 2007].**

In addition to surface backscatter, volume scattering can play an important role in the overall backscatter observed at the sensor. For example, scattering from forests, crops and even snow occurs at surfaces such as the ground, but also from targets within the volume of the medium such as snow grains. The orientation of the objects and the polarization of the EM radiation play an important role in determining how much incident radiation is scattered back towards the sensor. For example, backscatter from a vertically oriented surface feature such as a crop or forest is greater from the VV polarization than the HH polarization as the HH polarized wave will pass through/between the vertically oriented stalks/trees. This also means that HH is less sensitive to open water than VV. The cross polarization is often used to distinguish multiple scattering features, such as ship detection, as the multiple interactions with the surface change the phase angle (depolarize) the wave front. Furthermore the size and orientation of the components of the surface medium influence backscatter. Large snow grains are more likely to interact with radar waves simply due to their size. Depth hoar snow crystals can be 0.5 - 1.0 cm or larger in diameter. Brine channels and air bubbles can also reach sizes close to higher frequency RADAR waves such as Ku or X.

Snow and sea ice physical properties can thus influence backscatter directly by influencing the likelihood of interaction with a radar wave or indirectly by modifying the thermal and thus dielectric properties of the snow and ice. The effect of physical snow and ice properties on backscatter is also dependent on the orientation of the radar waves. The orientation of the radar wave and physical medium changes the probability and nature of the interaction.

### 2.3.5 Polarization Concepts

EM radiation can be expressed using wave theory as being composed of both electric and magnetic fields ([Schott, 2009]; Figure 2.3.4). The electrical and magnetic fields oscillate perpendicular to each other and to the direction of travel [Schott, 2009]. The direction of oscillation of the electric field is termed polarization [Schott, 2009]. EM radiation can be linearly, circularly or elliptically polarized, with linear and circular polarizations being seen as special cases of elliptical polarization [Schott, 2009]. Linearly polarized radiation can be horizontally (H) or vertically (V) polarized. Linear polarization results from oscillation along a fixed orientation angle and is the most common polarization for SAR sensors [Schott, 2009]. In the case of SAR sensors, the horizontal polarization or X-axis is parallel to the surface of the Earth.

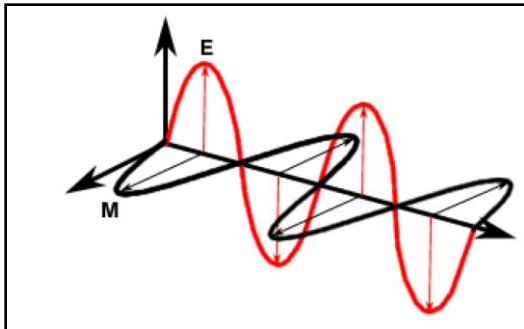


**Figure 2.3.4: Example of vertically polarized EM wave. M represents the magnetic field and E the electric field. The direction of travel is to the right. Figure reproduced with permission from the European Space Agency - ESA [E.S.A., 2007a].**

SAR sensors are able to transmit and receive EM radiation in both vertical and horizontal polarizations. This results in four possible polarization channels, HH, HV, VH, VV, where the first letter (t) denotes the transmitted wave polarization and the second letter (r) the received wave polarization. When  $t=r$ , the polarization channel is said to be co-polarized. When  $t\neq r$ , the polarization channel is said to be cross-polarized. SAR systems can be single, dual, or quad polarization systems, meaning that they can acquire backscatter data from one, two or all four polarization channels. The imagery utilized in this study (Envisat ASAR and TerraSAR-X) was acquired in dual polarization mode, with VV and VH or HH and VV or HV and HH polarizations being acquired together. The backscatter from targets at different polarizations provides information regarding the structure of the target medium such as alignment with respect to the radar, the importance of volume versus surface scattering and the randomness of the scattering surfaces [Canada Centre for Remote Sensing, Natural Resources Canada, 2001].

The VH cross polarization backscatter results from the depolarization of the transmitted vertically oriented radar waves as they interact with the surface. Depolarization requires the interaction of radar waves with targets, often requiring multiple interactions. More randomly oriented media such as forests provide opportunity for multiple interactions with radar waves, increasing the amount of incident energy that is depolarized. VH polarization backscatter is therefore also attributed to scattering within the volume of a medium instead of at surfaces, because of the numerous opportunities for multiple scattering.

In addition to information from the different polarizations, the different polarizations can be combined to provide further information such as the anisotropy in the properties of a medium[Drinkwater et al., 1992]. The number of parameters that can be derived depends on the number of channels available. For dual-polarized data, the co-polarization (HH/VV) and cross-polarization (HV/HH or VH/VV) ratios can be computed [Drinkwater et al., 1992]. Other parameters such as SPAN (the total power in the scattered field) and depolarization ratio (ratio of the cross-polarized channel to both co-polarized channels) require additional bands (three or more) and complex data. Calculating polarimetric decompositions provides information on the structure and orientation of the medium and the resulting backscatter from it. These additional datasets provide additional options for the classification of an image and potentially additional linkages to physical properties.

## 2.4 Multi-polarization and Multi-Frequency Observations of Snow and Sea Ice

In this section a review is presented of previous work performed on sea ice and snow property retrieval utilizing multiple polarization and/or multiple frequency SAR data. As the response of EM radiation from a target is frequency and polarization dependent it is sensible to examine targets at multiple frequencies and polarizations in order to provide the most information for target property retrieval. The proposed CoReH<sub>2</sub>O mission would collect the first space-borne multi-frequency polarimetric data since the SIR C/X SAR shuttle mission acquired fully polarimetric C, X, and L band data in 1994. If launched, CoReH<sub>2</sub>O will acquire coincident dual-polarization (VV and VH) X and Ku band SAR data with the main purpose of retrieving snowpack SWE. Below a review of multiple sea ice and snow parameter retrievals of interest in the context of the CoReH<sub>2</sub>O mission including extent, ice type, open water discrimination and others with a focus on the retrieval of properties such as depth, density, and SWE is provided. The review is focussed on results from space-borne platforms as these offer the widest spatial availability for users and are most relevant to the methods of this study. Furthermore, while much work has been performed using airborne SAR sensors, the system parameters of airborne sensors such as noise and spatial resolution and coverage are not representative of space-borne sensors. Airborne sensors typically exhibit far lower noise and much higher spatial resolution.

To date the majority of sea ice or snow studies involving polarimetric SAR at one or more frequencies have focussed on sea ice classification (e.g. [Partington and Flach, 2010; Geldsetzer and Yackel, 2009]). Both studies utilized C-band dual polarized imagery and found an increase in classification accuracy and improved separation of open water from ice by utilizing the co-polarization ratio. Partington and Flach (2010) noted that cross-polarized backscatter from Envisat ASAR is often near or below the noise floor because the sensor noise floor is quite high and the cross-polarized backscatter from sea ice and snow surfaces are quite low due to limited depolarization of the radar wave.

### Temporal Evolution of Backscatter

Few seasonal temporal studies have been conducted of backscatter over sea ice from either the Baltic Sea or the Arctic using SAR for purposes other than the detection of snow melt, onset of melt water ponding, or the duration of the ice season. Yackel et al. (2007) examined the C-band backscatter response of sea ice during the spring melt transition period from 1992-2002 in the Canadian Arctic Archipelago. Figure 2.4.1 presents the phenomenological C-band backscatter evolution for Arctic sea ice from that publication. For FYI, one clearly sees a decreasing in backscatter over the course of the winter with an increase associated with the onset of melt within the pendular snow wetness regime. The backscatter then decreases at the transition to the funicular snow wetness regime and finally increases with the onset of ponding. Increases in the brine volume of the sea ice surface, increasing snow wetness, and basal snow grain size have been proposed as the cause for the increase in backscatter associated with the pendular snow wetness regime. The decrease in backscatter at the funicular regime is caused by drainage of the water from the snow, reducing the effective grain size and flushing the sea ice surface with fresh water, diluting the brine. The increase in backscatter during the onset of melt pond formation is due to wind roughening the melt ponds.

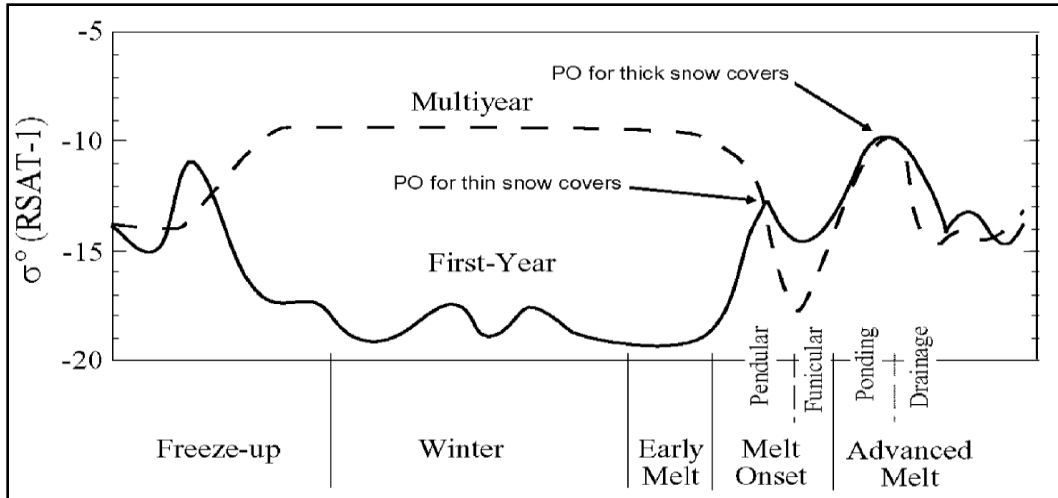


**Figure 2.4.1: Characteristic seasonal evolution of C-band microwave backscatter from Arctic sea ice. Ponding onset (PO) is indicated for thick and thin snow covers.** Copyright (2007) Wiley. Used with permission from Yackel, J. J., Barber, D. G., Papakyriakou, T. N. and Breneman, C. (2007), First-year sea ice spring melt transitions in the Canadian Arctic Archipelago from time-series synthetic aperture radar data, 1992–2002. *Hydrological Processes*, John Wiley and Sons.

Makynen et al. (2007) presented the seasonal evolution of C-band backscatter from the Envisat ASAR sensor over Baltic Sea ice. Their study examined backscatter from mid-February to early April, 2004, the transition from winter to spring melt conditions, and compared the results with an advanced high resolution 1D thermodynamic snow/ice model (HIGHTSI; [Makynen et al., 2007a]). In general an increasing trend in C-band backscatter was observed by Makynen et al. (2007) and is attributed to the formation of superimposed ice, increases in snow grain size, snow density and surface roughness. The study also compared backscatter to measured in-situ properties of snow and ice but found that no single variable exhibited a statistically significant correlation with the backscatter evolution.

### Ice Thickness

Yueh et al. (1997) found that dual polarized Ku-band scatterometer data from the Seasat-A scatterometer could be used to identify sea ice from open water based on the co-polarization ratio. They found that the co-polarization ratio of sea ice is much lower than that of sea water and can be used to distinguish between regions of high concentrations of sea ice and open water [Yueh et al., 1997]. However, Yueh et al. (1997) note that in areas where open water forms a majority of the pixel, or when melt ponds cover more than 20% of the sea ice surface, the signal could become dominated by the open water response resulting in underestimation of the presence of sea ice. Regions of thin ice showed a similar co-polarization ratio to open water, leading to further misclassification [Yueh et al., 1997] suggesting that even Ku band radar may be penetrating through the sea ice or depolarizing as a result of interactions with the ice. Furthermore, Yueh et al. (1997) noted backscatter returns from calm water at high incidence angles were near the noise limit of the sensor, resulting in greater uncertainty in the co-polarization ratio.

Kim et al. (2010) compared dual polarization data from RadarSAT-2 and TerraSAR-X with ice thickness measurements in the Arctic Ocean north of Greenland [Jin-woo Kim et al., 2010]. They found a strong relationship between the cross-polarization ratio at C-band with ice thickness when ice thickness and surface roughness are correlated [Jin-woo Kim et al., 2010]. Their work also showed a poor correlation between the TerraSAR-X cross-polarization ratio and ice thickness. However they note that the cross-polarization ratio was sensitive to surface roughness and thus ice thickness estimation ultimately requires that surface roughness and ice thickness be well correlated [Jin-woo Kim et al., 2010].

Similar results were also observed for the co-polarization ratio by Nakamura et al. (2009) using Envisat ASAR alternating polarization data for fast ice in the Antarctic [Nakamura et al., 2009]. Other works by Nakamura and colleagues have found strong correlation between the co-polarization ratio and ice thickness from Envisat ASAR in the Sea of Okhotsk [Nakamura et al., 2006].

Dual polarization X-band radar offers promise for the remote sensing of thin young ice as was recently shown by Busche et al. (2009). Busche and others compared changes in the polarimetric signatures to helicopter-borne sea ice thickness measurements of thin sea ice in the Arctic [Busche et al., 2009]. While the results indicate that some polarimetric decompositions including the complex correlation coefficient show similar trends to theoretical predicts at L-band SAR, limitations introduced by the system noise of TerraSAR-X and uncertainty in the in-situ validation data require that further studies be undertaken [Busche et al., 2009]. The results of Busche et al. (2009) provide further argument for the retrieval of thin sea ice thickness from the X and Ku-band frequencies proposed for CoReH<sub>2</sub>O.

### Snow Properties

Shi and Dozier (1995) used data from the VV and HH polarization channels and the real component of the cross product of the VV and HH complex scattering elements acquired by the Space-borne Imaging Radar (SIR) C-band SAR sensor to estimate snow wetness. [Shi and Dozier, 1995]. However, their inversion technique cannot be applied to Envisat ASAR dual polarization data as the different polarizations from the ASAR are not mutually coherent, a requirement for using the cross product of the VV and HH complex scattering elements [Raney, 2006]. Furthermore, the response of VV and HH are near similar at low incidence angles [Shi, 2008], providing little separation in the data and thus limited potential/resolution for retrieving snow wetness.

Shi and Dozier (2000, 2000b) also inferred snow pack properties from the C, X, and L band data from the SIR mission [Shi and Dozier, 2000a; Shi and Dozier, 2000b]. Shi and Dozier utilized the VV and HH polarizations at L-band to estimate dry snow density and the dielectric constant and roughness of the underlying surface and then estimated other snow parameters by removing the contribution of the ground surface to the total backscatter from the snow covered ground. While the results of Shi and Dozier show low relative error when compared to in-situ measurements, they were developed based on separating the scattering components into volume and surface scattering and distinguishing the surface scattering of the air-snow and snow/ground interfaces from the volume scattering; this requires that the surface below does not also cause a mixed surface/volume scattering signature and that the ground scattering component be

relatively stable. Furthermore, their technique required coherent, coincident data at three frequencies and multiple polarizations. These requirements simply cannot be met by any current satellite system, all of which operate at a single frequency. Over sea ice, where changes in temperature and salinity and the overlying snow can cause changes in the surface brine volume the ground scattering component is likely less stable. The penetration depth of EM radiation at L-band is significantly less sensitive to snow wetness and much greater than at C or X band. Furthermore in the case of low salinity MYI, volume scattering can play a significant role in the backscatter signal (Sections 2.1.4 and 2.1.5). Shi and Dozier note that up to 60% of the co-polarized backscatter from snow is due to volume scattering and that this contribution should be even greater at Ku band frequencies if the snow remains dry [Shi, 2008; Shi and Dozier, 2000b]. The results of the work by Shi (2008) and Shi and Dozier (2000b) provide strong argument for the launch of a dual X- and Ku-band frequency sensor such as CoReH<sub>2</sub>O.

Nghiem et al. (2001) compared QuikSCAT data with the NOAA National Snow Analysis SWE product and found a high degree of correlation. Furthermore, they state that backscatter from dry snow at Ku band is approximately 6 times stronger than at X-band, 48 times stronger than at C-band and several thousand times stronger than at S and L bands, further indication of the potential usefulness of a X and Ku-band space-borne SAR sensor.

Royer et al. (2010) successfully utilized QuikSCAT Ku band data to determine the onset of snowmelt in Eastern Canada across multiple terrain types. The study by Royer et al. (2010) agrees well with those of Wang et al. (2008) who also noted a correlation between QuickSCAT backscatter, melt onset, and snow off dates across the terrestrial Arctic and Howell et al. (2008; 2005) who compared QuikSCAT backscatter to the thermodynamic state of sea ice and the melt onset and freeze onset dates. It should be noted that there is an important difference in melt detection algorithms between land, first year sea ice and multi -year sea ice and a dependence on the depth of snow and penetration of the radar waves into the snow. Over land, glacial ice sheets, and snow covered MYI, backscatter decreases with increasing snow wetness. Recall that the dielectric constant and dielectric loss factor of water is much higher than ice, and thus when the snow is wet, it masks the contribution of scattering from the ice/ground surface below. In the case of MYI, the snow masks the contribution of surface and volume scattering from the top of the ice. Furthermore, as MYI is also associated with thicker snow cover than first year ice (FYI), the volume scattering component of the backscatter is also reduced. The upper surface of MYI typically has low salinity and thus increases in temperature may not result in substantial increases in brine volume at the sea ice surface. On FYI, many studies show an increase in backscatter at the onset of snow melt associated with an increase in the brine volume, the dielectric constant and the effective size of the basal layer snow grains (e.g. Howell et al. 2008; Howell et al 2005; Yackel et. al 2007). However, the frequency, penetration depth, and depth of snow must be considered when examining the change in backscatter. At high frequencies such as Ku band, the penetration depth decreases dramatically with even the slightest amount of liquid water within the snow. Thus if the snow wetness increases and the snow depth is great enough that little or no energy reaches the snow/ice-interface, backscatter may decrease even if the sea ice snow interface temperature increases.

Recently Markus et al. (2011) compared QuikSCAT Ku band scatterometer data (VV HH) with estimates of surface roughness from the NASA ICESAT satellite laser altimeter and found that while there is a good agreement between the two, further work is needed to determine the influence of snow and ice properties on backscatter at Ku band [Markus et al., 2011]. While uncertainty in the ICESAT estimates of surface roughness also exists, the other studies discussed highlight the fact that other snow properties influence QuikSCAT backscatter and may mask the signal of surface roughness.

## SWE

In the late 1990s, research into the retrieval of SWE using SAR sensors was earnestly underway. Measurements from ground based sensors and modelling studies in the 1980s by Matzler, Ulaby, Tiuri, and others had examined the dielectric properties of dry and wet snow (see Section 2.2). Bernier et al. (1998) examined airborne C-band data over Southern Quebec and observed that volume scattering from a shallow dry snow cover was undetectable where SWE was less than 200 mm. However, a relationship was found between the thermal resistance of the snow pack and backscatter, and between thermal resistance and SWE. The thermal resistance of the snowpack was determined using an empirical linear relationship between snow depth and the thermal conductivity of the snow pack based on temperature measurements. As was shown in Section 2.2, the thermal conductivity of snow is dependent on its density. As SWE is the product of snow depth and density the relationship between backscatter and SWE appears to be theoretically sound. Unfortunately changes in other properties such as grain size and wetness can also change the thermal conductivity of the snow pack and can influence the effective roughness near the snow and ice interface.

A similar algorithm for SWE retrieval was proposed by Yackel et al. (2002, 2007) for snow on sea ice [Yackel and Barber, 2002; Yackel and Barber, 2007]. In 2002, Yackel and others compared changes in SWE and changes in C-band backscatter from RADARSAT-1 near Resolute Bay, Nu. In these studies the link between backscatter and SWE is through the control of snow thermal resistance on the dielectric properties of the ice surface. Yackel et al. proposed that thin snow covers allow for greater changes in the snow and ice interface temperature and thus in brine volume and dielectric properties and ultimately backscatter than thick snow covers [Yackel and Barber, 2002]. The technique is limited to very smooth first year ice where small changes in backscatter due to changes in the snow/ice interface properties will be noticeable. The study also assumes that there are no changes in scattering from the snow. In the 2002 study, smaller changes in SWE exhibited a larger change in backscatter, indicating a thinner, less thermally resistive snow pack than at other sites where larger changes in SWE were linked to smaller changes in backscatter. In 2007 Yackel et al. repeated the comparison between SWE and C-band backscatter over land-fast FYI in the Canadian Arctic [Yackel and Barber, 2007]. Once again a large change in backscatter was observed for regions with low SWE change.

The relationship between C-band backscatter, the thermal resistance of a snowpack and SWE noted by Bernier et al. (1998) and Yackel et al. (2002, 2007) has been exploited in the EQeau snow water equivalence model [Bernier et al., 1999; Chokmani et al., 2006]. A sensitivity analysis by Chokmani et al. (2006) showed that uncertainty in density causes the highest uncertainty in SWE. As the EQeau model was tested and developed

over land, the errors associated with sea ice discussed in Yackel et al. (2007) are not present. The root mean squared error of the EQeau modelled SWE and observed SWE values was found to be 29 mm [Chokmani et al., 2006].

In 2003, Hallikainen et al. presented the first examination of the retrieval of SWE using the original resolution QuikSCAT data product and compared the results to SWE retrievals from SSM/I 37V-19V channels [Hallikainen et al., 2003]. In this study a correlation coefficient of just 0.4-0.5 was found for the QuikSCAT Ku backscatter and SWE changes [Hallikainen et al., 2003].

In 2009, Yueh et al. examined airborne Ku-band backscatter over Colorado during the second Cold Land Processes Experiment (CLPX-II). They observed a backscatter increase of 1 db/20 mm - 60 mm change in SWE increase [Yueh et al., 2009]. Rott and others also presented results of the CLPX-II experiment in Colorado, the SnowAlps 2007 and the HeliSnow 2008 campaigns in Austria. Rott et al. (2010) combined TerraSAR-X imagery with the airborne Ku data collected during CLPX-II to validate the CoReH2O concept [Rott et al., 2010]. Rott et al. 2010 reported results from forward modelling and the three aforementioned campaigns and noted a change of 1 db/35-40 mm SWE change from Ku band where SWE was less than 200 mm and 1 dB/100 mm SWE change from X band. However, airborne SAR sensors, like that used by Yueh et al. (2009) during CLPX-II have a much higher signal to noise ratio (SNR) than space-borne sensors and thus can measure even very low backscatter in the co- and especially the cross-polarized channels. A study examining the changes in backscatter associated with changing SWE from space-borne sensors is needed to understand if the lower SNR ratio of space-borne sensors strongly influences the retrieval of SWE using a dual-frequency X and Ku-band SAR sensor.

In March 2011, an airborne validation campaign acquired coincident X and Ku-band backscatter for the CoReH2O program [Trampuz et al., 2011]. The campaign provided the first coincidence airborne X and Ku band imagery using a system similar to that specified for CoReH2O [Trampuz et al., 2011]. At the time of writing, there has not been an article detailing any comparison between backscatter and in-situ snow or ice properties from the SnowSAR campaign.

In addition to examining backscatter response to SWE, repeat pass interferometry has been proposed as a means of accurately retrieving SWE [Deeb et al., 2011; Storvold et al., 2006; Guneriussen et al., 2001; Engen et al., 2004]. C-band interferometry poses issues largely due to the long repeat cycle of the current Envisat ASAR and Radarsat-2 sensors. Interferometry utilizes phase information and requires images to be acquired from the same position. Furthermore, separation of just a few days between images is needed or the images become de-correlated [Deeb et al., 2011].

One of the largest issues with SAR retrieval of snow and ice properties is the high number of co-evolving and competing variables that influence backscatter. This co-dependence was alluded to in Sections 2.1, 2.2, and 2.3 and highlighted again in the studies that compared SWE to backscatter via the thermal response of snow. This co-evolution and the competitive effects the snow and ice properties have on the dielectric properties and on backscatter causes great difficulty in generating a meaningful and robust retrieval algorithm for a single snow property. Makynen et al. (2007) performed

a time series study of C-band backscatter over the Baltic Sea and found that no single snow or ice variable could explain the changes in backscatter at a statistically significant level, even when using an advanced thermodynamic snow/ice model to improve the temporal resolution of in-situ measurements [Makynen et al., 2007a].

While much work has been done examining sea ice, snow, few studies have focussed on snow on sea ice. There have been very few studies that examined the retrieval the SWE of snow on sea ice and these were all limited to C-band because of the dominance of this frequency in past satellite SAR missions. Furthermore, much of the theoretical background work has been conducted using ground based sensors and ice tanks, or airborne sensors, both of which have very high SNRs and often very high spatial resolution. The SNR of space borne sensors is much lower than typical airborne sensors and therefore weak co- or cross-polarized backscatter values are not recorded. For example, the typical SNR ratio of TerraSAR-X is -24dB, while for PolSAR, the airborne Ku-band sensor used by Yueh et al. (2009), the SNR is -40dB [Yueh et al., 2009]. Another downside to airborne and ground-based sensors is that their higher spatial resolution and smaller areal coverage results in less spatial averaging of snow properties, and simpler quantification of the variability in the snow and ice properties within the image footprint.

## **Chapter 3. Study Site, Data, and Methods**

This chapter introduces the study site: Miquelon Lake, Alberta (Section 3.1: Study Site), the sources of data collected (Section 3.2: Data Sources and Methods) and the methodologies used for processing and analyzing the results (Section 0:

Methods). Previous studies conducted on Miquelon Lake are presented along with relevant results. Data for this study were collected in the winters of 2008/09 and 2009/10 on Miquelon Lake in Miquelon Lake Provincial Park, Alberta. Winters are defined as the period from the onset of an ice cover on the lake until the loss of ice in spring.

### **3.1 Study Site**

Miquelon Lake is a small saline lake approximately 50 kilometers southeast of Edmonton, Alberta (Figure 3.1.1). The site was chosen for its water salinity, size, depth and proximity to Edmonton along maintained roadways. Furthermore, a lake surface was selected for uniformity in its snow and ice properties. Miquelon Lake is a popular summer and winter recreational area. The salts present in the lake act to reduce algal bloom development and result in clear water [Mitchell and Prepas, 1990]. In the winter, the knob and kettle terrain surrounding the lake is widely used for country skiing. Snowmobiling and cross country skiing also take place on the lake itself. While part of the lake and surrounding area is designated as a provincial park, the rest remains classified as a bird sanctuary under Crown lands [Mitchell and Prepas, 1990]. Because of its recreational use, studies on the properties of the thickness of the ice can also provide important information regarding safe access to the lake. For example the heavy snowfall in 2010/11 resulted in extreme flooding conditions on the ice with a thin skim of snow and ice 5 cm thick overlying 30 cm of water with the actual lake ice below.

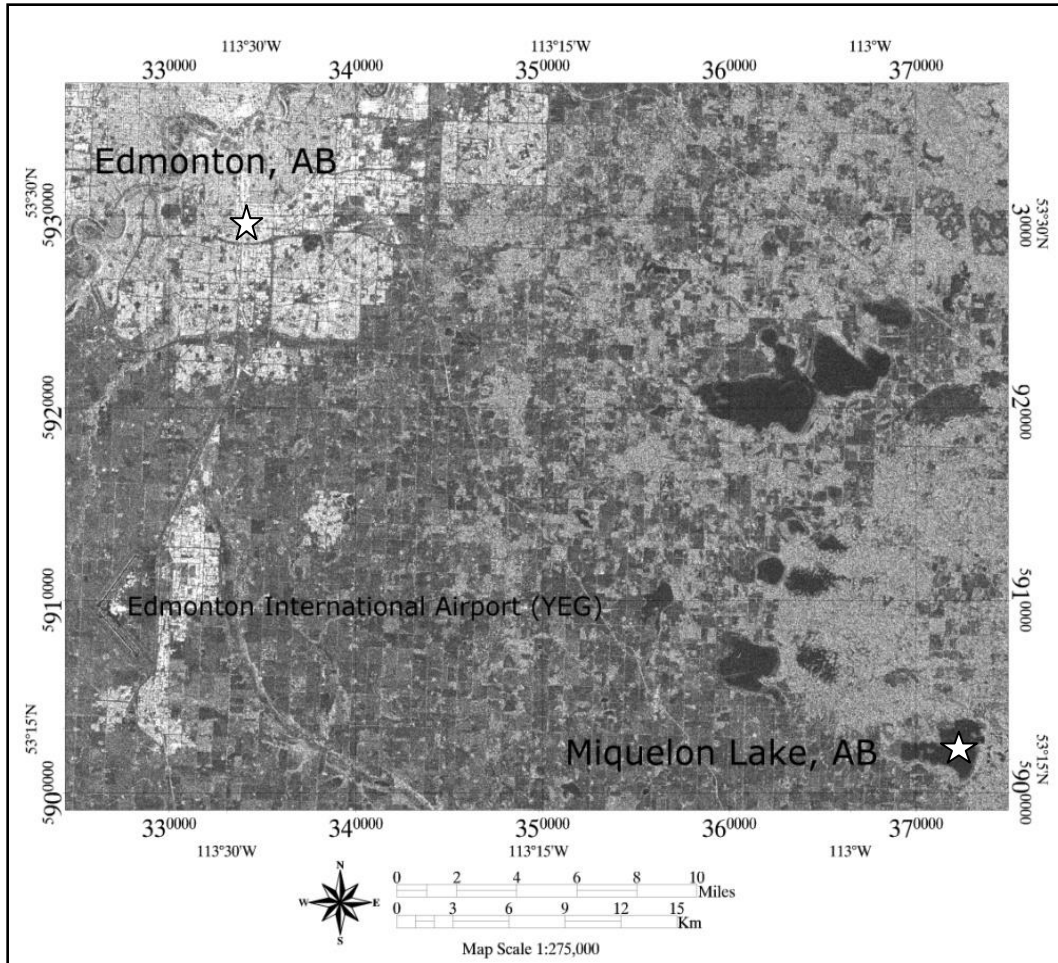


**Figure 3.1.1:** Envisat ASAR image showing location of Miquelon Lake, Alberta (lower right corner). One can also note Edmonton, Alberta (top left) and the Edmonton International Airport (YEG) at N 5910000, E 330000. Image is projected in UTM Zone 12N.

Miquelon Lake has been the subject of some previous studies. Biological studies of bird populations, phytoplankton and cyanobacteria comprise the majority of work on the lake. The lake's status as a bird sanctuary makes it an opportune place to examine various species including gulls ([Vermeer, 1969b; Vermeer, 1969a]), ducks [Dwemychuk and Boag, 1972] and owls [Grossman et al., 2008]. Furthermore, the saline nature of Miquelon Lake allows for unique studies on the phytoplankton and cyanobacteria of Miquelon Lake in regards to chemical and nutrient controls (e.g. [Bierhuizen and Prepas, 1985; Marino et al., 1990; Evans and Prepas, 1997]). Miquelon Lake is routinely monitored by the Alberta Government from a water quality perspective and information has been comprehensively collected and presented in the Atlas of Alberta Lakes [Mitchell and Prepas, 1990]. Recently, in addition to this study, two more studies on Miquelon Lake have begun. Anna Bramucci, a student in Biological Sciences at the University of Alberta under the supervision of Dr. Brian Lanoil is performing a study of the microbiology of the saline lake ice cover on Miquelon Lake. Furthermore, Dr. Glynnis Hood and collaborator Dr. David Larson at the Augustana Campus of the University of Alberta have conducted studies on the modifications beavers make to their habitat on ponds surrounding Miquelon Lake since 2007 [Hood, 2011].

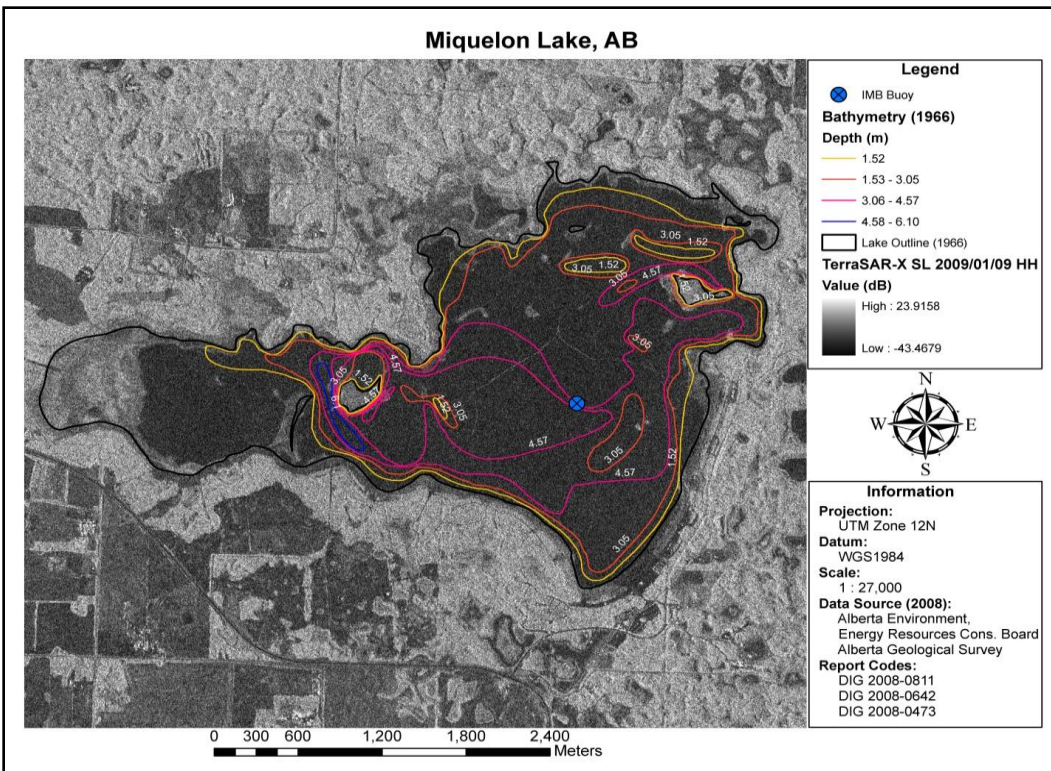
### **3.1.1 Physical Properties of Miquelon Lake**

Figure 3.1.2 presents surface elevation and bathymetric data for Miquelon Lake provided by Alberta Environment. The data are based on bathymetric studies conducted in the 1960s, along with data from the Shuttle Radar Topography Mission (SRTM). Miquelon Lake water levels have been monitored since 1972 and show a decline of approximately 1.5 m between 1991 and 2006 [Swanson and Zurawell, 2006]. Results from a GPS base station deployed on Miquelon Lake in March 2009, indicate a further drop of approximately 0.4 m. Table 3.1.1 below presents the main physical characteristics of Miquelon Lake and their development over the past half-century. One can also see the effect of decreased water levels by comparing the 1966 bathymetric and shoreline data to a current synthetic aperture radar image (Figure 3.1.2).

**Table 3.1.1: Physical Characteristics of Miquelon Lake, AB.** Values for elevation and maximum depth are estimated from GPS data and SRTM elevation [Swanson and Zurawell, 2006]. Surface area for 2009 was determined using image analysis of a TerraSAR image.

<b>Year</b>	<b>1966; 1982</b>	<b>2006</b>	<b>2009</b>
<b>Surface Elevation</b>	763.12	761.0	760.6
<b>Surface Area (km<sup>2</sup>)</b>	8.72; 7.8	N/A	<u>6.5±0.5</u>
<b>Volume (million m<sup>3</sup>)</b>	23.8	N/A	N/A
<b>Maximum Depth (m)</b>	6	4.5	4.1
<b>Mean Depth (m)</b>	2.7	N/A	N/A
<b>Drainage Basin Area (km<sup>2</sup>)</b>	35.4	35.4	35.4
<b>Residence Time (yrs)</b>	>100	>100	>100

In Figure 3.1.2 note the extension of previously denoted islands and the growth of new islands/water free areas. The lake surface can be distinguished by the dark grey color, with forest and land in lighter shades of grey. One can also observe a large region in the western end of the lake where it appears the water level has dropped sufficiently to expose the lake bed.



**Figure 3.1.2: Miquelon Lake Bathymetry and shore line overlain on geo-referenced TerraSAR-X Spotlight mode SAR image. Map created using data the Alberta Geological Survey Digital Datasets Archive [Alberta Environment et al., 2008].**

Past studies provide information on the evolution of the salinity of Miquelon Lake, AB. Figure 3.1.3 presents the long-term evolution of water salinity of Miquelon Lake from 1983 to 2010. As a result of the decreased water level the water salinity has increased over the past three decades (Figure 3.1.3). Additionally, as Miquelon Lake is groundwater fed, a change in the input water chemistry could also have occurred [Swanson and Zurawell, 2006]. Winter salinity values are higher than summer values as a result of brine rejection during the formation of the ice. Conductivity measurements from [Bierhuizen and Prepas, 1985; Marino et al., 1990; Evans and Prepas, 1997; Swanson and Zurawell, 2006] were converted to salinity using equations from [American Public Health Association et al., 1999] and the equation for the conductivity of a reference potassium chloride (KCl) solution at various temperatures [Chemiasoft, 2011].

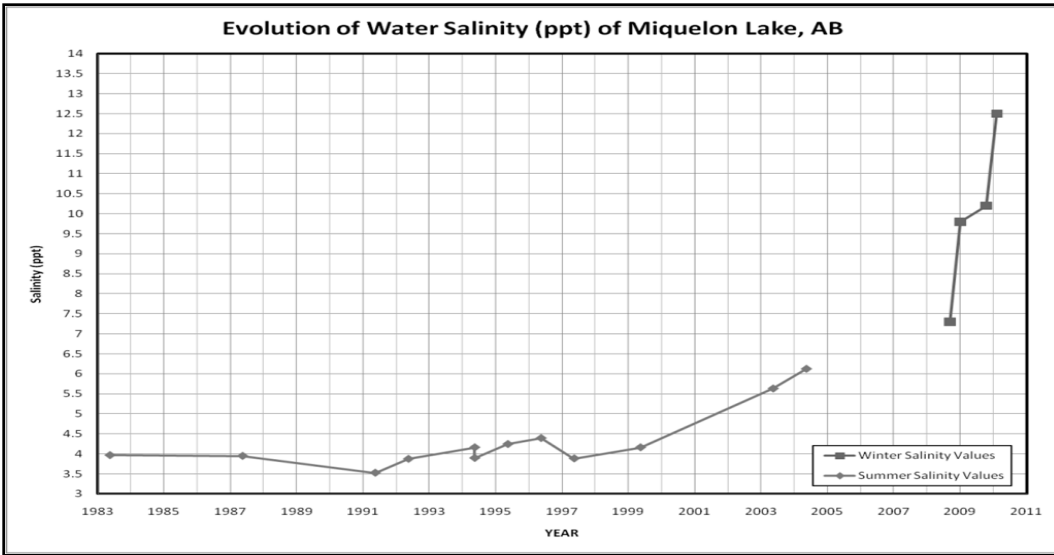


**Figure 3.1.3: Evolution of the salinity of Miquelon Lake.** Data in light grey (small diamond markers) were collected from previous studies which occurred during summer months. Values in dark grey (square-markers) were collected as part of the sampling program of this study and present winter values. Data sourced from [Bierhuizen and Prepas, 1985; Marino et al., 1990; Evans and Prepas, 1997; Swanson and Zurawell, 2006] and in-situ measurements collected during this study.

### 3.2 Data Sources and Methods

As the purpose of this study is to validate the theoretical basis for CoReH<sub>2</sub>O to retrieve snow and sea ice properties, numerous data sources are required. Section 3.2 presents the four main categories of data collected: 1) in-situ measurements, 2) autonomous measurements, 3) SAR imagery, and 4) auxiliary data.

#### 3.2.1 In-Situ Measurements

In-situ measurements of snow and ice properties were acquired using manual sampling and automated measurements by two Ice Mass Balance Buoys (IMB). Manual samples were collected approximately every two weeks with a focus on obtaining same-day measurements with SAR imagery whenever possible. In 2009/2010 the majority of measurements coincided with TerraSAR-X acquisitions, but not Envisat ASAR. Measurements were performed near the IMB on each sampling date. Manual snow sampling was conducted along an L-shaped course with two 50 m long transects oriented approximately N-S and E-W respectively. Snow depth was measured every 1m to the nearest half centimeter using a custom manufactured aluminum probe. Bulk snow density measurements were made using an Adirondack snow sampler every 10 m or 25 m along the transects depending on available time and manpower. The snow samples were placed in sealed plastic bags, and kept frozen until being weighed in the lab using a digital scale. Measurements of ice thickness, freeboard and draft were made every 10 m using a 1.10 m x 0.05 m auger powered by an 18V cordless drill, and a measuring tape. In addition, snow pits were dug and observations of the layering and snow grain size were made. In 2008-2009, several measurements of the snow's electrical parameters were made using an Insinööritoimisto Toikka oy Snow Fork. The snow fork provides measurements of the dielectric properties of the snow. Using

Equation 25-Equation 29 below, estimates of snow density and wetness were be made from the snow fork measurements. In equations 25 – 29 below, the symbols, B, and  $m_v$ , stand for bandwidth, liquid water content by volume, and liquid water content by weight, respectively.

$$\epsilon' = \left(\frac{870}{f}\right)^2 = \left(\frac{f_{air}}{f}\right)^2$$

**Equation 25: Calculation of complex dielectric constant for Finnish Snow Fork.**

$$B_{air} = 0.03 * f - 5.49$$

**Equation 26: Calculation of microwave bandwidth in air from data collected by the Finnish Snow Fork**

$$m_v = -0.06 + \sqrt{(0.06)^2 + \epsilon''/(0.0075 * f)}$$

**Equation 27: Calculation of the liquid volume content of a snow sample from data collected by the Finnish Snow Fork**

$$\epsilon'' = (B - B_{air})/f * \epsilon'$$

**Equation 28: Calculation of the complex dielectric loss factor from data collected by the Finnish Snow Fork**

$$\rho = -1.2142857 + \sqrt{(1.2142857)2 - (1 + 8.5 * m_v + 70 * m_v^2 - \epsilon')/0.07} + m_v$$

**Equation 29: Calculation of the density of a snow sample from data collected by the Finnish Snow Fork.**

Furthermore, ice cores were acquired using a Kovacs Mark II corer for ice salinity. The ice cores were sectioned immediately after removal from the water and placed in sealed containers to melt. Measurements of water temperature and water and ice salinity were acquired using a WTW Cond330i conductivity meter.

### 3.2.2 Autonomous Stations

IMBs from MetOcean/United States Army Cold Regions Research and Engineering Laboratory (CRREL) and the Scottish Association for Marine Science (SAMS) were deployed on the lake (Figure 3.2.1). The MetOcean/CRREL IMB utilizes a data logger to run and log the sensor data. Two sonic rangers measured the changes in snow and ice thickness with a published accuracy of 0.005 m [Richter-Menge et al., 2006]. However, issues with blowing snow and penetration into low density snow mean this value is optimistic. The MetOcean/CRREL IMB had a thermistor mounted in a solar radiation shield on the surface sonar mast at 1.5 m elevation for correction of the speed of sound for the surface sonic ranger and to provide an air temperature measurement [Richter-Menge et al., 2006]. A barometer, GPS sensor and an Argos or Iridium transmitter are also included in the IMB system [Richter-Menge et al., 2006]. The MetOcean/CRREL IMB was deployed with two of a possible three 1.5 m long thermistor strings. The thermistor strings are comprised of PVC pipe filled with an insulative material with YSI thermistors spaced every 0.10 m along the outside edge of the PVC pipe. The YSI thermistors have a temperature accuracy better than 0.1°C [Richter-Menge et al., 2006]. The top of the string was situated at 0.8 m in 2008/09 and 0.9 m in 2009/10 and thus provides measurements of air, snow, ice and water temperatures. The IMB provided measurements every two hours.

The IMB from SAMS employed a flexible circuit board with thermistors spaced every 0.04m to measure air, snow, ice and water temperatures. Heater elements are placed below each thermistor to allow for heating of the thermistor. The SAMS IMB has two unique measurement modes, temperature and thermal response. In temperature measurement mode, the temperatures of the thermistors are recorded, while in thermal response measurement mode, the thermistor is heated by its underlying heater for a prescribed amount of time. The temperature rise that occurs after the set time of heating is recorded. The temperature response of the sensor depends on the thermal conductivity of the material the sensor is within (snow/ice/water). Two heating measurements, with heating for 15 and 60 seconds (D1, D2) respectively were used in this study. The differential heating measurements were recorded once per day at approximately 1500 local. The SAMS IMB recorded temperature every 2 hours; however, this interval was adjusted several times throughout the study.

Figure 3.2.1 shows the set up of the IMB buoys on the lake in December 2009. The MetOcean/CRREL IMB in the background consists of the logger buoy, surface and subsurface (not shown) sonic rangers and the thermistor string. The SAMS IMB in the foreground consists of the logger/modem enclosure and the digital thermistor circuit.

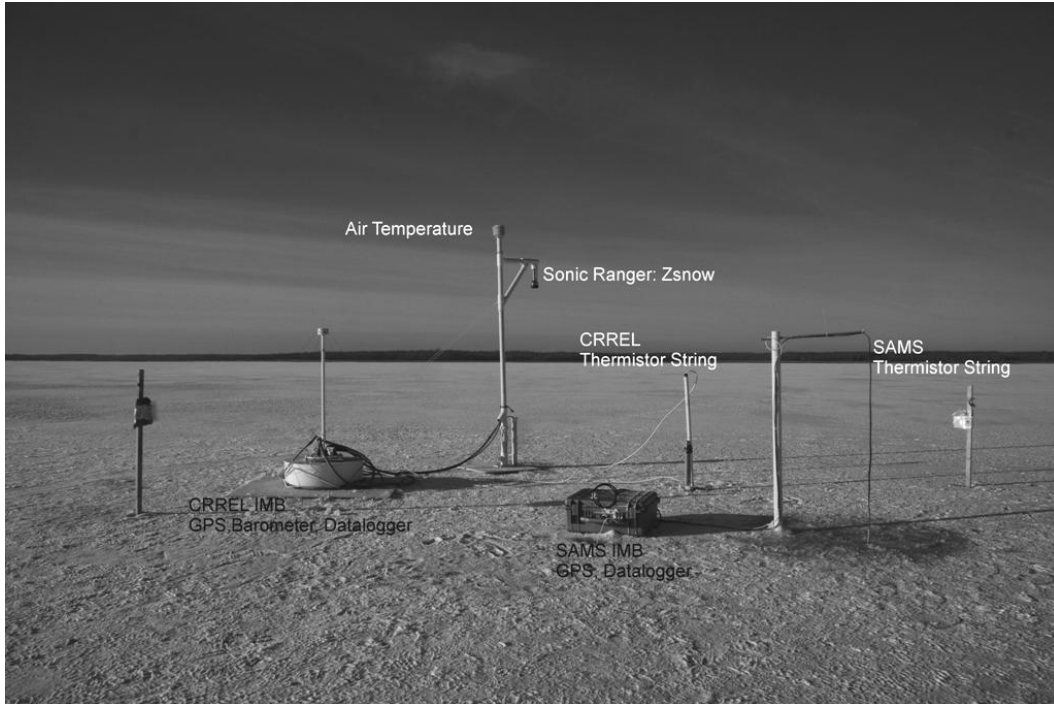


**Figure 3.2.1: MetOcean/CRREL and SAMS Ice Mass Balance Buoys deployed on Miquelon Lake on December 3, 2009. Photo Courtesy of Dr. Marcel Nicolaus.**

### 3.2.3 Synthetic Aperture Radar Imagery

#### ENVISAT ASAR

Envisat, a major earth observation satellite platform was launched in 2002 by the European Space Agency (ESA). The Advanced Synthetic Aperture Radar (ASAR) instrument on board of Envisat is a C band SAR operating at 5.3 GHz [E.S.A., 2012; E.S.A., 2007b]. The ASAR system is able to acquire images at multiple look angles (incidence angles), at a variety of polarizations, resolutions and swath coverage areas. The Envisat

ASAR sensor can acquire alternating polarization imagery [E.S.A., 2007b]. The repeat cycle for Envisat is 35 days, but the revisit rate over Miquelon Lake is on average  $15 \pm 8$  days due to changes in track spacing with latitude and the width of imaging swaths [E.S.A., 2007b]. StripMap mode Alternating Polarization Mode Precision Images (SM\_APP) with 30 m spatial resolution, 12.5 m pixel spacing and VV/VH polarizations were acquired for this study (Figure 3.2.2). Twenty-one images from swaths IS6 and IS4 were acquired in 2008/09 and 14 images from swaths IS2 and IS6 were acquired in 2009/10. Envisat ASAR processing steps and methodology are detailed in Section 3.3.1.

### TerraSAR-X

TerraSAR-X is an X band SAR operating at 9.65 GHz. It was launched in 2007 by the German Aerospace Center (DLR) [German Aerospace Centre (DLR), 2010]. Like Envisat, TerraSAR-X also acquires images at multiple polarizations, resolutions, and incidence angles [German Aerospace Centre (DLR), 2010]. TerraSAR-X has an 11 day revisit cycle for each image swath. As we acquired images from two or three images swaths in 2009/10 and 2008/09, respectively, we acquired an image every  $5 \pm 2$  days. The TerraSAR-X sensor offers much higher spatial resolution than Envisat ASAR but at the cost of reduced spatial coverage. TerraSAR-X can acquire single, dual and quad polarization imagery in several different imaging modes [German Aerospace Centre (DLR), 2010]. Twenty-four Multilooked Ground Range Detected (MGD) Radiometrically Enhanced (RE) Strip Map (SM) mode Dual (D) Polarization, VV/VH polarization, images and twelve Single Look Complex (SSC) Spotlight (SL) and Strip Map (SM) mode HH/VV polarization images were acquired in 2008/09. Seventeen SSC\_SM\_D HH/HV polarization images were acquired in 2009/10. The spatial resolution of the images acquired varies from 1.6 m to 8.6 m in the range direction and 3.2 m to 8.6 m in the azimuth direction [German Aerospace Centre (DLR), 2010]. Figure 3.2.2 shows the outline of the Envisat ASAR and TerraSAR-X images acquired for this study.



**Figure 3.2.2: SAR Image Footprints from Envisat ASAR and TerraSAR-X Imagery Acquired for this study. Yellow marker is located in Miquelon Lake. Top Left: Envisat ASAR APP. Top Right: TerraSAR-X MGD\_RE\_D. Bottom Left: TerraSAR-X SSC\_SL\_D. Bottom Right: TerraSAR-X SSC\_SM\_D.**

### 3.2.4 Additional Data Sources

As a space borne Ku-band SAR sensor currently does not exist, Ku-band RAR imagery was acquired from the SeaWinds sensor on the QuikSCAT satellite. The sensor is referred to in the literature as QuikSCAT, a notation followed here. QuikSCAT was a rotating pencil-beam Ku-band scatterometer that operated at 13.4GHz and acquired both V and H polarization imagery of  $\sigma^{\circ}$ . QuikSCAT was launched in 1999 but unfortunately the mission ended in November 2009 allowing for only one year of comparison to ice and SAR data over the lake [Bartsch, 2010]. Enhanced Resolution Image products derived from the QuikSCAT "egg mode" measurements were acquired from the NASA Scatterometer Climate Record Pathfinder project at Brigham Young University Center for Remote Sensing. The "egg mode" images were selected in preference to the higher spatial resolution "slice mode" images due to their lower radiometric noise [Early and Long, 2001; Howell et al., 2005; Long and Hicks, 2010]. The egg mode enhanced resolution images have a pixel spacing of  $4.45 \text{ km}^2$  with an effective spatial resolution of  $8\text{-}10 \text{ km}^2$  [Howell et al., 2005; Long and Hicks, 2010]. A description of the enhanced image mode processing is provided in Long et al., 1993, Early and Long (2001), Long and Hicks (2010). Backscatter values were extracted from a single pixel centered over the lake (Figure 3.3.1). Unfortunately, the grid cell size of the QuikSCAT pixel over Miquelon Lake is larger than the lake itself and incorporates returns from the surrounding land and forest. The Ku band comparison requires that we assume that the snow properties do not vary dramatically between the lake and the surrounding land and forest though this is likely not the case. This assumption is necessary because snow properties were only acquired on the lake and thus are the only data available for

application to the other regions. The majority of Ku-band backscatter from the forest surrounding the lake will occur in the canopy due to the large number of scattering surfaces.

SWE data was acquired from the Advanced Microwave Scanning Radiometer - Earth Observing System data product available from the National Snow and Ice Data Center [Tedesco et al., 2004]. The AMSR-E/AQUA L3 V009 Daily Snow Water Equivalent EASE-Grid Product was obtained from the National Snow and Ice Data Center. While the spatial resolution of the AMSR-E SWE product is very coarse with  $25 \text{ km}^2$  pixels, it provides high temporal resolution estimates of SWE.

### 3.3 Methods

#### 3.3.1 SAR Image Processing

Both Envisat ASAR and TerraSAR-X require significant processing to produce usable data. All processing was performed using the Next Envisat SAR Toolbox developed by Array Inc. under contract from the European Space Agency. Based on another highly successful open-sourced software package developed for ESA, NEST was commissioned to read, calibrate, and analyze data from current and future SAR missions. NEST is an open source-Java based software tool for reading, processing and analyzing radar data from a wide-variety of sensors including Envisat, TerraSAR-X, RadarSat 1/2, ALOS PALSAR, COSMO-Skimmed, and ESA ERS 1/2 and is capable of reading a large number of image modes from each sensor including the scientific single look complex multi-polarization products from RadarSAT-2 and TerraSAR-X. The ability of NEST to read and process TerraSAR-X images was not introduced until 2010.

In order to assess the effects of different processing routines, several different processing chains were implemented. Processing chains also varied between sensors and between different products from the same sensor. A detailed description of the processing chain and processes applied to the TerraSAR-X single look complex spotlight mode images is presented in section 3.3.1.1. In section 3.3.1.2 a short description of the processes applied to the other products is given.

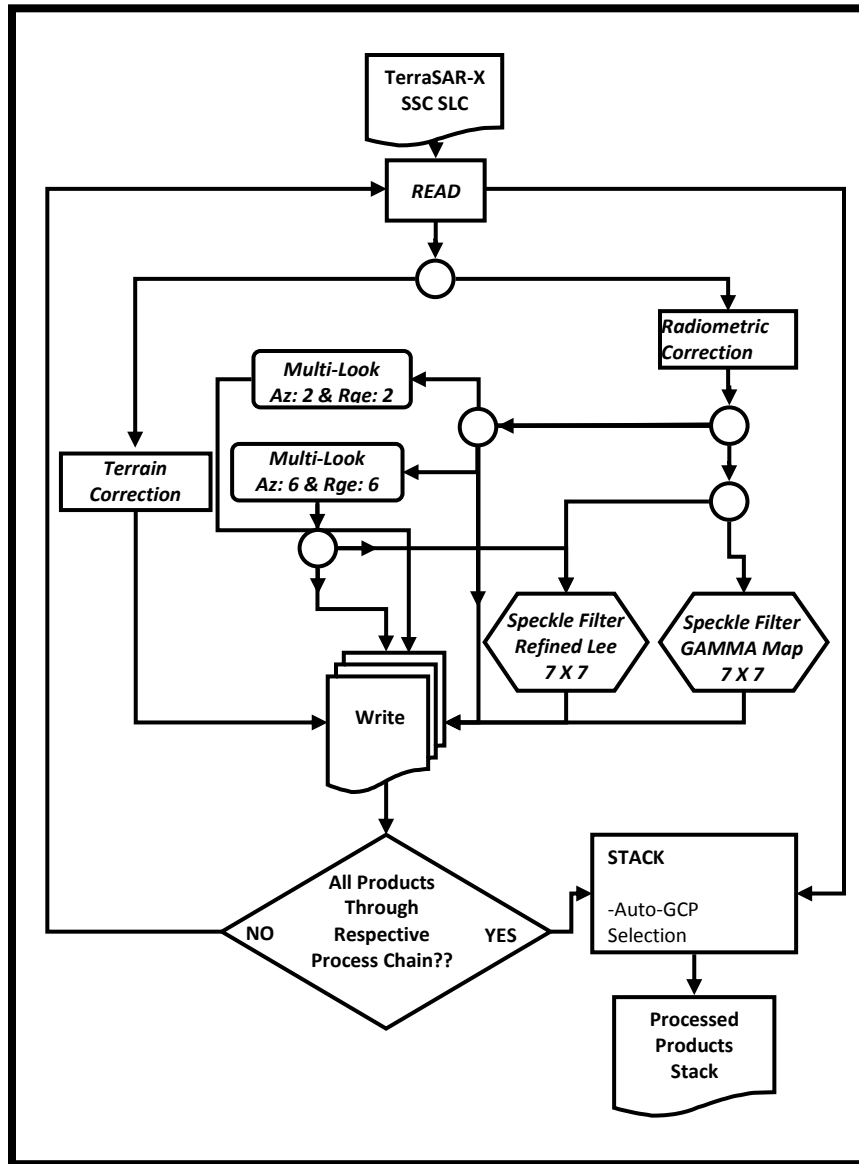
##### 3.3.1.1 TerraSAR-X SLC SL Mode Processing

The TerraSAR-X SLC SL mode images were selected to provide illustrative examples of the effects of the different processing steps (in addition to the actual snow/ice comparison data. In all, eight different processing chains were utilized, including the unprocessed imagery as it is received. The images are first loaded unprocessed into a new NEST “*Project*” using the Product Library tool. Flow Chart 3.1 illustrates the processing chains applied to the TerraSAR-X SLC SL imagery. The setup of processing chains in NEST is similar to the flow diagram here, and utilizes the “*Graph Builder*” tool to create the processing chains. A processing chain begins with a “*read*” operator and ends with a “*write*” operator. Numerous operators exist in the NEST toolbox including:

- a) Ocean Tools (i.e. Wind-Field-Estimation)
- b) SAR (i.e. radiometric calibration, multilooking, speckle-filtering)
- c) Geometry (i.e. orthorectification)
- d) Interferometric SAR products (i.e. Complex Interferogram)

- e) Analysis(i.e. EM Cluster Analysis)
- f) Utility Operators (i.e. data resampling, filtering)

For the TerraSAR-X SLC SL imagery images were imported into NEST in unprocessed form. The Batch Processing tool was utilized to process through each possible step outlined in Flow Chart 3.1.



**Flow Chart 3.1: Full set of SAR processing performed on TerraSAR-X SSC\_SL\_D imagery. All SLC imagery was run through each possible process illustrated above.**

As Flow Chart 3.1 indicates, images were either processed or sent straight to the stack operator. Statistics from the unprocessed images were extracted to illustrate the need for processing. If images were selected for processing, the first step was to apply either Range-Doppler Terrain Correction with Radiometric corrections (TC) or Radiometric Calibration. TC removes the effect of terrain on the backscatter values by utilizing the information of radar time, slant to ground range parameters, the precise orbit geometry

of the satellite, and a reference DEM. The DEM used in this study was the SRTM 3 arc second (90 m) DEM. The DEM GeoTiffs were automatically downloaded by NEST for the acquired imagery. The Terrain Correction operator corrects the incidence angle of the product using the DEM to geolocate the image accurately in three dimensions. The radiometric calibration is performed using this local incidence angle. Then the operator applies radiometric normalization. The other option to begin processing was to apply radiometric calibration and use the incidence angle interpolated from the corner dimensions for Envisat ASAR, or the pixel locations provided with the TerraSAR-X products. In the case of TerraSAR-X, a simplified calculation of backscatter,  $\sigma^*$ , that ignores the noise estimated beta naught (NEBN) is used by NEST. The NEBN is a measure of the noise of the SAR system such as elevation antenna patter, transmitted power, and received [Infoterra GmbH, 2008]. Signals below the NEBN cannot be differentiated between thermal noise or changing properties of the scattering medium. However, coherent signals and images can be formed from information below the NEBN. When examining relative change, it is unclear if changes in backscatter below the NEBN (or Noise Estimated Sigma Zero, NESZ) are valid or not.

The simplified calculation used for calculating backscatter is taken from the Radiometric Calibration of TerraSAR-X Data document and is presented in Equation 30 below [Infoterra GmbH, 2008].

$$\sigma^* = (c_s \cdot |DN|^2) * \sin \theta_i$$

**Equation 30: Simplified equation for calculating  $\sigma^*$  for TerraSAR-X products.  $c_s$  is the calibration and processor scaling factor, DN is the pixel intensity value,  $\theta_i$  is the local incidence angle.**

After either radiometric calibration or TC was applied, the images were either written to files or sent to a filter operator. SAR images are often filtered to reduce speckle or noise. Speckle is caused by multiple scatter returns from within a pixel which result in constructive and destructive interference and produce a grainy or “speckled” texture in the imagery [Canada Centre for Remote Sensing, Natural Resources Canada, 2001; GlobeSAR-2 and Canada Centre for Remote Sensing, 2001]. There are two main ways of dealing with “speckle”, applying a speckle filter or multi-looking an image. Multi-looking involves acquiring multiple looks of the same point as the satellite passes overhead, effectively averaging the pixel. Multi-looking is done during image formation. Speckle filters are applied to previously formed images. Speckle filtering uses statistical measures of a subsample of image pixels using moving windows. Numerous types of speckle filters exist, from simple mean or median filters to advanced adaptive filters such as the Refined Lee speckle filter or the Gamma MAP speckle filters which can remove speckle while keeping edges or linear features sharp (for a more detailed description of these filters see [Lopes et al., 1990; Jong-Sen, 1983]. Both speckle filtering and multi-looking result in a decrease in the effective spatial resolution of the data.

In one of the processing chains, both speckle filtering and multi-looking were applied in order to examine the effect of applying both processes to the SAR backscatter values. Once all the images had been run through the processing chain, the images from a particular chain were then stacked into a single product using the automatic co-registration feature of NEST. NEST stacks the images using co-registration by finding a

specified number of ground control points from the imagery (200-300 were used in this case). The images are then warped to each other based on the control points. In the case of the TerraSAR-X SLC SL mode images, all images are acquired from the same reference orbit and all in descending mode, meaning that the co-registration between images is already quite good before warp. The co-registration of images for TerraSAR-X is much better than for Envisat ASAR due to the high accuracy of the orbit information of the TerraSAR-X orbit ([German Aerospace Centre (DLR), 2010]. DLR estimates that the pixel geolocation error of TerraSAR-X is on the order of 1 m when ignoring the effects of terrain but accounting for approximately 20cm of uncertainty in the position of the satellite [German Aerospace Centre (DLR), 2010; German Aerospace Centre (DLR), 2007]. Furthermore, stacking allows for easy application of regions of interest to the SAR images from which to retrieve backscatter statistics, the next step in the processing of images.

Once images had been processed, regions of interest (ROIs) were selected and applied to the images (Figure 3.3.1). The four regions of interest are:

- 1) **land** which represents agricultural fields.
- 2) **forest** which is a section of mixed wood forest near the lake.
- 3) **lake** which composes the study area on Miquelon Lake.
- 4) **QSCAT** which represents the area of the QuikSCAT pixel used for Ku-band backscatter analysis.

A region of interest defined by the positions of the regular in-situ measurements on the lake was selected using the GPS coordinates of the snow depth profile lines. Regions of forest and agricultural land or open fields near Miquelon Lake were also selected for analysis. While the agricultural land is harvested each fall, stubble is often left on the fields to capture snow and minimize soil erosion in the fall and spring. Furthermore, some lands may be pastureland, while others may be left fallow for a season. Miquelon Lake Provincial Park lies within the mixed-wood sub-region of the boreal forest and contains a mix of deciduous and coniferous trees. Although the deciduous trees would be bare during the study periods, the coniferous trees can capture snow within their canopy structure and both can provide significant roughness for SAR backscatter. A region of interest corresponding to the QuikSCAT pixel used for Ku band comparison was also created. The lake occupies roughly 40% of the QuikSCAT pixel area. Agricultural land occupies roughly 20% and the forest represents approximately 30% with 10% being unclassified or mixed.

After examining the results from the TSAR-X SSC SL imagery presented in Figure 3.3.2, it was decided that the number of process chains should be reduced as little information was being gained from processing all images through each of the possible chains illustrated in Flow Chart 3.1. For the TerraSAR-X SSC SM imagery, terrain correction with radiometric normalization was applied. For the TerraSAR-X MGD-RE only radiometric calibration was applied due to errors in the ESA NEST software that prohibit the terrain correction operator from being applied to these image types. Terrain correction is the method of image processing proposed for the CoReH2O mission while

the more simple radiometric calibration method is currently the normal method of calibration over flat surfaces such as sea ice or the ocean.

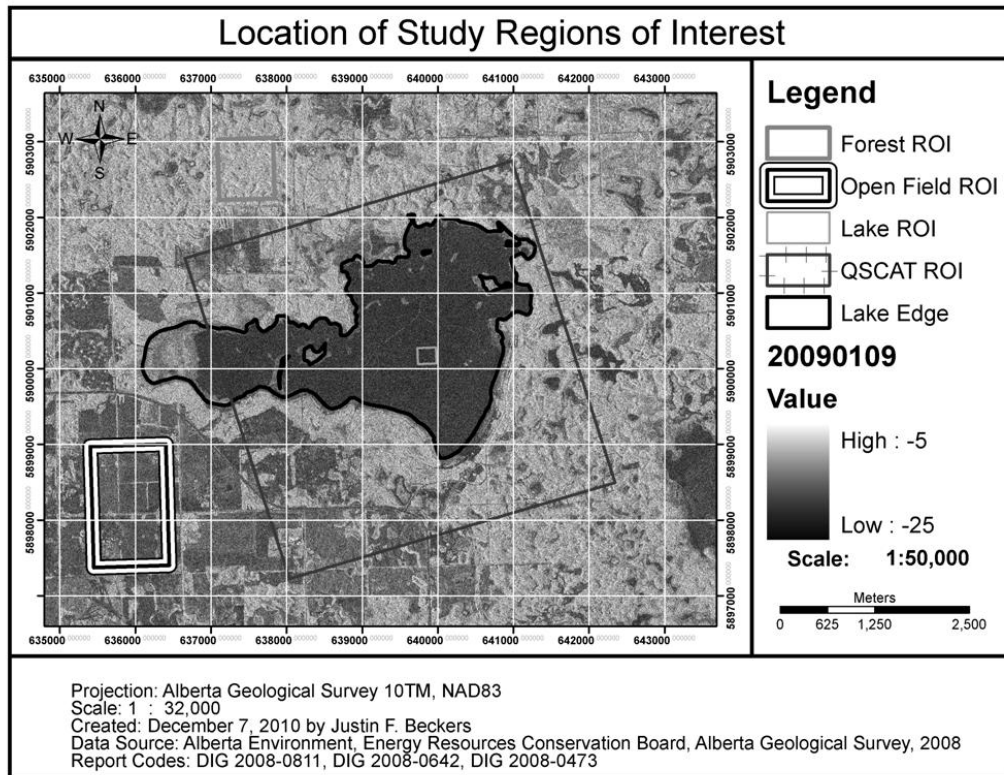


**Figure 3.3.1: Location of regions of interest (ROIs) for which backscatter statistics were extracted and analyzed. The QuikSCAT pixel over Miquelon Lake is the red ROI, the blue ROI defines the region of in-situ measurements and is referred to as the Lake ROI. The white/black and green ROIs represent land and forest regions. TerraSAR-X image ©DLR 2009.**

The terrain correction with radiometric normalization operator was also applied to the Envisat ASAR APP images in order to properly correct the imagery as it corrected the image geocoding. Terrain correction provides the most accurate results over the topography of the land, forest and the QuikSCAT pixel area. Flow Chart 3.2 presents the processing steps for each of the products used in the statistical comparison in Chapter 4.

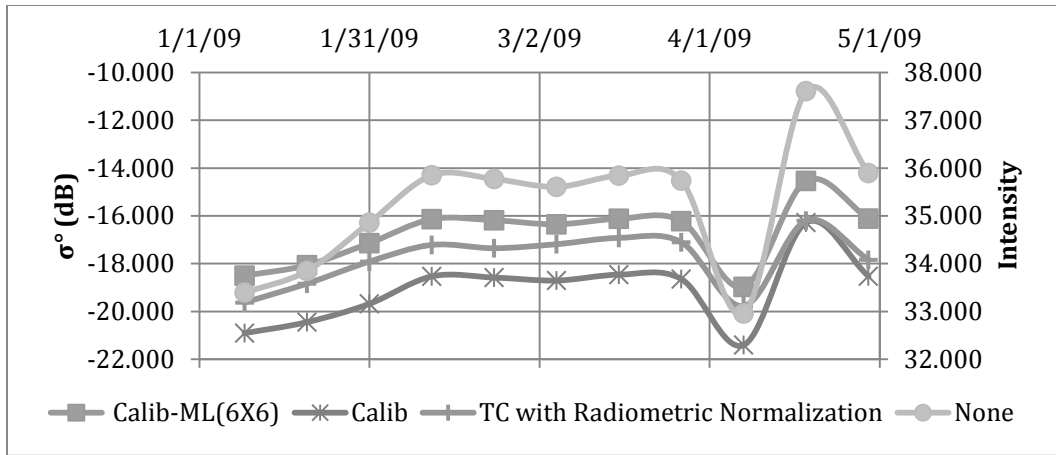
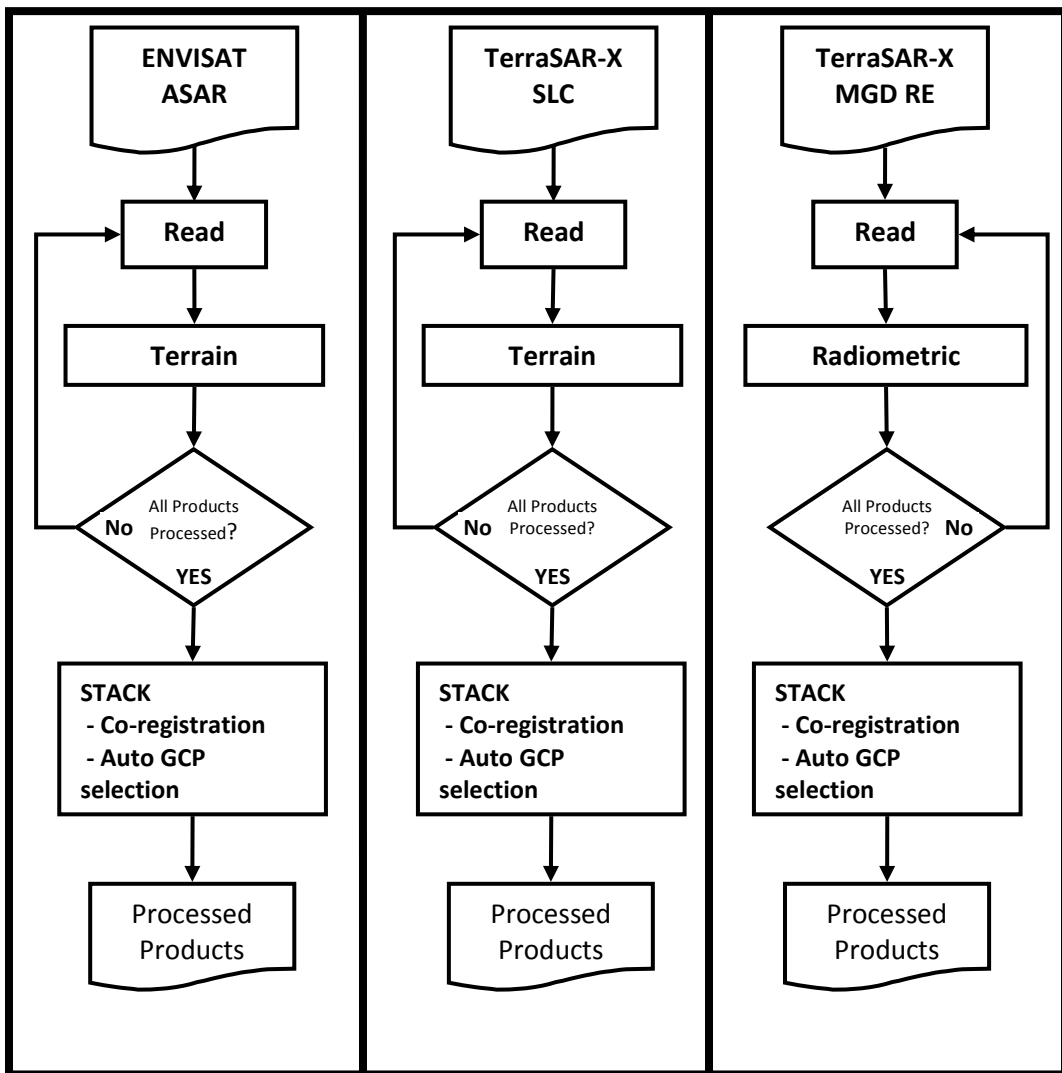


Figure 3.3.2: TerraSAR-X SL results from the Lake ROI for four selected processing chains.



Flow Chart 3.2: Flow chart outlining the processing steps used for each type of SAR image acquired for the study and used in the statistical analysis.

## Chapter 4. Results and Discussion

### 4.1 Seasonal evolution of ice, snow, and environmental properties

In order to assess the suitability of Miquelon Lake as a sea ice analogue it is important to compare and contrast the physical snow and ice properties found on the lake to the marine sea ice environment. One of the key requirements must be that the lake ice that forms is saline. Similarities in properties such as length of the ice season, ice thickness, and snow properties contribute to the assessment of Miquelon Lake as a sea ice analogue. The presence of ridges, rafting, flooding, and snow-ice formation are features often associated with brackish and marine sea ice and their presence on Miquelon Lake provide additional evidence for the lake as an analogous study site for sea ice research. Data from 2008/09 and 2009/10 are compared and contrasted to each other, to marine sea ice environments such as the Arctic Ocean and to brackish sea ice environments such as the Baltic Sea. The inter-annual comparison also provides context on the representativeness of the observed conditions, as well as inter-annual variability.

#### 4.1.1 Comparison of Snow, Ice and Meteorological Conditions

Measurements of snow and ice properties, SAR backscatter and measurements of water, ice, snow and air temperatures were conducted for two winters on Miquelon Lake, AB. In this section the seasonal evolution of the snow and ice properties are presented, beginning with water and moving upwards through the ice into the snow and air.

##### Water Salinity

The salinity of Miquelon Lake varied between 7 and 13 ppt during the study (Figure 4.1.1). As a result of Miquelon Lake's low water volume and lack of through-flow, the salinity of the lake increases throughout the winter as brine is rejected during ice formation. The coefficient of determination ( $R^2$ ) between ice thickness and water salinity was greater than 0.95 in both 2008/09 and 2009/10 (Figure 4.1.1). The water salinity also influences the ice growth rate as the freezing point of the water decreases as the salinity increases throughout the winter. The salinity of Miquelon Lake at the beginning of the 2009/10 ice-season was 10.1 ppt, the same as the peak water salinity associated with the maximum ice thickness in 2008/09. This suggests that the water level and lake volume dropped over the summer of 2009 as the melting of ice would have freshened the water.

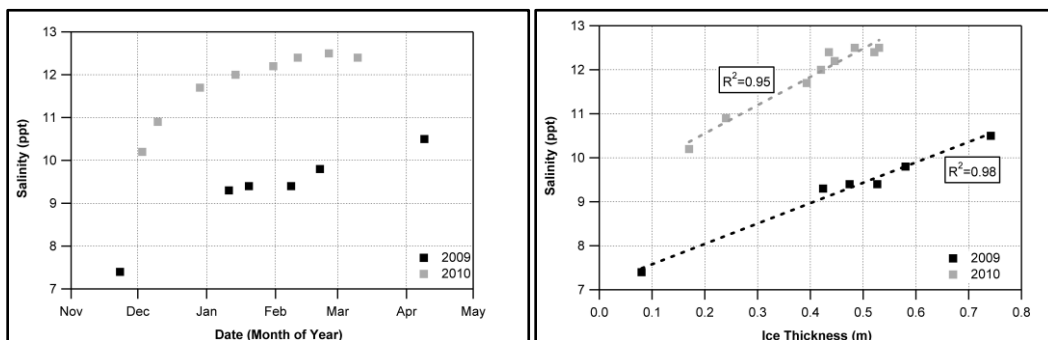
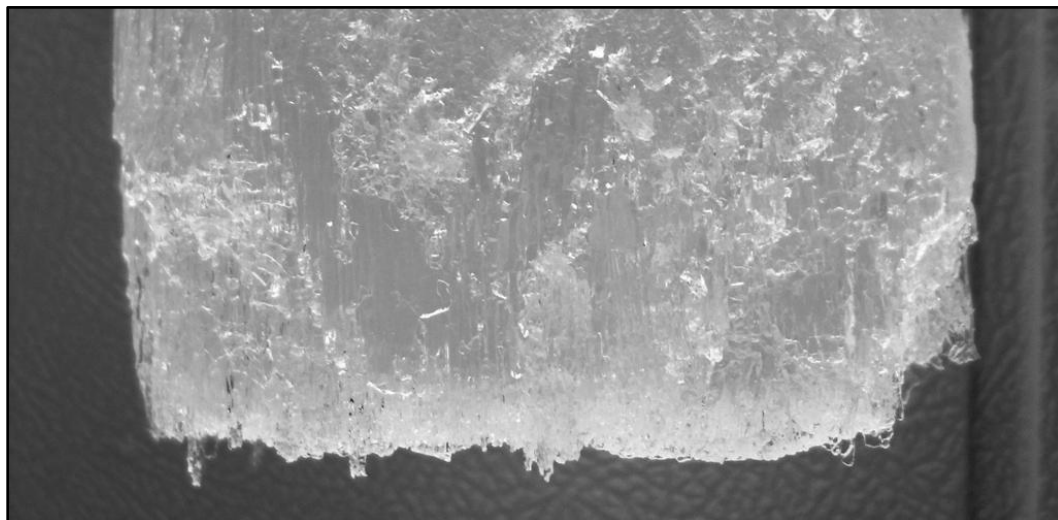


Figure 4.1.1: Left: Evolution of water salinity of Miquelon Lake from 2008-2010. Right: Correlation between ice thickness and water salinity.

The salinity of Miquelon Lake is much lower than the Arctic Ocean but similar to the Baltic Sea (3 ppt - 9 ppt; [Leppäranta and Myrberg, 2009; Granskog et al., 2003]). Ocean currents play an important role in determining water salinity within the Baltic Sea, and are not observed in Miquelon Lake as it has no inlet or outlet streams [Swanson and Zurawell, 2006]. The salinity of Miquelon Lake is controlled by ice thickness during the winter and by the water balance during the summer. Surface runoff also influences the salinity of surface waters in the Baltic Sea.

### **Ice Structure**

The different micro-scale properties of ice are an important mechanism for distinguishing between fresh and brackish water ice and saline ice. Unfortunately, a freezer break down resulted in the loss of all archived ice cores from Miquelon Lake before analysis of the ice crystal type, size and orientation could be completed. Photographs of the cores provide macro-scale structural information. The bottom 2-3 cm of ice on Miquelon Lake exhibits the same lamellar, or "skeleton layer", at the ice water interface as sea ice and ice from the Baltic Sea. This layer results from brine rejection and constitutional super-cooling at the ice-water interface and it is not found in freshwater lake ice(Figure 4.1.2,Figure 4.1.3; [Petrich and Eicken, 2010]).



**Figure 4.1.2:** Skeletal (lamellar) ice layer at the bottom of an ice core extracted from Miquelon Lake on January 20, 2009. Bottom of the ice core is at the bottom of the photograph. Skeletal layer consists of vertically oriented lamellar dendritic crystals formed as salts are rejected from the ice.

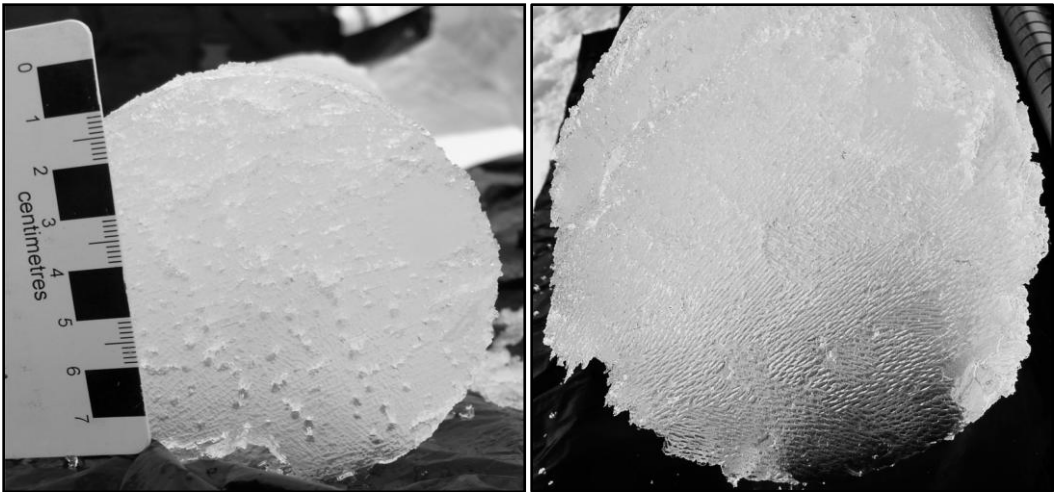


**Figure 4.1.3:** Left: Brine drainage channels (circles) and skeletal ice layer (faint lines) in ice core acquired on Miquelon Lake on March 21, 2010. Right: Skeletal ice layer (faint thin lines) in ice core from Miquelon Lake.

Photographs also reveal the presence of large brine drainage channels that develop as brine migrates through the ice through the winter season (Figure 4.1.3). Neither brine drainage channels nor the lamellar ice layer are found in freshwater ice. Snow-ice was observed at the top of some of the ice cores in 2008/09 and 2009/10 and indicates flooding events (Figure 4.1.4). Figure 4.1.4 shows that 25-30% of the ice core may be snow-ice. Snow-ice has been shown to contribute 20-35% to the total ice thickness in the Baltic Sea as well [Granskog et al., 2003].

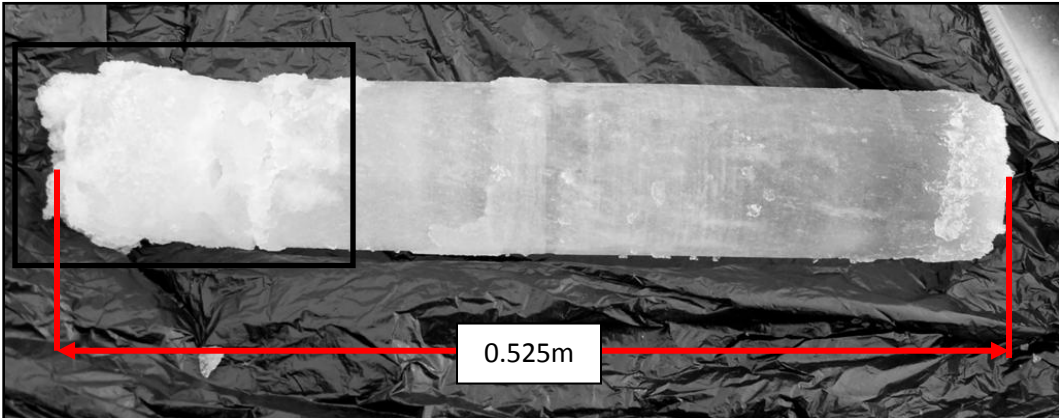


**Figure 4.1.4:** Snow-ice (black box) at the top of a 0.525m long ice core acquired from Miquelon Lake on March 21, 2010.

### **Ice Salinity**

Interpretation of the changes in salinity within the ice cores through the two seasons is complicated. Figure 4.1.5 presents the data for 2008/09 and shows a C shaped profile typical of Arctic sea ice for December 4, 2008, while the other cores show a reversed C or S shaped salinity profile. Ice salinity in the upper layers increases in February of both seasons, presumably due to flooding. Most cores do show an increase in the salinity of the bottom sample where water is freezing and desalinization processes do not occur. The April 9, 2009 core shows a strong decrease in the salinity of the upper 0.1 m, and

lower salinities than measured previously in the season through much of the core. By April 9, 2009, temperatures were high enough to melt the snow, which in turn drains through and flushes the salt out of the ice. The data from 2009/10 is presented in Figure 4.1.6 the and it shows a reversed C for most of the cores except December 3, 2009, and February 11, 2010. The situation in 2009/10 was complicated by a very early heavy snowfall that caused negative freeboards beginning December 29, 2009 although no flooding was observed until the next in-situ measurement on January 14, 2010. Negative freeboards were observed up to and including the field visit on March 10, 2010, when it appears that the flooded snow was incorporated as snow-ice. Furthermore, estimates of freeboard derived from the IMB suggest a long period of negative freeboards. Although the buoy estimated freeboards are more negative than observed in the field, in-situ observations of snow-ice in the acquired ice cores (Figure 4.1.4) suggest that significant flooding occurred early in the season forming a substantial amount of snow-ice that resulted in changes in salinity of the top layers of the ice. A possible sampling bias is that snow-ice was included in the ice core salinity analysis. Further observations in 2010/11 suggest that flooding is a common occurrence on Miquelon Lake and is dependent on the timing of major snowfall events. Snow-ice formation and flooding is also a common occurrence in the Baltic Sea, with snow-ice often contributing 20-35% of the total sea ice thickness [Granskog et al., 2003].

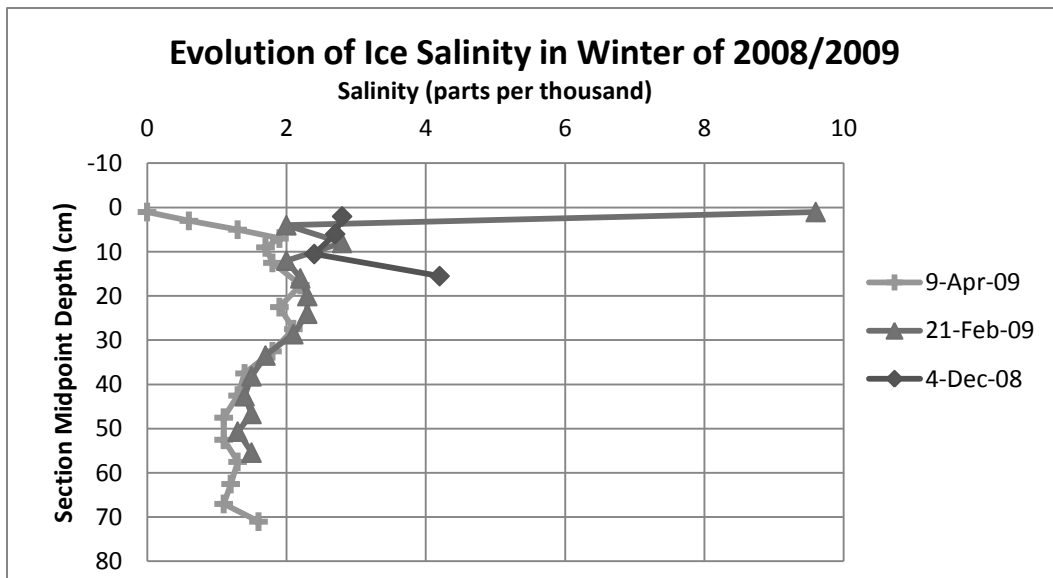
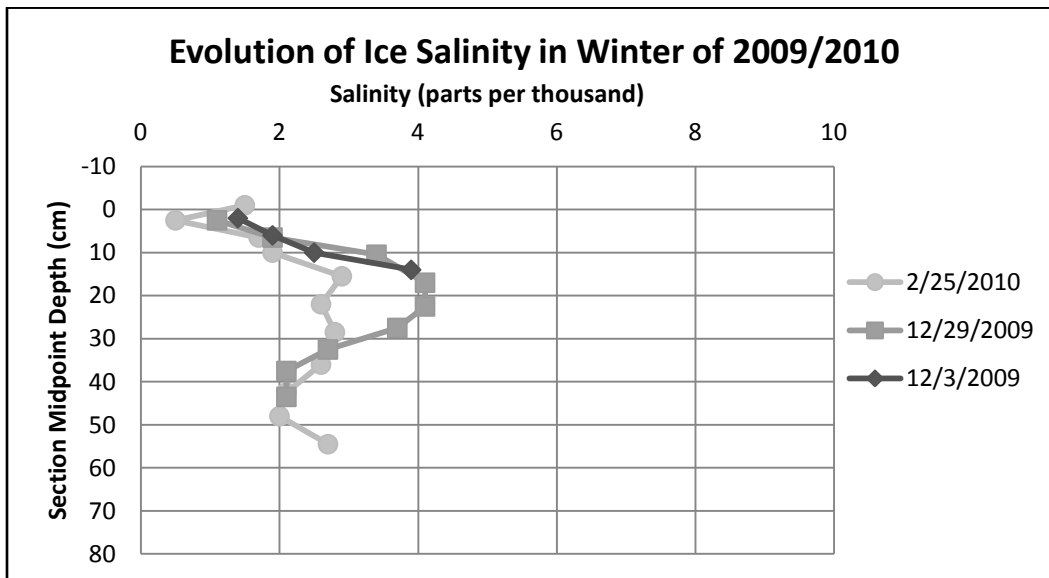


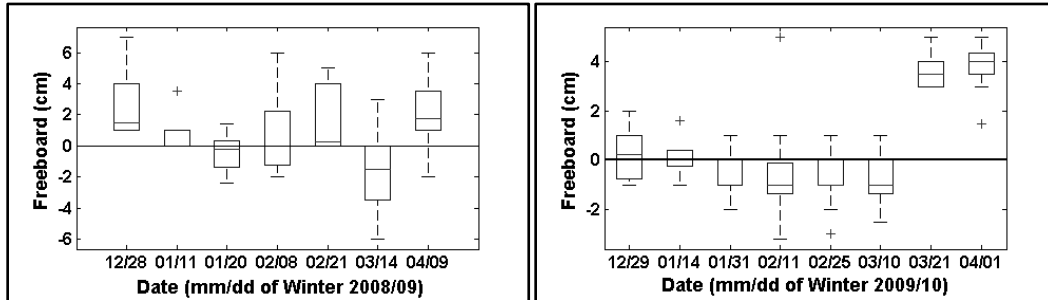
**Figure 4.1.5: Seasonal evolution of ice salinity on Miquelon Lake in the winter of 2008/2009.**  
Note the decrease in salinity over the course of the winter.

Salinity values for sea ice in the Arctic range from 0-4 ppt for multiyear sea ice and 4-10 ppt for first year sea ice with salinity decreasing as the ice ages due to the desalinization processes described in Section 2.1.4. The ice salinity on Miquelon Lake more closely approximates multi-year sea ice than first year ice in the Arctic. The salinity of the lake ice was often slightly higher than the 2 ppt or less observed in the Baltic Sea [Granskog et al., 2003; Granskog et al., 2003; Kawamura et al., 2001; Granskog et al., 2004; Granskog et al., 2006; Vihma and Haapala, 2009]. The salinity values of Miquelon Lake ranged from 0 - 4 ppt with the majority of the samples lying between 1 and 3 ppt. Salinity is also influenced by the growth rate of ice and variations in the growth rate

because of the temperature fluctuations observed over Miquelon Lake may explain some of the salinity variations particularly near the bottom of the ice. Kawamura et al. (2001) and Granskog et al. (2003; 2004) observed a significant difference in the salinity between the upper granular layers of ice and the lower columnar ice suggesting that different salt entrapment and retention mechanisms exist [Granskog et al., 2003; Granskog et al., 2004; Kawamura et al., 2001]. Unfortunately archived ice cores from Miquelon Lake were lost due to a freezer malfunction before texture analysis could occur. While the bottom portion of the ice from Miquelon lake is likely composed of columnar ice crystals as evidenced by the skeletal layer at the ice-water interface (Figure 4.1.2), the upper portion may similarly be composed of granular layers resulting from the incorporation of snow-ice. FYI in the Arctic typically exhibits a C - shaped salinity profile with depth [Petrich and Eicken, 2010]. The salinity profile of seasonal ice in the Baltic Sea does not show this C-shape, nor does the ice formed in Miquelon Lake [Granskog et al., 2006]. Ice salinity also depends on growth rate. Given the strong correlation between ice thickness and water salinity and the decrease in the freezing point of water with increasing salinity, it is very likely that the ice growth rate and thus ice salinity changed over the course of the season. Unlike in the Baltic Sea or the Arctic Ocean, Miquelon Lake is a completely enclosed water body and thus as the ice thickness increased, the salinity of the lake increased, slowing ice growth. Water currents and mixing of the upper waters below the ice in the Baltic Sea or Arctic Ocean result in only minor changes in the salinity of the upper waters under the ice.

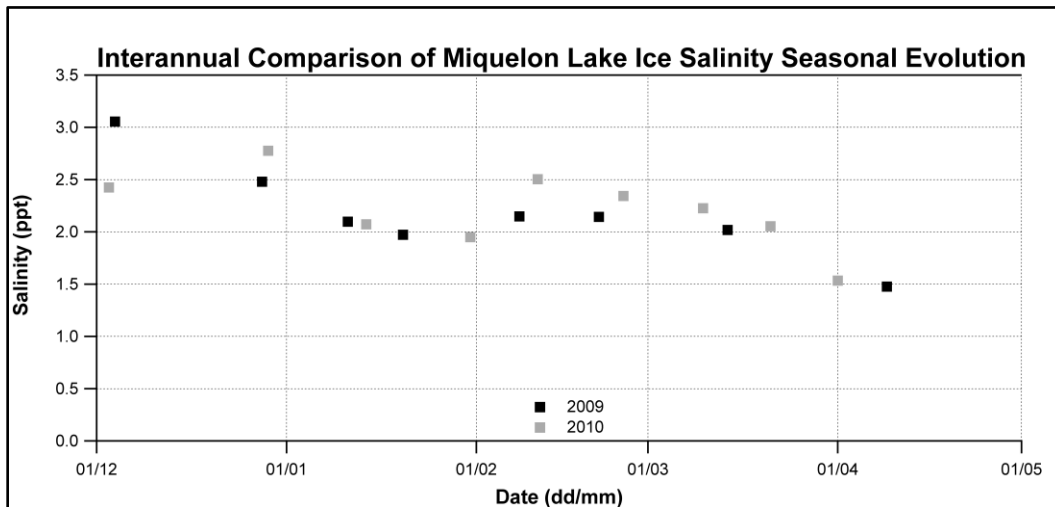


further evidence for surface flooding and snow-ice formation. Calculations of freeboard using in-situ measurements of ice and snow thickness and snow density indicate negative freeboard measurements at several times throughout the year (Figure 4.1.7). However, Figure 4.1.7 shows that positive freeboards were also observed throughout much of the 2008/09 winter. In 2009/10, freeboard calculations indicate the possibility of flooding as early as December 29 - January 14, 2010. The measured freeboards were mostly negative until late March 2010 when the snow had largely disappeared.



**Figure 4.1.7: In-situ measurements of ice freeboard on Miquelon Lake. Left and Right present the data for the winters of 2008/09 and 2009/10 respectively.**

Further evidence of flooding was observed in photographs and data from several ice cores collected in 2010 and from in-situ observations. Elevated salinity values were recorded from the snow near the ice interface and negative freeboards were observed at the manual drill holes. Ice salinity was higher in 2009/10 than 2008/09 as expected with the increased water salinity.



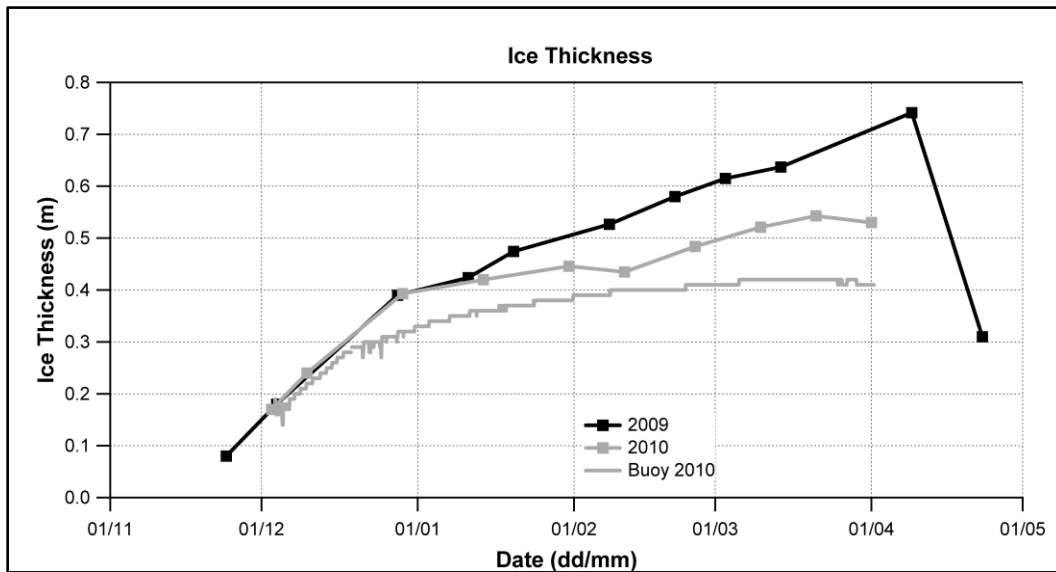
**Figure 4.1.8: Comparison of the seasonal evolution of bulk ice salinity on Miquelon Lake.**

Figure 4.1.8 above shows the non-linear reduction in bulk ice core salinity observed in the ice on Miquelon Lake. Interestingly, an increase in the bulk salinity was observed in early February of both winters. In 2010, a storm event deposited upwards of 0.1 m of snow in a short period of time in early February, potentially lowering the ice surface below water level (Figure 4.1.7). In 2009, a small increase in snow depth was observed near the end of January. The snow density also increased by approximately  $100 \text{ kgm}^{-3}$  between January 20 and February 8, 2009. The mass of snow overlying the ice can be

enough to lower the height of the ice surface to lie below the water surface. The flooded snow surface may eventually freeze to form saline snow-ice. As snow-ice was not distinguished from sea ice in salinity or thickness measurements it is possible that the observed increase in bulk salinity is due to the incorporation of snow-ice.

### **Ice Thickness**

The ice thickness on Miquelon Lake differed significantly between 2008/09 and 2009/10 (Figure 4.1.9). Maximum ice thickness in 2008/09 was  $0.89 \pm 0.01$  m near the observed ice ridge and  $0.78 \pm 0.01$  m in the thermodynamically grown level ice, whereas in 2009/10 the maximum observed ice thickness was  $0.60 \pm 0.01$  m. Ice thickness measured at the CRREL IMB in 2010 was consistently less than drill hole measurements and exhibits a plateau at  $0.41 \pm 0.05$  m. At first glance it appears that the stabilization of ice thickness may be an artifact caused by the sonic ranger of the CRREL IMB being closer to the ice bottom than its minimum distance requirement. However, the SAMS IMB differential heating measurements also estimate a maximum ice thickness between 0.40 m and 0.50 m (Figure 4.1.10). As both buoys show a strong decrease in the ice growth rate and a leveling off of ice thickness at approximately  $0.45 \pm 0.05$  m, the signal is real and not due to minimum distance errors from the sonic ranger in the CRREL IMB. Slight differences in the ice and snow cover may be responsible for the differences between the averaged in-situ ice thickness measurements and the point measurement of the IMB and between the two buoys. In 2008/09, the ice surface was closer to the under-ice thickness sensor than the minimum required distance after only 16 days and therefore buoy ice thicknesses for that year are not included in Figure 4.1.9.



**Figure 4.1.9: Inter-annual comparison of seasonal evolution of ice thickness on Miquelon Lake.**

The thickness of sea ice in the Baltic Sea is the result of both thermodynamic and dynamic growth. Ridging and rafting play an important role in ice thickness development in regions with surface wind and ocean currents, and where ice cover is discontinuous. Wind forcing can cause ridging or rafting on Miquelon Lake but only during the short period when the lake is not completely ice covered. Thermal expansion can also cause cracks and ridges on Miquelon Lake. The thickness of level ice in the

Baltic Sea ranges from 0.3 to 0.8 m depending on the region and severity of the winter [Vihma and Haapala, 2009]. As a comparison to Miquelon Lake, in 2010, the level fast ice thickness in the Baltic Sea ranged from 0.4 - 0.85 m [Vainio et al., 2010].

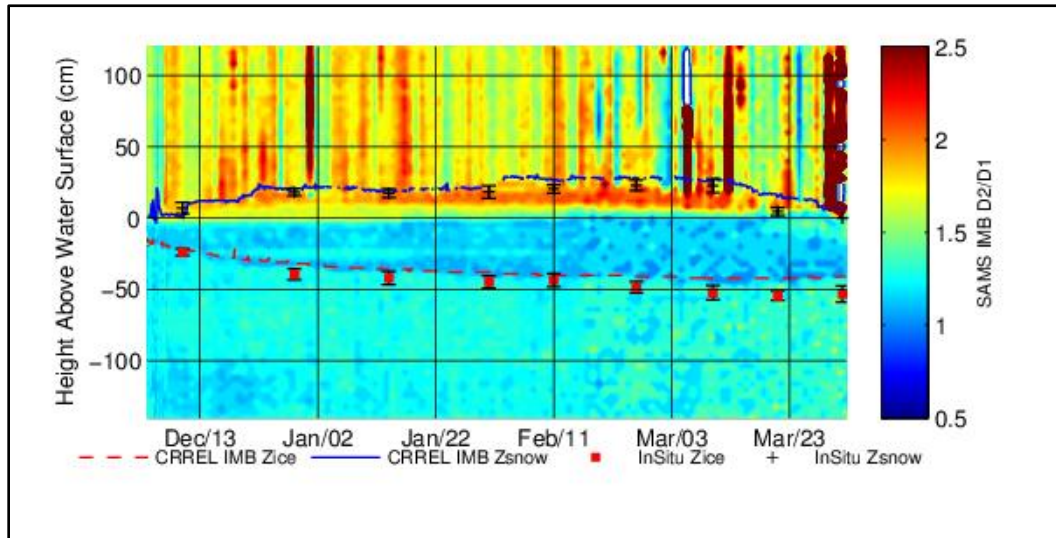


**Figure 4.1.10:** Ice thermal conductivity parameterization from the SAMS IMB deployed on Miquelon Lake in 2009/10. Heat is applied to the temperature sensors. The temperature increase observed is inversely proportional to the thermal conductivity of the medium surrounding the sensor. The data shown is the ratio of the amount of heating after 60s and after 15s. The plot shows the in-situ and autonomous snow and ice thickness data where  $Z$  represents thickness.

However, ice affected by dynamic processes can have mean thickness values greater than 1.5m [Vihma and Haapala, 2009; Haas, 2004]. In 2008/09 a small ridge formed in the ice on Miquelon Lake (Figure 4.1.11 and Figure 3.1.2). Thickness values over the ridge ranged from  $0.66 \pm 0.01$  m to  $0.89 \pm 0.01$  m when the surrounding level ice thickness was on average  $0.62 \pm 0.01$  m. The ridge is also clearly visible in the SAR imagery (Figure 3.1.2, Appendix B.3).



**Figure 4.1.11:** Ice ridge that developed on Miquelon Lake in 2008/09.

## Snow Depth

The snow cover on Miquelon Lake showed inter- and intra-annual spatial and temporal variability in properties including snow depth, variations in the timing of snow fall events, snow density, and as a result, SWE (Figure 4.1.12.). Figure 4.1.12 shows that snow depth increased during short lived events that deposited 0.10-0.15 m, rather than through small repeated contributions. The histograms show narrower, more peaked, depth distributions in 2008/09 than 2009/10. The histograms show earlier onset of deep snow in December 2009 compared to 2008 but that the modal snow depth was the same for February and March of both years. Figure 4.1.12a,b shows that the maximum snow depth was greater in the winter of 2008/09. The figure also shows that the duration of snow cover on the lake was approximately three weeks less in 2009/10 than the previous winter, melting in the second week of March instead of early April.

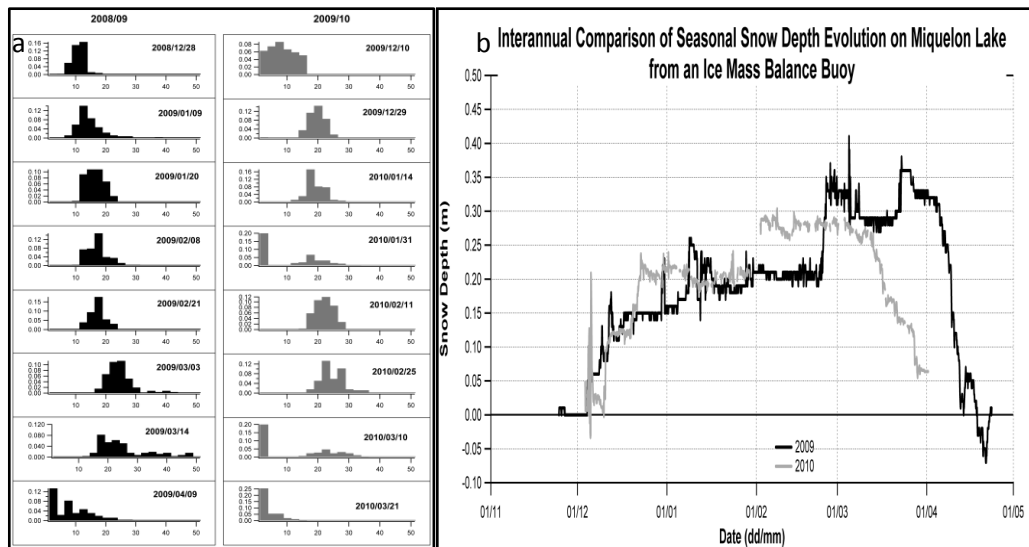


**Figure 4.1.12: Inter-annual comparison of seasonal evolution of snow depth on Miquelon Lake. Histograms of snow thickness are presented in Figure 4.1.12a. Buoy derived snow depths are presented in Figure 4.1.12b.**

The thickness was also less variable in 2009/10 than the previous winter. Snow melt decreased rapidly between the March 10 and 21, 2010. Stable Semi-regularly spaced drifted snow features were observed on Miquelon Lake through much of the 2009/10 season. The variability in thickness associated with the drifts influenced ice thickness and account for some of the difference between the IMB ice thickness measurements and those made in drill holes.

The snow depth record exhibits some short term variability as a result of persistent high winds causing blowing snow (Figure 4.1.13). In Figure 4.1.13 periods of high wind and fluctuations in snow depth are indicated by black arrows. Suspended windblown snow can influence the SAR backscatter response if the thickness and density of the blowing snow is high enough.

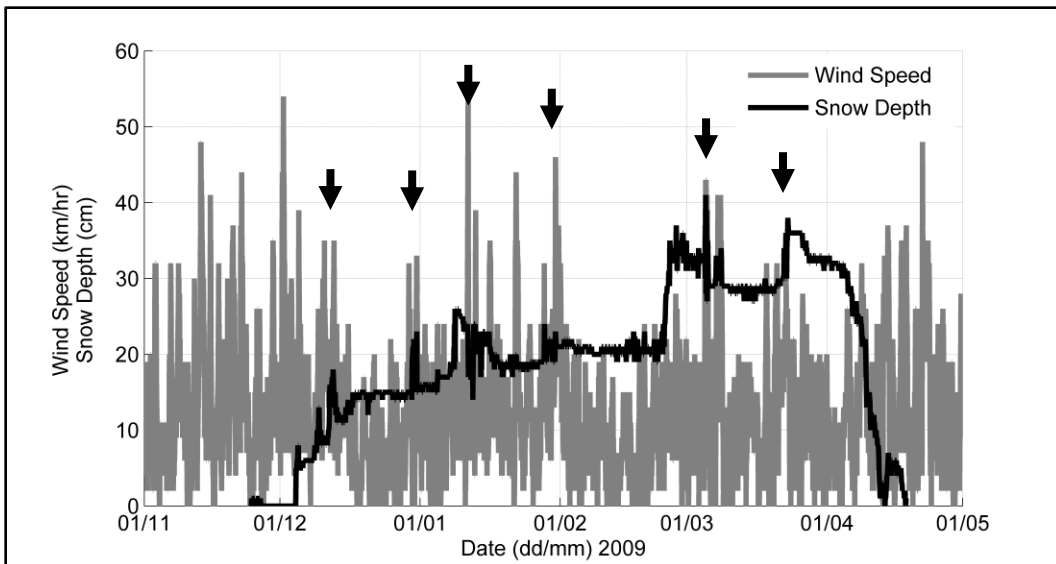


**Figure 4.1.13: Visual correlation between short-term variability in snow depth and wind speed.** Wind speed data acquired from the Camrose, AB weather station and snow depth is from the CRREL IMB surface sonic ranger. Grey lines are wind speeds in km/hr while the black line is the snow depth in cm. Arrows indicate times of high winds and sudden changes in snow depth. Note that negative snow depths are indicated by the sonic ranger in late April.

### Snow Density

Figure 4.1.14 presents the bulk snow density measurements for the study. Snow density values were greater in 2008/09 especially during February where the difference was 150  $\text{kg m}^{-3}$ . The measurement for April 9, 2009 suggests a very dense wet snow pack and agrees well with the observed high temperatures (Figure 4.1.15) and the onset of snow melt (Figure 4.1.12b). Figure 4.1.14 shows that the density of snow on Miquelon Lake was typically between 180 and 400  $\text{kg m}^{-3}$ . Mean snow density in the Arctic is 340  $\text{kg m}^{-3}$  with a narrow range of variability [Sturm et al., 2002a]. The long Arctic winter allows for the development of a very hard wind slab layer that overlies depth hoar. The same snow layering was observed on Miquelon Lake. Measurements of snow density in the Baltic Sea by Crocker in 1988 ranged from 170-300  $\text{kg m}^{-3}$ , similar to the values from Miquelon Lake before the onset of melt.

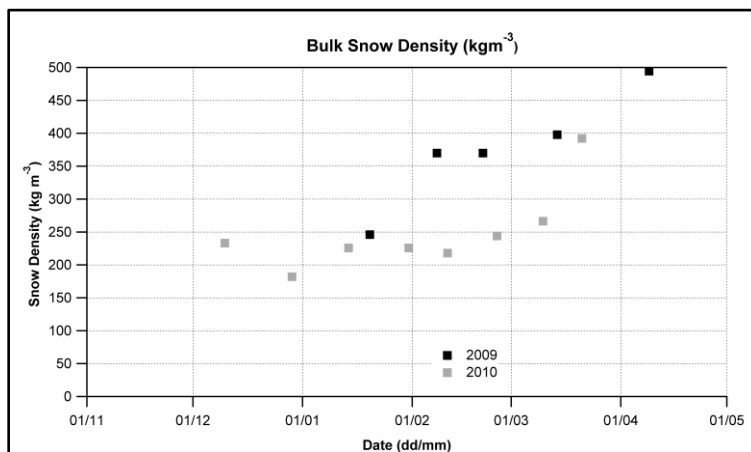


**Figure 4.1.14: Inter-annual comparison of the evolution of snow density on Miquelon Lake.**

## Air Temperature

As the flux of energy between the water and atmosphere exerts a strong influence on the growth and melt of sea ice, and with the aforementioned differences in both ice and snow properties it is unsurprising that air temperatures showed different trends between the two seasons. Figure 4.1.15 reveals the differences in the mean daily air temperature during the two seasons of study. Mean air temperature values were computed from the CRREL IMB in both years. Air temperatures were very similar in December and January of both years except that 2008/09 saw more positive air temperatures in January (Figure 4.1.15). The beginning of February 2009 had warmer temperatures than in February 2010. However after early February, air temperatures were higher in 2010 than 2009 with mean daily temperatures above -10°C for most of this period in 2010. The warm temperatures resulted in very rapid melting of snow in 2010.

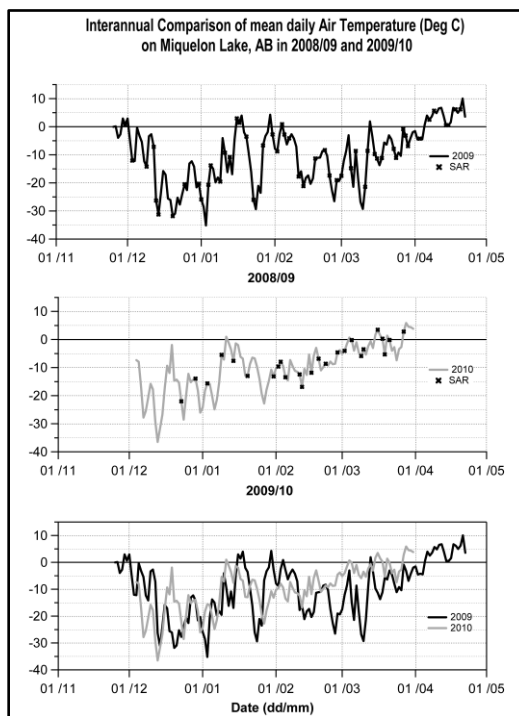


**Figure 4.1.15: Comparison of mean daily air temperatures on Miquelon Lake for the winters of 2008/09 and 2009/10. Black dots indicate days where SAR images were acquired.**

Another way of examining the different ice and air temperature characteristics between the two seasons is through the use of positive and negative degree-days (PDD and FDD, respectively). Figure 4.1.16 below presents the cumulative freezing degree days and positive degree days from the lake calculated using the IMB temperature record. PDDs and FDDs are derived using -0.55°C as the freezing temperature of water in Miquelon Lake, as this temperature was often observed in the lake just below the ice surface in 2008/09. This temperature also corresponds to the freezing temperature of water with a salinity of 10 ppt. A freezing (positive) degree-day is the number of degrees below (above) the freezing point for each day using the mean daily air temperature. Empirical relationships between the cumulative sum of freezing/positive degree days and ice growth/decay have been estimated by many authors (e.g. Lebedev, 1938 in [Wadhams,

2000]; [Anderson, 1961]). The equation of Lebedev (1938) as presented in Wadhams (2000), where Zice, the ice thickness is related to the cumulative sum of freezing degree days

$$Z_{\text{ice}} = 1.33 * \sum \text{FDD}^{0.58}$$

estimates 0.94 m and 0.8 m of sea ice growth on the lake in 2008/09 and 2009/10 respectively. The simple equation of Lebedev does not account for the insulating effect of the snow but clearly shows the influence of the different numbers of FDDs in the two years. The role of air temperature on ice growth is strongly influenced by the presence and properties of the snow pack (Section 2.2). Figure 4.1.16 also shows that the rate of accumulation of freezing degree days was similar between December and February of both years. Figure 4.1.16 shows the warm air temperatures in early December and February 2008/09 as decreases in the slope of the cumulative FDDs and increases in the cumulative PDDs. In 2009/10, the accumulation rate of FDDs slows dramatically after mid-February and agrees well with the stabilization of ice thickness measured by the CRREL IMB (Figure 4.1.9). Figure 4.1.16 also shows that fewer positive degree days were accumulated during the middle of winter between January and early March in 2009/10 than the previous year. Examining Figure 4.1.15 and 4.1.16, one can see that positive air temperatures which could have caused snow melt were observed only in the middle of January 2010 but occurred multiple times through January, February and March in the previous winter.

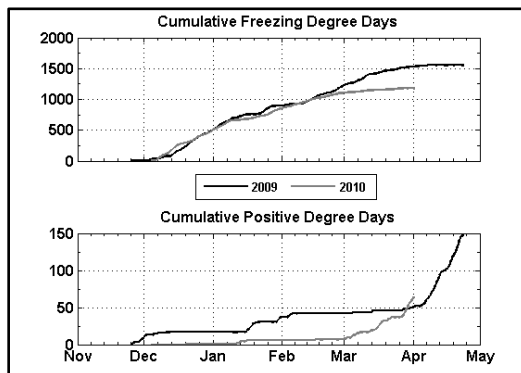


**Figure 4.1.16: Comparison of cumulative positive and negative degree days for Dec. to May, 2008/09 and 2009/10. Degree days were calculated using the IMB on Miquelon Lake.**

Sustained warm air temperatures result in increased temperatures within both the snowpack and the ice. The high air temperatures observed in March/early April of 2008/09 would have increased the liquid water content of the snow pack. As liquid water is a strong absorber of microwave energy, SAR signals do not penetrate through the wet snow and thus give measurements of only the upper few cm (see Section 2.1.3). As penetration depth also decreases with increasing frequency, X and Ku band SAR are much more sensitive to snow wetness than C band. Figure 4.1.15 reveals that several SAR acquisitions occurred on days where mean daily air temperatures were above 0°C and in some cases had been so for at least a day or so. The number of SAR images acquired on days with positive mean daily air temperatures was lower in the second study season than in the first, largely as a result of fewer mid-winter melting events in the second year.

Because measurements of snow properties were only performed on the lake, the use of QuikSCAT and AMSR-E data assumes that the values on the lake are similar to those for the surrounding forest and agricultural land. However, snow depth over these land types is likely higher than the open environment of the lake due to increased surface roughness that acts to reduce wind transport of the snow. An extensive snow depth survey performed on March 3 2009, showed that wind distribution and surface roughness from ground level foliage resulted in increased snow depths in the shore area adjacent to the lake than over the lake surface (see Figure 4.1.17.).

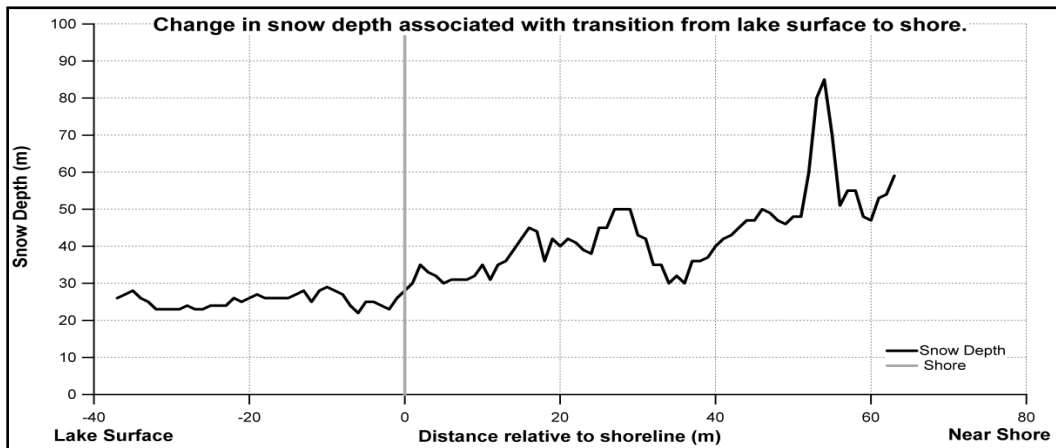


**Figure 4.1.17:** Snow thickness across the transition from lake surface to near shore environment. Survey was performed on March 03, 2009. Snow depths on the lake are representative for the day.

The snow properties on Miquelon Lake, AB are assumed to be similar to those of the larger region because the lake presents an open environment. Furthermore the assumption is required as no snow property information was acquired for land and forest surrounding the lake. Figure 4.1.18 shows that the agreement between AMSR-E derived SWE and in-situ measurements of SWE is relatively good in 2008/09 only.. The agreement between AMSR-E SWE and in-situ SWE in 2009/10 is quite poor as the AMSR-E SWE values are several times larger than the in-situ measurements of SWE performed on the lake. Possible explanations for this discrepancy include the conversion of snow to snow ice during flooding events on the lake and changes in passive microwave signature of the region due to changing snow and ice properties such as wetness, grain size and the presence of ice lenses.

The presence of snow-ice resulting from negative freeboards and flooding of the ice surface in 2009/10 could potentially explain the difference between the AMSR-E and in-situ SWE measurements. Negative freeboards were noted more often in 2009/10 than the previous year (Figure 4.1.7). The formation of snow ice would remove the contribution of that snow layer to SWE as snow-ice thickness was not measured. The AMSR-E dataset provides much higher temporal resolution than the in-situ measurements but at a spatial resolution of approximately  $25 \text{ km}^2$ . The AMSR-E SWE estimates are based on passive microwave measurements and are sensitive to changes in the snow properties such as wetness and grain size. Although there is substantial disagreement in the magnitude of SWE derived from AMSR-E and in-situ measurements, the timing of increases and decreases of SWE are similar between the two methods.

The difference between the AMSR-E estimate and the in-situ measurement of SWE also illustrates some of the problems associated with these two commonly used retrieval methods.

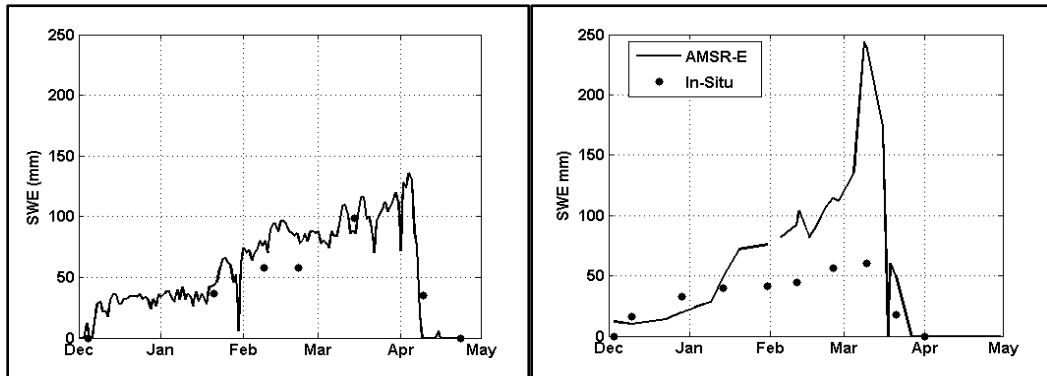


**Figure 4.1.18: Comparison of SWE measurements from AMSR-E and in-situ measurements on Miquelon Lake in 2008/09 and 2009/10 presented on left and right, respectively.**

### Summary

Natural variability plays an important role in the development of the snow and ice properties over the lake. The variability shown between just these two years alone is large. Snow depth, and density were found to be more similar to the Baltic Sea than the Arctic. The snow depth in the Arctic is not very different from the Baltic or Miquelon Lake but the snow density is higher owing to the longer winter and strong winds that form wind slab type snow. Snow-ice, which forms from flooding of the ice surface by the saline water underneath was observed on the ice formed in Miquelon Lake. Snow-ice was more prevalent in 2009/10 than the year before and observations in 2010/11 showed even more snow-ice and significant flooding over the lake. Snow-ice is not common in the Arctic but is common in the Baltic Sea as a result of the relatively thin ice but thick snow pack.

The ice properties of Miquelon Lake were found to be much more similar to those of the Baltic Sea than the Arctic. Salinity and thickness values were similar to the Baltic Sea, reflecting both the lower salinity of the source waters and the temperatures observed during the winter. The macroscopic structure of the ice in Miquelon Lake showed characteristic features of saline ice including the lamellar ice layer at the ice - water interface and the presence of brine channels.

The similarity of the lake's snow and ice properties to those of the Baltic Sea provides a strong argument for the suitability of Miquelon Lake to act as a Baltic Sea analogue. Snow and ice properties on the lake were also observed to be highly homogeneous. This makes the lake an excellent remote sensing study site as spatial averaging of snow, ice, and image properties can be used to reduce noise such as the speckle found in radar images. Furthermore, since the lake becomes completely covered with ice, ice motion is not an issue in the analysis of the ice and its snow cover. The logistical ease and affordability of conducting measurements on the lake, its size and homogeneity combined with its seasonal snow and ice cover make it an excellent alternative to ice

tank studies. Data from ground, air and space-borne sensors can be calibrated and validated while ice tanks only allow for ground-based sensors.

## 4.2 Temporal Evolution of Radar Backscatter

While the CoReH<sub>2</sub>O mission involves only X- and Ku-band frequencies, we decided to include C band data with the objective of retrieving information about the ice on Miquelon Lake. As the ice is thin and has low salinity, it was thought that information regarding properties such as ice thickness, bulk salinity, or brine properties could be retrieved. Previous work has also shown that the penetration depth of C band radar into sea ice can be significant [Hallikainen and Winebrenner, 1992]. Furthermore, the literature on the response of C-band backscatter to changing snow properties is confused. While many studies suggest that C-band backscatter does not respond to changes in the properties of dry snow, particularly when the snow cover is thin, others have suggested that C-band backscatter can be used to monitor SWE, either through the thermal control of snow on sea ice surface temperature and thus backscatter or by interferometry as was discussed in Section 2.4.

In the following section the temporal evolution of the C-, X-, and Ku-band backscatter in 2008/09 and 2009/10 will be presented and discussed. Statistical information was gathered from the following four regions of interest (ROIs):

- 1) **land** which represent agricultural land.
- 2) **forest** which is a section of mixed-wood forest near the lake.
- 3) **lake** which composes the study area on the Miquelon Lake
- 4) **QSCAT** which represents the area of the QuikSCAT pixel used for Ku-band backscatter analysis.

The ROIs will henceforth be denoted in the discussed as lake, land, forest and QSCAT. The ROIs are denoted as lake, land, forest and QSCAT in the labels of figures. In addition to the plots in Section 4.2, subsets of each SAR image are presented in Appendix B, with Appendix B.1 containing the Envisat ASAR images from 2008/09, Appendix B.2 and Appendix B.3 present the TerraSAR-X images for 2008/09 and Appendix B.4 and Appendix B.5 present the Envisat and TerraSAR-X images for 2009/10 respectively. All images in Appendix B have been scaled to the same brightness values of -24dB to 0dB.

### 4.2.1 Temporal Evolution of ASAR C-Band Backscatter

Figure 4.2.1 presents the C-band backscatter coefficients,  $\sigma^0$ , from Envisat ASAR imagery acquired over Miquelon Lake in the winter of 2008/09. All images were acquired from one of two swaths, where a swath includes a certain incidence angle range. Although, the repeat cycle of Envisat is 35 days, the swath width and decreased track separation with increasing latitude result in several images being acquired each month from a particular swath at varying incidence angles within the swath range. For each unique incidence angle only two to three images were acquired. Backscatter decreases with increasing (more shallow) incidence angle as more energy is scattered away from the sensor than towards it, especially for smooth surfaces such as the lake. Corrections for this effect can be made when enough images are acquired at a particular incidence angle over a short time and with assumed stability in the physical and EM properties of the target medium. Unfortunately, the combination of too few images from a particular

incidence angle and the instability in the physical and EM properties of the snow and ice means that a robust correction for incidence angle could not be made and so the change in backscatter is contaminated by changes in incidence angle. To reduce the effect of incidence angle on  $\sigma^0$  analysis, the images were split into their respective swaths (see Section 2.3.3 ;Figure 4.2.1, Figure 4.2.2). The published worst case noise estimated sigma zero (NESZ, see Section 3.3.1) is also included in each plot to illustrate the backscatter noise floor.

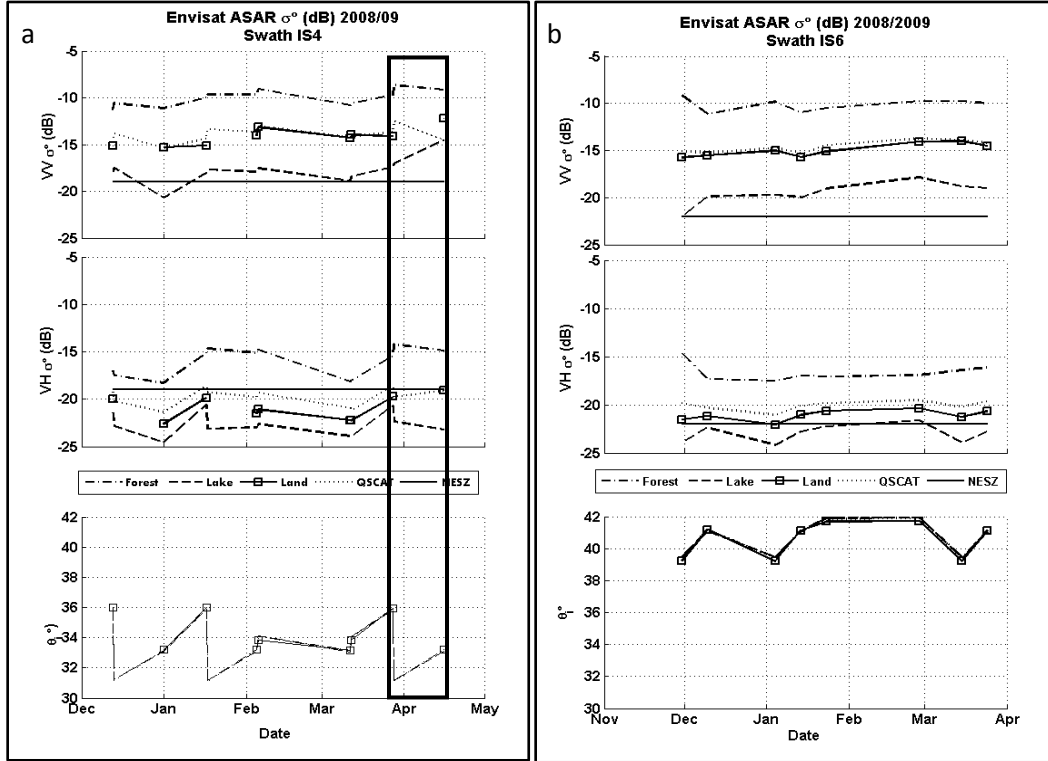


**Figure 4.2.1:** Seasonal evolution of Envisat ASAR C-band backscatter over Miquelon Lake in 2008/09. Figure 4.2.1a on the left presents the results from Swath IS4 which has an incidence angle range of 30-36°. Figure 4.2.1b on the right presents the results from Swath IS6 which has an incidence angle range of 39-42°.  $\theta_i$  is the incidence angle of the image measured at the study site on the lake. The NESZ is the noise estimated sigma zero (see Section 3.3.1).

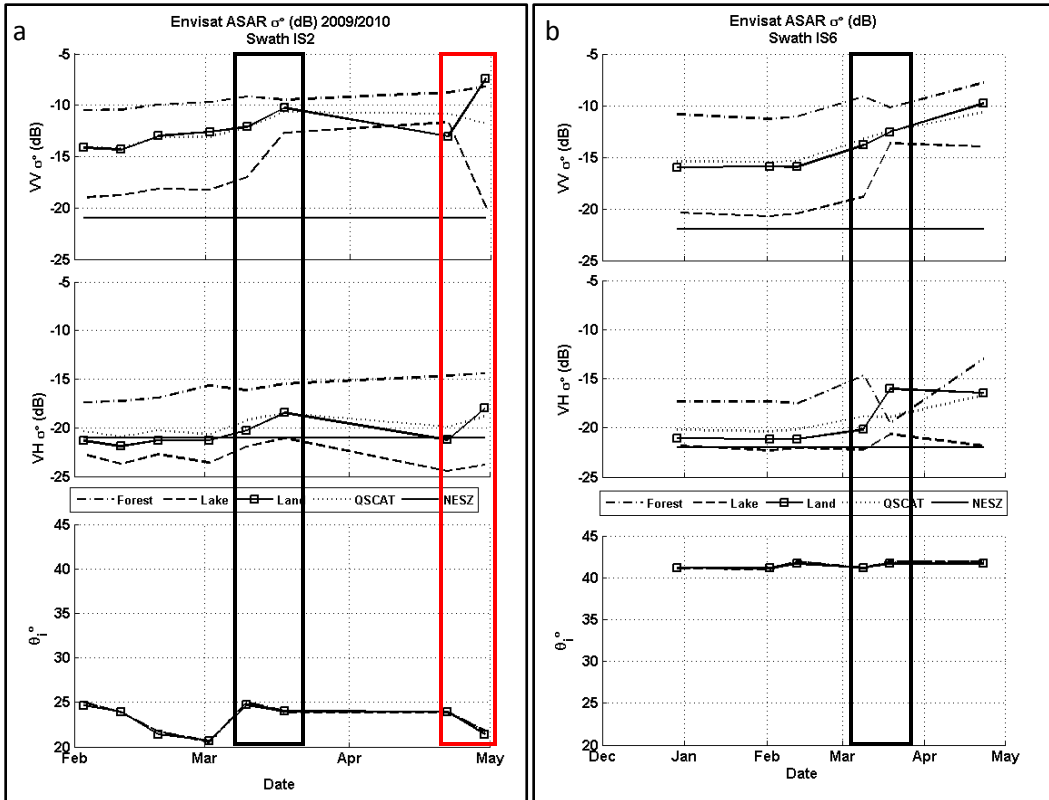
Backscatter in the VV polarization ranged from -12 to -9 dB for the forest, -16 to -12 dB for the land and QSCAT and -22 to -14 dB over the lake. Backscatter in the VH polarization ranged from -18 to -14 dB for the forest, -22 to -19 dB from the land and QSCAT and -25 to -21 dB over the lake. Backscatter from the forest is higher than from the other regions because of its significant surface roughness and numerous opportunities for volume and surface scattering. Furthermore, it is possible that at C-band the radar wave can penetrate through the lake ice or that it is absorbed by the brine of the upper ice. As expected, backscatter from Swath IS6 is generally lower than from Swath IS4. However, over Miquelon Lake in 2008/09 several instances of increased backscatter associated with an increase in incidence angle were observed, particularly in the cross-polarized (VH) channel.

Figure 4.2.1 indicates that backscatter from all ROIs but the forest are below the noise level of the VH polarization images from Swath IS4. If the changes in backscatter observed in the VH channel are a result of changes in system noise, then the lack of signal indicates either that the C-band signal is being absorbed or that the lake surface is smooth enough for specular reflectance. Backscatter values from the VV polarization were above the NESZ. VH backscatter from the lake was below the NESZ for Swath IS6 in 2008/09.

All ROIs exhibited a backscatter increase of 1 dB from January to March. An increase of approximately 2 dB was observed between March 28 and April 15 at the VV polarization but a 1 dB decrease in the VH channel. Unfortunately the poor temporal resolution makes it difficult to gain further insight from the time series from 2008/09.

Figure 4.2.2 presents the evolution of C-band backscatter for the winter of 2009/10. In comparison to the previous winter, the backscatter evolution in the winter of 2009 was much less variable within a swath even though images were still acquired at multiple incidence angles. The VV response for the lake is very similar between the two swaths, and appears to be simply offset by approximately 2 dB as a result of the greater incidence angle of swath IS6. The VH band shows more within-swath variability. The differences in within-swath variability between 2008/09 and 2009/10 may indicate a difference in the structure of the scattering medium between the two years and may be related to the presence of a substantial snow-ice layer in 2009/10 and decreased absorption or penetration into the ice.

A system error with Envisat ASAR resulted in no image acquisitions until late December 2009 followed by a large gap until February 2010. Backscatter from all ROIs is very stable over the winter with just a small increase until early March. Forest C-band backscatter decreases between early and mid-March. The backscatter from the land, lake and QSCAT increases at this time. Daily mean air temperatures became positive in early March of 2010 and thus the drop in backscatter from the forest may be indicative of liquid water within the snowpack contained in the forest canopy or the loss of the snow from within the canopy. An increase in backscatter from the lake, land, and QSCAT was observed by TerraSAR-X at this time as well, indicating that both C and X-band responded to changes in snow wetness and not changes in ice properties. The VH channel exhibits greater variability associated with incidence angle, contrary to other studies that suggest that VH is less sensitive to changes in incidence angle [Partington and Flach, 2010]. VV backscatter remains elevated over the lake until late April, and does not drop before May 1, 2010 over the forest. The drop in backscatter over the lake at the end of April is caused by the complete disappearance of ice and the appearance of open water on a calm day.



**Figure 4.2.2: Evolution of Envisat ASAR C-band backscatter over Miquelon Lake in 2009/10.**  
**Figure 4.2.2a(left)** presents results from Swath IS2 which has an incidence angle range of 20°-26°. **Figure 4.2.2b (right)** presents results from Swath IS6 which has an incidence angle range of 39°-43°. Black box indicates the period of snow melt. Red box indicates the disappearance of the ice.

C-band backscatter from the study region showed only limited change from freeze onset until the beginning of melt onset. Both years show a strong increase in backscatter that appears to be associated with onset of melt. This increase in backscatter has been reported in several other studies of FYI and has been suggested to be the result of increased volume scattering from an increasingly wet snow pack where the wetness remains below 3% by volume. Other factors that contribute to the increase in backscatter include a rapid increase of the size of the snow grains near the bottom of the snow pack and an increase in the brine volume of the ice near the surface [Yackel and Barber, 2007; Yackel and Barber, 2002]. Saline, wet snow was measured within the basal layer of the snowpack during the onset of snow melt over Miquelon Lake. However, one could also expect that as snow wetness increased towards 3%, the penetration depth and thus the contribution of changing ice surface properties would be greatly reduced, potentially decreasing backscatter. At a snow wetness of 3% by volume, the penetration depth of C,X, and Ku-band radar waves is reduced to just 9,4 and 3cm respectively.

#### 4.2.2 Temporal Evolution of X-band Backscatter

Numerous image types and polarizations were acquired from the TerraSAR-X satellite over Miquelon Lake. For the CoReH<sub>2</sub>O mission, X-band is used to provide measurements of SWE in deep snow, as it is less sensitive to changes in SWE than the Ku band. The X-

band SAR is also used to observe any backscatter changes from the underlying soil. Finally, X-band radar is believed to be sensitive to ice thickness up to 0.3 m [Clissold, 2009]. Over less saline ice such as Miquelon Lake, TerraSAR-X may be sensitive to even thicker ice. The TerraSAR-X time series is presented for a brief discussion of trends and comparison between the ROIs, the different products and to compare the two seasons of data.

Unlike the Envisat ASAR data, which was taken from a very large number of discrete incidence angles, the TerraSAR-X images were all acquired from one of three incidence angles in 2008/09 and one of two angles in 2009/10. Figures Figure 4.2.4, Figure 4.2.5, Figure 4.2.8, present the time series of backscatter over the Miquelon Lake study region. While most studies need to consider incidence angle effects within an image, the small scene widths of the imagery used in this study result in very narrow incidence angle ranges (e.g.  $<2^\circ$ ) across the scene. Furthermore, to mitigate the effect of incidence angle on backscatter, images have been separated into their respective swaths.

### **2008/09: TerraSAR-X MGD-RE**

Figure 4.2.4 presents the mean backscatter values from the four regions of interest in 2008/09 from the TerraSAR-X Multi-Looked Ground Range Radiometrically Enhanced (MGD-RE) images. As expected, backscatter decreased with increasing incidence angle. VV backscatter increases sharply from the land, lake and QSCAT in early February. VV backscatter was constant through March and a rapid increase in late March/early April. Backscatter decreases in early to mid-April. This rapid change from increased to decreased backscatter is related to the onset of snow melt and the transition from the pendular to the funicular snow wetness regimes. VV backscatter changes in the forest are of smaller magnitude with a slight increasing trend through the winter and a decrease in spring. Backscatter from the forest was much greater than from the other ROIs.

The VH backscatter is mostly below the noise threshold from both incidence angles but exhibits similar trends as the co-polarized channel. The low VH backscatter values suggest only the forest causes large amounts of depolarization of the vertically transmitted waves. The dense three dimensional structure of forests provides numerous scattering opportunities from leaves, branches, trunks and the ground. Waves that are scattered several times within the forest canopy before being scattered back to the sensor are more likely to experience depolarization and therefore increase the measured cross-polarized backscatter. A strong increase in VH backscatter from the lake, land, and QSCAT was observed in early February and is associated with positive air temperatures and an increase in snow density. Though the values are well below the worst-case noise floor of the sensor, the increase was also observed for the co-polarized (VV) channel and thus is likely real. Furthermore, the actual noise level of the images may be lower. The increase in VH backscatter could be indicative of increased volume and multiple bounce scattering from the snow pack, or potentially changes in the brine volume due to observed increased sea ice temperatures, an increase in the snow grain size due to brine wicking and the joining of snow grains by liquid water, or the development of snow-ice due to surface flooding and refreeze. Given that all of these parameters can cause an increase in the backscatter it is extremely difficult to determine which variable it was. It is also very interesting to note that X-band

backscatter did not increase with the deposition of 10cm of dry snow that occurred at the end of February (see Figure 4.1.12b), indicating minimal sensitivity to dry snow.

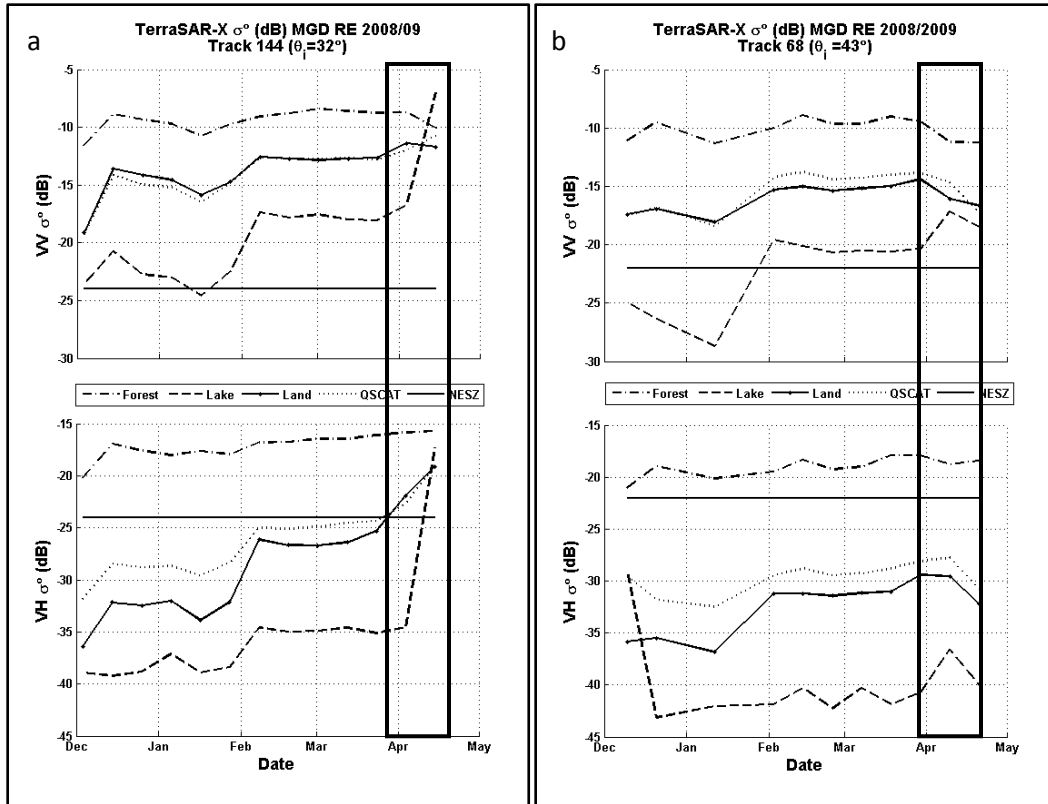
If one examines the TerraSAR-X images in Appendix B.2 and Appendix B.3, one can see regions of very low backscatter at the periphery of the lake beginning in February. The best example is the image from March 18 below (Figure 4.2.3). The large dark region extending north from the southern bay of the lake is believed to be grounded ice where ice has frozen to the lake bed. Duguay et al. (2002) suggested that there is no liquid water between the bed and the ice and thus the dielectric constants of the two media are similar, resulting in very little backscatter from this interface [Duguay et al., 2002].



Figure 4.2.3: TerraSAR-X MGD RE image acquired on March 18, 2009. Red box outlines feature that is suggested to be grounded ice.

If the X-band waves were able to penetrate through the ice for part of the season, it is unsurprising that there is little sensitivity to dry snow. It also indicates that the C-band radar waves likely penetrated through the ice for part of the season as well. The other explanations for the dark regions in Figure 4.2.3 are open water or standing water. However both of these are unlikely as the temperature was so low and the ice cover was continuous over the lake.

The increase in backscatter in early April is much stronger over the lake in VH than VV, further evidence of an increase in volume scattering from the snowpack associated with an increase in snow density and snow wetness within the pendular regime [Yackel and Barber, 2007; Yackel and Barber, 2002]. The increase in VV backscatter in April could be the result of increased brine volume in the upper ice and increasing liquid water content in the basal snow pack but within the pendular snow wetness regime as a result of the warm air temperatures [Yackel and Barber, 2002].



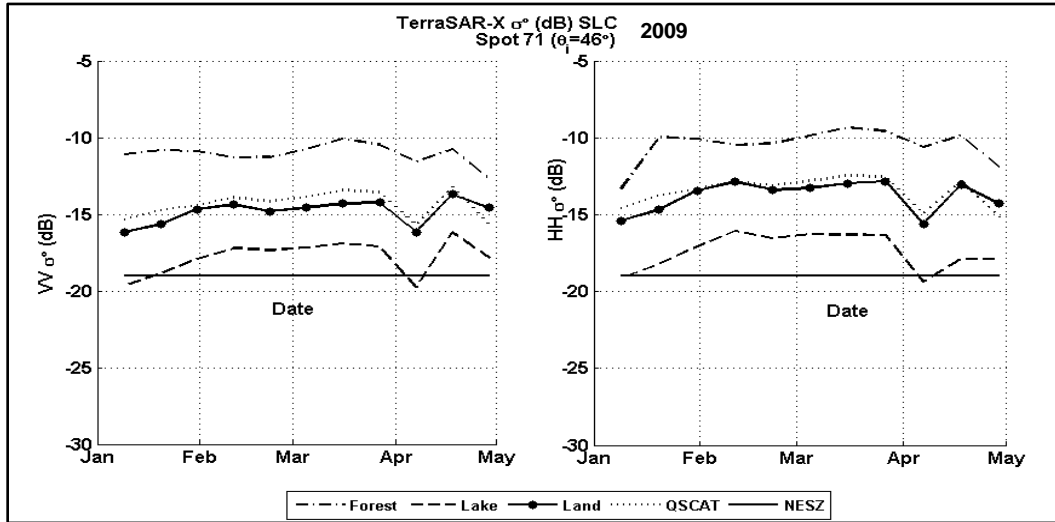
**Figure 4.2.4: Seasonal Evolution of X-band backscatter over Miquelon Lake in a) 2008/09.**  
**Figure 4.2.4a on the left presents results from one swath Track 144 ( $\theta_i = 32^\circ$ ).** Figure 4.2.4b on the right presents results from Track 68, ( $\theta_i = 43^\circ$ ). Incidence angles given are from over the Lake. The black boxes indicates the period of snow melt where backscatter increases sharply in early April and decreases in mid-April.

As the increase in backscatter was observed over land as well as over the lake, the change in backscatter is therefore largely due to changes in the snow pack or at the interface between the snow and underlying surface. Changes in ice properties such as brine volume or surface roughness could cause the difference in the magnitude of change observed over the lake versus the land. The backscatter increase in February was stronger in the VV polarization than VH from the lake but weaker over the land. Properties unique to the lake such as brine volume must have strongly influenced surface scattering contribution from the lake at this time as brine volume would not increase over the surrounding land and thus could not contribute to increased backscatter. The smaller increase in VV versus VH backscatter from land suggests that over the open fields the change is primarily in volume scattering related to the snow cover and not from changes in the surface properties.

#### 2008/09: TerraSAR SL-SLC

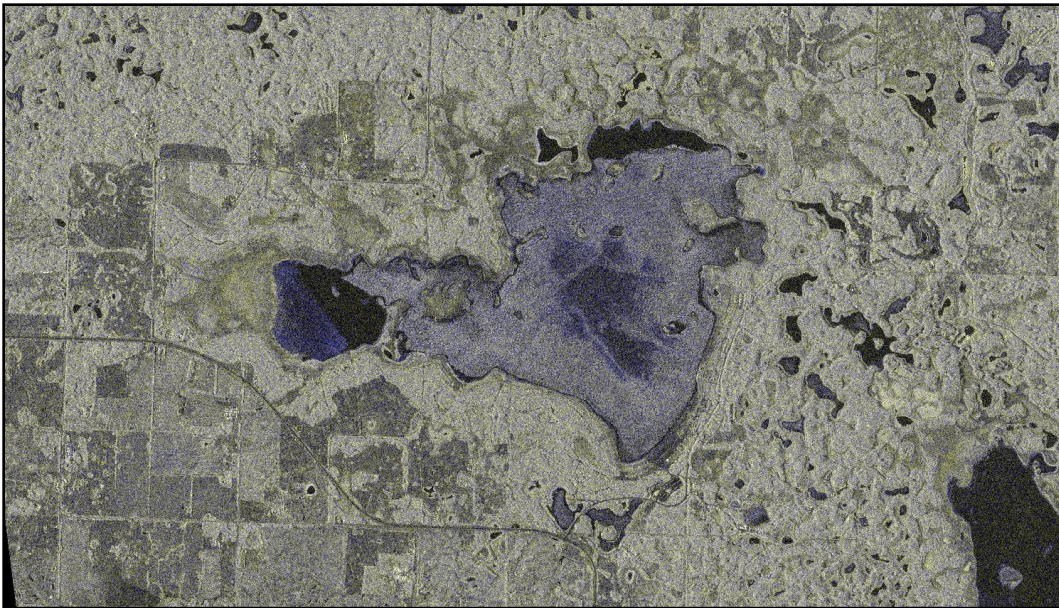
Figure 4.2.5 presents the results from the TerraSAR-X spotlight mode Single Look Complex imagery (SLC) that was acquired at the HH and VV polarizations. The data from the two co-polarized channels provide information on the structure of the target medium and helps to identify anisotropy in the structure. Horizontally polarized radar waves can penetrate further into vertically oriented structures than vertically polarized

radar waves and vice versa. Figure 4.2.5 shows that the HH backscatter was typically 1 dB greater than the VV backscatter over all the regions of interest throughout 2009.



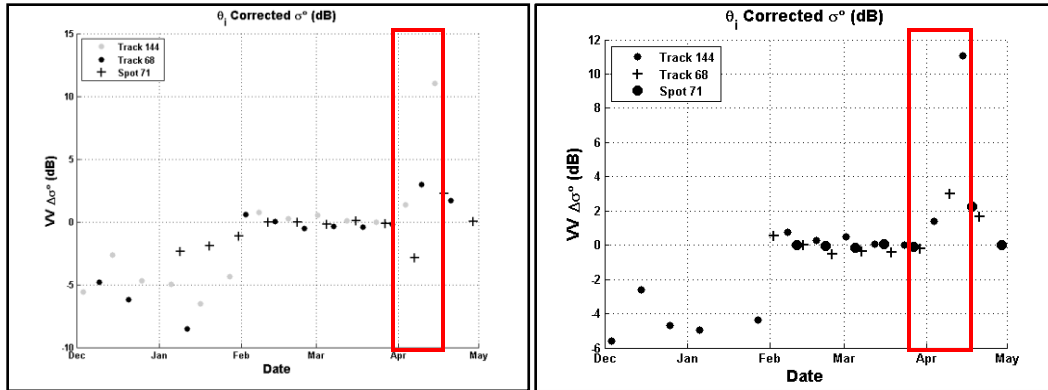
**Figure 4.2.5:** Seasonal Evolution of X-band backscatter over Miquelon Lake from TerraSAR-X spotlight mode complex images acquired in 2009 (Spot 71,  $\theta_i = 46^\circ$ ). Spotlight mode images were acquired at HH and VV polarizations.

Figure 4.2.6 presents the TerraSAR image acquired on April 18, 2009. Air temperatures were high on this day, and snow melt was well advanced and thus the wetness of the ice surface was high and perhaps covered by melt ponds. The image shows higher backscatter for vertically polarized waves than horizontally polarized waves over the central portion of the lake due to the presence of melt ponds. In this image one can also see regions of very low backscatter that indicate open water forming at the periphery of the lake.



**Figure 4.2.6:** TerraSAR-X spotlight mode image from April 18, 2009 over Miquelon Lake. North is up. Image is a false color composite composed from R=HH, G=HH, B=VV. Blue indicates high backscatter from VV polarized radar waves. Dark regions indicate absorption of radar waves by open water, wet snow or a flooded ice surface. TerraSAR-X image ©DLR 2009.

To view the complete time series of all TerraSAR-X images acquired at different incidence angles, curve fitting was used to normalize the backscatter to winter conditions that occurred in 2008/09 and to an incidence angle of 43°. Curve fitting could only reasonably be performed for 2008/09 as all images in 2009/10 were acquired at one of two incidence angles, whereas in 2008/09, images were acquired at one of three incidence angles. The correction works well for February/March as indicated by the small change in backscatter,  $\Delta\sigma^0$ , due to the curve fitting process during this time. The fit in December and January is poor as many values are below the NESZ and exhibit greater variability than in February-March. Generally, backscatter was low in December and January, increased sharply at the end of January and into early February and then stabilized in February and March. In early April the backscatter increased on April 3<sup>rd</sup>, and again on April 14. Between April 14th and 18th, backscatter decreased sharply. This was followed by continued decrease until the end of the TerraSAR-X imagery record on April 29th. The complete time series with and without removal of values below the NESZ is presented in Figure 4.2.7. The increase in backscatter in early February is suggested to be due to the influence of warm temperatures (Figure 4.1.15) causing increasing grain size (Section 2.2), brine volume (Equation 10) and snow wetness within the pendular regime as per the findings of Yackel et al. (2002; 2007), or a result of the formation of snow-ice or some combination of the two.



**Figure 4.2.7:** Full X-band Time Series over Miquelon Lake for 2008/09. Images are incidence angle corrected and are normalized to the conditions found in mid winter (February). Values below the NESZ have been removed from the plot on the right. Red boxes indicates the period of snow melt. Data after snow melt believed to result from ice covered by melt ponds.

#### 2009/10: TerraSAR-X SM-SLC

In 2009/10, TerraSAR-X StripMap (SM) mode Single Look Complex (SLC) images were acquired with HH and HV polarizations. Figure 4.2.8 presents the seasonal evolution of the X-band backscatter from the lake in 2009/10 from these images. Temporally, the backscatter evolution is very different in 2009/10 from the previous year. No images were acquired in early December when ice onset occurred.

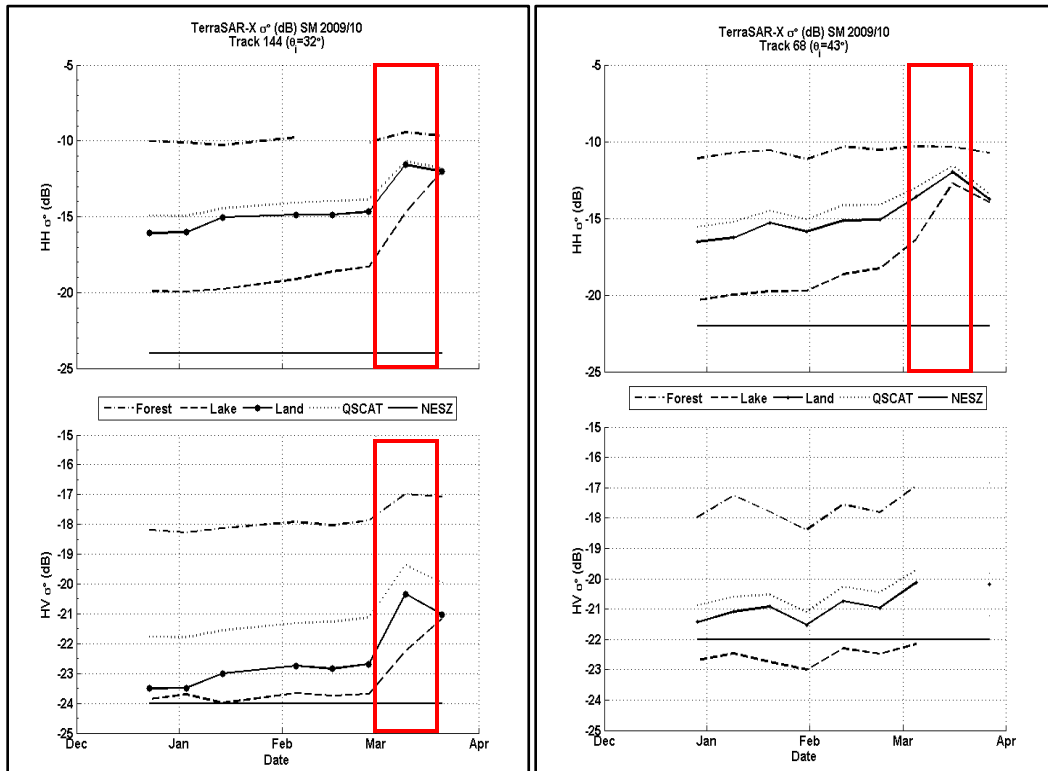


**Figure 4.2.8:** Seasonal Evolution of X-band backscatter over Miquelon Lake in 2009/10. Figure 4.2.8a on the left presents results from one swath (Track 144,  $\theta_i = 32^\circ$ ). Figure 4.2.8b on the right presents results from Track 68 ( $\theta_i=43^\circ$ ). Red boxes indicates the period of snow melt.

Backscatter from the forest was very stable at approximately -11 to -10 dB throughout the winter. Backscatter from the other ROIs increased slowly in January and February. A sharp increase in backscatter driven by the onset of snow melt occurred in early March for these regions.

In 2009/10, the backscatter at HH appears to be less sensitive to incidence angle than in 2008/09. This may be a result of differences in the processing of the complex mode stripmap mode imagery acquired in 2009/10 versus the radiometrically enhanced ground range imagery acquired in 2008/09 (Figure 4.2.8), or due to anisotropy in the orientation of the medium. The cross polarized backscatter HV is much higher in 2009/10 than the VH cross polarization in 2008/09. If the different magnitude of the cross polarization is not dependent on the DLR RE processing, then significant differences in the cross polarization are due to the snow and ice properties, or anisotropy in the medium causing preferential depolarization of horizontally polarized radiation. While the response from 2009 is very different than the previous year, the HH and VV responses in 2008 were very similar to each other for much of the season.

Following the work by Barber et al. (1995) Yackel et al. (2007), the increase in backscatter results from an increase in temperature causing increases in the dielectric constant of the ice, and in the brine volume. The increased air temperatures can also cause increased volume scattering from the snow cover due to rapid depth hoar development, brine wicking, an increase in the wetness of the snow pack within the pendular regime and an increase in snow density [Barber et al., 1995; Yackel et al., 2007].

#### **4.2.3 Temporal Evolution of Ku-Band Backscatter**

The time-series of Ku-band backscatter for the pixel centered over Miquelon Lake (see Figure 3.3.1) is presented in Figure 4.2.9. The lowest observed values of Ku-band backscatter appear in the middle of November 2008 when ice formation had just begun and the Ku-band radar waves were reflected away from the sensor by the smooth ice. Ice was observed on Miquelon Lake during a site visit on November 16, 2008.

The presence of snow beginning in early December causes the backscatter to increase sharply, a consequence of backscatter from the snowpack volume and/or additional surface roughness causing diffuse scattering. Backscatter decreased from the middle of December to mid January and rose from then on. Backscatter reaches peak values between February and the end of March before decreasing sharply in early April. The sharp decline is indicative of the sensitivity of Ku-band backscatter to the increase in snow pack wetness when the snow begins to melt. Due to their higher frequency and shorter wavelength, Ku-band radar waves have lower penetrating power than C- or X-band and thus are more strongly influenced by the presence of moisture within the snow cover. Referring back to Figure 2.2.2, even one percent volumetric liquid water content within the snowpack reduces the penetration power of Ku-band waves significantly more than X- and C-bands. The decreased penetration depth of Ku-band with wet snow results in decreased volume scattering from the snow, masking of surface scattering from the snow/ice interface and absorption of the signal by the liquid water.

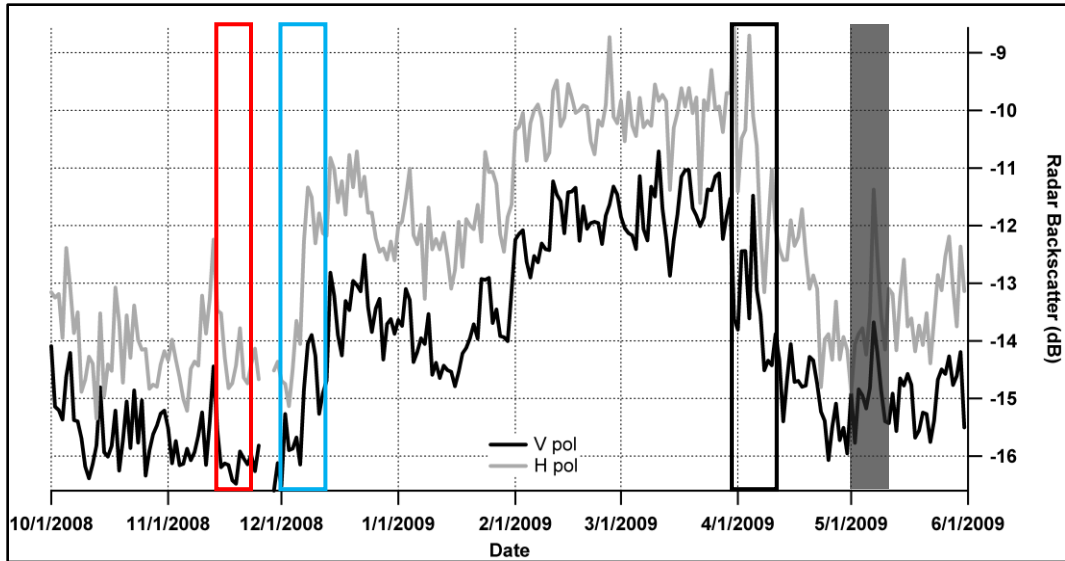


**Figure 4.2.9: Temporal evolution of Ku-band backscatter over Miquelon Lake from the QuikSCAT sensor. The first box (red outline) indicates the period of ice onset, The second box (blue) indicates the initial deposition of snow, the third box (black) indicates the period of snow melt and the four box (shaded dark grey) indicates period of complete ice melt.**

Similar behaviour has been observed over both MYI in the Arctic and freshwater lakes [Howell et al., 2008; Howell et al., 2009]. On Miquelon Lake, the snow depth and increase in snow wetness as melt began were sufficient to reduce the surface scattering component from the snow/ice interface, lowering the backscatter. The cycles of backscatter increases and decreases in April are associated with freeze thaw cycles ([Howell et al., 2009]; Figure 4.2.10).

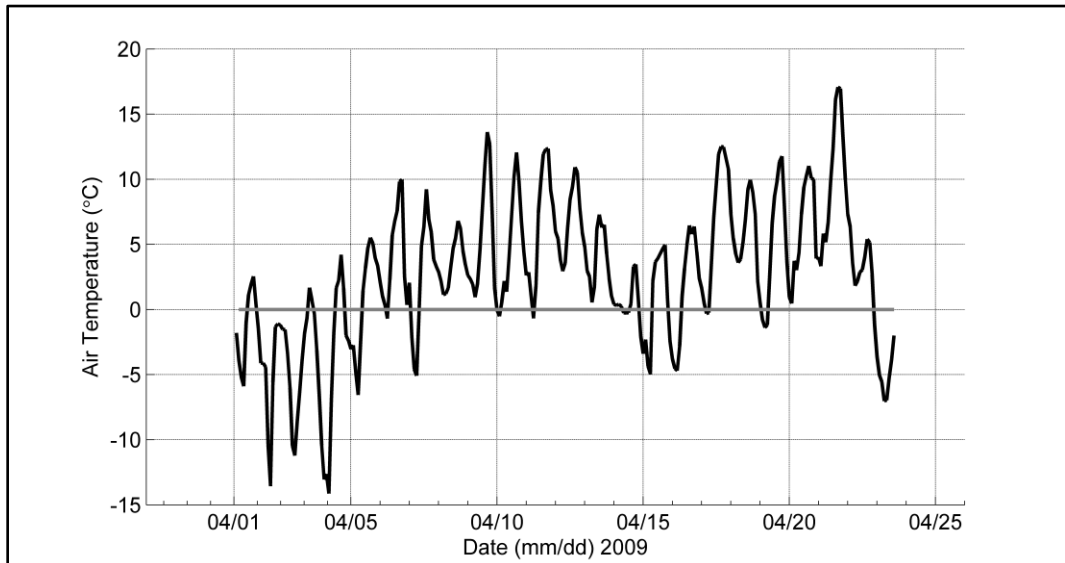


**Figure 4.2.10: Semi-hourly air temperature measurements over Miquelon Lake in April 2009 acquired by the CRREL IMB. Note the daily freeze thaw cycles.**

It is difficult to determine when the ice was completely absent from Miquelon Lake but it occurred between May 1 and May 9, 2009 as indicated by the Landsat images presented in Figure 4.2.11.

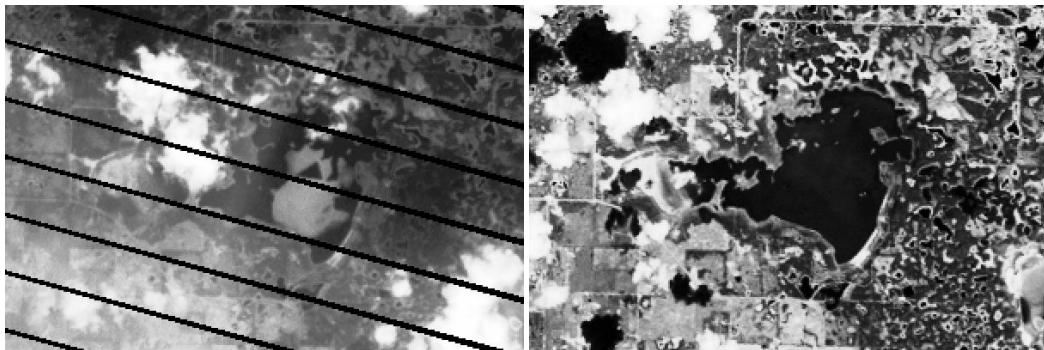


Figure 4.2.11: Left: Landsat 7TM image showing ice present on Miquelon Lake on May 1, 2009. Right: Landsat 5TM image showing no ice on Miquelon Lake on May 9, 2009. Landsat images courtesy of the U.S. Geological Survey [US Geological Survey, 2011].

Unfortunately the QuikSCAT sensor failed in November 2009, and a second winter study of Ku-band response to snow and ice properties was not possible for the 2009/10 season. However, given the previous studies by [Howell et al., 2008; Howell et al., 2009; Howell et al., 2009; Wang et al., 2008] it is well established that Ku-band radar is more sensitive to snow properties than ice properties especially where the snowpack is greater than 0.2 m deep.

## Summary

The time series data reveal the sensitivity of C, X and Ku band radars to changing snow and ice conditions, especially the onset of snow and ice melt and freeze up. Ku band is suggested to be most sensitive to changing snow properties due to its short wavelength. X band radar should be sensitive to snow and ice properties while C band is expected to be primarily sensitive to properties of the ice cover until the onset of snow melt. Changes in backscatter resulting from different incidence angles complicate the interpretation of the Envisat ASAR and TerraSAR-X MGD imagery. Nevertheless, it was shown that backscatter response was different between the two seasons, a result of differences in the ice and snow conditions observed.

Furthermore, a general trend of increasing backscatter over the course of the winter season was observed at both C- and X-band backscatter and agrees well with the observations of Makynen et al. (2007) from the Baltic Sea. The backscatter did not evolve similarly to the first year ice backscatter presented by Yackel et al. (2007). Indeed both the results of Makynen et al. (2007) and this study suggest that the time-series evolution of the low salinity ice is somewhat similar to the backscatter evolution of freshwater lakes, though the backscatter is a function of different ice properties and mechanisms. C-band backscatter of freshwater lakes shows a general increase over time with increasing ice thickness [Duguay et al., 2002]. The Ku-band backscatter showed a similar response to previous studies with backscatter increasing during the ice

season and decreasing with snow melt due to the high sensitivity of Ku-band to changes in snow properties.

The time series examination has provided evidence of links between microwave radar backscatter and changes in the snow and ice properties over Miquelon Lake. The potential of retrieving information on the changes in snow and ice properties are examined in the next section.

### **4.3 Co-Variability of Radar Backscatter and Snow Properties**

Given the observed changes in snow and ice conditions in each season and the variations in backscatter that seem temporally correlated, a more detailed analysis of individual snow and ice properties with C, X, and Ku radar backscatter was conducted and is presented below. As previously stated the four regions of interest for C and X bands are:

- 1) **land** which represents the open agricultural fields.
- 2) **forest** which is a section of mixed wood forest near the lake.
- 3) **lake** which composes the study area on Miquelon Lake.
- 4) **QSCAT** which represents the area of the QuikSCAT pixel used for Ku-band backscatter analysis.

#### **4.3.1 Snow Depth**

Although SWE is of ultimate interest because it contains information on the mass of snow/volume of water within the snowpack, one would expect that a sensor designed to retrieve SWE would also show sensitivity to the components of SWE (snow density and depth) as it is the number of scatterers in the volume that determine the backscatter response from the volume. Dry snow is largely transparent to C-band radars at the depths typically observed over first year sea ice in the Arctic or the Baltic Sea. However, some studies have nevertheless suggested that snow depth, density, and SWE may be monitored using C-band radars (see Section 2.4). C, X, and Ku band radars are sensitive to the presence of wet snow. X and Ku band radars have been used for the detection of snow melt with Ku band being theoretically more sensitive to changing snow properties due to its weaker penetrating power and shorter wavelength.

The snow properties for all ROIs are taken and extrapolated from the measurements conducted over the lake. In reality, the different regions had different snow depths and densities, particularly in the forest where the coniferous canopy can trap snow, or ground blown snow can collect as a result of reduced wind transport within the forest. SWE from in-situ observations and estimates derived from AMSR-E are presented in order to show potential differences between the lake and the surrounding region.

#### **C-Band**

Figure 4.3.1 presents the comparison between C-band backscatter and snow depth obtained on Miquelon Lake. One would expect that as snow depth increased, the

volume scattering contribution to backscatter would increase. The volume scattering contribution should be most apparent in the cross polarization channel (VH).

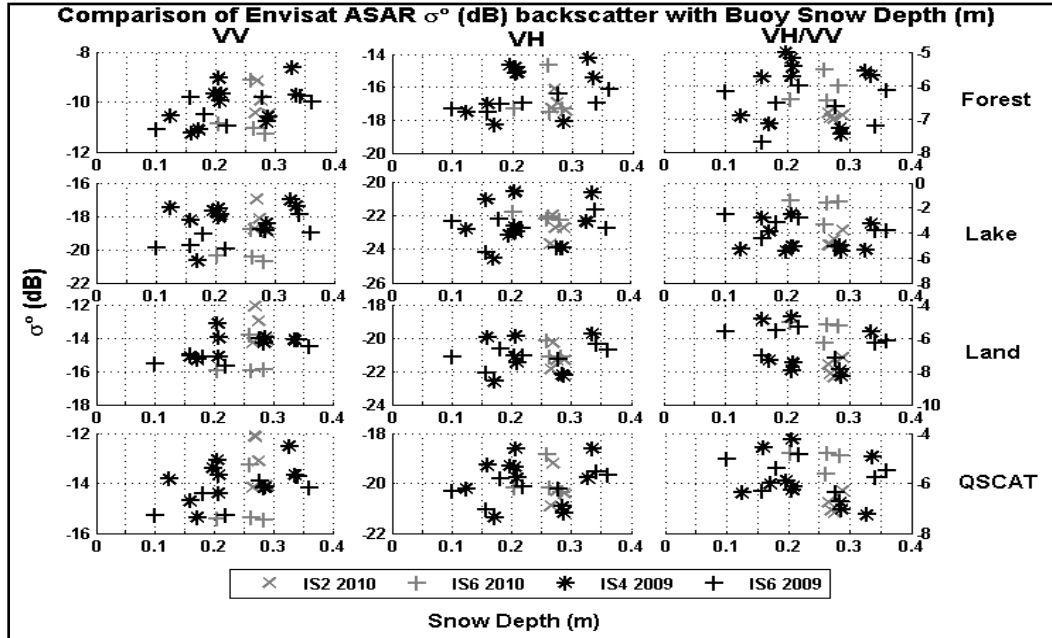


**Figure 4.3.1:** Envisat ASAR C-band backscatter response to changing snow depth over the study region in 2008/09 and 2009/10.

Unfortunately, Figure 4.3.1 shows a large degree of scatter for all regions and polarizations. In addition, given that backscatter from the lake, agricultural land and QSCAT was often below the NESZ in 2008/09, the changes may be the result of system noise and not an actual signal. As C-band is easily able to penetrate through dry snow, and has a wavelength of 0.06 m, which is much larger than the snow grains it is more likely that the signal is primarily the result of interactions with the ice surface and perhaps even the ice volume than with the snow.

### X-Band

X-band has been shown to be sensitive to SWE and thus should be sensitive to snow depth as well [Rott et al., 2010]. The 2008/09 X-band backscatter comparison with snow depth exhibited a high amount of scatter with no visible trends and is not shown. Figure 4.3.2 below presents the comparison of X-band and snow depth for the 2009/10 winter. The HH polarization data for 2009/10 shows little separation between the two incidence angle ranges and also reveals that the backscatter from the open fields and QSCAT exhibits low scatter and a slight positive trend. The HH response from the lake exhibits some scatter but a positive trend overall. The HH backscatter from the forest shows low scatter but also no trend. The cross polarization channel HV exhibits strong separation between the two incidence angles except from the forest. Furthermore, the HV backscatter from the land, lake and QSCAT shows a weak positive trend and lower scatter.

As would be expected, there is decreased scatter in the backscatter values at X-band than at C-band but X-band only exhibits weak sensitivity to snow depth. Under dry snow

conditions X-band SAR may still penetrate completely through the snow pack and into the ice (Figure 2.2.2).

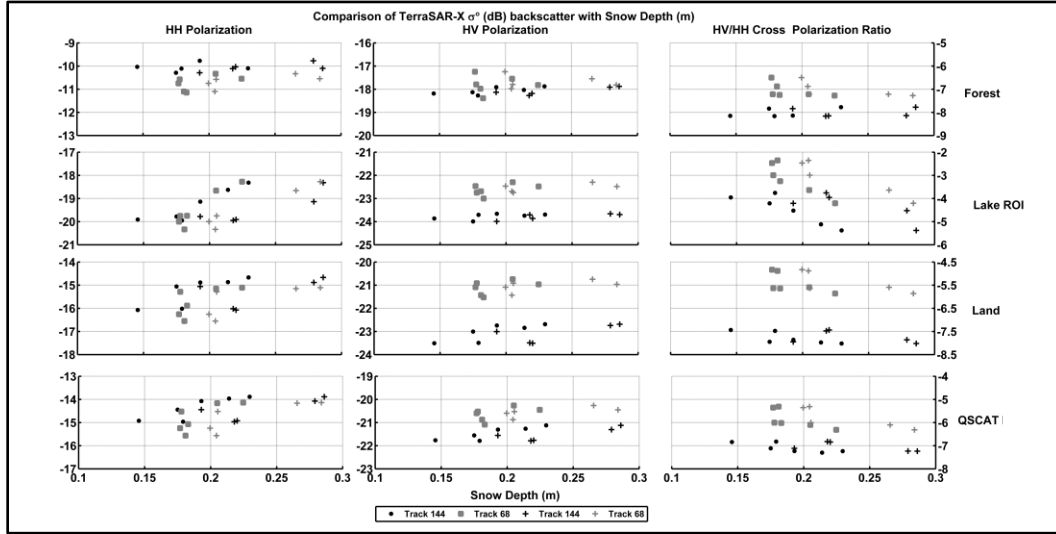


**Figure 4.3.2: Comparison of X-band backscatter with snow depth over the study site in 2009/10.**

Figure 4.3.3 focuses on the backscatter from the lake only. It shows that in 2009/10 a weak linear trend of approximately 1 dB/0.05 m snow depth between backscatter and snow depth in the co-polarization channel existed (Figure 4.3.3). A linear correlation with the cross-polarization channel, HV is also observed but the magnitude of change is only 0.5 dB over the observed snow depth range. Interestingly the cross-polarization ratio (HV/HH) shows a stronger decreasing trend with increasing snow depth of approximately 2 dB.

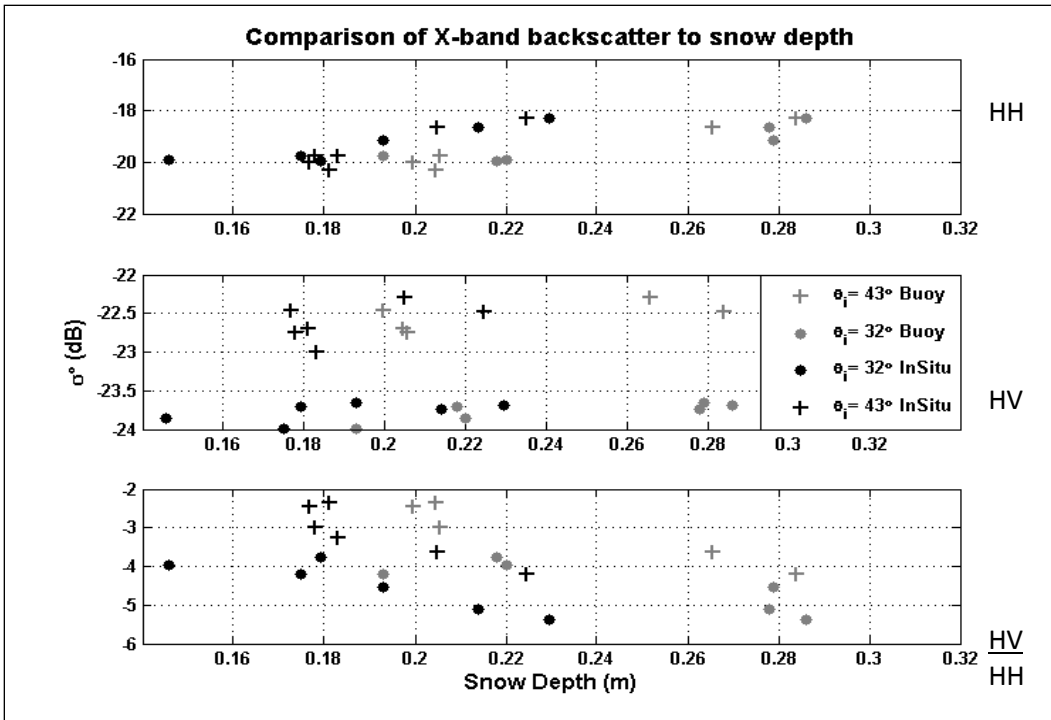


**Figure 4.3.3: Comparison of X-band lake backscatter with snow depth measurements in the winter of 2009/10 over Miquelon Lake.**

### Ku-Band

Ku-band should be most sensitive to changing snow properties based on its short wavelength and on the findings of previous studies. Background work for the CoReH2O proposal has shown that Ku-band data are sensitive to changes in SWE when the snow is dry and thus QuikSCAT should be also be responsive to changes in the depth of snow as SWE is the product of depth and density [Rott et al., 2010; Yueh et al., 2009]. Figure 4.3.4 illustrates the seasonal evolution of Ku-band backscatter observed by the QuikSCAT sensor and the snow depth measured by the CRREL IMB.

As expected, Figure 4.3.4 reveals that the Ku backscatter is highly temporally correlated with snow depth. This is also well shown in Figure 4.3.5, which presents a scatter plot of Ku backscatter and snow depth. Figure 4.3.4 clearly shows that increases and decreases in snow depth are linked to increases and decreases in backscatter respectively. This suggests the total backscatter is largely comprised of volume scattering from within the snow pack. The decrease in Ku backscatter slightly precedes the observed decrease in snow depth, an indication of attenuation of the radar signal within an increasingly wet snowpack and a decrease in volume scattering from the snow pack.

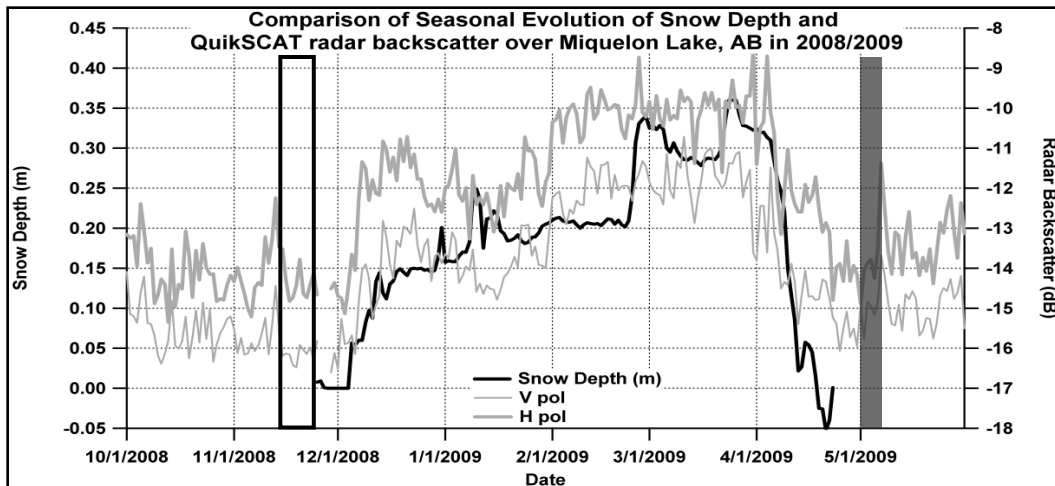


**Figure 4.3.4:** Evolution of Ku-band radar backscatter (db) and CRREL IMB Snow Depth (m) on Miquelon Lake, AB in winter 2008/09. The black box show the period of ice onset and the grey filled box shows ice off period. Negative snow depth indicates melt of the ice surface.

Previous studies have shown that snow melt leads to a series of strong backscatter decreases and increases associated with freeze/thaw cycles of liquid water within the snowpack [Yackel et al., 2007; Wang et al., 2008]. The backscatter data shows far greater variability than the snow depth, suggesting that while snow depth and backscatter are correlated in the broad sense, the actual backscatter is only partially dependent on snow depth but also on some other property. Previous studies have shown that Ku band backscatter is sensitive to diurnal variations in snow wetness caused by daily air temperature cycles [Nghiem et al., 2000].

Figure 4.3.5 shows a low scatter, linear increase in backscatter with increasing snow depth indicating some sensitivity of Ku-band to snow depth. The coefficient of determination from regression analysis between snow depth and the H and V polarizations are 0.57 and 0.62 respectively indicating that over half of the variability in backscatter is explained by snow depth. Figure 4.3.5 also shows that the backscatter value stabilizes at approximately -10 dB after a depth of 0.3 m of snow depth is reached. Based on the penetration power of Ku-band radar waves into snow, the snowpack may have contained some small fraction of liquid water (<1% by volume) that would cause the signal to dampen. Another potential cause of the saturation could be the increase in the snow depth past the maximum penetration depth of the Ku-band radar. If the Ku backscatter response is primarily due to volume scattering from the snow pack and the maximum depth of penetration was reached, then the contribution would continue to be from the same number of scatterers within the snow.

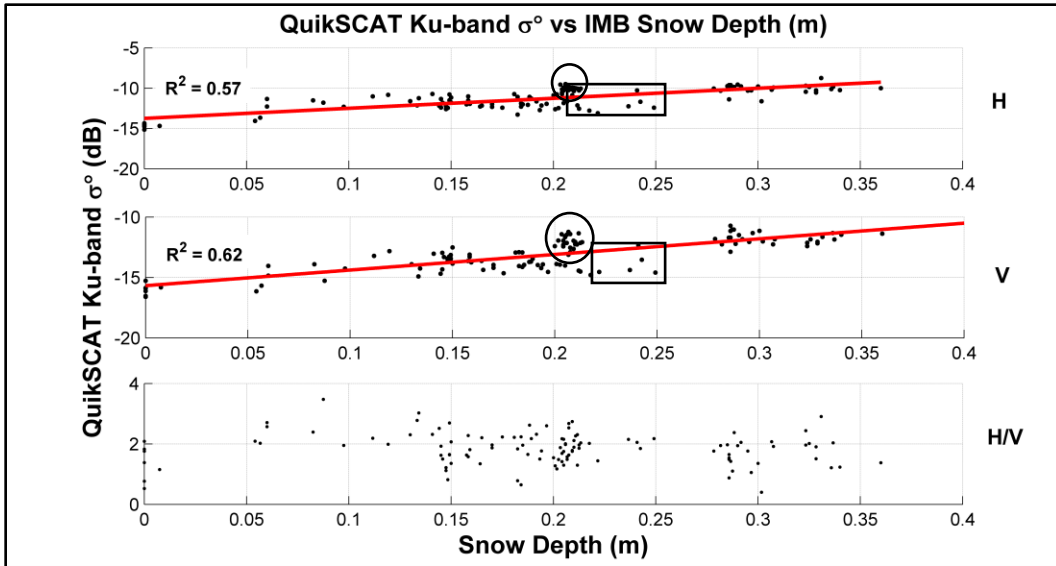


**Figure 4.3.5:** Scatter plot of Ku-band backscatter versus snow depth measured by the CRREL IMB. Values from after snow melt have been removed in this figure. Red line presents the linear regression fit to the data.

### Summary

The data show that as the wavelength of the radar sensor decreased, the sensitivity to snow depth increased, likely a result of increased sensitivity to the volume scattering from the snow pack volume. Although it cannot be proven that the snowpack was perfectly dry, it seems that for the majority of the time this must have been the case or radar penetration would have become very low and the liquid water would have attenuated the radar signal. Given the low sensitivity of C-band to snow depth, the sensitivity to SWE was also expected to be very low. X-band showed less scatter than C-band but also showed little backscatter change over observed snow depths. The high temporal resolution of the QuikSCAT data provides the most robust comparison with snow depth. A linear trend was clearly visible in Figure 4.3.5, though there is some scatter. The scatter could be the result of blowing snow or other parameters such as changes in snow grain size, snow density and snow wetness. However it is believed that snow wetness was very low, otherwise the Ku-band signal could not have penetrated into the snowpack, and the absorption of the signal by the water would have resulted in reduced backscatter as was observed during snow melt.

### 4.3.2 SWE

Snow Water Equivalence (SWE) is a highly sought after hydrologic parameter as it represents the volume, or mass, of water that is represented by a snowpack. SWE can also influence the freeboard or height of the ice surface above the water, the main parameter used by radar and laser altimeters such as Cryosat-2 to estimate sea ice thickness in the Arctic. The CoReH<sub>2</sub>O mission aims to improve measurements of SWE. Although CoReH<sub>2</sub>O will utilize X and Ku band radar, some studies suggest that C-band is responsive to changes in SWE, although primarily through phase information or through its control on the snow thermal conductivity. As a result we compared the backscatter response to changes in SWE for C, X, and Ku bands. We utilized in-situ measurements

and the AMSR-E derived estimates of SWE in order to improve our temporal resolution in SWE. While there was a large discrepancy between the in-situ SWE and AMSR-E derived SWE in 2009/10 it is not known if the issue is in the AMSR-E data or caused by flooding and superimposed ice/snow-ice. The AMSR-E and in-situ measurements of SWE agreed reasonably well in 2008/09 (Figure 4.1.18).

### C-Band

Figure 4.3.6 presents the comparison of SWE and Envisat ASAR backscatter over the lake in 2008/09. Despite being hampered by the low temporal resolution of coincident in-situ measurements, at first glance there appears to be a weak correlation as backscatter increases by one to three decibels over the range of observed SWE values. However the uncertainty in the backscatter is approximately 1 dB, and the backscatter value for 0 mm SWE can change due to changes in the properties of other factors.

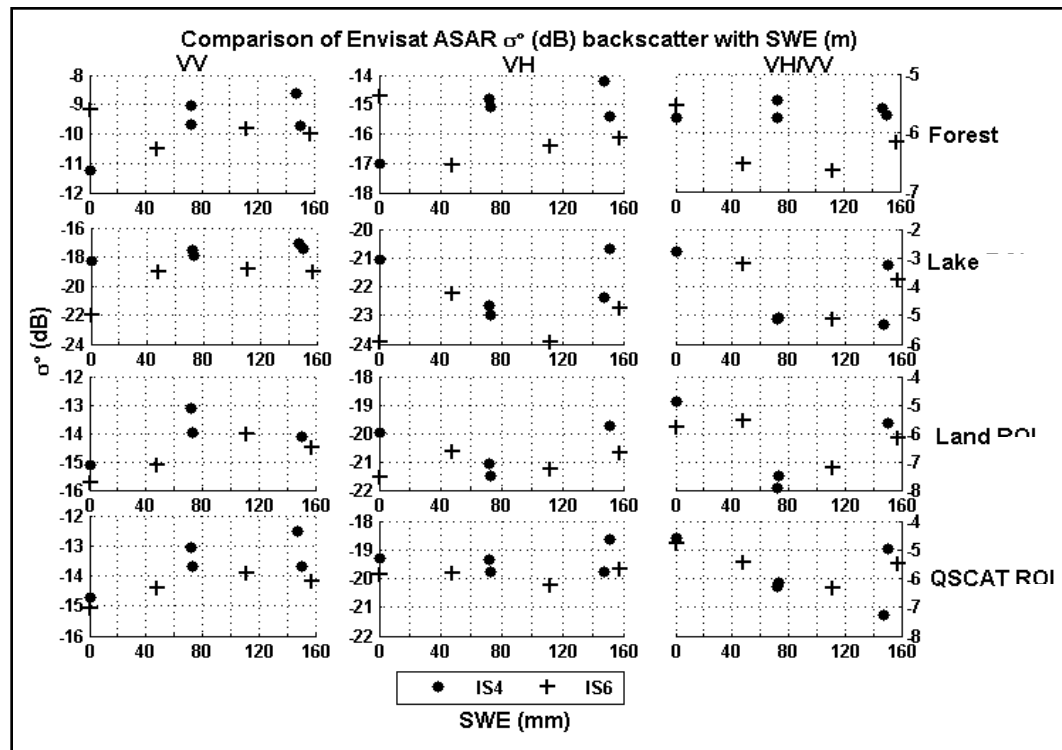


**Figure 4.3.6: Envisat ASAR C-band backscatter response to SWE over different surfaces in 2008/09. SWE was taken from the measurements performed over the lake.**

Figure 4.3.7 compares in-situ measurements of SWE to C-band backscatter in 2009/10. In contrast to 2008, there appears to be a slightly stronger correlation between SWE and C-band backscatter in 2009, with a greater range in the backscatter change with snow depth of 2 - 4 dB. However, given the relatively long wavelength and high penetration power of C-band radar waves, the observed correlation between SWE and C-band backscatter is simply the result of both SWE and backscatter being positively correlated with time between the deposition of snow and snow melt onset. The SWE values are uncertain in 2009/10 as AMSR-E estimates of SWE are significantly higher than in-situ measurements and the in-situ values seem too low. As previously discussed in Section 4.1.1, snow-ice formation appeared to be greater in 2009/10 than 2008/09 and would

lead to erroneous snow depth and density measurements and therefore an incorrect value for SWE.

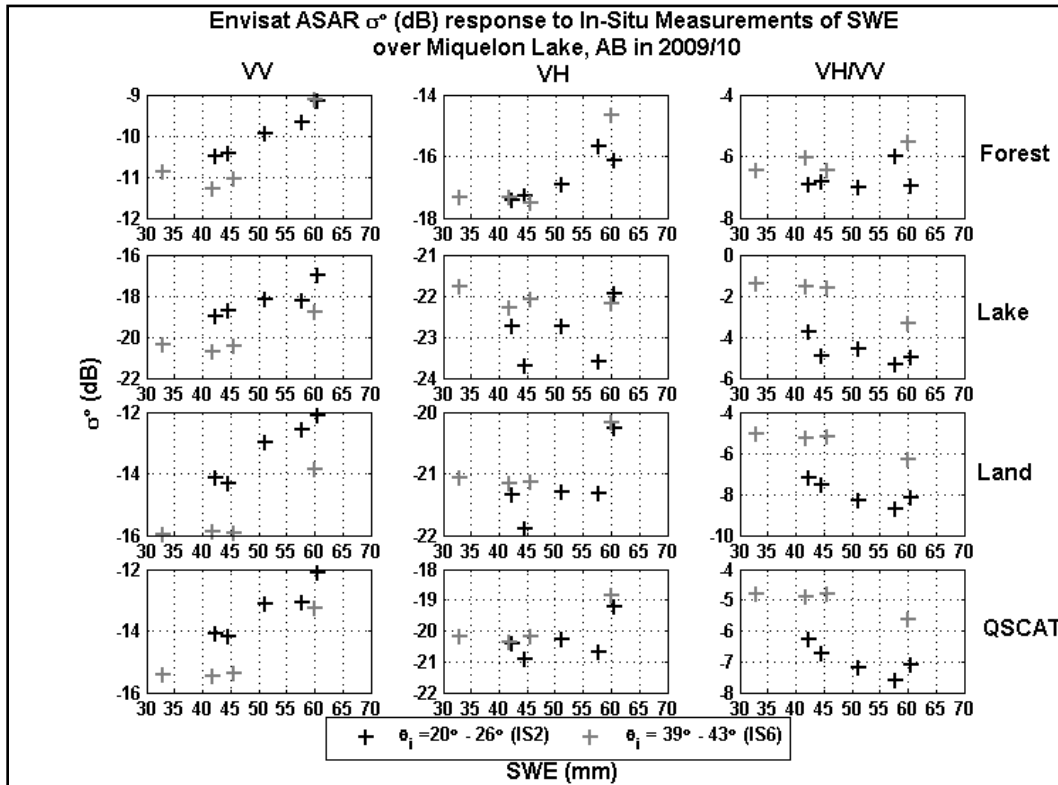


**Figure 4.3.7: Envisat ASAR C-band backscatter response to SWE over different surfaces in 2009/10. SWE was taken from the measurements performed over the lake.**

Given the lack of response of C-band to snow, the high scatter and small observed trends in backscatter associated with SWE are unsurprising. Previous studies have linked C-band backscatter to SWE using the thermal resistance of the snow and its control on sea ice surface temperature and brine volume [Yackel and Barber, 2007; Yackel and Barber, 2002]. However, a requirement of their method is the presence of very smooth first year sea ice which is much more saline than Miquelon Lake. Furthermore these studies build the relationship using multiple study sites with differing snow packs which may exhibit slight and uncharacterized differences in the properties influencing backscatter, such as surface roughness, brine volume and salinity. The apparent correlation between C backscatter and SWE is likely only weakly due to SWE and more to the co-evolution of other snow and ice properties increasing backscatter.

### X-Band

Figure 4.3.8 below shows the backscatter response of X-band backscatter from TerraSAR-X to AMSR-E derived estimates of SWE for all four regions of interest in 2008/09. The AMSR-E SWE values agree reasonably well with the in-situ measurements of SWE in 2008/09. Furthermore, the high temporal resolution of the AMSR-E estimated SWE provides a more robust comparison to both the Ku-band and X-band backscatter. As CoReH2O proposes to use these frequencies we will present the AMSR-E SWE values for both. Figure 4.3.8 shows relatively low scatter linear trends between backscatter and

AMSR-E SWE. The trends increase for the VV, HH, and VH polarizations. The response of the cross polarization ratio (VH/VV) is dependent on the surface type, being very stable from the forest increasing from the agricultural fields and decreasing over the lake. Figure 4.3.8 reveals that the increase in VH backscatter from the lake, land and QSCAT is between 5 and 15 dB over just 120 mm of SWE. This is far higher than the published 1 dB/100 mm SWE change noted by Rott et al. (2010). The large magnitude of increase is likely the response of the co-evolution of other snow and ice properties such as brine volume and snow grain size with SWE.

The studies of Rott et al. and Yueh et al. were conducted over land where changes in the dielectric properties of the ground surface would be minimal in comparison to the changes in the dielectric properties of the ice observed in this study. This makes removing the scattering contribution from the surface below the snow pack over low salinity sea ice more difficult, especially where the X-band radar can potentially penetrate into the ice providing further changes in scattering associated with volume scattering from within the ice.

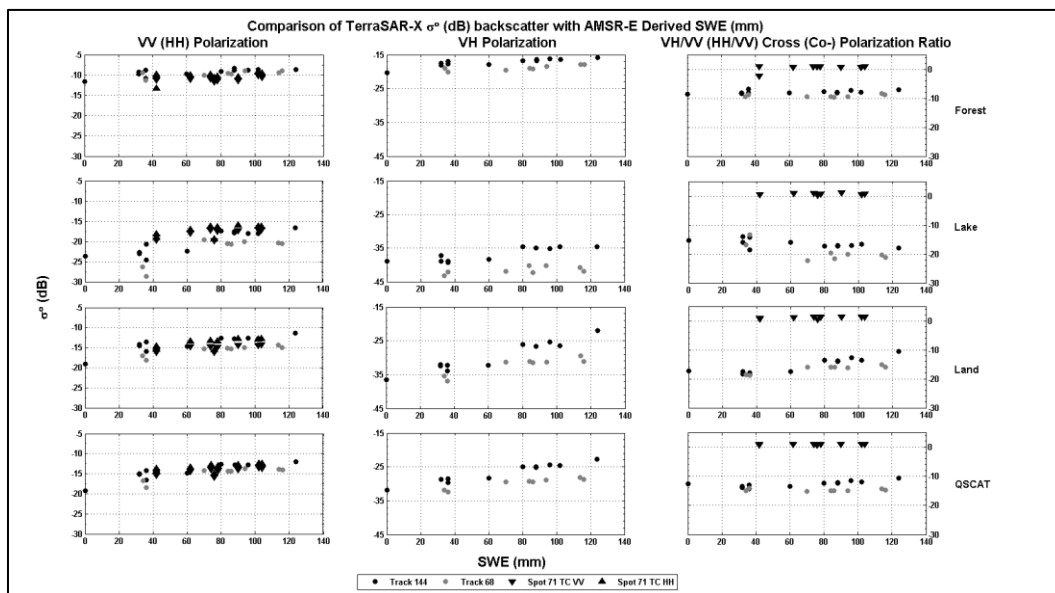


**Figure 4.3.8: Comparison of X-band backscatter with AMSR-E derived SWE in 2008/09. Symbols indicate different incidence angles.**

In 2008/09 the VH backscatter was well below the NESZ for all regions but the forest. This suggests that the volume scattering contribution of the snow and ice were minimal. The linearity of the trend suggests that the values below the NESZ may be valid, as one would not expect a linear increase in backscatter below the NESZ if the signal was just due to noise. The co-polarization ratio (HH/VV) shows very little change for all regions, suggesting that changes in SWE are not associated with changes in the magnitude of backscatter at HH versus VV. This suggests that there is no change in the structure of the medium with increasing SWE and that the scatterers are largely isotropic. The cross polarization ratio shows a sharp increase from the land and a weaker one from the QSCAT. There appears to be very little change in the forest co polarization ratio and a slight decrease over the lake.

Figure 4.3.9 compares the AMSR-E SWE and X-band backscatter in 2009/10. The response of X-band SAR to SWE has been reported to be approximately 1 dB/100 mm SWE [Rott et al., 2010]. The changes in backscatter observed from the agricultural fields and QSCAT is similar to the value reported by Rott et al. (2010) at approximately 1 db/90-130 mm. For the Lake and QSCAT, the properties of the lake may have influenced the backscatter when the SWE values were low. Retrieval of snow information from forested regions has proven troublesome for most sensor systems because only a very small amount of the emitted microwave energy ever reaches the forest floor and backscatter is mostly dependent on forest structure. This is reflected in the weak trends from the forest in Figure 4.3.9 below.

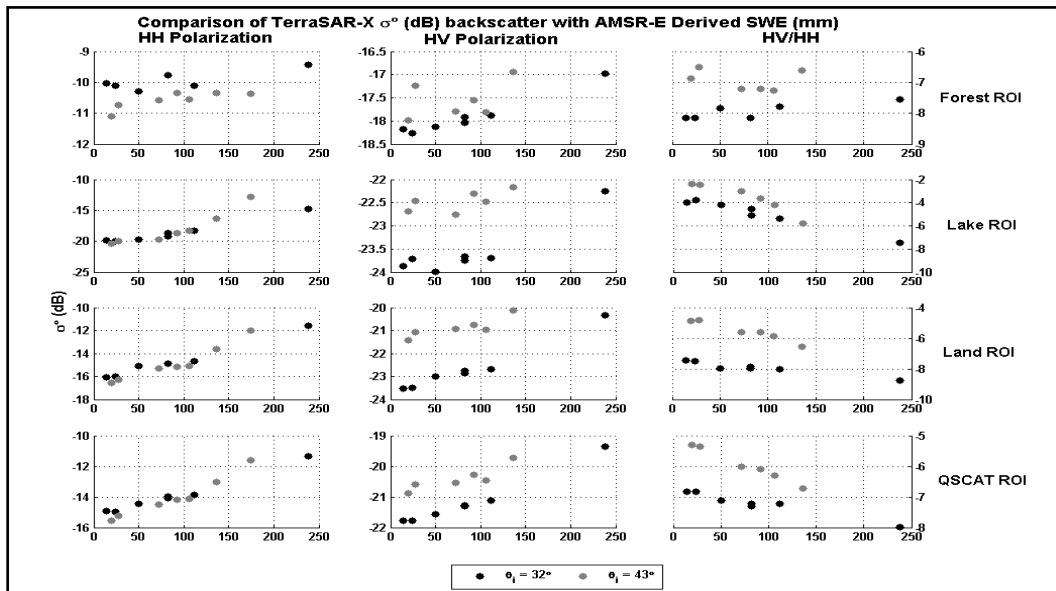


**Figure 4.3.9: Comparison of X-band backscatter with AMSR-E derived SWE in 2009/10. Symbols indicate different incidence angles.**

In comparison to the C-band, X-band cross polarization backscatter shows good separation between the two incidence angles of acquisition for all surface types but the forest. At X-band the larger, more shallow incidence angle shows increased VH backscatter. The cross polarization ratio exhibits little change from the forest but a sharp and linear decrease from the other surface types.

Unfortunately, as already mentioned, AMSR-E SWE values and in-situ SWE values were very different in 2009/10. Snow-ice was observed in this year but not included in the calculation of SWE and no surveys of snow depth were conducted over the surrounding land or lake shore. However, Figure 4.3.8 and Figure 4.3.9 show stronger and less scattered response to SWE than C-band especially in the cross polarization channels (HV or VH) which should be responding to volume scattering while the co-polarized channels (VV or HH) should be responding to surface scattering.

### Ku-Band

Ku-band was expected to show the highest sensitivity to SWE based on its short wavelength and the results of previous studies. As aforementioned, AMSR-E SWE data obtained for 2008/09 compared well to in-situ values collected on Miquelon Lake and

thus are compared to the Ku backscatter below (Figure 4.3.10). Figure 4.3.10 shows less scatter and a 4 dB change in backscatter over the observed SWE range. Above 90 mm SWE, the backscatter stabilizes at approximately -10 dB. This is believed to be due to increased snow wetness associated with positive air temperatures reducing the penetration depth and causing some absorption or to exceeding the maximum penetration depth given some small snow wetness value.

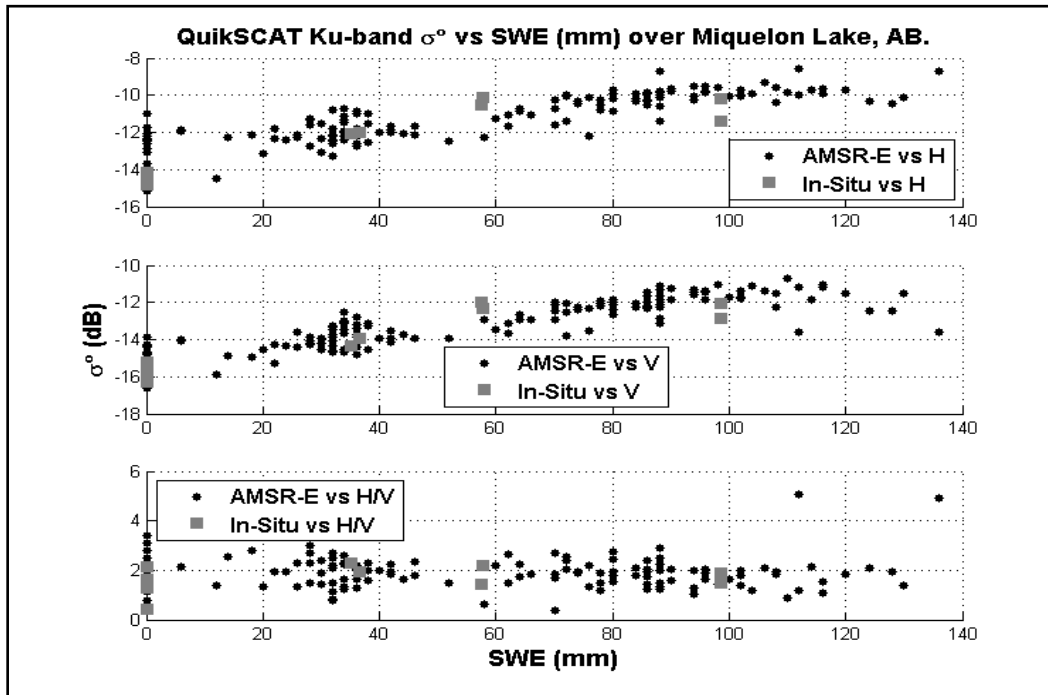


**Figure 4.3.10: Comparison of QuikSCAT backscatter with AMSR-E and in-situ measurements of SWE over Miquelon Lake, AB in 2008/09.**

Regression analysis indicates a statistically significant linear trend between the AMSR-E SWE value and the Ku-band backscatter at both the H and V polarizations observed on Miquelon Lake in 2008/09 ( Greater snow density results from decreased separation between the snow grains but also means that there are a higher number of scatterers within the snow pack. As snow depth increases, the number of scatterers associated with a layer of snow of a certain density also increases. The contribution seems to be 20-40% due to Snow density and 50-60% due to snow depth, assuming that variability in these two variables explain 100% of the variability in backscatter.

Table 4.3.1). Greater snow density results from decreased separation between the snow grains but also means that there are a higher number of scatterers within the snow pack. As snow depth increases, the number of scatterers associated with a layer of snow of a certain density also increases. The contribution seems to be 20-40% due to Snow density and 50-60% due to snow depth, assuming that variability in these two variables explain 100% of the variability in backscatter.

Table 4.3.1 shows that between 78 and 88 percent of the variability in Ku band backscatter is explained by variability in the AMSR-E SWE estimates, depending on the polarization and if using a linear or quadratic model. The  $R^2$  value indicates either that

another variable besides SWE is influencing the Ku-backscatter, or that there is some noise/measurement error in the results, or a combination of both. SWE explains a higher percentage of the variability in Ku-backscatter than snow depth alone did, illustrating the influence of snow density. Greater snow density results from decreased separation between the snow grains but also means that there are a higher number of scatterers within the snow pack. As snow depth increases, the number of scatterers associated with a layer of snow of a certain density also increases. The contribution seems to be 20-40% due to Snow density and 50-60% due to snow depth, assuming that variability in these two variables explain 100% of the variability in backscatter.

**Table 4.3.1: Regression statistics between QuikSCAT Ku band backscatter and AMSR-E derived SWE.  $\alpha$  value of 0.05 used.**

Polarization	Model	Adj. R <sup>2</sup> (%)	Eqn.
Horizontal	Linear	78.2	QSCAT_H = - 13.45 + 0.03856*(AMSRE_SWE) SWE = (QSCAT_H +13.45)/0.03856
Vertical	Linear	86.3	QSCAT_V = - 15.41 + 0.04055*(AMSRE_SWE) SWE = (QSCAT_V+15.41)/0.04055
Horizontal	Quadratic	81.5	QSCAT_H = - 14.05 + 0.06978*AMSRE_SWE - 0.000280*(AMSRE_SWE) <sup>2</sup>
Vertical	Quadratic	87.3	QSCAT_V = - 15.74 + 0.05830*(AMSRE_SWE) - 0.000159*(AMSRE_SWE) <sup>2</sup>

The change in Ku VV backscatter with SWE over the lake was approximately 1db/25mm AMSR-E derived SWE or in-situ SWE. Rott et al. (2010) observed a change in backscatter with SWE of approximately 1 dB/35-40 mm SWE at Ku-band at VV polarization [Rott et al., 2010]. Yueh et al. (2009) observed changes in Ku backscatter of 1 dB/20 - 60 mm SWE. The observations over the lake are within the range of the observations of Yueh et al. (2009), providing further evidence for the validity of the results and for the usefulness of Ku-band to retrieve SWE. Differences may result from the spatial mixture of forest, lake and agricultural fields while the study regions of Rott et al. (2010) were more uniform. Furthermore, the studies of Rott et al. (2010) and Yueh et al. (2009) were over study regions large enough for averaging of QuikSCAT pixels, which can reduce noise in the backscatter statistics. In addition, properties of the snow cover such as grain size and wetness, and surface temperature of the ice likely changed with changing meteorological conditions and time, further complicating the results in this study. For example, the relatively warm water and ice surface create a strong thermal gradient within the snowpack and resulted in the constructive metamorphism of the basal snow grains. Scatter in the data also results from uncertainty and variability in the QuikSCAT and AMSR-E SWE estimates. The AMSR-E SWE value is derived from a much larger footprint and thus is affected by variability in the surround land cover type/percentage. The in-situ values of backscatter and SWE correlate well with the AMSR-E values in this year.

### Summary

C-band backscatter showed very weak non-significant correlations with SWE particularly from the cross polarization channels. This is unsurprising given the long wavelength and high penetrating power of C. X-band backscatter showed higher sensitivity to SWE but

uncertainty in the backscatter values in 2008/09 and in the SWE values in 2009/10 limit the interpretation. X-band backscatter from the QuikSCAT pixel area and over the agricultural fields showed a similar change in backscatter with SWE as has been reported by Rott et al. (2010). As expected, Ku-band backscatter showed strong sensitivity to SWE. SWE was found to explain over 75% of the variance in Ku backscatter in 2008/09. The magnitude of backscatter change with SWE was found to be within the range reported by Yueh et al. (2009) from an airborne Ku band campaign and only slightly below the values obtained by Rott et al. (2010).

#### 4.4 Co-Variability of Radar backscatter and Ice Properties

While SWE is currently one of the most sought after parameters for operational SAR monitoring, the retrieval of the thickness of thin sea ice using SAR is also highly desired. As outlined in Section 2.4, numerous studies have examined C, X, and Ku band radar for the retrieval of ice thickness. Previous studies have suggested that X-band SAR can retrieve the thickness of thin sea ice up to 0.3 m thick [Clissold, 2009; Busche et al., 2009; Beaven et al., 1995]. Previous Ku band studies are limited to ice that is less than 0.15 m thick. As signal penetration depth is partially dependent on the salinity of the ice, the X-band SAR should be able to penetrate some distance into/through the ice (refer back to Section 2.1.3).

Furthermore, both C and X-band radar should penetrate through the snowpack and interact with the sea ice below. In the case of C-band it is expected that the signal is largely unaffected by the typical snow depths and conditions over sea ice, except when the snow is wet or icy. For X-band there is evidence of backscatter response to very heavy atmospheric moisture, snow and sea ice properties. Furthermore, the CoReH2O proposal aims to use the X-band information to account for changes in the surface properties and surface scattering component resulting from the surface below the snowpack be it ground or sea ice [Rott et al., 2010].

##### 4.4.1 Ice Thickness

###### C-Band

Figure 4.4.1 illustrates the relationship between C-band backscatter and ice thickness. Although there is a statistically significant relationship between C-band backscatter at VV polarization and ice thickness, the amount of variance in backscatter explained by ice thickness is only 20%. The increase in VV backscatter could also be related to changes in the surface ice properties such as brine salinity that co-evolves to some degree with ice thickness. Figure 4.4.1 combines the results from both the continuous automated buoy measurements, interpolated averages of in-situ measurements and separates the different incidence angle ranges. The low regression coefficient indicates that other variables besides ice thickness are influencing the backscatter or that the relationship is not valid over the full range of thicknesses. Furthermore, all imagery from 2009/10 was acquired when ice thickness was increased by less than 0.2m. The lack of a relationship between VH polarization and ice thickness could result from the signal being below the noise floor for most of the winter in both years. While the image may be interpretable, changes in the calculated backscatter values within the lake ROI could be the result of fluctuations in system noise overlying any real backscatter change. The least scattered trend comes from the high incidence angle IS6 swath, which theoretically is also most

responsive to volume scattering. Given the low salinity and surface roughness of the ice, much of the C-band radar energy may have penetrated through the ice and been absorbed by the water, at least until the onset of snow melt.

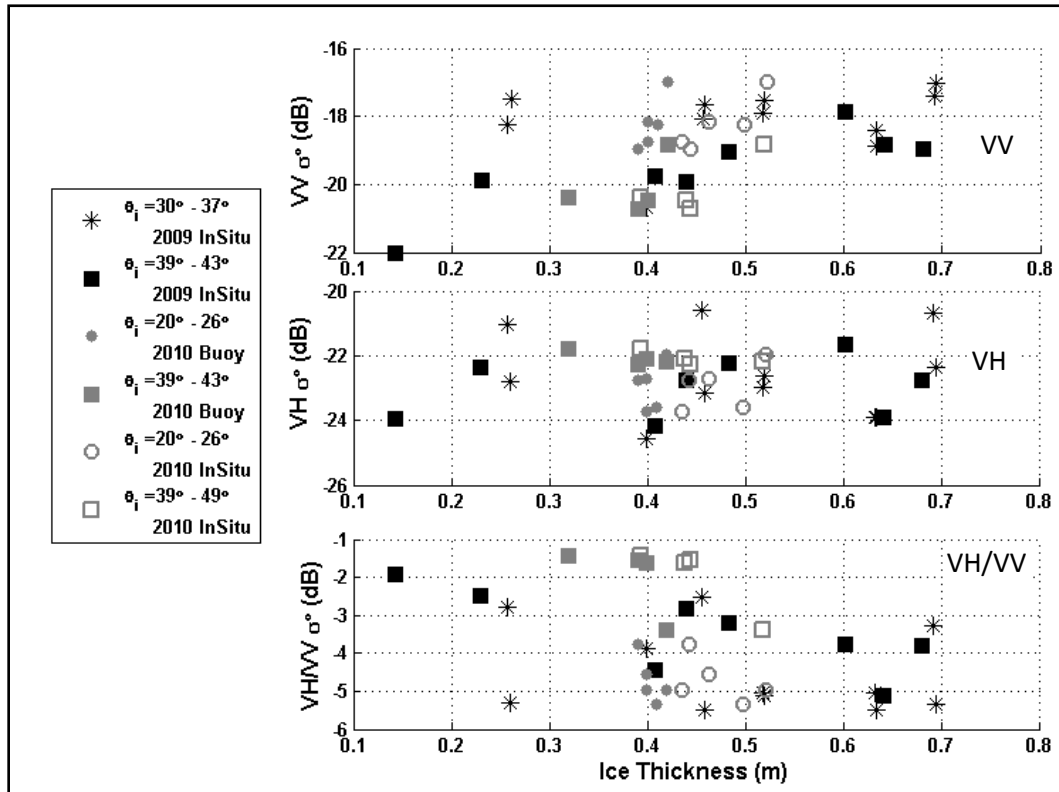


Figure 4.4.1: Comparison of C-band backscatter and ice thickness of Miquelon Lake, AB.

### X-Band

X-band has been suggested to be sensitive to ice thickness up to 0.3 m in the Arctic. Over the lower salinity ice found in Miquelon Lake the signal may be able to penetrate to even greater depths. Figure 4.4.2 and Figure 4.4.3 show that the correlation between X-band backscatter and ice thickness varies significantly between the two years. In 2008/09 the relationship between backscatter and ice thickness changes when the ice thickness reaches 0.45 m (Figure 4.4.2). However, the backscatter appears to level off after ice thickness reaches 0.55 m at least in the MGD imagery. However, the backscatter from the MGD imagery was often well below the NESZ and changes in the backscatter could be due to noise differences rather than changing ice thickness. The high incidence angle complex mode images show backscatter change of a few decibels but the correlation with ice thickness is very low.

In 2009/10 the backscatter changes very little until the ice thickness reaches 0.45m whereupon backscatter increases almost 8 dB in HH, 3 dB in HV and decreases 6 dB in the cross polarization ratio as the ice thickness increases to 0.55 m (Figure 4.4.3). The ice thickness did not increase past 0.6 m making it impossible to assess the recurrence of levelling off of backscatter at greater ice thicknesses. One possible explanation for the lack of response until 0.45 m of ice growth in both 2008/09 and 2009/10 could be that

until this ice thickness is reached, the majority of the signal is penetrating completely through the ice cover and is largely being absorbed by the underlying water. Although the ice is growing it is possible that the volume scattering contribution from the ice is minimal.

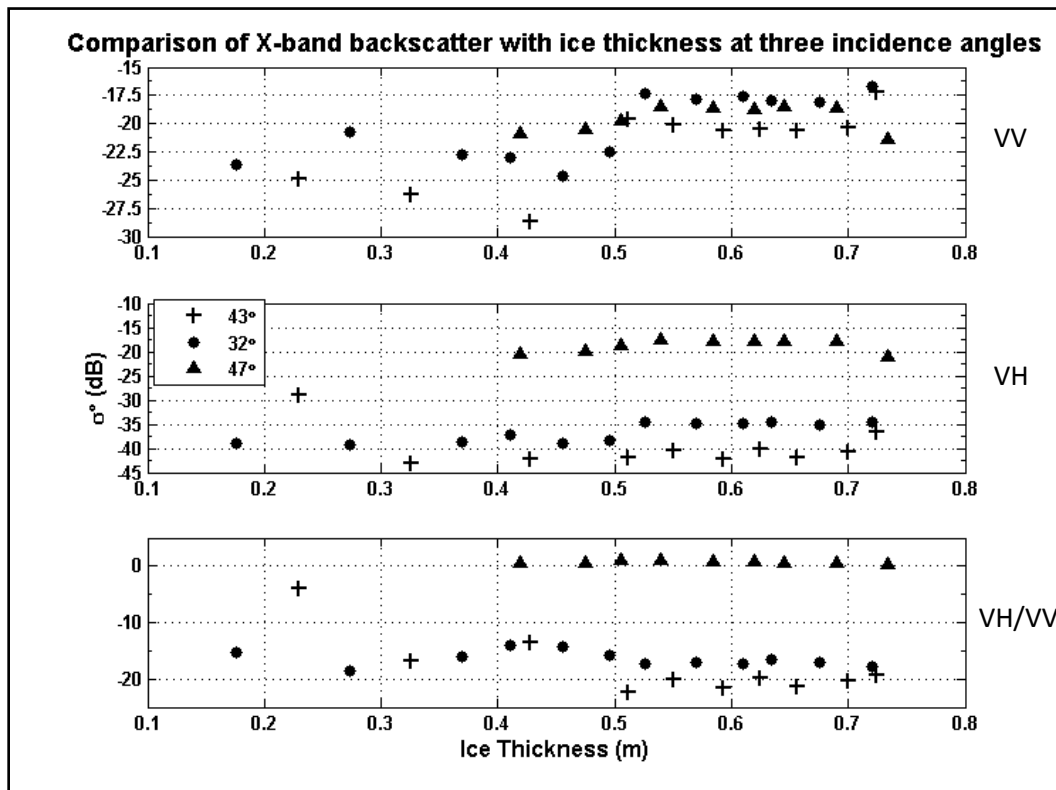


**Figure 4.4.2: Response of TerraSAR-X backscatter with ice thickness over the Lake in 2008/09.**

Another explanation is that the signal is absorbed by the ice until the formation of snow-ice. At the time of backscatter increase in both years, the freeboard became negative and snow-ice formed from flooding. The snow-ice would increase the surface roughness of the ice and increase the amount of energy scattered back to the sensor. There is strong correlation between ice thickness and TerraSAR-X HH backscatter and the cross-polarization ratio in 2010. Interestingly the correlation is much greater for images from the higher incidence angle,  $\theta_i = 43^\circ$ , than when  $\theta_i = 32^\circ$  ( $R^2 > 0.85$  vs.  $R^2 = 0.65$ ). As would be expected from Figure 4.4.3 below, the correlation between ice thickness and the HV cross-polarized channel is lower. Given the low salinity and surface roughness of the ice, it is not unreasonable to suggest that much of the C and X-band microwave energy passed through the snow and ice. While some HV backscatter would result from volume scattering within the snow or the ice and surface scattering at the snow/ice interface would occur, given the theoretical penetration of 0.05-0.8 m at X band, much of the signal would have been a) absorbed with the saline water or b) specularly reflected away and thus not be subjected to multiple reflections required for depolarization of the transmitted horizontally polarized waves to vertically polarized received waves.. Further evidence for penetration of C and X-band backscatter through the ice is given by low backscatter regions in X-band imagery that developed in February and persisted until early April in 2009 (Appendix B.2 and Appendix B.3). These low

backscatter regions are all near the shoreline and are believed to be the result of ice that has frozen to the bed of the lake. Ice that has frozen to the lake bed is referred to as grounded ice. Low backscatter from grounded ice has been observed by previous studies over fresh water lake ice [Duguay et al., 2002]. Similar features were not observed in 2009/10 possibly due to increased backscatter from the snow-ice that formed earlier in the year.

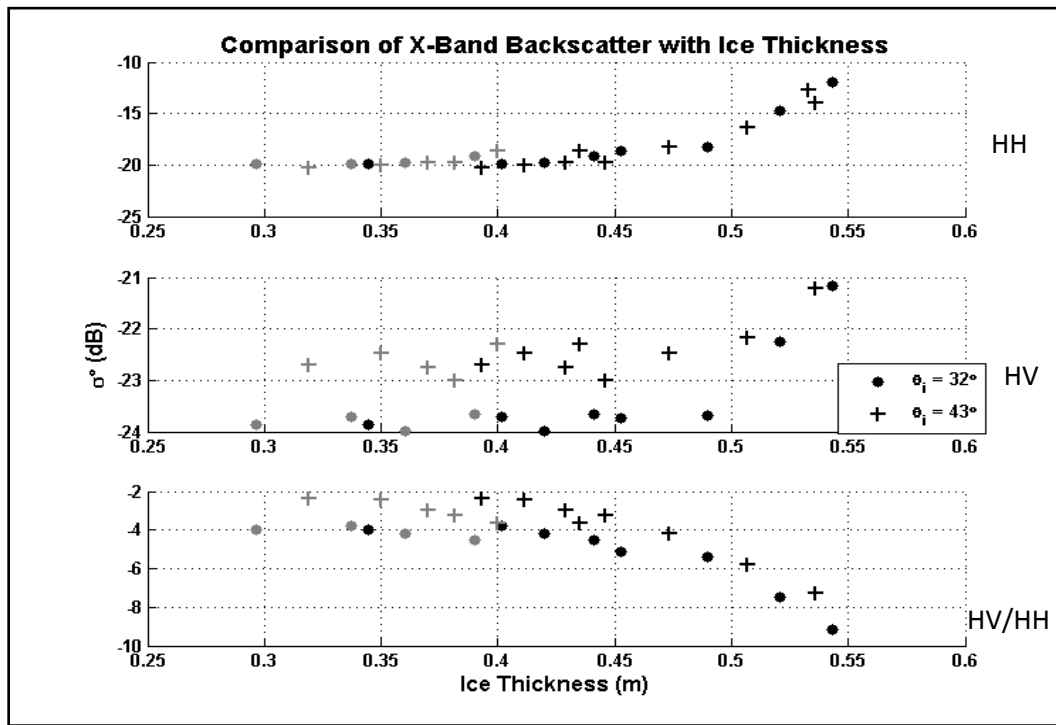


**Figure 4.4.3: Response of TerraSAR-X backscatter with ice thickness over Miquelon Lake in 2009/10. Black symbols denote ice thickness values from interpolated averaged in-situ measurements. Grey symbols are used for ice thicknesses derived from the CRREL IMB.**

Figure 4.4.4 presents the Ku band response to changing ice thickness. Due to issues with the ice thickness retrieval from the CRREL IMB in 2008/09, the ice thickness values used in the comparison are interpolated from averages of the in-situ measurements. The values in red occurred after the onset of snow melt and suggest that post melt onset backscatter can no longer be compared with ice thickness. While correlation between ice thickness and Ku-band backscatter may not be expected, Figure 4.4.4 indicates that one does exist. However, one can see that there are rises and dips within the series, particularly between 0.4 and 0.5 m ice thickness. The backscatter between 0.2 and 0.5 m and 0.5 and 0.7 m ice thickness is very uniform. The pattern looks very similar to the time-series of Ku-band backscatter over the lake but with a hysteresis loop where backscatter decreases strongly during snow melt and levels out despite changes in ice thickness. The timing of snow melt coincides with the decrease in Ku-band backscatter. Furthermore, the increases in backscatter at 0.5m coincide with increases in snow depth. The hysteresis loop is likely caused by liquid water in the snow pack absorbing much of the microwave energy. This removes the backscatter contribution of the snow/ice interface as well as some of the volume scattering component from the

snow pack. Backscatter is reduced even before ice thickness changes occur. A similar hysteresis loop was observed for snow depth.

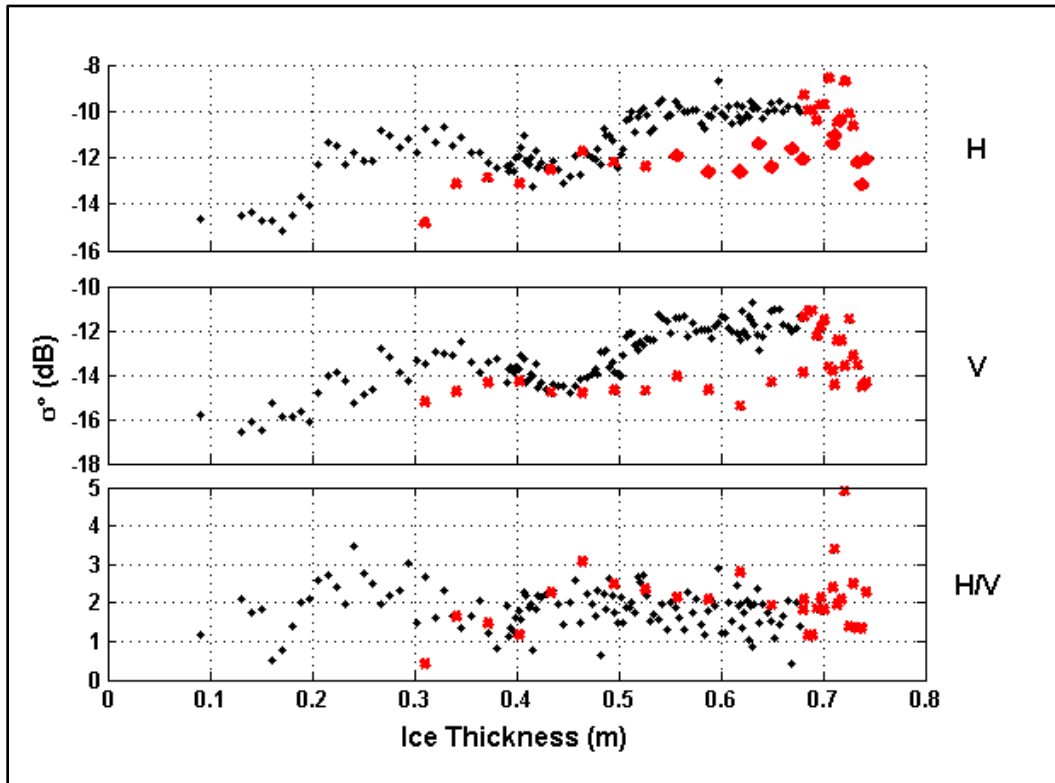


**Figure 4.4.4: Ku-band backscatter correlation with ice thickness over Miquelon Lake. Red (larger) markers indicate values from after the onset of snow melt.**

The correlation between Ku-band and ice thickness is most likely the result of the co-evolution of ice thickness and snow depth as the penetration depth of Ku band into sea ice is just a few centimeters. Further evidence for the lack of a true relationship between Ku-band and ice thickness lies in the fact that backscatter decreases and increases while ice thickness increases as increasing ice thickness should result in increased volume scattering from the ice, or a consistent decrease due to absorption. Furthermore, under wet snow conditions the Ku-band signal would not penetrate the overlying snow and thus not respond to the ice.

### Summary

While Ku was found to be correlated to ice thickness, the correlation is likely just the result of the co-evolution of ice thickness and snow depth over the course of the winter as the penetration depth of Ku-band into sea ice is low. C-band backscatter shows a slight increase with increasing ice thickness and is believed to be the result of increased scattering from the sea ice volume. The same is also observed for X-band in 2009/10 although the development of snow-ice could also have caused the observed X-band backscatter increase in 2009/10. Some of the C- and X-band images from 2008/09 in Appendix B show regions of low backscatter corresponding to grounded ice. This suggests complete penetration of the X-band signal through at least some of the ice on the lake.

#### 4.4.2 Ice Surface Temperature

Sea ice surface temperature was chosen for discussion because it is linked to other sea ice properties such as brine volume, brine salinity and wetness at the snow - ice interface (see Section 2.1.3). These properties influence the dielectric constant and loss factor of the ice and thus backscatter.

##### C-Band

Figure 4.4.5 presents the correlation between C-band backscatter and sea ice surface temperature. As ice temperature increases, the brine salinity decreases and the brine volume increases. While the data in 2008/09 are quite scattered, the 2009/10 data clearly show that C-band backscatter increases with increasing ice surface temperature, particularly at VV polarization, which is more sensitive to surface conditions. The response in VH is less noticeable, but is stronger for the low incidence angle swath IS2 than swath IS6. Once again the poor temporal resolution of the ASAR dataset limits the observations.

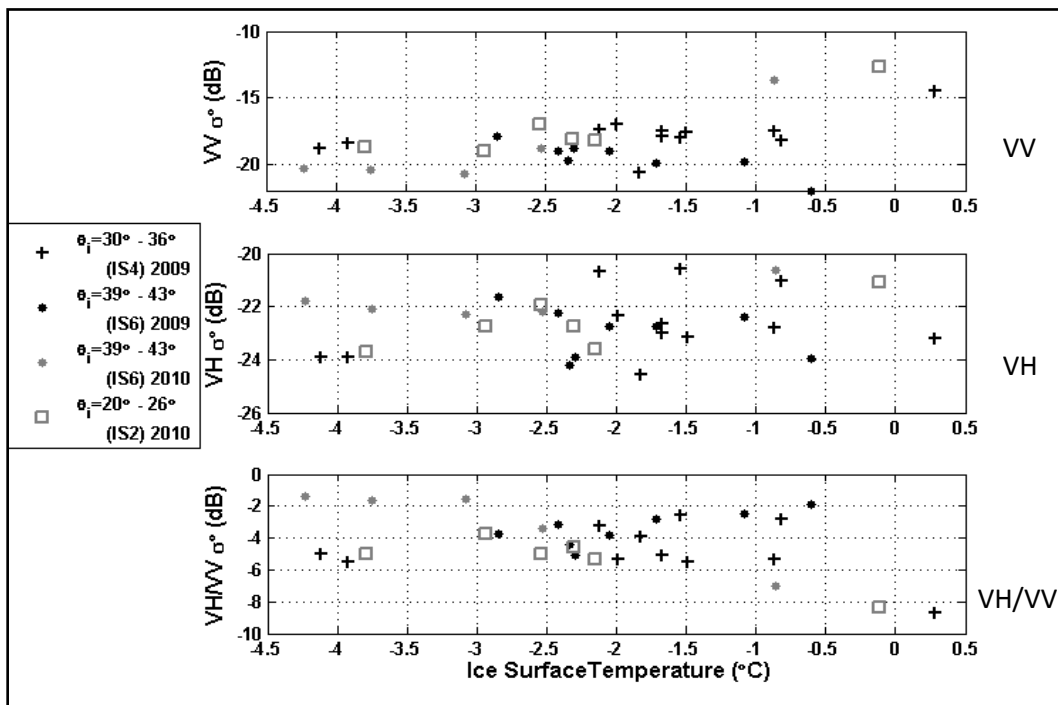


**Figure 4.4.5: Comparison of Envisat ASAR C-band backscatter with ice surface temperature. Temperatures acquired from the CRREL and SAMS IMB in 2008/09 and 2009/10 respectively. Temperatures were taken from the nearest hour to the SAR acquisition.**

The increase in ice surface temperatures and the resulting increase in brine volume have been proposed to increase backscatter at C-band while the snow wetness is still within the pendular regime [Yackel and Barber, 2002; Yackel et al., 2007]. This relationship has also been used to estimate SWE through the linkage of temperature and the thermal resistance of the snow pack [Yackel and Barber, 2002; Bernier et al., 1999; Chokmani et al., 2006; Yackel et al., 2007].

## X-Band

The TerraSAR-X data lack a relationship with ice temperature in the 2008/09 season but Figure 4.4.6 clearly shows that in 2009/10, backscatter increased as the snow/ice-interface temperature increased from -7°C to -1°C. Figure 4.4.6 suggests that backscatter increases with decreasing brine salinity and increasing brine volume at the snow/ice-interface. The response of X-band to changing surface properties is expected and utilized by the CoReH2O mission retrievals of SWE to filter the Ku-band backscatter for response to the snowpack. However, given that X-band also shows some sensitivity to volume scattering in the snow and therefore SWE, the removal of the ice surface and volume scattering components will be difficult over sea ice.

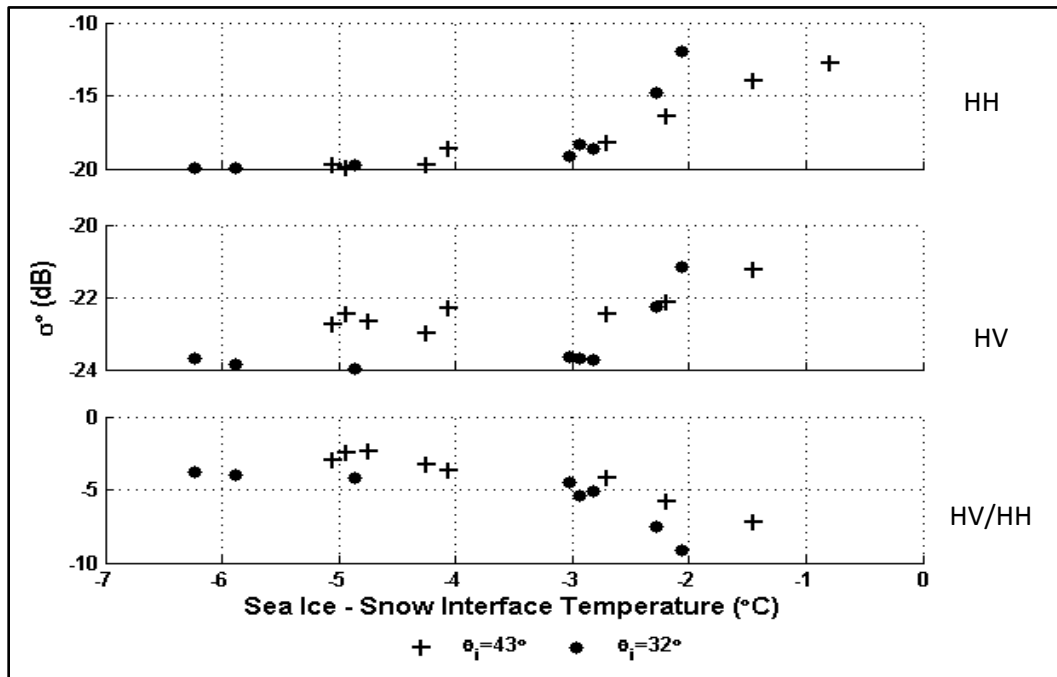
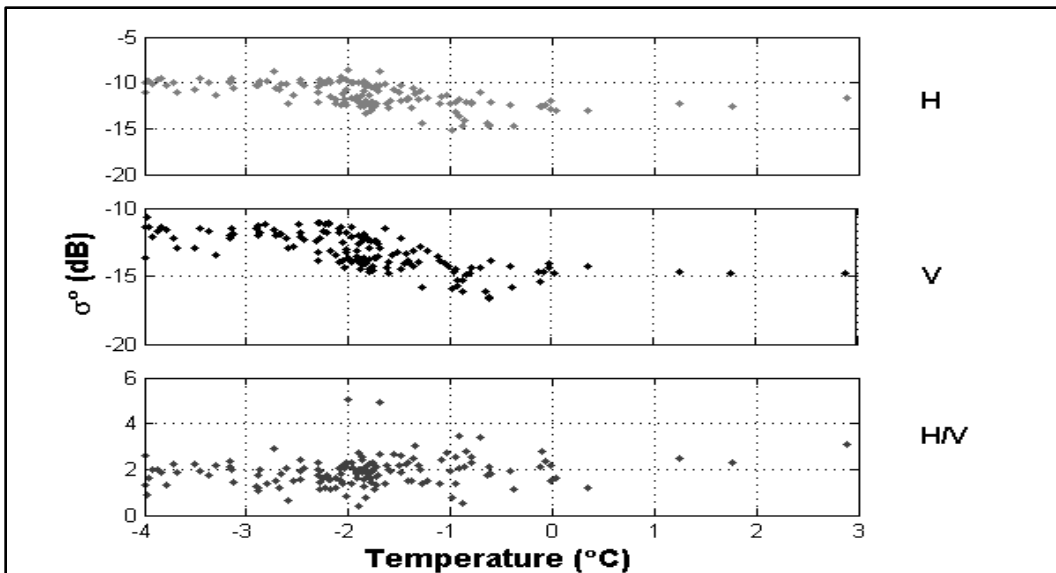


Figure 4.4.6: X-band backscatter response to changes in the temperature at the snow/ice-interface in 2009/10.

## Ku-Band

The Ku-band backscatter shows a weak but statistically significant correlation with the temperature of the snow/ice-interface ( $\text{Adj. } R^2 = 0.45, p < 0.05$ ), but temperatures explains far less of the variance observed than either SWE or snow depth. While the trend is scattered, there is a clear decrease in backscatter as the snow/ice interface temperature approaches the melting point. While C and X band showed an increase in backscatter with an increase in the temperature at the ice and snow interface, the Ku-band backscatter decreases. This may be the result of increased snow wetness causing decreased penetration and increased absorption by the liquid water within the snow. The decreased penetration of the Ku-band signal could have resulted in the loss of any surface scattering contribution from the snow/ice-interface.



**Figure 4.4.7:** Ku-band backscatter comparison with changes in the snow and ice interface temperature.

### Summary

Increases in the ice surface temperature were correlated with an increase in C- and X-band backscatter over the lake. As temperature increases, brine salinity decreases but brine volume increases driving an increase in the dielectric constant. Ku-band backscatter was found to decrease as ice surface temperature increased. In order for the ice temperature to increase, the snow temperature must also have increased. As snow temperature increases so does snow wetness, a parameter that Ku-band is very sensitive to. Even low snow wetness, between one and two percent by volume can cause a significant decrease in the penetration depth of Ku-band backscatter.

While ice surface temperature has been used by Yackel et al. (2002, 2007) to relate C-band backscatter to SWE, we can see here that their method really only works for the very smooth, saline FYI study site as they have discussed. This strongly limits the applicability of their retrieval, as first year sea ice is not always very smooth. Furthermore, even when the ice is smooth other factors such as changes in the snow grain size may influence the thermal conductivity of the snow and the ice surface temperature without changing SWE.

In addition to the aforementioned snow and ice properties, numerous other measured variables were compared to C, X and Ku-band backscatter. Some of the variables including snow density, brine volume and salinity, exhibited correlation with backscatter. However the correlations and physical basis for them were described by SWE, and ice surface temperature and thus were not presented separately. Other variables such as air temperature play a more indirect role in the development of other snow properties such as wetness, density, and snow-ice interface temperature and thus the correlations between air temperature and backscatter are weak and better explained by covariance with other properties. Variables such as lake water salinity showed no clear correlation and were not discussed.

## Chapter 5. Summary and Conclusions

In this study we have examined the evolution of radar backscatter at various frequencies in response to snow and saline ice properties of a temperate saline lake, Miquelon Lake. The study was conducted during the winters of 2008/09 and 2009/10 in the periods between ice onset to ice melt. The study presents one of the first complete time series observations of backscatter over saline lake ice using three SAR frequencies. Furthermore it is the first study of the evolution of snow and ice properties on Miquelon Lake, and temperate saline lakes in general. In addition, the majority of studies utilizing dual polarization TerraSAR-X imagery have so far focussed on sea ice classification only.

We have examined the radar backscatter response to these changing snow and ice conditions with a focus on X and Ku-band frequencies. The proposed CoReH2O satellite mission aims to use these frequencies to retrieve sea ice and snow property information, with a focus on snow water equivalence, or SWE. SWE provides information on the volume or mass of water contained in a snowpack, an important parameter for hydrological models. The snow strongly modifies the exchange of heat, gas, and radiation between the atmosphere, sea ice, and the ocean. Furthermore, SWE represents the mass of the snow per unit area, or the volume of water per unit area that results if the snow is melted. The weight of the snow influences the height of the sea ice surface above the water. The surface height is currently the most widely used method for estimating sea ice thickness from satellites. In addition to X and Ku-bands, C-band radar imagery was also acquired. C-band is currently the most widely used frequency for sea ice research. It was hypothesized that C-band radar backscatter may be linked to the thickness of the ice cover on Miquelon Lake. The CoReH2O mission also aims to use X-band to improve the detection and thickness estimation of thin sea ice.

### C Backscatter Response

C-band backscatter over Miquelon Lake was acquired from the Envisat ASAR sensor. Backscatter was uncorrelated with most of the snow and ice properties that were measured. C-band backscatter from the lake was found to be very low in both the VV and VH polarizations. As VV is mainly responsive to surface scattering and VH to volume scattering, this suggests that the lake was either very smooth or that the signal largely penetrates the ice and was absorbed. The onset of snow melt was detected by an increase in backscatter. Yackel et al. (2007) attributed the increase in backscatter at C-band to increasing brine volume in the upper ice and an increase in grain size and wetness of the snow near the ice interface. An increase in backscatter was observed with increasing temperatures and brine volume at the snow and ice interface in this study lending credence to this assertion. However, other factors such as snow grain size can also increase backscatter. It was hypothesized that C-band backscatter may be correlated with ice thickness, but the results were found to be inconclusive. It is possible that the thin, low salinity lake ice was completely penetrated by the C-band radar waves. Given that the ice is relatively young, volume scattering from the lake ice would be minimal as any brine channels or pockets would be much smaller than the radar wavelength. The presence of snow-ice can increase backscatter as larger air pockets can exist within it. Snow-ice also adds significant roughness to the surface and increased surface scattering.

## X Backscatter Response

X-band backscatter over Miquelon Lake was acquired from TerraSAR-X. Backscatter over the lake was low, especially in the cross polarizations (VH or HV). X-band backscatter exhibited a weak response to snow depth and SWE of between 90-140 mm SWE per decibel. Previous studies by Rott et al. (2010) reported sensitivities of 100 mm SWE per decibel at X-band. The CoReH2O proposal and work by Busche et al. (2009) suggested that X-band backscatter should respond to changes in thin ice thickness. Once again the low salinity and low porosity of the ice in Miquelon Lake allowed for complete penetration of X-band through the ice with little generation of volume scattering for much of the season as indicated by observations of grounded ice, very low backscatter from the lake and a sudden increase when ice thickness increased past 0.4m. As aforementioned the increase could also have been due to the formation of snow-ice. X-band was observed to respond to snow melt similarly to C band as increases in ice surface temperature and thus brine volume were well correlated with increases in backscatter late in the season.

## Ku Backscatter Response

As there is currently no Ku-band SAR sensor, data were acquired from the QuikSCAT Ku-band scatterometer. This real aperture radar provided lower spatial resolution but high temporal resolution images. A single pixel centered over Miquelon Lake was utilized to acquire backscatter statistics and data were compared to the in-situ measurements over the lake. The lake surface makes up the majority of the pixel area followed by forest and agricultural fields. Ku backscatter was found to be more sensitive to changes in snow depth and SWE than C or X-band. Ku backscatter increased with the presence of snow on the lake and decreased with snow melt onset. The sensitivity observed in this study was approximately 1 dB/25 mm SWE. This is slightly higher than was observed by Rott et al. (2010) but falls within the range reported by Yueh et al. (2009). Unlike C and X-band, Ku band was not found to be sensitive to ice thickness and showed a decrease in backscatter as ice surface temperatures increased as a result of increased wetness and absorption within the snow.

### 5.1 Study Limitations

Although this study examined a large number of snow and ice properties and presents the first time series analysis of a study region using three SAR frequencies combined with in-situ validation data there are some limitations to the work. The limitations largely result from the poor temporal resolution of the in-situ measurements which limit observations of event based parameters such as snow melt and surface flooding and subsequent snow-ice formation. Other limitations such as the loss of the QuikSCAT Ku-band sensor could not be foreseen or prevented. Another unforeseen loss of data resulted when an ice core storage freezer suffered a mechanical failure over a weekend and the ice cores that had been acquired for studying the texture and structure of the lake ice melted.

Measurements of snow grain size and snow density were not performed at the same temporal resolution as the other parameters. While depth hoar was observed and

measured several times, a careful study of changes in the grain size of the various snow layers was not conducted. Given the recent work by Arslan et al. (2011) who showed a high sensitivity of X and Ku band backscatter to snow grain size the lack of snow grain size and depth hoar observations in this study is extremely unfortunate. The increase in snow grain size and depth hoar can increase the backscatter dramatically. The size of snow grains and depth rapidly changes when either a strong temperature gradient exists within the snowpack or when there is sufficient liquid water within the snow to join grains.

Snow-ice was observed in the ice cores and there was further evidence for flooding through negative freeboard near drill holes. However the sparse temporal resolution of the in-situ measurements makes it likely that periods of flooding and subsequent snow-ice formation were not observed. The presence of snow-ice can result in increased backscatter due to an increase in the surface roughness.

The loss of the QuikSCAT sensor and the Ku-band backscatter imagery in the early winter of 2009 was a major limitation to the 2009/10 season analysis. X-band imagery was also not acquired until late December 2009 and C-band imagery was largely unavailable until February 2010. While satellites offer large volumes of data during their operations, sudden failures or re-tasked space program objectives can result in problematic data gaps. Data from the Indian Ku-band scatterometer on board Oceansat-2 have recently been made available but high-resolution products remain in the alpha processing stage [BYU Center for Remote Sensing et al., 2011]. Once the validity of these products has been confirmed the Ku-band backscatter over Miquelon Lake can be assessed for the 2009/10 season as well. Furthermore, because the QuikSCAT pixel over the lake combines the backscatter return from the lake, forest, and agricultural land, some effort to perform spectral un-mixing by monitoring the backscatter from pixels of pure forest and agricultural land near the lake should be made.

One of the limitations of this study that is common to studies of radar over natural targets is the co-evolution and competition of multiple snow and ice properties, and as a result, the dielectric properties. Radar backscatter is strongly influenced by multiple parameters and their influence is determined by the magnitude and history of themselves and the other parameters. For example, the presence of warm air temperatures early in the winter can cause an increase in the liquid water content of the snow. The increase is dependent on the temperature and the duration of positive air temperatures. The warm air temperatures can also cause increased brine volume at the interface of the ice and snow. While increased brine volume increased the dielectric constant of the ice and therefore increases the surface backscatter that results from the sea ice surface the increase in liquid water content within the snow pack can reduce backscatter from within the snow volume. Melting snow and brine at the surface can result in superimposed ice formation and an increase in surface roughness. Increased air temperatures also influence the density of the snow and its grain size. The combination of the number of parameters, and the importance of both their current and past magnitudes results in a system that is extremely complicated to compare. In the study by Makynen et al. (2007) where C-band backscatter changes were compared to in-situ observations and the output from a thermodynamic snow and sea ice model, no single variable explained a statistically significant amount of the backscatter variation. While it is no surprise that backscatter is dependent on multiple competing factors, this study

clearly shows that the retrieval of any one parameter is also highly dependent on the correct assumption or observations of all potential variables.

This study has presented the first comparison of changing sea ice and snow properties in the context of radar backscatter from a temperate saline lake. This study is also one of the first time-series examinations of radar backscatter from a saline lake combining multiple frequencies and polarizations with regular detailed in-situ observations throughout the winter. The study presented some interesting results that were not expected. It was expected that C-band radar would show some relationship with ice thickness, and while this is the case, the results are somewhat unclear. Furthermore, it appears as though X-band is also sensitive to the thickness of the ice. Furthermore, it was interesting to observe the strong agreement between AMSR-E SWE estimates and in-situ observations in 2008/09 but the complete disagreement in 2009/10, immediately illustrating the need for improved SWE parameterization.

Given the large number of variables that influence radar backscatter at X and Ku-band frequencies it will prove extremely difficult to retrieve SWE from sea ice in the Arctic or the Baltic. In these regions, not only does one have to deal with changing snow and ice properties, but also dynamic changes in the structure, distribution and spatial location of the ice and snow that result from ice motion. The main weakness of the mission concept is the complicated co-evolution of multiple snow and ice parameters and the competing changes in the dielectric properties that result. Different retrieval algorithms will likely be needed for different underlying surfaces, such as smooth FYI, rough FYI, multiyear ice. Sea ice has such high spatial and temporal variability in its properties that due to dynamics it will prove very difficult to retrieve information on the changes in snow and ice properties such as SWE for any ice but landfast ice. Without knowledge of the initial in-situ properties, the retrieval of SWE will come to rely very heavily on modelled snow and ice properties with their inherent inaccuracy and limitations.

## 5.2 Suitability of Study Site for Future Work

Given the results of the study, Miquelon Lake seems to serve as a suitable analogue for sea ice studies, particularly for low salinity sea ice as is found in the Baltic Sea. Although suitability is largely a subjective measure based on the requirements of the study, the following general observations about the suitability of Miquelon Lake as a sea ice analogue site can be made.

The absence of ice motion and a continuous ice cover on Miquelon Lake results in high homogeneity of ice properties such as salinity and density and where the ice is not grounded, ice thickness. Two transects across the entire lake running East-West and North-South respectively, showed little variation in the thickness of the ice and snow. The uniformity and logistical simplicity means that the lake is extremely well suited for remote sensing studies. Other than the development of an expansion crack in 2008/09 there was little evidence for heterogeneity in any of the snow properties in the open lake environment.

Snow and ice and meteorological conditions over Miquelon Lake were observed to be similar to the Baltic Sea including thickness of snow and ice, snow density, the presence of snow-ice and even the length of the ice season. One of the major issues with Miquelon Lake as a sea ice analogue is the large amount of inter-annual variability in the

snow and ice and meteorological conditions. The 2009/10 snow cover duration was three weeks shorter than the previous year with melt beginning in early March. Furthermore, in-situ observations from 2010/11 showed extreme snow depth and large amounts of snow-ice formation. The current winter, 2011/12, has seen little snow fall and air temperatures 10-15°C above seasonal for much of November and December 2011. However, inter-annual variability is an issue for all study sites, even outdoor artificial ice tanks such as at CRREL or at the University of Manitoba.

Miquelon Lake is an ideal location for the study of properties and processes associated with microwave radar backscatter evolution from saline ice formed from brackish water bodies. The homogeneity of the lake ice and snow over a much larger area than an ice tank allows for satellite based remote sensing studies. Furthermore, the lake is relatively simple and affordable from a logistical perspective due to its proximity to the University of Alberta in Edmonton.

### 5.3 Future Work

Although this study has presented the first complete time series of backscatter evolution of a saline lake at C, X, and Ku-bands, several shortcomings have been discussed throughout this thesis including:

1. No Ku-backscatter data for 2009/10
2. Low temporal resolution of C and X-band imagery
3. Low spatial resolution of Ku-band scatterometer data
4. Poor monitoring of snow grain size and wetness
5. Inadequate study of lake ice structure

Based on these short comings, to improve our understanding of the response of backscatter to changing snow and ice properties on Miquelon Lake future work could either utilize and expand upon the current validation data set, or gather new and improved data during another study campaign.

#### A. Current Validation Set

- i) OceanSAT Ku scatterometer data for 2009/10
- ii) Calculate changes in polarimetric decompositions, and the interferometric phase shift for comparison to snow and ice properties

#### B. New Campaign

- i) Airborne X, Ku (SNOWSAR)
- ii) Ground based Ku, X, and C
- iii) C,X, and Ku SAR imagery from all available incidence angles
- iv) Study of the structure and chemical composition of the ice.
- v) Deployment of weather station including IMB with wind and solar radiation sensors.
- vi) Daily in-situ measurements

It is clear from this study that Ku band holds significant promise for the retrieval of snow properties such as SWE from sea ice. The loss of the QuikSCAT sensor in November 2009 limited the study of snow properties and Ku to just 2008/09. However, data from

OceanSAT, a Ku-band scatterometer launched by the Indian Space Agency, has recently been made available to the NASA Scatterometer Pathfinder Record. High-resolution image generation of the OceanSAT data is in an alpha stage and requires validation. This data would allow for the extension of the Ku-band analysis for 2009/10 providing a more complete and robust understanding of the relationship between Ku-band backscatter and SWE over low salinity sea ice.

In addition to the co and cross polarization data acquired by TerraSAR-X for this study, it is possible to calculate polarimetric decompositions that may provide additional information. These decompositions are detailed in Schott (2009) and Lee and Pottier (2009). Some of the polarimetric decompositions provide detailed information on the volume scattering and isotropy of the medium while others are sensitive to double bounce[Lee and Pottier, 2009]. The eleven TerraSAR-X spotlight mode images acquired in 2008/09 and the Stripmap mode images acquired in 2009/10 were all dual polarization complex mode images that allow for polarimetric studies. The examination of the polarimetric decompositions was originally planned for this study but software capable of polarimetric processing of the TerraSAR-X imagery has only been developed very recently. The analysis of these decompositions requires further ongoing software development.

If conducting an additional campaign there are numerous other improvements that could be made. The coarse spatial resolution of QuikSCAT and the differences in backscatter observed between the land, forest, and lake surfaces of Miquelon Lake suggest that the open fields and forest adjacent to the lake may influence the signal from the QuikSCAT pixel. Independent data should be acquired for all land cover types. Currently there is no space-borne Ku band SAR sensor but an airborne version of the proposed CoReH2O system was flown over a test site in Finland in February of 2011 [Trampuz et al., 2011]. The airborne system provides the opportunity to collect coincident Ku and X band SAR with high spatial resolution and should be flown over other targets of interest for SWE retrieval including Arctic and Baltic sea ice, regions with significant topography and a variety of land surface covers. Unfortunately airborne campaigns are dramatically more expensive than satellite and multiple flights at various times throughout the winter would be required. As such, a study using a ground based scatterometer would be financially and logically feasible and of great value. Ku and X band ground based scatterometers have been also developed for CoReH2O validation at the University of Waterloo.

An important aspect of studying the seasonal evolution of snow and ice properties is ensuring a dense time series. In this study images were only acquired from a few different incidence angle ranges due to cost/quota limitations, orbit configurations and constraints, and time considerations. If all incidence angle ranges were acquired, one could properly examine incidence angle effects and provide an accurate incidence angle correction for the data. The density of time series observations would be increased by including all incidence angle ranges and could provide more information during initial ice formation and freeze-up. For C-band studies over Miquelon Lake, acquisitions from RadarSAT-2 could be included to increase the time series density at C-band and to provide high resolution and quad-polarization imagery. Inclusion of imagery from TanDEM-X, a second X-band SAR from the German Aerospace Center (DLR) would

increase the sampling at X-band. The proposed CoReH2O mission would include an initial three day repeat orbit for calibration and validation purposes.

Fully polarimetric complex mode imagery would allow for the study of the change in polarimetric decompositions with the observed changes in snow and ice properties. Furthermore, interferometric processing techniques that utilize the phase information in SAR would provide the study of interferometric techniques for SWE retrieval [Engen et al., 2004; Esmaeily-Gazkohani et al., 2010].

Original plans included examining the structure and texture of the retrieved ice cores from Miquelon Lake. Cross-polarized visible light can be used to examine the crystal structure of ice cores and identify different growth periods and snow-ice formation. The study would also have allowed a comparison with ice cores acquired in the Baltic Sea and an examination of the presence and contribution of snow-ice to the ice thickness of Miquelon Lake. However, a mechanical breakdown of the ice core storage freezer resulted in the melt and loss of the Miquelon Lake ice cores. A future study of the texture, structure and changes in the contribution of snow-ice to overall ice thickness should be undertaken for Miquelon Lake in order to improve the comparison to sea ice from the Baltic Sea.

While the IMB on Miquelon Lake proved extremely useful in that it provided high temporal resolution snow and ice data as well as a temperature profile throughout the winter, improvements to automated monitoring of the study site would provide for new avenues of examination. The IMB developed by SAMS showed very promising and interesting results, but with the numerous changes to settings and a reduction in the data rate from hourly to once per day minimized its usefulness. A consistent temporal resolution record from this sensor would allow for interesting studies into the variability in snow and ice properties from differential heating channels. Furthermore, the inclusion of a weather station with wind speed, relative humidity, and short-wave and long-wave radiation sensors would provide accurate input for executing some of the advanced snow models like SNATHERM and SNOPAC. These models would provide increased temporal resolution by estimating the in-situ snow properties such as depth, density, SWE and grain size.

One of the most interesting experiments to conduct on Miquelon Lake in the view of retrieving snow and ice properties would be to combine many of the above suggestions and conduct daily in-situ field measurements. Daily in-situ measurements and multiple experimental sites along the lake would provide high temporal and spatial resolution validation dataset. Care to measure and observe all relevant parameters could be made and would provide a complete picture of the cause of changes in backscatter. Such an in-situ measurement campaign would be relatively inexpensive and logically simple in comparison to conducting a seasonal study in the Arctic or even the Baltic Sea.

Given the covariance of the snow and ice properties and their influence on backscatter, accurate retrieval of SWE over sea ice and thin ice thickness from the CoReH2O mission will prove extremely difficult. The competition of snow and ice properties such as density, grain size, wetness, surface brine volume, surface roughness, salinity and other factors such as snow-ice formation, flooding and brine wicking, air temperature, ice lenses will require acceptance of large uncertainties or numerous algorithms designed

for very specific ranges of those properties. The co-evolution of the various snow and ice properties has and will continue to complicate their retrieval from SAR imagery. Furthermore the dynamic nature of the ice pack and the large amount of variability in the surface properties of the ice influence backscatter differently for different ice types will further complicate SWE and ice property retrieval from CoReH2O. Nonetheless, the SAR data will provide useful high spatial and temporal resolution Ku and X band imagery of the sea ice and its snow cover.

## Bibliography

Alberta Environment, Energy Resources Conservation Board, and Alberta Geological Survey (2008), Miquelon Lakes, Alberta - GIS Data (DIG 2008-0811). Available online at [http://www.agi.gov.ab.ca/publications/abstracts/DIG\\_2008\\_0811.html](http://www.agi.gov.ab.ca/publications/abstracts/DIG_2008_0811.html).

American Public Health Association, American Water Works Association, and Water Environment Federation (1999), *Standard methods for the examination of water and wastewater*, American Public Health Association, Washington.

Anderson, D. L. (1961), Growth rate of sea ice. *Journal of Glaciology*, **3(30)**, 1170-1172.

Arrigo, K. R., T. Mock, and M. P. Lizotte (2010), Primary Producers and Sea Ice, in *Sea ice*, edited by D. N. Thomas et al., pp. 283-326, Wiley-Blackwell Pub., Chichester, U.K.; Iowa, USA.

Arslan, A. N., J. Pullainen, J. Lemmetynen, T. Nagler, H. Rott, and M. Kern (2011), Effects of snowpack parameters and layering processes at X- and Ku-band backscatter, paper presented at 2011 IEEE International Geoscience and Remote Sensing Symposium (IGARSS 2011), 24-29 July 2011, Vancouver, Canada.

Barber, D. G., T. N. Papakyriakou, E. F. Ledrew, and M. E. Shokr (1995), An examination of the relation between the spring period evolution of the scattering coefficient ( $\sigma$ ) and radiative fluxes over jandfast sea-ice. *International Journal of Remote Sensing*, **16(17)**, 3343-3363, doi:10.1080/01431169508954634.

Barnett, T. P., J. C. Adam, and D. P. Lettenmaier (2005), Potential impacts of a warming climate on water availability in snow-dominated regions. *Nature*, **438(7066)**, 303-309, doi:10.1038/nature04141

Barry, R. G., R. Armstrong, T. Callaghan, J. Cherry, S. Gearheard, A. Nolin, D. Russel, and C. Zöckler (2007), Snow, in *Global outlook for ice & snow*, edited by J. Eamer et al., pp. 39-62, Division of Early Warning and Assessment (DEWA), United Nations Environmental Programme, Nairobi, Kenya.

Bartsch, A. (2010), Ten Years of SeaWinds on QuikSCAT for Snow Applications. *Remote Sensing*, **2(4)**, 1142-1156, doi:10.3390/rs2041142.

Beaven, S. G., G. L. Lockhart, S. P. Gogineni, A. R. HosseinMostafa, K. Jezek, A. J. Gow, D. K. Perovich, A. K. Fung, and S. Tjuatja (1995), Laboratory measurements of radar backscatter from bare and snow-covered saline ice sheets. *International Journal of Remote Sensing*, **16(5)**, 851-876, doi:10.1080/01431169508954448.

Bernier, M., J.P. Fortin, Y. Gauthier, R. Gauthier, R. Roy, and P. Vincent (1999), Determination of snow water equivalent using RADARSAT SAR data in eastern Canada.

*Hydrological Processes*, **13(18)**, 3041-3051, doi:10.1002/(SICI)1099-1085(19991230)13:18<3041::AID-HYP14>3.0.CO;2-E.

Bierhuizen, J. F. H., E. E. Prepas (1985), Relationship between nutrients, dominant ions, and phytoplankton standing crop in prairie saline lakes. *Canadian Journal of Fisheries and Aquatic Science.*, **42**, 1588-1594, doi:10.1139/f85-199.

Bluhm, B. A., R. R. Gradinger, and S. B. Schnack-Schiel (2010), Sea Ice Meio- and Macrofauna, in *Sea ice*, edited by D. N. Thomas et al., pp. 357-394, Wiley-Blackwell Pub., Chichester, U.K.; Ames Iowa, USA.

Brown, R., C. Derksen, and L. Wang (2010), A multi-data set analysis of variability and change in Arctic spring snow cover extent, 1967–2008. *Journal of Geophysical Research*, **115**, D16111, doi:10.1029/2010JD013975.

Busche, T., I. Hajnsek, K. Papathanassiou, T. Krumpen, L. Rabenstein, J. Hoelemann, C. Haas, and S. Willmes (2009), Comparison of helicopter-borne thin sea ice thickness profiles with polarimetric signatures of dual-pol Terrasar-X data, paper presented at 2009 IEEE International Geoscience and Remote Sensing Symposium, 12-17 July 2009, Cape Town, South Africa.

BYU Center for Remote Sensing, NASA Jet Propulsion Laboratory, and European Space Agency, 2011: Oceansat-2 Scatterometer Enhanced Resolution Image Products (version 0). Accessed online at [http://www.scp.byu.edu/data/OSCAT/SIR/OSCAT\\_sir.html](http://www.scp.byu.edu/data/OSCAT/SIR/OSCAT_sir.html).

Canada Centre for Remote Sensing, Natural Resources Canada (2001), *Fundamentals of remote sensing*. Canada Centre for Remote Sensing. Accessed online at [http://www.nrcan.gc.ca/sites/www.nrcan.gc.ca.earth-sciences/files/pdf/resource/tutor/fundam/pdf/fundamentals\\_e.pdf](http://www.nrcan.gc.ca/sites/www.nrcan.gc.ca.earth-sciences/files/pdf/resource/tutor/fundam/pdf/fundamentals_e.pdf).

Caron, D. A., R. J. Gast (2010), Heterotrophic Protists Associated with Sea Ice, in *Sea ice*, edited by D. N. Thomas et al., pp. 327-356, Wiley-Blackwell Pub., Chichester, U.K.; Iowa, USA.

Carsey, F. D., R. G. Barry, and W. F. Weeks (1992), Introduction, in *Microwave remote sensing of sea ice*, edited by F. D. Carsey, pp. 1-7, American Geophysical Union. Washington DC, USA.

Chemiasoft, 2011: Conductivity of a reference KCl solution. Available online at <http://www.chemiasoft.com/salinitycalc.html>.

Chokmani, K., M. Bernier, and Y. Gauthier (2006), Uncertainty analysis of EQeau , a remote sensing based model for snow water equivalent estimation. *International Journal of Remote Sensing*, **27(19)**, 4337-4346, doi:10.1080/01431160600835879.

Clissold, P. (2009), Six candidate earth explorer core missions - reports for assessment. *ESA SP1313*, ESA Communication Office, Noordwijk, The Netherlands.

Colbeck, S. C., E. Akitaya, R. Armstrong, H. Gubler, J. Lafeuille, K. Lied, D. M. McClung, and E. M. Morris (1990), *International Classification For Seasonal Snow On The Ground*. International Commission for Snow and Ice, World Data Center A for Glaciology, University of Colorado, Boulder, CO, USA.

Cox, G. F. N., W. F. Weeks (1983), Equations for determining the gas and brine volumes in sea-ice samples. *Journal of Glaciology*, **29(102)**, 306-316.

Deeb, E. J., R. R. Forster, and D. L. Kane (2011), Monitoring snowpack evolution using interferometric synthetic aperture radar on the North Slope of Alaska, USA. *International Journal of Remote Sensing*, **32(14)**, 3985-4003, doi:10.1080/01431161003801351.

Deming, J. W. (2010), Sea Ice Bacteria and Viruses, in *Sea ice*, edited by D. N. Thomas et al., pp. 247-282, Wiley-Blackwell Pub., Chichester, U.K.; Iowa, USA.

Derkzen, C. (2008), The contribution of AMSR-E 18.7 and 10.7 GHz measurements to improved boreal forest snow water equivalent retrievals. *Remote Sensing of Environment*, **112(5)**, 2701-2710, doi:10.1016/j.rse.2008.01.001.

Dieckmann, G. S., H. H. Hellmer (2010), The Importance of Sea Ice: An Overview, in *Sea ice*, edited by D. N. Thomas et al., pp. 1-22, Wiley-Blackwell Pub., Chichester, U.K.; Iowa, USA.

Drinkwater, M. R., R. Kwok, E. J. M. Rignot, H. Israelson, R. G. Onstott, D. P. Winebrenner, E. J. Rignot, H. Israelsson, and F. D. Carsey (1992), Potential applications of polarimetry to the classification of sea ice, in *Sea ice*, edited by D. N. Thomas et al., pp. 531-577, Wiley-Blackwell Pub., Chichester, U.K.; Iowa, USA.

Duarte, C. M., Y. T. Prairie, C. Montes, J. J. Cole, R. Striegl, J. Melack, and J. A. Downing (2008), CO<sub>2</sub> emissions from saline lakes: A global estimate of a surprisingly large flux. *Journal of Geophysical Research*, **113**, G04041, doi:10.1029/2007JG000637.

Duguay, C. R., T. J. Pultz, P. M. Lafleur, and D. Draai (2002), RADARSAT backscatter characteristics of ice growing on shallow sub-Arctic lakes, Churchill, Manitoba, Canada. *Hydrological Processes*, **16(8)**, 1631-1644, doi:10.1002/hyp.1026.

Dwemychuk, L. W., D. A. Boag (1972), Ducks nesting in association with gulls - an ecological trap? *Can. J. Zool.*, **50**, 559-563.

E.S.A., 2007a: ASAR User Guide: Glossary: Geometry Glossary. European Space Agency (E.S.A.), 564-417. Accessed online at <http://envisat.esa.int/handbooks/asar/CNTR5-5.htm>.

E.S.A. (2007b), Envisat ASAR Product Handbook(2.2). European Space Agency (E.S.A.), Accessed online at  
[http://envisat.esa.int/pub/ESA\\_DOC/ENVISAT/ASAR/asar.ProductHandbook.2\\_2.pdf](http://envisat.esa.int/pub/ESA_DOC/ENVISAT/ASAR/asar.ProductHandbook.2_2.pdf).

E.S.A., 2012: Envisat ASAR Instrument Design Characteristics. Accessed online at [https://earth.esa.int/web/guest/missions/esa-operational-eo-missions/envisat/instruments/asar/design#\\_56\\_INSTANCE\\_2sWV\\_matmp](https://earth.esa.int/web/guest/missions/esa-operational-eo-missions/envisat/instruments/asar/design#_56_INSTANCE_2sWV_matmp).

Early, D. S., D. G. Long (2001), Image reconstruction and enhanced resolution imaging from irregular samples. *IEEE Transactions on Geoscience and Remote Sensing*, **39(2)**, 291-302, doi:10.1109/36.905237.

Engen, G., T. Guneriussen, and Y. Overrein (2004), Delta-K interferometric SAR technique for snow water equivalent (SWE) retrieval. *IEEE Geoscience and Remote Sensing Letters*, **1(2)**, 57-61, doi:10.1109/LGRS.2003.822880.

Esmaeily-Gazkohani, A., H. B. Granberg, and Q. H. Gwyn (2010), Repeat-pass cross-track interferometric SAR to measure dry snow water equivalent and depth. *Canadian Journal of Remote Sensing*, **36(S2)**, S316-S326, doi:10.5589/m10-064.

Evans, J. C., E. E. Prepas (1997), Relative importance of iron and molybdenum in restricting phytoplankton biomass in high phosphorus saline lakes. *Limnology and Oceanography*, **42(3)**, 461-472, doi:10.4319/lo.1997.42.3.0461.

Frei, A., D. A. Robinson (1999), Northern hemisphere snow extent: Regional variability 1972-1994. *International Journal of Climatology*, **19(14)**, 1535-1560, doi:10.1002/(SICI)1097-0088(19991130)19:14<1535::AID-JOC438>3.0.CO;2-J.

Geldsetzer, T., J. J. Yackel (2009), Sea ice type and open water discrimination using dual co-polarized C-band SAR. *Canadian Journal of Remote Sensing*, **35(1)**, 73-84, doi:10.5589/m08-075.

German Aerospace Centre (DLR) (2007), TerraSAR-X Ground Segment Level 1b Product Format Specification, *TX-GS-DD-3307(1.3)*, 1-257. Accessed online at <http://sss.terrasar-x.dlr.de/pdfs/TX-GS-DD-3307.pdf>

German Aerospace Centre (DLR) (2010), TerraSAR-X Ground Segment Basic Product Specification Document, *TX-GS-DD-3302(1.7)*, 1-109. Accessed online at <http://sss.terrasar-x.dlr.de/pdfs/TX-GS-DD-3302.pdf>

Ghatak, D., A. Frei, G. Gong, J. Stroeve, and D. Robinson (2010), On the emergence of an Arctic amplification signal in terrestrial Arctic snow extent. *Journal of Geophysical Research*, **115**, D24105, doi:10.1029/2010JD014007.

GlobeSAR-2, Canada Centre for Remote Sensing (2001), Educational resources for radar remote sensing. Accessed online at <http://www.nrcan.gc.ca/sites/www.nrcan.gc.ca.earth-sciences/files/pdf/resource/tutor/gsarcdf/pdf/gsarcde.pdf>.

Granskog, M. A., T. A. Martma, and R. A. Vaikmae (2003), Development, structure and composition of land-fast sea ice in the northern Baltic Sea. *Journal of Glaciology*, **49(164)**, 139-148, doi:10.3189/172756503781830872.

Granskog, M. A., M. Lepparanta, T. Kawamura, J. Ehn, and K. Shirasawa (2004), Seasonal development of the properties and composition of landfast sea ice in the Gulf of Finland, the Baltic Sea. *Journal of Geophysical Research*, **109**, C02020, doi:10.1029/2003JC001874.

Granskog, M. A., H. Kaartokallio, H. Kuosa, D. N. Thomas, and J. Vainio (2006), Sea ice in the Baltic Sea – A review. *Estuarine, Coastal and Shelf Science*, **70(1-2)**, 145-160, doi:10.1016/j.ecss.2006.06.001.

Granskog, M. A., H. Kaartokallio, and H. Kuosa (2010), Sea Ice in Non-polar Regions, in *Sea ice*, edited by D. N. Thomas et al., pp. 531-577, Wiley-Blackwell Pub., Chichester, U.K.; Iowa, USA.

Grossman, S. R., S. J. Hannon, and A. Sanchez-Azofeifa (2008), Responses of Great Horned Owls (*Bubo virginianus*), Barred Owls (*Strix varia*), and Northern Saw-whet Owls (*Aegolius acadicus*) to forest cover and configuration in an agricultural landscape in Alberta, Canada. *Canadian Journal of Zoology*, **86(10)**, 1165-1172, doi:10.1139/Z08-095.

Guneriussen, T., K. A. Hogda, H. Johnsen, and I. Lauknes (2001), InSAR for estimation of changes in snow water equivalent of dry snow. *IEEE Transactions on Geoscience and Remote Sensing*, **39(10)**, 2101-2108, doi:10.1109/36.957273.

Haas, C. (2004), Airborne EM sea-ice thickness profiling over brackish Baltic sea water, paper presented at Proceedings of the 17th international IAHR symposium on ice, , 2004, All-Russian Research Institute of Hydraulic Engineering (VNIIG), Saint Petersburg, Russia.

Hallikainen, M., F. T. Ulaby, and M. Abdelrazik (1986), Dielectric properties of snow in the 3 to 37 GHz range. *IEEE Transactions on Antennas and Propagation*, **34(11)**, 1329-1340, doi:10.1109/TAP.1986.1143757.

- Hallikainen, M., D. P. Winebrenner (1992), The Physical Basis for Sea Ice Remote Sensing, in *Microwave remote sensing of sea ice*, edited by F. D. Carsey, pp. 29-46, American Geophysical Union, Washington, DC USA.
- Hallikainen, M., P. Halme, M. Takala, and J. Pulliajainen (2003), Combined active and passive microwave remote sensing of snow in Finland, paper presented at 2003 IEEE International Geoscience and Remote Sensing Symposium, 21-25 July 2003, Toulouse, France.
- Hammer, U. T. (1978), The Saline Lakes of Saskatchewan I. Background and Rationale for Saline Lakes Research. *Internationale Revue der gesamten Hydrobiologie und Hydrographie*, **63(2)**, 173-177, doi:10.1002/iroh.19780630205.
- Hammer, U. T., R. C. Haynes (1978), The Saline Lakes of Saskatchewan II. Locale, Hydrography and other Physical Aspects. *Internationale Revue der gesamten Hydrobiologie und Hydrographie*, **63(2)**, 179-203, doi:10.1002/iroh.19780630206.
- Hood, G., 2011: Professional web page of Dr. Glynnis Hood. Accessed online at <http://www.augustana.ualberta.ca/profs/ghood/>.
- Howell, S. E. L., J. J. Yackel, R. De Abreu, T. Geldsetzer, and C. Breneman (2005), On the utility of SeaWinds/QuikSCAT data for the estimation of the thermodynamic state of first-year sea ice. *IEEE Transactions on Geoscience and Remote Sensing*, **43(6)**, 1338-1350, doi:10.1109/TGRS.2005.846153.
- Howell, S. E. L., A. Tivy, J. J. Yackel, B. G. T. Else, and C. R. Duguay (2008), Changing sea ice melt parameters in the Canadian Arctic Archipelago: Implications for the future presence of multiyear ice. *Journal of Geophysical Research*, **113**, C09030, doi:10.1029/2008JC004730.
- Howell, S. E. L., L. C. Brown, K. Kang, and C. R. Duguay (2009), Variability in ice phenology on Great Bear Lake and Great Slave Lake, Northwest Territories, Canada, from SeaWinds/QuikSCAT: 2000–2006. *Remote Sensing of Environment*, **113(4)**, 816-834, doi:10.1016/j.rse.2008.12.007.
- Infoterra GmbH (2008), Radiometric Calibration of TerraSAR-X Data: Beta Naught and Sigma Naught Coefficient Calculation, *TSXX-IDT-TN-0049-radiometric\_calculations\_i1.00*, 1-16. Accessed online at [http://www.astrium-geo.com/files/pmedia/public/r465\\_9\\_tsxx-itd-tn-0049-radiometric\\_calculations\\_i1.00.pdf](http://www.astrium-geo.com/files/pmedia/public/r465_9_tsxx-itd-tn-0049-radiometric_calculations_i1.00.pdf).
- Jensen, J. R. (2007), Chapter 9: Active and Passive Microwave Remote Sensing, in *Remote sensing of the environment : an earth resource perspective*, pp. 291-335, Pearson Prentice Hall, NJ, USA.

Jin-woo Kim, K. Duk-jin, and J. H. Byong (2010), Estimation of sea ice thickness in the Arctic Sea using polarimetric parameters of C- and X-band space-borne SAR data, paper presented at 2010 IEEE International Geoscience and Remote Sensing Symposium, 25-30 July 2010, Honolulu, Hawaii, USA.

Jong-Sen, L. (1983), Digital image smoothing and the sigma filter. *Computer Vision, Graphics, and Image Processing*, **24(2)**, 255-269, doi:10.1016/0734-189X(83)90047-6.

Kawamura, T., K. Shirasawa, N. Ishikawa, A. Lindfors, K. Rasmus, M. A. Granskog, J. Ehn, M. Lepparanta, T. Martma, and R. Vaikmae (2001), Time-series observations of the structure and properties of brackish ice in the Gulf of Finland. *Annals of Glaciology*, **33(1)**, 1-4, doi:10.3189/172756401781818950.

Kubat, I., G. W. Timco, S. Loset, B. Bonnemaire, and M. Bjerkas (2003), Vessel damage in the Canadian Arctic, paper presented at 17<sup>th</sup> international conference on Port and ocean engineering under arctic conditions, 16-19 June 2003, Trondheim, Norway.

Kwok, R., D. A. Rothrock (2009), Decline in Arctic sea ice thickness from submarine and ICESat records: 1958–2008. *Geophysical Research Letters*, **36(15)**, L15501, doi:10.1029/2009GL039035.

Langlois, A., D. G. Barber (2008), Advances in seasonal snow water equivalent (SWE) retrieval using in situ passive microwave measurements over first-year sea ice. *International Journal of Remote Sensing*, **29(16)**, 4781-4802, doi:10.1080/01431160801908145.

Langlois, A., T. Fisico, D. G. Barber, and T. N. Papakyriakou (2008), Response of snow thermophysical processes to the passage of a polar low-pressure system and its impact on in situ passive microwave radiometry: A case study. *Journal of Geophysical Research*, **113**, C03S04, doi:10.1029/2007JC004197.

Langlois, A., A. Royer, and K. Goita (2010), Analysis of simulated and spaceborne passive microwave brightness temperatures using in situ measurements of snow and vegetation properties. *Canadian Journal of Remote Sensing*, **36(S1)**, S135-S148, doi:10.5589/m10-016.

Lee, J., E. Pottier (2009), *Polarimetric radar imaging : from basics to applications*, CRC Press, Boca Raton, FL, USA.

Lemke, P., S. Solomon, D. Qin, M. Manning, M. Marquis, K. Averyt, M. M. B. Tignor, H. L. Miller Jr., C. Zhenlin, S. Solomon, D. Qin, M. Manning, Z. Chen, M. Marquis, K.B. Averyt, M. Tignor, H.L. Miller, and I. Working Group (2007), Observations: changes in snow, ice and frozen ground, in *Climate Change 2007: The Physical Science Basis. Contribution Of Working Group I To The Fourth Assessment Report Of The Intergovernmental Panel On Climate Change*, 337-383.

Leppäranta, M., T. Manninen (1988), The brine and gas content of sea ice with attention to low salinities and high temperatures. *Finnish Institute of Marine Research Internal Report 88-2*, Helsinki.

Leppäranta, M., K. Myrberg (2009), *Physical oceanography of the Baltic Sea*, Praxis Pub., Berlin, Germany; NY, USA; Chichester, UK.

Long, D. G., B. R. Hicks (2010), Standard BYU QuikSCAT and Seawinds Land/Ice Image Products, *MERS Technical Report 05-04*, 1-30. Accessed online at <http://www.scp.byu.edu/docs/pdf/QscatReport6.pdf>.

Long, D. G., P. J. Hardin, and P. T. Whiting (1993), Resolution enhancement of spaceborne scatterometer data. *IEEE Transactions on Geoscience and Remote Sensing*, **31(3)**, 700-715, doi:10.1109/36.225536.

Lopes, A., E. Nezry, R. Touzi, and H. Laur (1990), Maximum A Posteriori Speckle Filtering And First Order Texture Models In SAR Images, paper presented at 1990 IEEE International Geoscience and Remote Sensing Symposium, 20-24 May 1990, College Park, MD , USA.

Makynen, M. P., B. Cheng, M. H. Simila, T. Vihma, and M. T. Hallikainen (2007a), Comparisons between SAR backscattering coefficient and results of a thermodynamic snow/ice model for the Baltic Sea land-fast sea ice. *IEEE Transactions on Geoscience and Remote Sensing*, **45(5)**, 1131-1141, doi:10.1109/TGRS.2007.893735.

Makynen, M. P., B. Cheng, M. Simila, T. Vihma, and M. Hallikainen (2007b), Interpretation of C-band SAR backscattering coefficient time series for the Baltic sea landfast sea ice using a 1-D thermodynamic snow/ice model, paper presented at 2007 IEEE International Geoscience and Remote Sensing Symposium, 23-27 July 2007, Barcelona, Spain.

Marino, R., R. W. Howarth, J. Shamess, and E. Prepas (1990), Molybdenum and Sulfate as Controls on the Abundance of Nitrogen-Fixing Cyanobacteria in Saline Lakes in Alberta. *Limnology and Oceanography*, **35(2)**, 245-259, doi:10.4319/lo.1990.35.2.0245.

Markus, T., R. Massom, A. Worby, V. Lytle, N. Kurtz, and T. Maksym (2011), Freeboard, snow depth and sea-ice roughness in East Antarctica from in situ and multiple satellite data *Annals of Glaciology*, **52(57)**, 242-248, doi:10.3189/172756411795931570.

Markus, T., J. C. Stroeve, and J. Miller (2009), Recent changes in Arctic sea ice melt onset, freezeup, and melt season length. *Journal of Geophysical Research*, **114**, C12024, doi:10.1029/2009JC005436.

Massom, R., H. Eicken, C. Haas, M. Jeffries, M. Drinkwater, M. Sturm, A. Worby, X. Wu, V. Lytle, S. Ushio, K. Morris, P. Reid, S. Warren, and I. Allison (2001), Snow on Antarctic Sea ice. *Reviews of Geophysics*, **39(3)**, 413-445, doi:10.1029/2000RG000085.

Maykut, G. A., N. Untersteiner (1971), Some Results from a Time-Dependent Thermodynamic Model of Sea Ice. *Journal of Geophysical Research*, **76(6)**, 1550-1575, doi:10.1029/JC076i006p01550.

Meybeck, M. (1995), Global distribution of Lakes, in *Physics and Chemistry of Lakes*, edited by A. Lerman et al., pp. 1-35, Springer-Verlag, Berlin, Germany; New York, USA.

Mitchell, P., E. E. Prepas, 1990: Atlas of Alberta Lakes. Accessed online at <http://sunsite.ualberta.ca/Projects/Alberta-Lakes/>.

Nakamura, K., H. Wakabayashi, S. Uto, K. Naoki, F. Nishio, and S. Uratsuka (2006), Sea-ice thickness retrieval in the Sea of Okhotsk using dual-polarization SAR data. *Annals of Glaciology*, **44(1)**, 261-268, doi:10.3189/172756406781811420.

Nakamura, K., H. Wakabayashi, S. Uto, S. Ushio, and F. Nishio (2009), Observation of Sea-Ice Thickness Using ENVISAT Data From Lutzow-Holm Bay, East Antarctica. *IEEE Geoscience and Remote Sensing Letters*, **6(2)**, 277-281, doi:10.1109/LGRS.2008.2011061.

NASA Earth Observatory, 2011: Remote Sensing: Absorption Bands and Atmospheric Windows. Available online at [http://earthobservatory.nasa.gov/Features/RemoteSensing/Images/atmos\\_win.gif](http://earthobservatory.nasa.gov/Features/RemoteSensing/Images/atmos_win.gif).

Nghiem, S. V., W. -. Tsai, G. Neumann, M. Sturm, D. K. Perovich, B. Taras, and B. Elder (2000), Global snow signature in Ku-band backscatter, paper presented at 2000 IEEE International Geoscience and Remote Sensing Symposium, 24-28 July 2000, Honolulu, Hawaii.

Notz, D., M. G. McPhee, M. G. Worster, G. A. Maykut, K. H. Schlunzen, and H. Eicken (2003), Impact of underwater-ice evolution on Arctic summer sea ice. *Journal of Geophysical Research*, **108(C7)**, 3223, doi:10.1029/2001JC001173.

NRCAN, 2009: The Atlas of Canada: Hydroelectric Generation. Accessed online at <http://atlas.nrcan.gc.ca/auth/english/maps/freshwater/consumption/hydroelectric/1>.

NSIDC, 2011: Arctic Sea Ice News & Analysis: Ice extent low at start of melt season; ice age increases over last year. Accessed online at <http://nsidc.org/arcticseainews/2011/040511.html>.

Partington, K. C., J. D. Flach (2010), Dual-Polarization C-Band Radar Observations of Sea Ice in the Amundsen Gulf. *IEEE Transactions on Geoscience and Remote Sensing*, **48**(6), 2685-2691, doi:10.1109/TGRS.2009.2039577.

Perovich, D. K. (1996), The optical properties of sea ice. *US Army Cold Regions Research and Engineering Laboratory (CRREL) Report 96-1*. Hanover, NH, USA.

Perovich, D. K., J. A. Richter-Menge (1994), Surface Characteristics of Lead Ice *Journal of Geophysical Research*, **99**(C8), 16341-16350, doi:10.1029/94JC01194.

Petrich, C., H. Eicken (2010), Growth, Structure and Properties of Sea Ice, in *Sea ice*, edited by D. N. Thomas et al., pp. 23-78, Wiley-Blackwell Pub., Chichester, U.K.; Iowa, USA.

Perovich, D. K., J. Richter-Menge, K. F. Jones, B. Light, B. C. Elder, C. Polashenski, D. Laroche, T. Markus, and R. Lindsay (2011), Arctic sea-ice melt in 2008 and the role of solar heating. *Annals of Glaciology*, **52**(57), 355-359, doi:10.3189/172756411795931714.

Prairie Provinces Water Board (Canada) (1992), *The 1969 Master Agreement on Apportionment and bylaws, rules and procedures*, Prairie Provinces Water Board, Regina, Sask.

Pringle, D. J., H. Eicken, H. J. Trodahl, and L. G. E. Backstrom (2007), Thermal conductivity of landfast Antarctic and Arctic sea ice. *Journal of Geophysical Research*, **112**, C04017, doi:10.1029/2006JC003641.

Pulliainen, J., M. Hallikainen (2001), Retrieval of Regional Snow Water Equivalent from Space-Borne Passive Microwave Observations. *Remote Sensing of Environment*, **75**(1), 76-85, doi:10.1016/S0034-4257(00)00157-7.

Raney, R. K. (2006), Dual-polarized SAR and Stokes parameters. *IEEE Geoscience and Remote Sensing Letters*, **3**(3), 317-319, doi:10.1109/LGRS.2006.871746.

Richter-Menge, J. A., D. K. Perovich, B. C. Elder, K. Claffey, I. Rigor, and M. Ortmeyer (2006), Ice mass-balance buoys: a tool for measuring and attributing changes in the thickness of the Arctic sea-ice cover. *Annals of Glaciology*, **44**(1), 205-210, doi:10.3189/172756406781811727.

Rott, H., S. H. Yueh, D. W. Cline, C. Duguay, R. Essery, C. Haas, F. Heliere, M. Kern, G. Macelloni, E. Malnes, T. Nagler, J. Pulliainen, H. Rebhan, and A. Thompson (2010), Cold Regions Hydrology High-Resolution Observatory for Snow and Cold Land Processes. *Proceedings of the IEEE*, **98**(5), 752-765, doi:10.1109/JPROC.2009.2038947.

Saloranta, T. (2000), Modeling the evolution of snow, snow ice and ice in the Baltic Sea. *Tellus Series A-Dynamic Meteorology and Oceanography*, **52(1)**, 93-108, doi:10.1034/j.1600-0870.2000.520107.x.

Schott, J. R. (2009), *Fundamentals of polarimetric remote sensing*, SPIE, WA, USA.

Serreze, M. C. (2011), Climate change: Rethinking the sea-ice tipping point. *Nature*, **471(7336)**, 47-48, doi:10.1038/471047a.

Shi, J. (2008), Active Microwave Remote Sensing Systems and Applications to Snow Monitoring, in *Advances in land remote sensing: system, modelling, inversion and application*, edited by S. Liang, pp. 19-49, Springer, Dordrecht, The Netherlands.

Shi, J. C., J. Dozier (1995), Inferring snow wetness using C-Band data from SIR-C's polarimetric synthetic aperture radar. *IEEE Transactions on Geoscience and Remote Sensing*, **33(4)**, 905-914, doi:10.1109/36.406676.

Shi, J. C., J. Dozier (2000a), Estimation of snow water equivalence using SIR-C/X-SAR, part I: Inferring snow density and subsurface properties. *IEEE Transactions on Geoscience and Remote Sensing*, **38(6)**, 2465-2474, doi:10.1109/36.885195.

Shi, J. C., J. Dozier (2000b), Estimation of snow water equivalence using SIR-C/X-SAR, part II: Inferring snow depth and particle size. *IEEE Transactions on Geoscience and Remote Sensing*, **38(6)**, 2475-2488, doi:10.1109/36.885196.

Shokr, M. E., D. G. Barber (1994), Temporal evolution of physical and dielectric-properties of sea-ice and snow during the early melt season - Observations from SIMS '90 experiment. *Journal of Glaciology*, **40(134)**, 16-30.

Storvold, R., E. Malnes, Y. Larsen, and K. A. Hogda (2006), SAR Remote Sensing of Snow Parameters in Norwegian Areas - Current Status and Future Perspective. *Journal of Electromagnetic Waves and Applications*, **20(13)**, 1751-1759, doi:10.1163/156939306779292192.

Sturm, M., R. A. Massom (2010), Snow and Sea Ice, in *Sea ice*, edited by D. N. Thomas et al., pp. 153-204, Wiley-Blackwell Pub., Chichester, U.K. ; Iowa, USA.

Sturm, M., J. Holmgren, and D. Perovich (2002a), Winter snow cover on the sea ice of the Arctic Ocean at the Surface Heat Budget of the Arctic Ocean (SHEBA): Temporal evolution and spatial variability. *Journal of Geophysical Research*, **107(C10)**, 8047, doi:10.1029/2000JC000400.

Sturm, M., D. Perovich, and J. Holmgren (2002b), Thermal conductivity and heat transfer through the snow on the ice of the Beaufort Sea. *Journal of Geophysical Research*, **107(C10)**, 8043, doi:10.1029/2000JC000409.

Sturm, M., J. A. Maslanik, D. K. Perovich, J. C. Stroeve, J. Richter-Menge, T. Markus, J. Holmgren, J. F. Heinrichs, and K. Tape (2006), Snow depth and ice thickness measurements from the Beaufort and Chukchi seas collected during the AMSR-Ice03 campaign. *IEEE Geoscience and Remote Sensing Letting*, **44(11)**, 3009-3020, doi:10.1109/TGRS.2006.878236.

Swanson, H., R. Zurawell (2006), *Miquelon Lake water quality monitoring report*, Provincial Park Lakes Monitoring Program, Monitoring and Evaluation Branch, Environmental Assurance Division, Alberta Environment, Accessed online at <http://environment.gov.ab.ca/info/library/7730.pdf>

Tedesco, M., R. Kelly, J. L. Foster, and A. T. C. Chang (2004), AMSR-E/Aqua daily L3 global snow water equivalent EASE-Grids V009, Oct 2008 - May 2010. Boulder, Colorado USA: National Snow and Ice Data Center. Digital media.

Tiuri, M. E., A. H. Sihvola, E. G. Nyfors, and M. T. Hallikainen (1984), The complex dielectric constant of snow at microwave frequencies. *IEEE Journal of Oceanic Engineering*, **9(5)**, 377-382, doi:10.1109/JOE.1984.1145645.

Trampuz, C., A. Coccia, E. Imbembo, MetaSensing, and European Space Agency (2011), Technical Assistance for the Development and Deployment of an X- and Ku-band MiniSAR Airborne System: Final Report, *MS-Snowsar-D7(2.0)*, 1-103. Accessed online at [http://earth.esa.int/campaigns/DOC/SnowSAR-FinalReport\\_DataSet\\_Desc.pdf](http://earth.esa.int/campaigns/DOC/SnowSAR-FinalReport_DataSet_Desc.pdf)

Tucker III, W. B., D. K. Perovich, A. J. Gow, W. F. Weeks, and M. R. Drinkwater (1992), Physical Properties of Sea Ice Relevant to Remote Sensing, in *Microwave remote sensing of sea ice*, edited by F. D. Carsey, pp. 9-28, American Geophysical Union, Washington DC, USA.

Tynan, C. T., D. G. Ainley, and I. Stirling (2010), Sea Ice: A Critical Habitat for Polar Marine Mammals and Birds, in *Sea ice*, edited by D. N. Thomas et al., pp. 395-424, Wiley-Blackwell Pub., Chichester, U.K. : Iowa, USA.

Ulaby, F. T., W. H. Stiles, and M. A. Abdelrazik (1984), Snowcover influence on backscattering from terrain. *IEEE Transactions on Geoscience and Remote Sensing*, **GE-22(2)**, 126-133, doi:10.1109/TGRS.1984.350604.

US Geological Survey, 2011: United States Geological Survey Global Visualization Browser: Landsat Image Archive. Accessed online at <http://glovis.usgs.gov/>.

Vainio, J., P. Eriksson, N. Schmelzer, J. Holfort, and L. Lind, 2010: The ice season 2009-2010. Accessed online at [http://www.helcom.fi/BSAP\\_assessment/ifs/ifs2010/en\\_GB/iceseason/](http://www.helcom.fi/BSAP_assessment/ifs/ifs2010/en_GB/iceseason/).

- Vermeer, K. (1969a), Comparison of the helminth fauna of California gulls, *Larus californicus*, and ring-billed gulls, *Larus delawarensis*, at Beaverhill and Miquelon Lakes, Alberta. *Canadian Journal of Zoology*, **47(3)**, 267-270, doi:10.1139/z69-057.
- Vermeer, K. (1969b), Egg measurements of California and Ring-billed Gull eggs at Miquelon Lake, Alberta, in 1965. *Wilson Bulletin*, **81(1)**, 102-103.
- Vihma, T., J. Haapala (2009), Geophysics of sea ice in the Baltic Sea: A review. *Progress in Oceanography*, **80(3-4)**, 129-148, doi:10.1016/j.pocean.2009.02.002.
- Wadhams, P. (2000), *Ice in the ocean*, Gordon and Breach, Australia.
- Wang, L., C. Derksen, and R. Brown (2008), Detection of pan-Arctic terrestrial snowmelt from QuikSCAT, 2000-2005. *Remote Sensing of Environment*, **112(10)**, 3794-3805, doi:10.1016/j.rse.2008.05.017.
- Warren, S. G., I. G. Rigor, N. Untersteiner, V. F. Radionov, N. N. Bryazgin, Y. I. Aleksandrov, and R. Colony (1999), Snow depth on Arctic sea ice. *Journal of Climate*, **12(6)**, 1814-1829, doi:10.1175/1520-0442(1999)012<1814:SDOASI>2.0.CO;2.
- Yackel, J., D. Barber (2002), Validation of a Snow Water Equivalence Algorithm over landfast first-year sea ice using RADARSAT-1, paper presented at 2002 IEEE International Geoscience and Remote Sensing Symposium, 24-28 June 2002, Toronto, ON, Canada.
- Yackel, J. J., D. G. Barber (2007), Observations of snow water equivalent change on landfast first-year sea ice in winter using synthetic aperture radar data. *IEEE Transactions on Geoscience and Remote Sensing*, **45(4)**, 1005-1015, doi:10.1109/TGRS.2006.890418.
- Yackel, J. J., D. G. Barber, T. N. Papakyriakou, and C. Breneman (2007), First-year sea ice spring melt transitions in the Canadian Arctic Archipelago from time-series synthetic aperture radar data, 1992-2002. *Hydrological Processes*, **21(2)**, 253-265, doi:10.1002/hyp.6240.
- Yueh, S., R. Kwok, Shu-Hsiang Lou, and Wu-Yang Tsai (1997), Sea ice identification using dual-polarized Ku-band scatterometer data. *IEEE Transactions on Geoscience and Remote Sensing*, **35(3)**, 560-569, doi:10.1109/36.581968.
- Yueh, S., S. J. Dinardo, A. Akgiray, R. West, D. W. Cline, and K. Elder (2009), Airborne Ku-Band Polarimetric Radar Remote Sensing of Terrestrial Snow Cover. *IEEE Transactions on Geoscience and Remote Sensing*, **47(10)**, 3347-3364, doi:10.1109/TGRS.2009.2022945.

## Appendix A.Image Acquisition Information

**Appendix A 1:Envisat ASAR Strip Map Alternating Polarization Precision (SM\_APP) Mode Images Acquired for Processing and Analysis.**

Acquisition Date YYYY/MM/DD	Start Time UTC	Beam Mode	Pol	Orbit Direction	Swath	Incidence Angle	Resolution Range*Azimuth (m)
2008/11/28	05:19:26	SM_APP	VV/VH	Ascend	IS6	39-43	30 x 30
2008/12/09	17:41:41	SM_APP	VV/VH	Descend	IS6	39-43	30 x 30
2008/12/12	17:47:24	SM_APP	VV/VH	Descend	IS4	30-36	30 x 30
2008/12/13	05:10:54	SM_APP	VV/VH	Ascend	IS4	30-36	30 x 30
2008/12/31	17:50:15	SM_APP	VV/VH	Descend	IS4	30-36	30 x 30
2009/01/01	05:13:44	SM_APP	VV/VH	Ascend	IS4	30-36	30 x 30
2009/01/04	05:19:26	SM_APP	VV/VH	Ascend	IS6	39-43	30 x 30
2009/01/13	17:41:40	SM_APP	VV/VH	Descend	IS6	39-43	30 x 30
2009/01/16	17:47:22	SM_APP	VV/VH	Descend	IS4	30-36	30 x 30
2009/01/17	05:10:52	SM_APP	VV/VH	Ascend	IS4	30-36	30 x 30
2009/01/23	05:22:16	SM_APP	VV/VH	Ascend	IS6	39-43	30 x 30
2009/02/04	17:50:13	SM_APP	VV/VH	Descend	IS4	30-36	30 x 30
2009/02/05	05:13:43	SM_APP	VV/VH	Ascend	IS4	30-36	30 x 30
2009/02/27	05:22:18	SM_APP	VV/VH	Ascend	IS6	39-43	30 x 30
2009/03/11	17:50:15	SM_APP	VV/VH	Descend	IS4	30-36	30 x 30
2009/03/12	05:13:44	SM_APP	VV/VH	Ascend	IS4	30-36	30 x 30
2009/03/15	05:19:27	SM_APP	VV/VH	Ascend	IS6	39-43	30 x 30
2009/03/24	17:41:40	SM_APP	VV/VH	Descend	IS6	39-43	30 x 30
2009/03/27	17:47:22	SM_APP	VV/VH	Descend	IS4	30-36	30 x 30
2009/03/28	05:10:52	SM_APP	VV/VH	Ascend	IS4	30-36	30 x 30
2009/04/15	17:50:12	SM_APP	VV/VH	Descend	IS4	30-36	30 x 30
2009/12/29	17:41:36	SM_APP	VV/VH	Descend	IS6	39-43	30 x 30
2010/02/02	17:41:35	SM_APP	VV/VH	Descend	IS6	39-43	30 x 30
2010/02/03	05:05:06	SM_APP	VV/VH	Ascend	IS2	20-26	30 x 30
2010/02/11	17:58:40	SM_APP	VV/VH	Descend	IS2	20-26	30 x 30
2010/02/12	05:22:12	SM_APP	VV/VH	Ascend	IS6	39-43	30 x 30
2010/02/19	05:02:14	SM_APP	VV/VH	Ascend	IS2	20-26	30 x 30
2010/03/02	18:01:31	SM_APP	VV/VH	Descend	IS2	20-26	30 x 30
2010/03/09	17:41:34	SM_APP	VV/VH	Descend	IS6	39-43	30 x 30
2010/03/10	05:05:06	SM_APP	VV/VH	Ascend	IS2	20-26	30 x 30
2010/03/18	17:58:41	SM_APP	VV/VH	Descend	IS2	20-26	30 x 30
2010/03/19	05:22:13	SM_APP	VV/VH	Ascend	IS6	39-43	30 x 30
2010/04/22	17:58:39	SM_APP	VV/VH	Descend	IS2	20-26	30 x 30
2010/04/23	05:22:10	SM_APP	VV/VH	Ascend	IS6	39-43	30 x 30
2010/04/30	05:02:13	SM_APP	VV/VH	Ascend	IS2	20-26	30 x 30

**Appendix A 2: TerraSAR-X Multilooked Ground Range Detected Radiometrically Enhanced StripMap Dual Polarization Images (MGD\_RE\_SM\_D) Images Acquired for Processing and Analysis**

Acquisition Date YYYY/MM/DD	Start Time UTC	Beam Mode	Polarization	Orbit Direction	Swath	Incidence Angle deg	Resolution Range*Azimuth (m)
2008/12/03	13:53:46	MGD_RE_SM_D	VV/VH	Descend	SN_08	31.9-33.5	8.66 x 8.59
2008/12/09	13:45:12	MGD_RE_SM_D	VV/VH	Descend	SF_13	42.7-43.8	7.63 x 7.59
2008/12/14	13:53:46	MGD_RE_SM_D	VV/VH	Descend	SN_08	31.9-33.5	8.57 x 8.57
2008/12/20	13:45:11	MGD_RE_SM_D	VV/VH	Descend	SF_13	42.7-43.8	7.56 x 7.54
2008/12/25	13:53:45	MGD_RE_SM_D	VV/VH	Descend	SN_08	31.9-33.5	8.57 x 8.57
2009/01/05	13:53:45	MGD_RE_SM_D	VV/VH	Descend	SN_08	31.9-33.5	8.57 x 8.57
2009/01/11	13:45:09	MGD_RE_SM_D	VV/VH	Descend	SF_13	42.7-43.8	7.56 x 7.54
2009/01/16	13:53:42	MGD_RE_SM_D	VV/VH	Descend	SN_08	31.9-33.5	8.57 x 8.57
2009/01/27	13:53:42	MGD_RE_SM_D	VV/VH	Descend	SN_08	31.9-33.5	8.57 x 8.57
2009/02/02	13:45:08	MGD_RE_SM_D	VV/VH	Descend	SF_13	42.7-43.8	7.56 x 7.54
2009/02/07	13:53:42	MGD_RE_SM_D	VV/VH	Descend	SN_08	31.9-33.5	8.57 x 8.57
2009/02/13	13:45:08	MGD_RE_SM_D	VV/VH	Descend	SF_13	42.7-43.8	7.56 x 7.54
2009/02/18	13:53:42	MGD_RE_SM_D	VV/VH	Descend	SN_08	31.9-33.5	8.57 x 8.57
2009/02/24	13:45:09	MGD_RE_SM_D	VV/VH	Descend	SF_13	42.7-43.8	7.56 x 7.54
2009/03/01	13:53:42	MGD_RE_SM_D	VV/VH	Descend	SN_08	31.9-33.5	8.57 x 8.57
2009/03/07	13:45:09	MGD_RE_SM_D	VV/VH	Descend	SF_13	42.7-43.8	7.56 x 7.54
2009/03/12	13:53:43	MGD_RE_SM_D	VV/VH	Descend	SN_08	31.9-33.5	8.57 x 8.57
2009/03/18	13:45:09	MGD_RE_SM_D	VV/VH	Descend	SF_13	42.7-43.8	7.56 x 7.54
2009/03/23	13:53:44	MGD_RE_SM_D	VV/VH	Descend	SN_08	31.9-33.5	8.57 x 8.57
2009/03/29	13:45:10	MGD_RE_SM_D	VV/VH	Descend	SF_13	42.7-43.8	7.56 x 7.54
2009/04/03	13:53:44	MGD_RE_SM_D	VV/VH	Descend	SN_08	31.9-33.5	8.57 x 8.57
2009/04/09	13:45:10	MGD_RE_SM_D	VV/VH	Descend	SF_13	42.7-43.8	7.56 x 7.54
2009/04/14	13:53:44	MGD_RE_SM_D	VV/VH	Descend	SN_08	31.9-33.5	8.57 x 8.57
2009/04/20	13:45:10	MGD_RE_SM_D	VV/VH	Descend	SF_13	42.7-43.8	7.56 x 7.54

**Appendix A 3: TerraSAR-X Single Look Complex Spotlight Model Dual Polarization (SSC\_SL\_D)  
Images Acquired for Processing and Analysis.**

Acquisition Date YYYY/MM/DD	Start Time UTC	Beam Mode	Polarization	Orbit Direction	Swath	Incidence Angle (deg)	Resolution Range*Azimuth (m)
2009/01/09	01:21:19	SSC_SL_D	HH/VV	Ascend	Spot_071	46.5-47.2	1.6 x 3.2
2009/01/20	01:21:18	SSC_SL_D	HH/VV	Ascend	Spot_071	46.5-47.2	1.6 x 3.2
2009/01/31	01:21:18	SSC_SL_D	HH/VV	Ascend	Spot_071	46.5-47.2	1.6 x 3.2
2009/02/11	01:21:17	SSC_SL_D	HH/VV	Ascend	Spot_071	46.5-47.2	1.6 x 3.2
2009/02/22	01:21:18	SSC_SL_D	HH/VV	Ascend	Spot_071	46.5-47.2	1.6 x 3.2
2009/03/05	01:21:18	SSC_SL_D	HH/VV	Ascend	Spot_071	46.5-47.2	1.6 x 3.2
2009/03/16	01:21:19	SSC_SL_D	HH/VV	Ascend	Spot_071	46.5-47.2	1.6 x 3.2
2009/03/27	01:21:19	SSC_SL_D	HH/VV	Ascend	Spot_071	46.5-47.2	1.6 x 3.2
2009/04/07	01:21:20	SSC_SL_D	HH/VV	Ascend	Spot_071	46.5-47.2	1.6 x 3.2
2009/04/18	01:21:20	SSC_SL_D	HH/VV	Ascend	Spot_071	46.5-47.2	1.6 x 3.2
2009/04/29	01:21:20	SSC_SL_D	HH/VV	Ascend	Spot_071	46.5-47.2	1.6 x 3.2

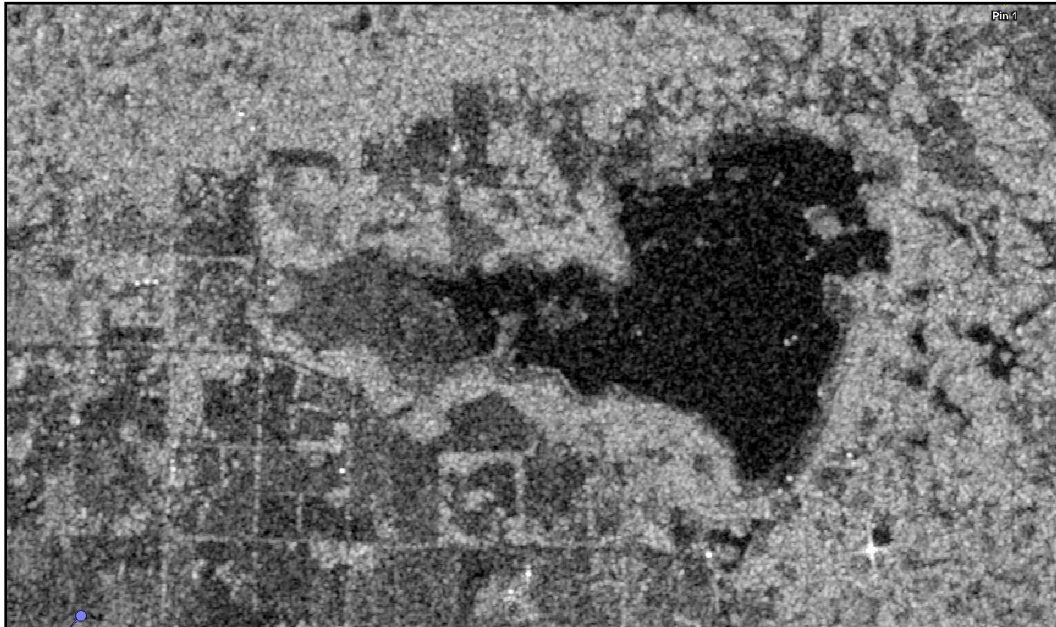
**Appendix A 4: TerraSAR-X Single Look Complex StripMap Mode Dual Polarization (SSC\_SM\_D)  
Images Acquired for Processing and Analysis**

Acquisition Date YYYY/MM/DD	Start Time UTC	Beam Mode	Polarization	Orbit Direction	Swath	Incidence Angle (deg)	Resolution Range*Azimuth (m)
2008/12/03	13:53:45	SSC_SM_D	VV/VH	Descend	SN_08	31.9-33.5	2.18 x 6.60
2009/12/23	13:53:50	SSC_SM_D	HH/HV	Descend	SN_08	31.9-33.5	2.18 x 6.60
2009/12/29	13:45:16	SSC_SM_D	HH/HV	Descend	SF_13	42.7-43.8	1.72 x 6.60
2010/01/03	13:53:49	SSC_SM_D	HH/HV	Descend	SN_08	31.9-33.5	2.18 x 6.60
2010/01/09	13:45:15	SSC_SM_D	HH/HV	Descend	SF_13	42.7-43.8	1.72 x 6.60
2010/01/14	13:53:49	SSC_SM_D	HH/HV	Descend	SN_08	31.9-33.5	2.18 x 6.60
2010/01/20	13:45:15	SSC_SM_D	HH/HV	Descend	SF_13	42.7-43.8	1.72 x 6.60
2010/01/31	13:45:14	SSC_SM_D	HH/HV	Descend	SF_13	42.7-43.8	1.72 x 6.60
2010/02/05	13:53:48	SSC_SM_D	HH/HV	Descend	SN_08	31.9-33.5	2.18 x 6.60
2010/02/11	13:45:14	SSC_SM_D	HH/HV	Descend	SF_13	42.7-43.8	1.72 x 6.60
2010/02/16	13:53:48	SSC_SM_D	HH/HV	Descend	SN_08	31.9-33.5	2.18 x 6.60
2010/02/22	13:45:14	SSC_SM_D	HH/HV	Descend	SF_13	42.7-43.8	1.72 x 6.60
2010/02/27	13:53:49	SSC_SM_D	HH/HV	Descend	SN_08	31.9-33.5	2.18 x 6.60
2010/03/05	13:45:15	SSC_SM_D	HH/HV	Descend	SF_13	42.7-43.8	1.72 x 6.60
2010/03/10	13:53:49	SSC_SM_D	HH/HV	Descend	SN_08	31.9-33.5	2.18 x 6.60
2010/03/16	13:45:16	SSC_SM_D	HH/HV	Descend	SF_13	42.7-43.8	1.72 x 6.60
2010/03/21	13:53:50	SSC_SM_D	HH/HV	Descend	SN_08	31.9-33.5	2.18 x 6.60
2010/03/27	13:45:17	SSC_SM_D	HH/HV	Descend	SF_13	42.7-43.8	1.72 x 6.60

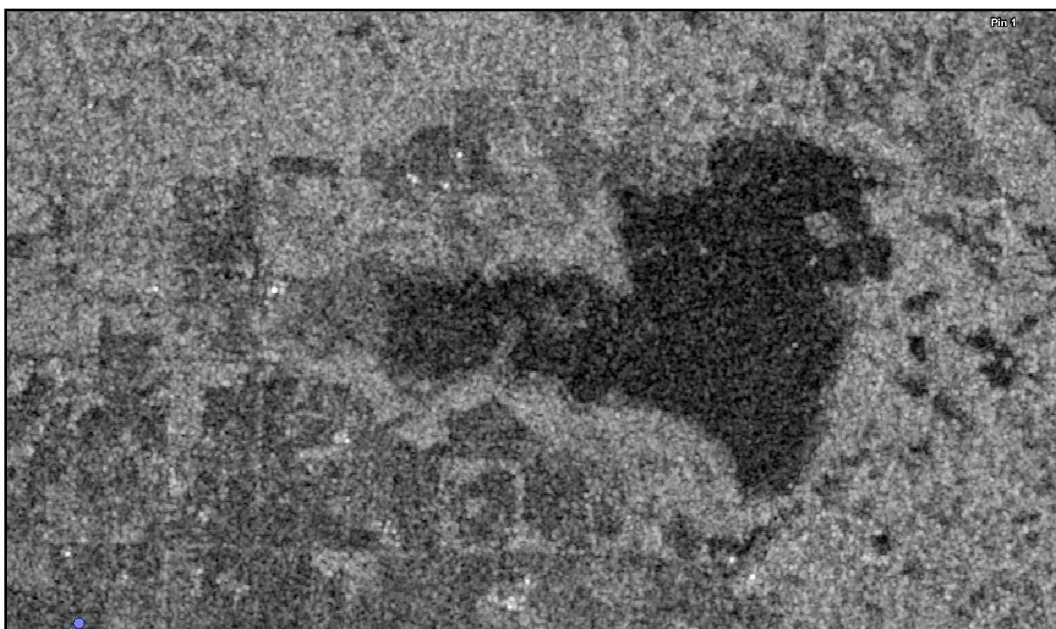
## Appendix B. Synthetic Aperture Radar Images

### Appendix B.1 Envisat ASAR APP VV Images 2008/09

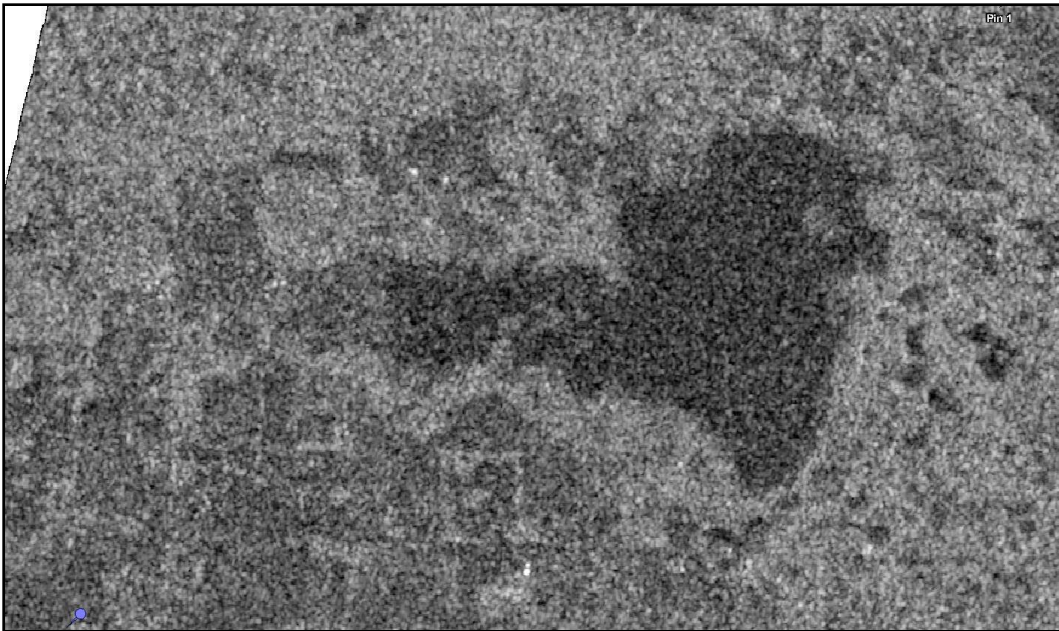
This appendix presents the Envisat ASAR Alternating Polarization Precision Mode images acquired over Miquelon Lake in 2008/09. The images presented are the VV polarization channel and are all presented with the same grayscale (-24dB and 0 dB).



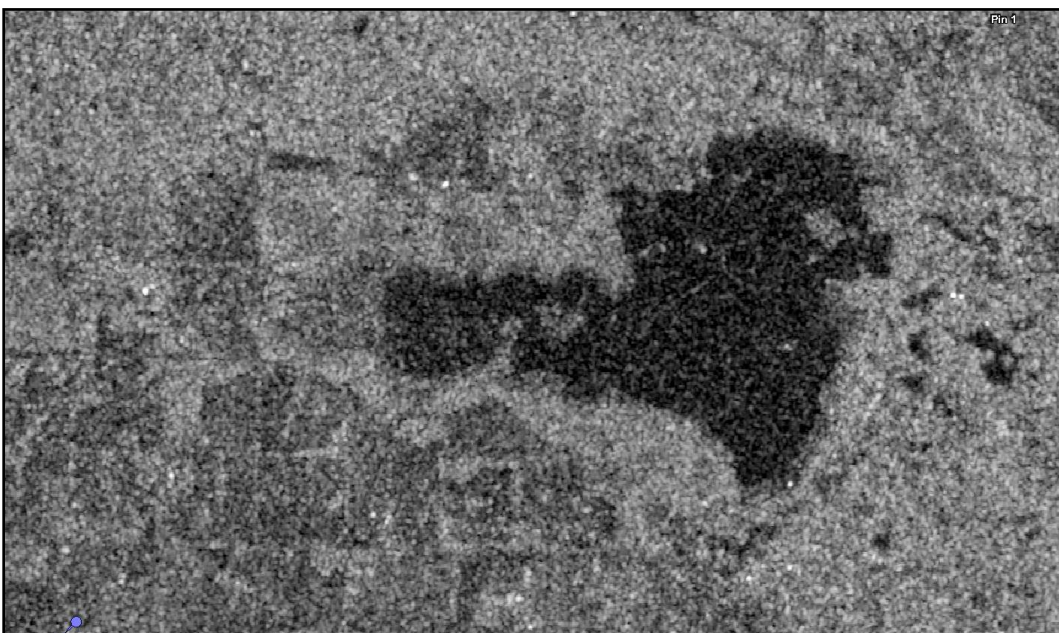
November 30, 2008. ©ESA, 2008



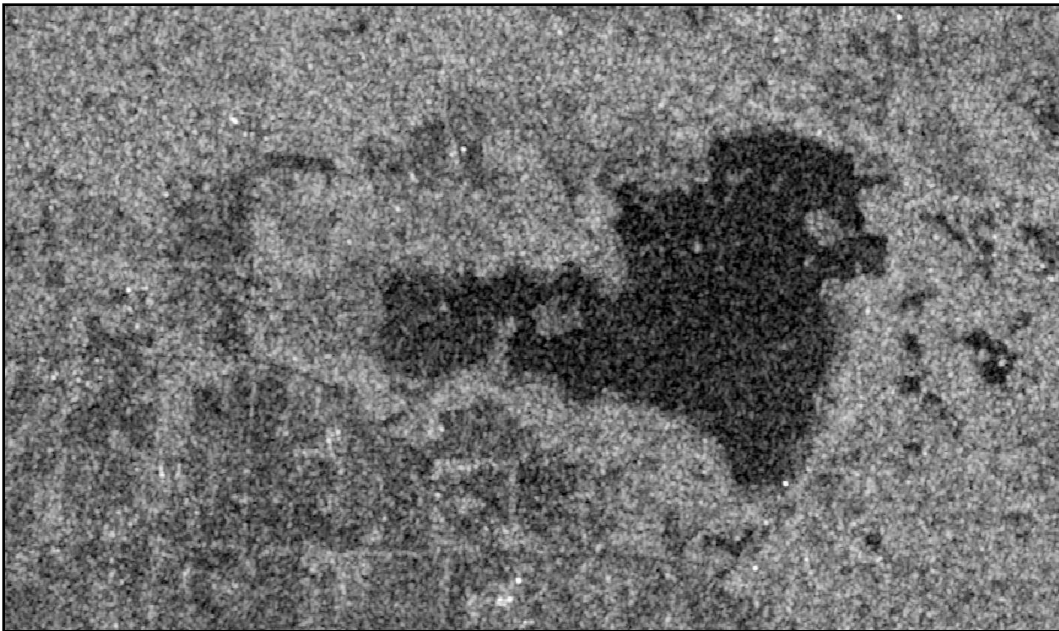
December 09, 2008. ©ESA, 2008



December 12, 2008. ©ESA, 2008



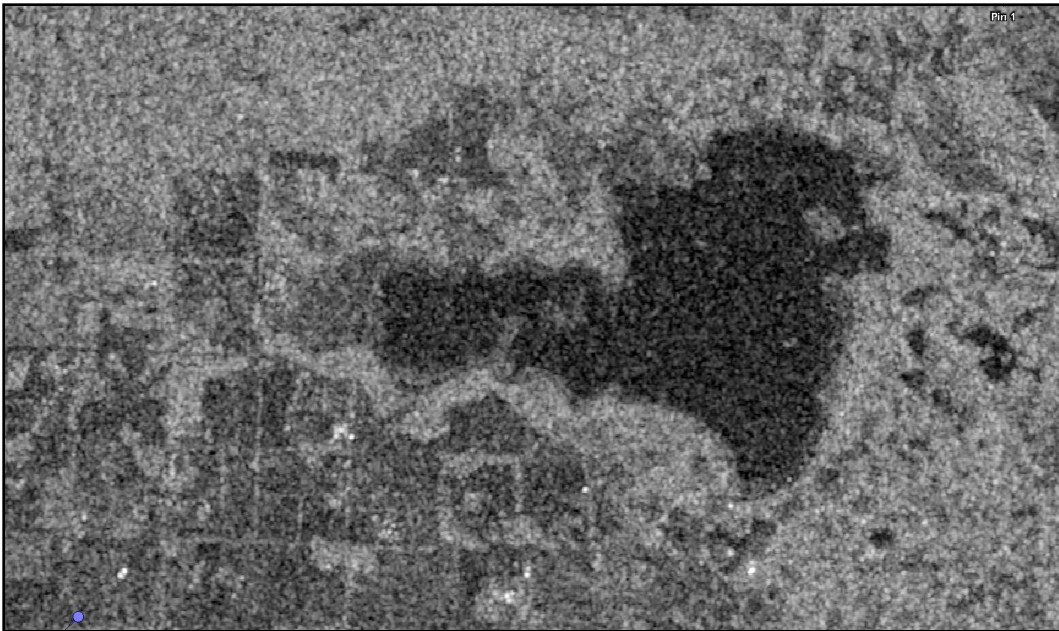
December 31, 2008. ©ESA, 2008



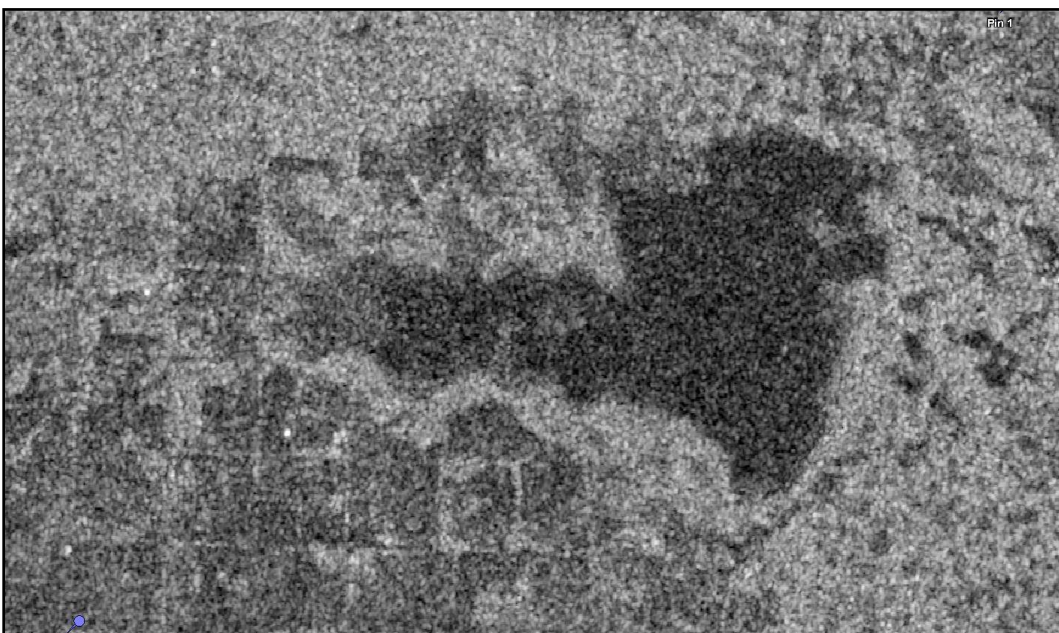
January 01, 2009. ©ESA, 2009



January 04, 2009. ©ESA, 2009



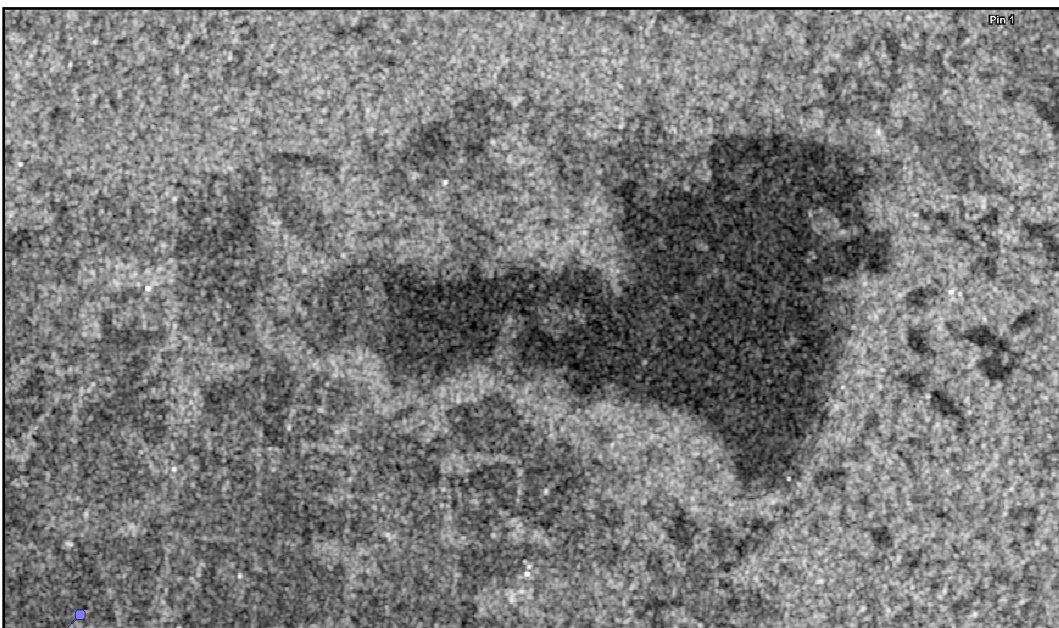
January 13, 2009. ©ESA, 2009



January 16, 2009. ©ESA, 2009



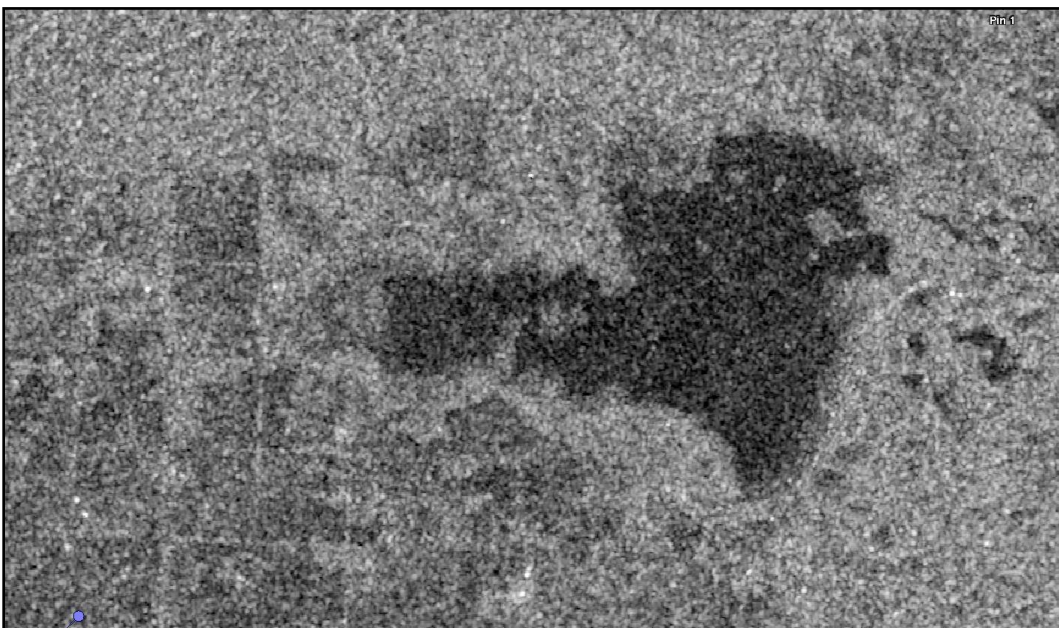
January 23, 2009. ©ESA, 2009



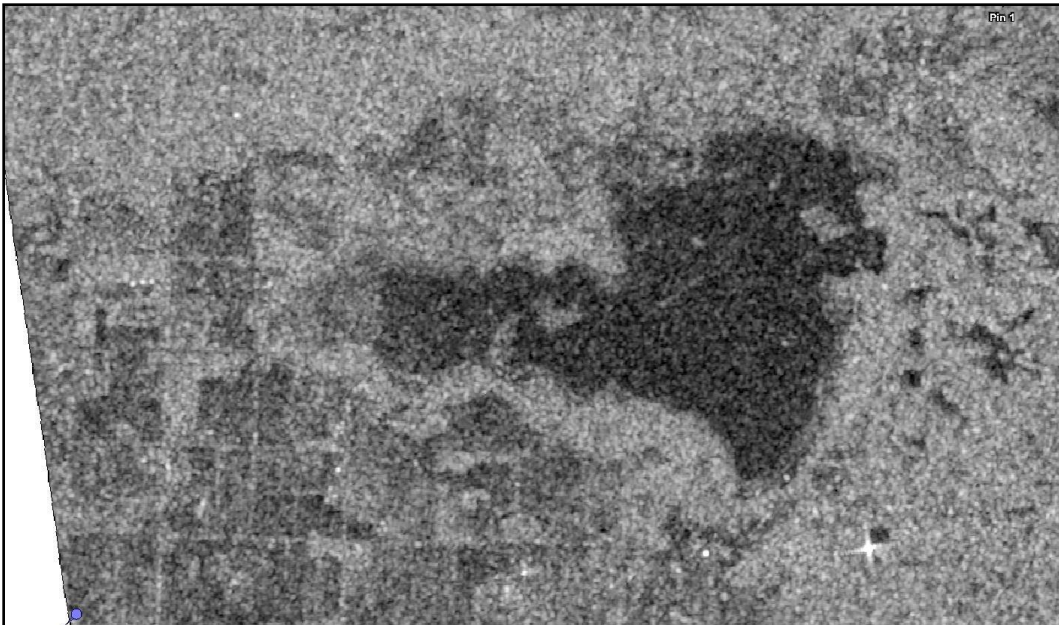
February 04, 2009. ©ESA, 2009



February 27, 2009. ©ESA, 2009



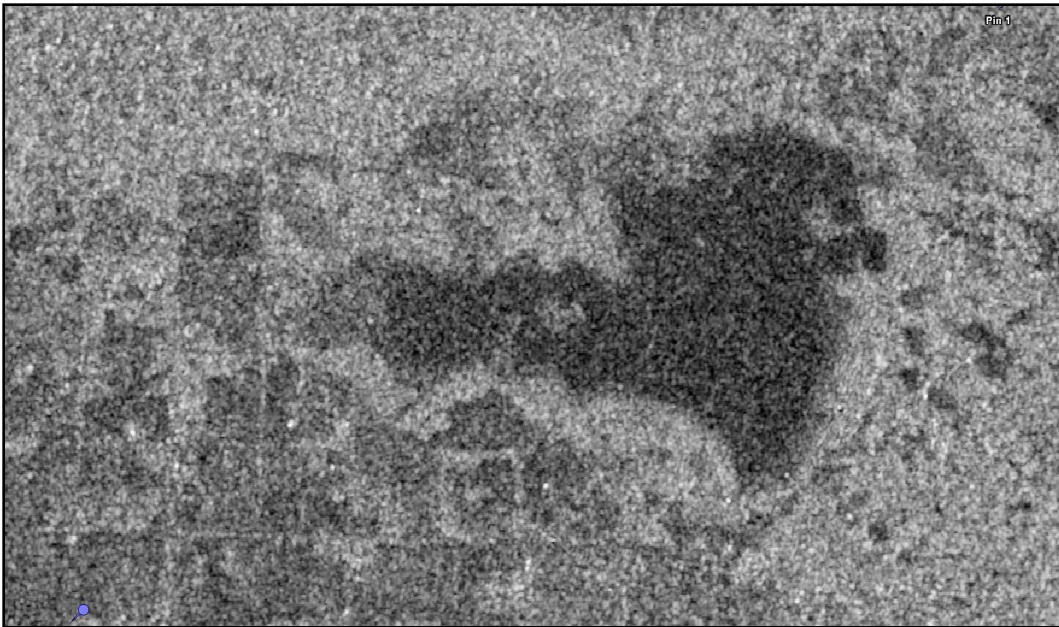
March 11, 2009. ©ESA, 2009



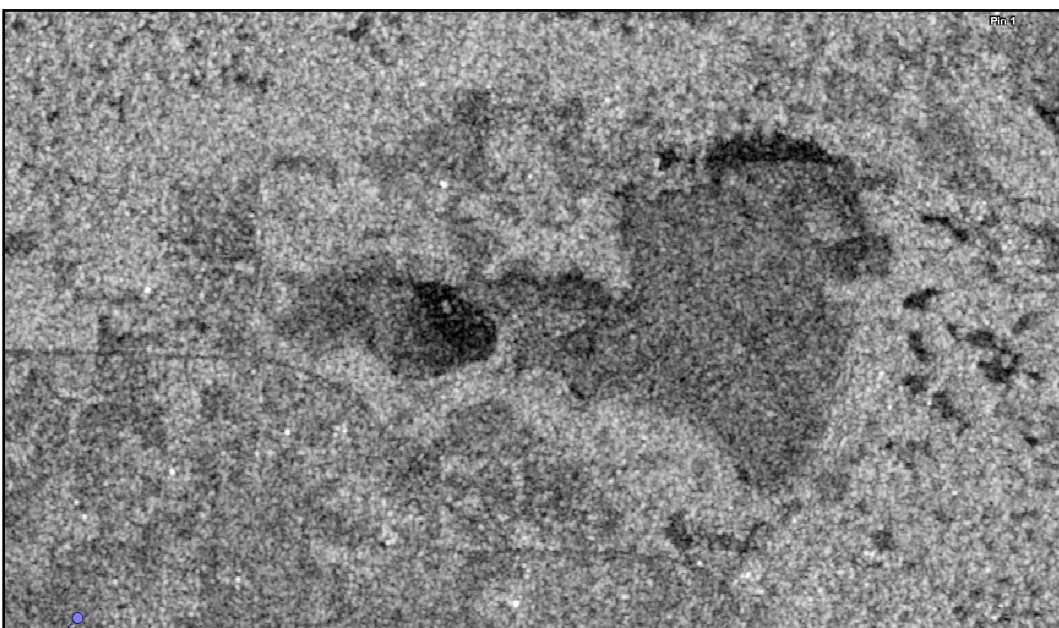
March 15, 2009. ©ESA, 2009



March 24, 2009. ©ESA, 2009



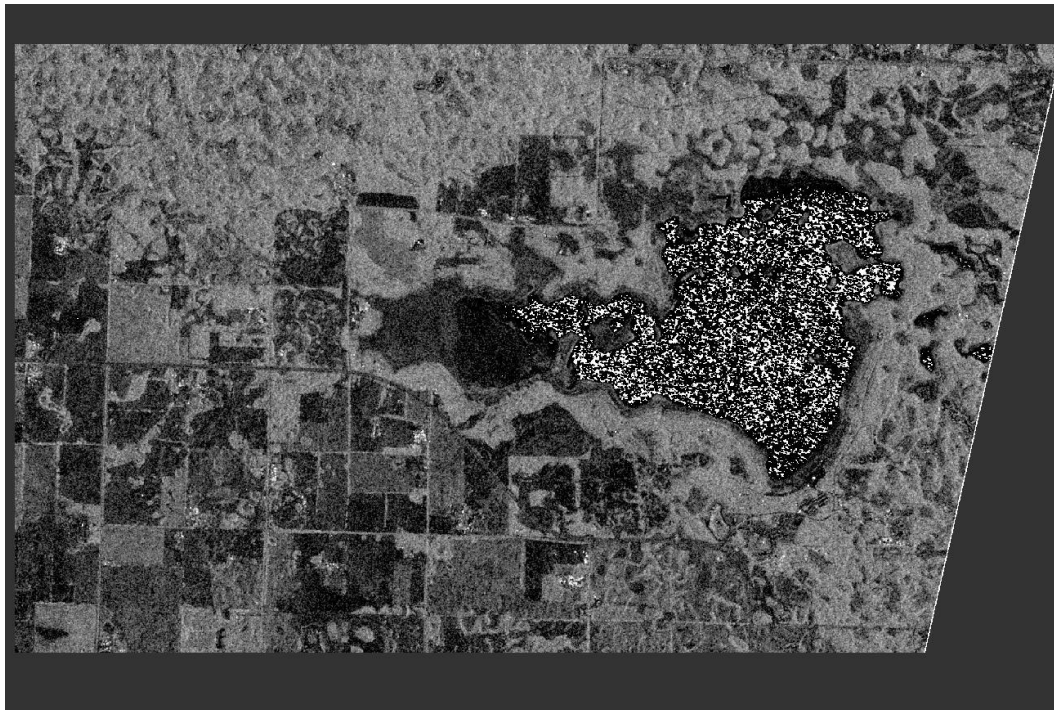
March 27, 2009. ©ESA, 2009



April 15, 2009. ©ESA, 2009

## Appendix B.2      **TerraSAR-X MGD RE VV Images 2008/09**

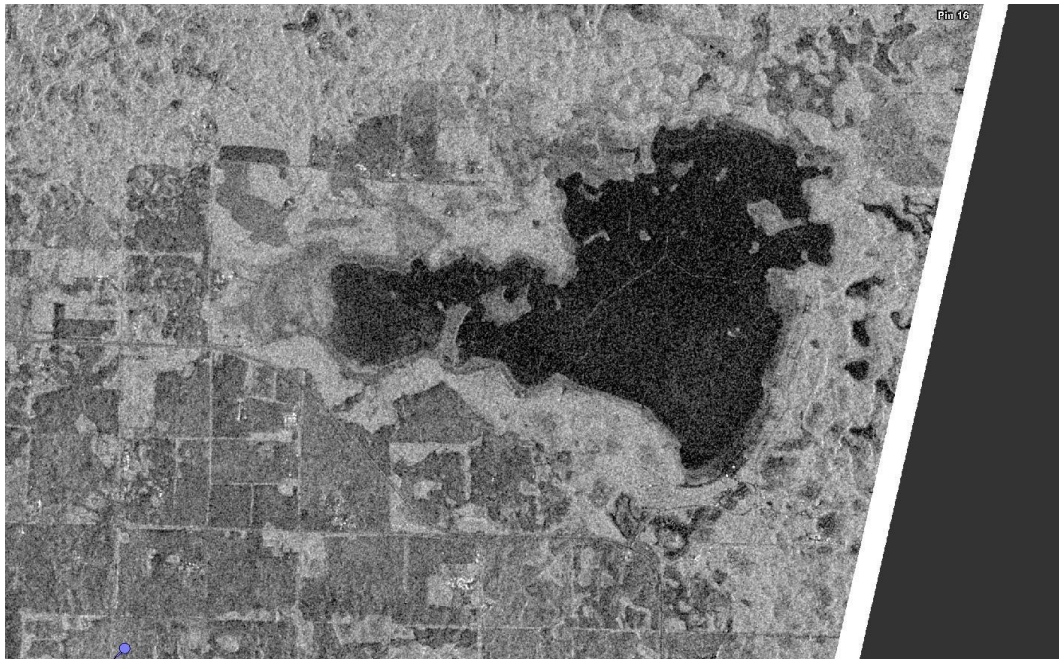
This appendix presents the TerraSAR-X Multi-looked Ground Range Detected Radiometrically Enhanced images acquired over Miquelon Lake in 2008/09. The images presented are the VV polarization channel and are all presented with the same grayscale (-24dB and 0 dB).



December 03, 2008. ©DLR 2008



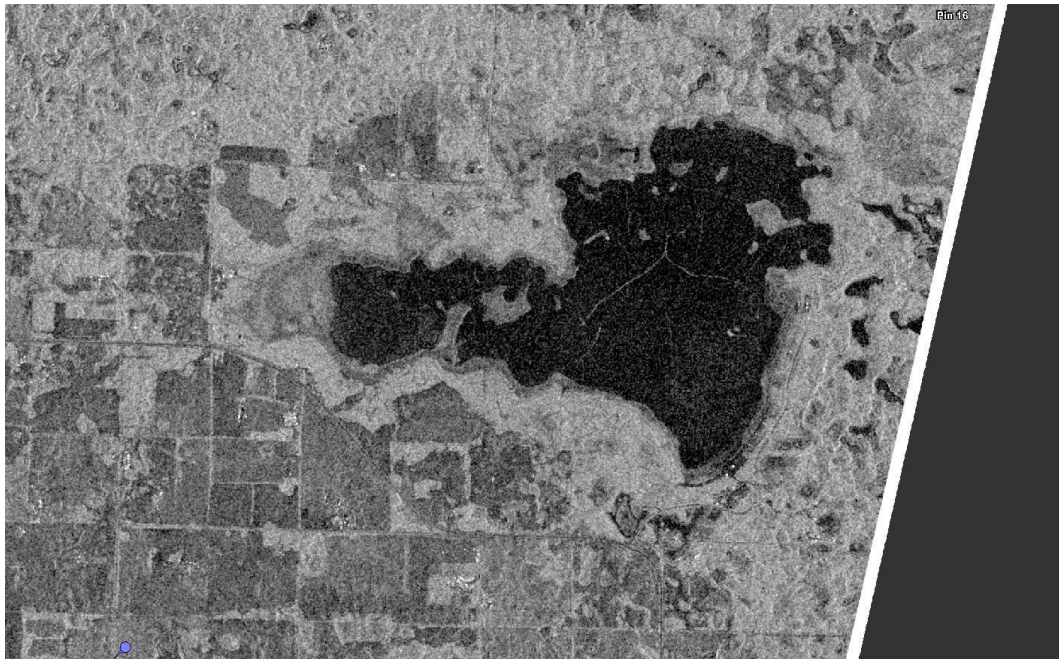
December 09, 2008. ©DLR 2008



December 14, 2008. ©DLR 2008



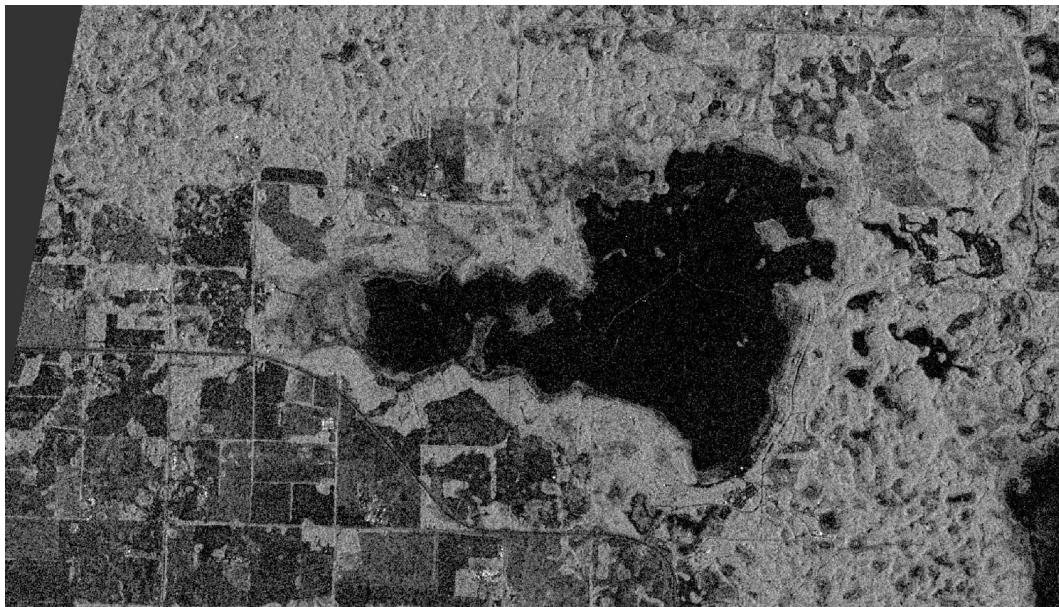
December 20, 2008. ©DLR 2008



December 25, 2008. ©DLR 2008



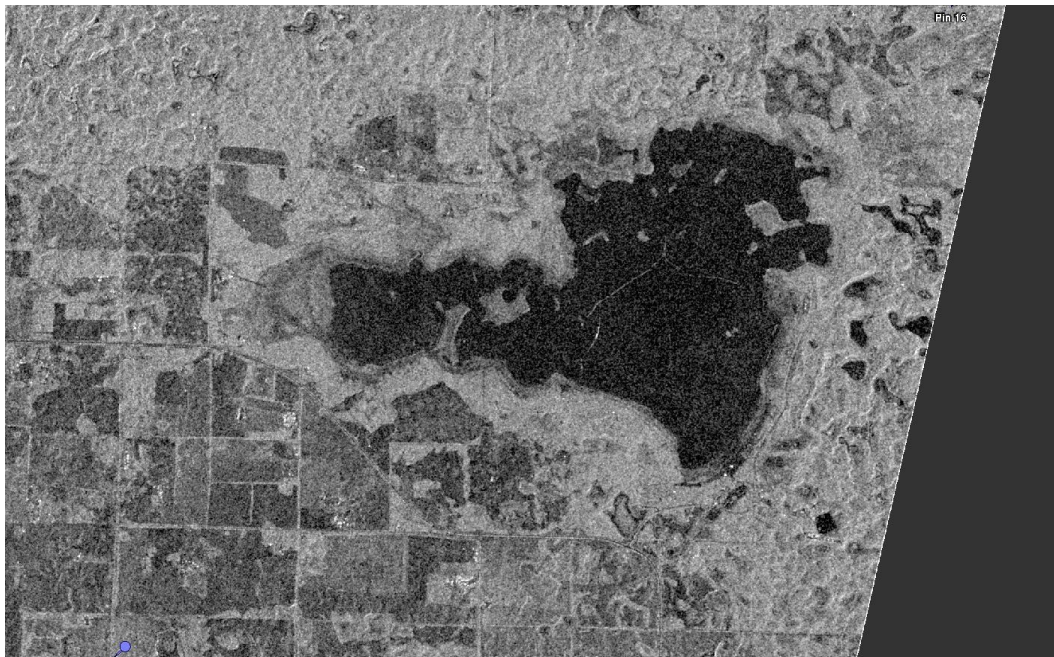
January 05, 2009. ©DLR 2009



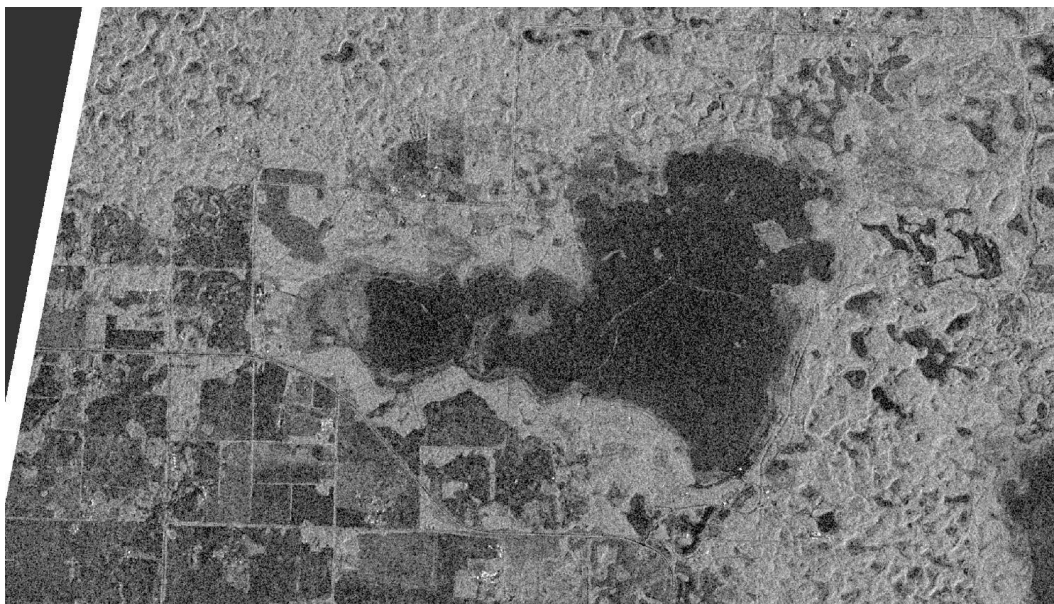
**January 11, 2009.©DLR 2009**



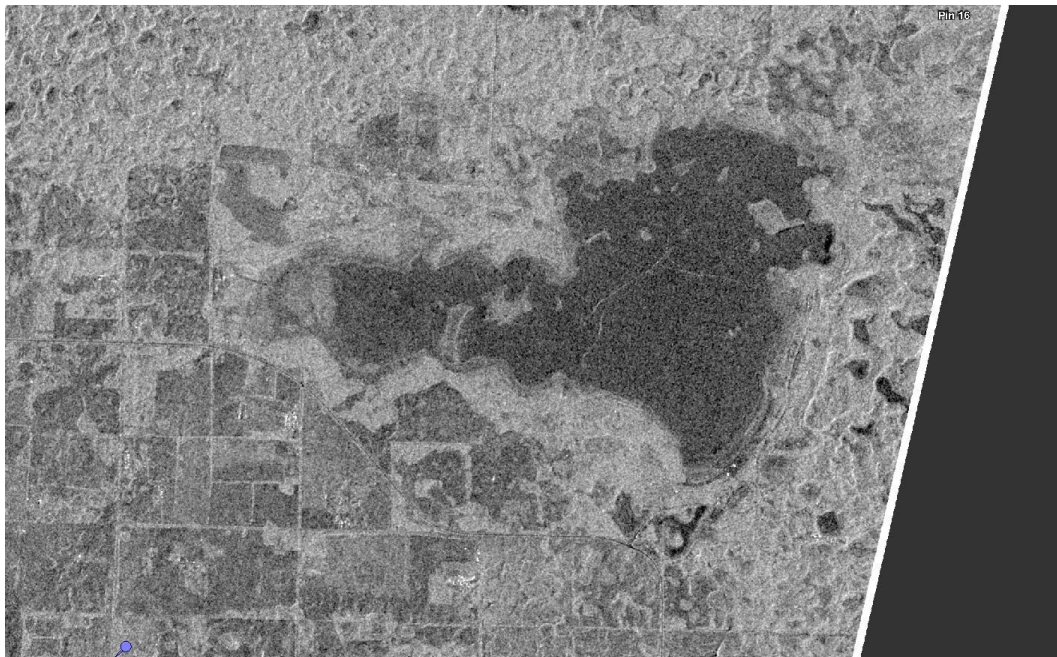
**January 16, 2009.©DLR 2009**



**January 27, 2009.©DLR 2009**



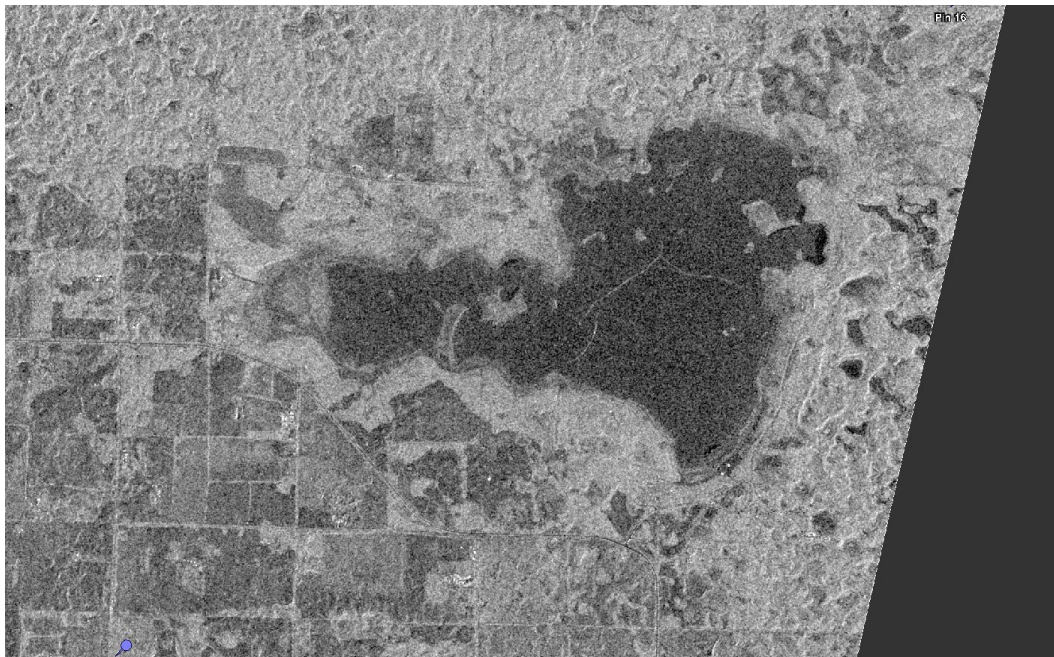
**February 02, 2009.©DLR 2009**



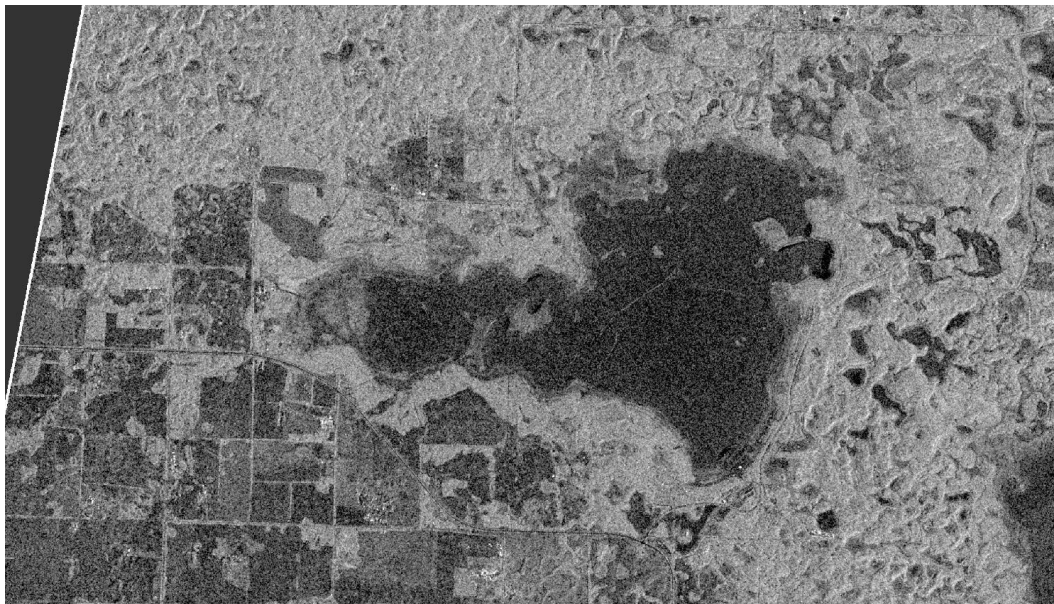
February 07, 2009. ©DLR 2009



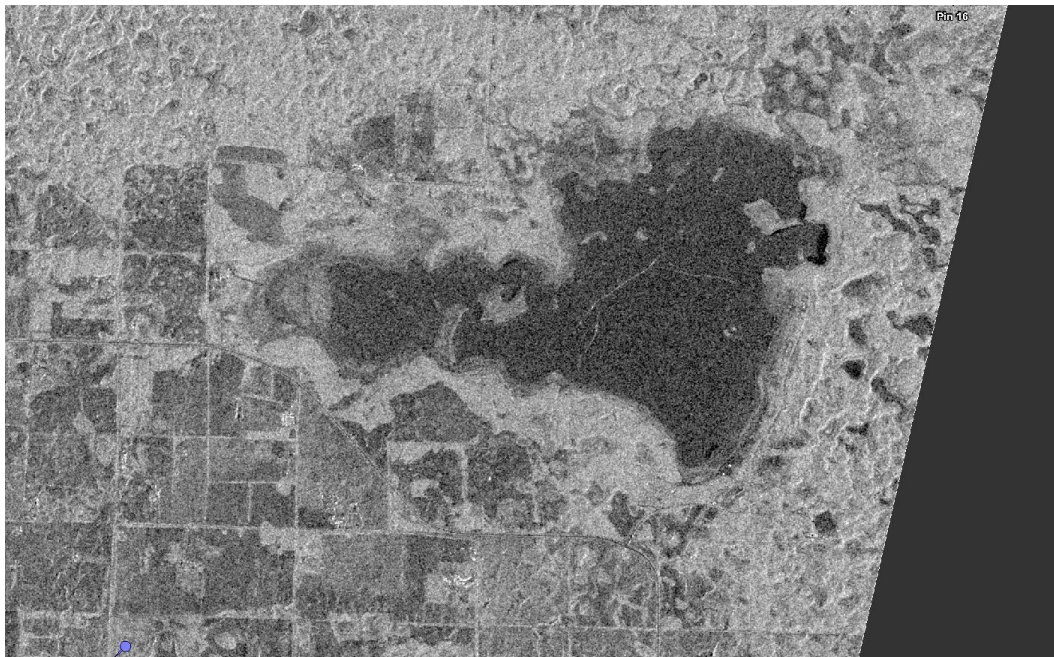
February 13, 2009. ©DLR 2009



February 18, 2009. ©DLR 2009



February 24, 2009. ©DLR 2009



March 01, 2009. ©DLR 2009



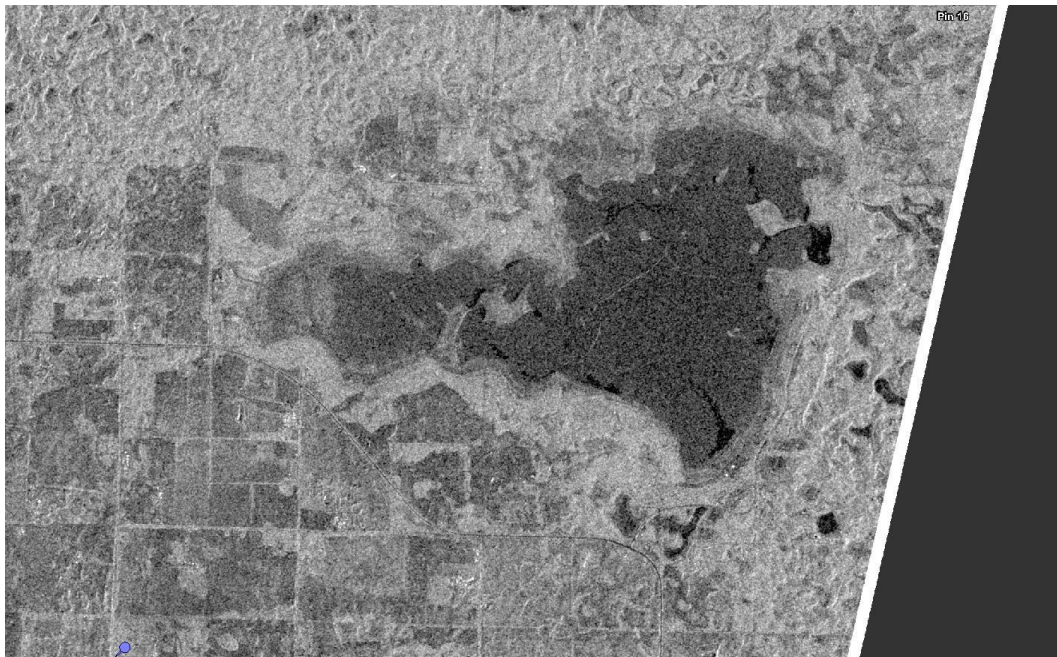
March 07, 2009. ©DLR 2009



March 12, 2009. ©DLR 2009



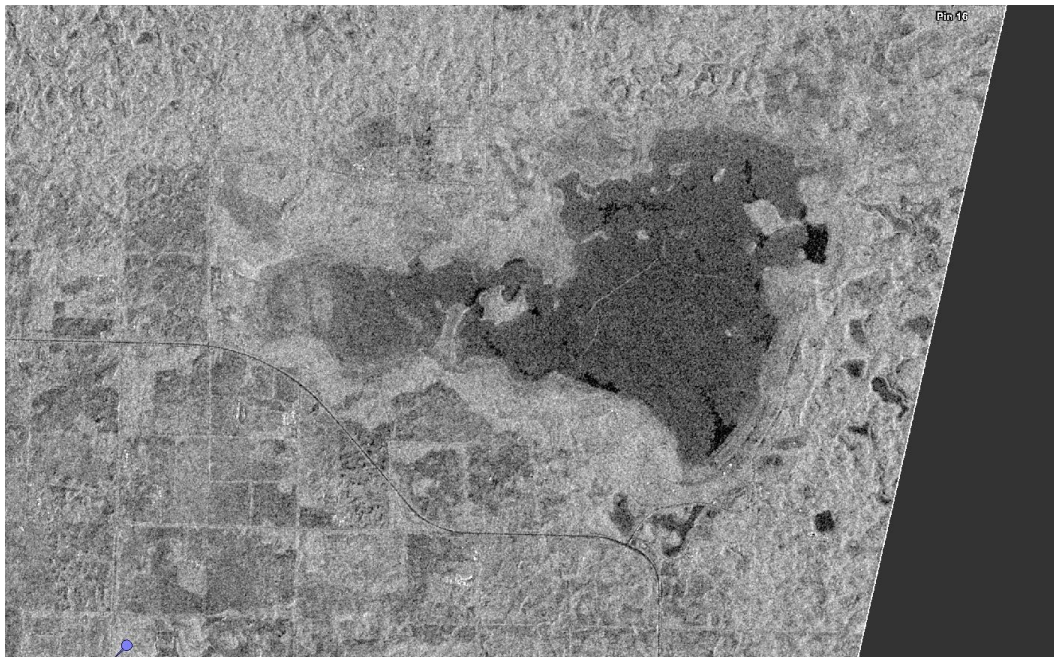
March 18, 2009. ©DLR 2009



March 23, 2009. ©DLR 2009



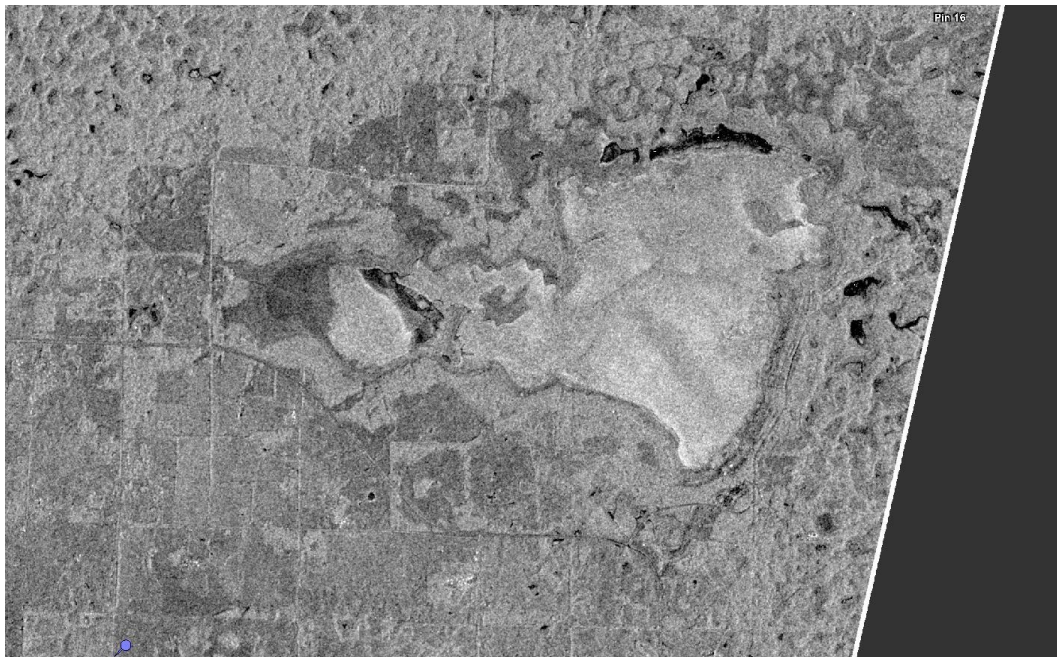
March 29, 2009. ©DLR 2009



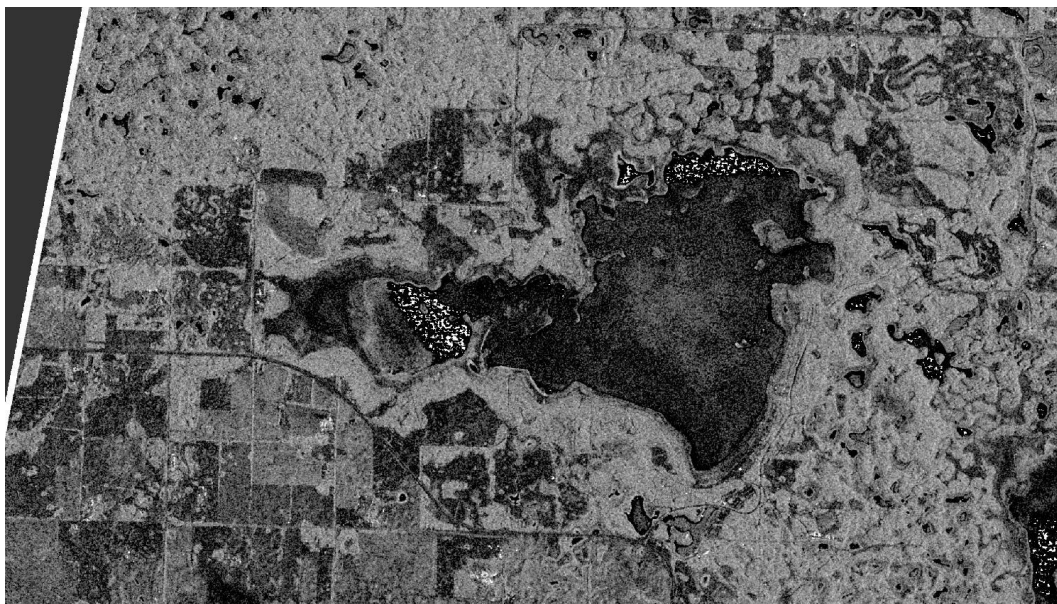
April 03, 2009. ©DLR 2009



April 09, 2009. ©DLR 2009



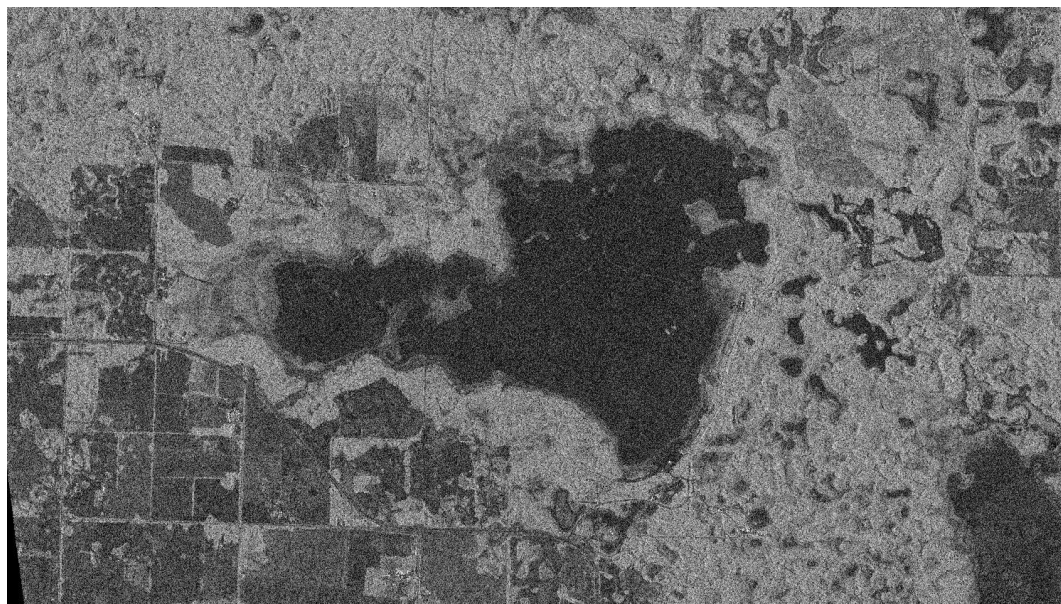
April 14, 2009. ©DLR 2009



April 20, 2009. ©DLR 2009

### Appendix B.3      TerraSAR-X SLC VV Images 2008/09

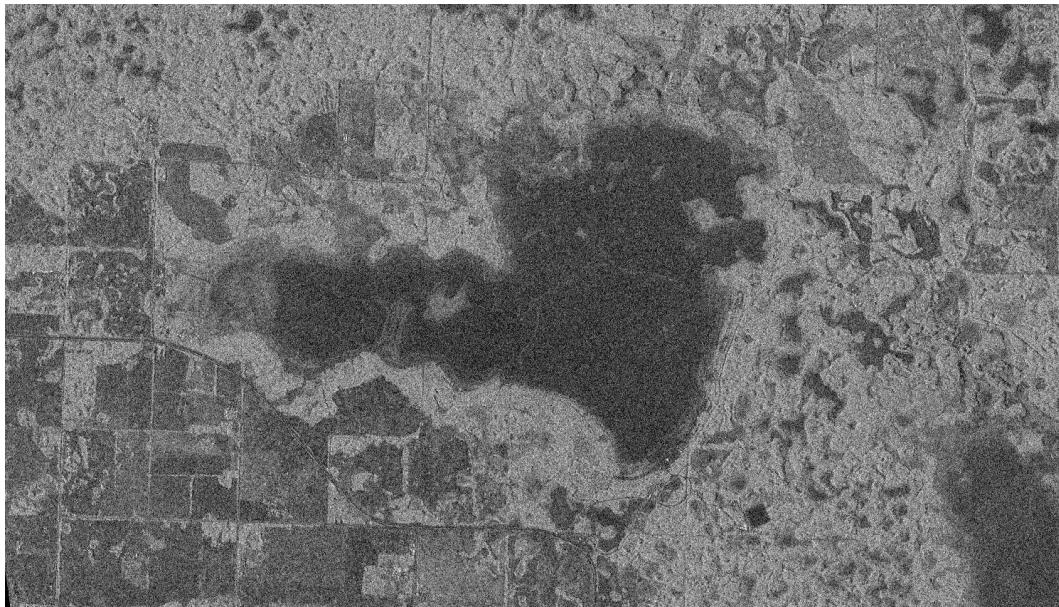
This appendix presents the TerraSAR-X Spotlight Mode Single Look Complex images acquired over Miquelon Lake in 2008/09. The images presented are the VV polarization channel and are all presented with the same grayscale (-24dB and 0 dB).



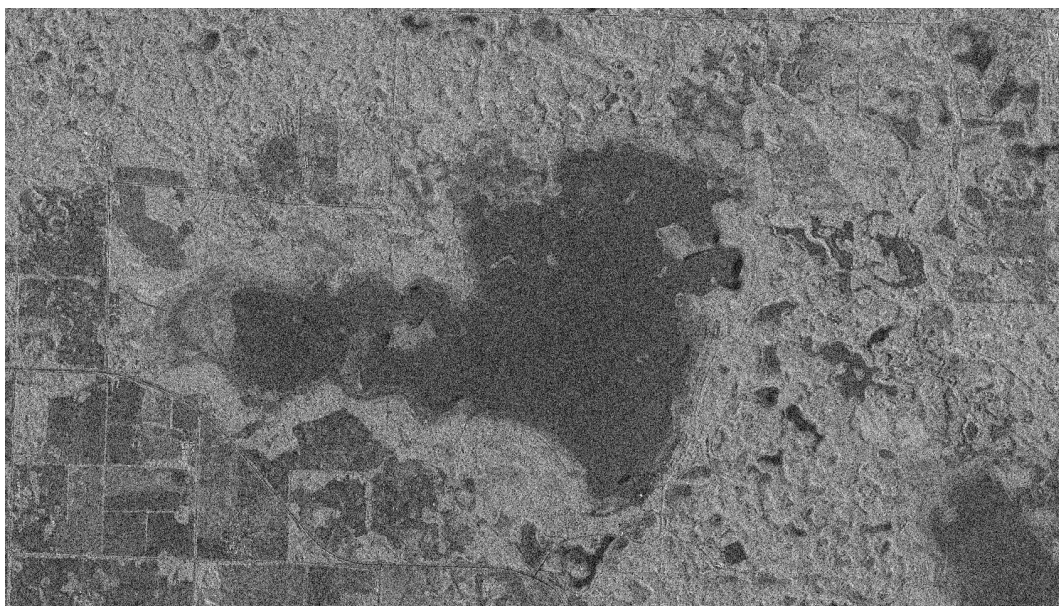
January 09, 2009. ©DLR 2009



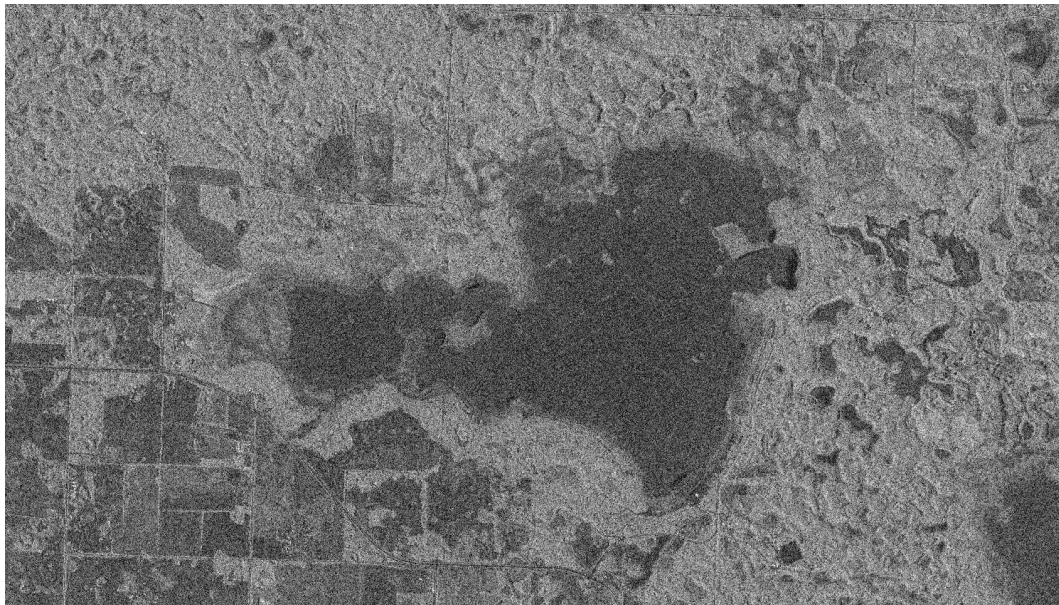
January 20, 2009. ©DLR 2009



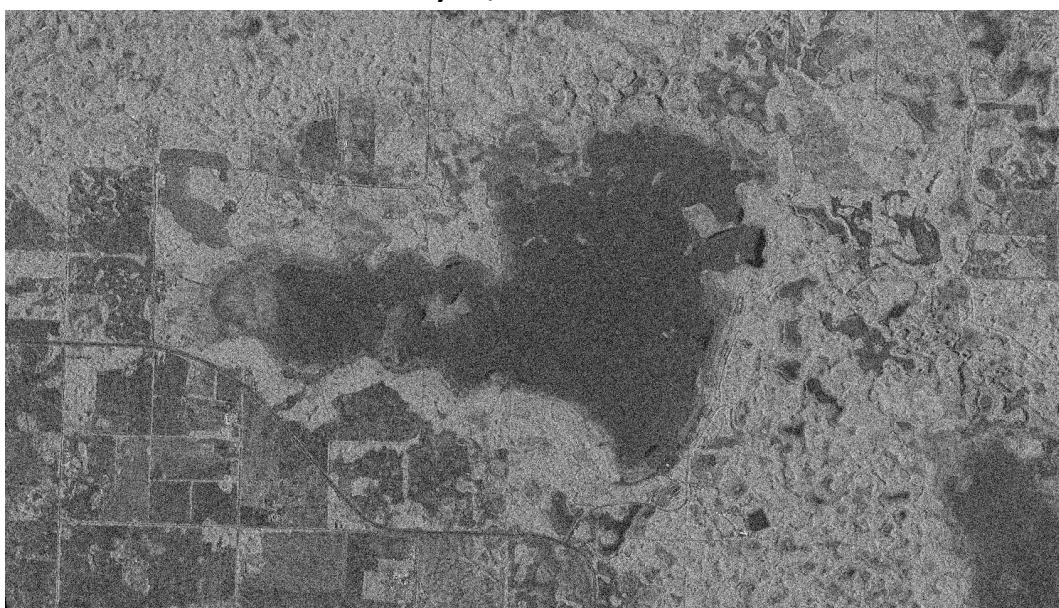
**January 31, 2009.©DLR 2009**



**February 11, 2009.©DLR 2009**



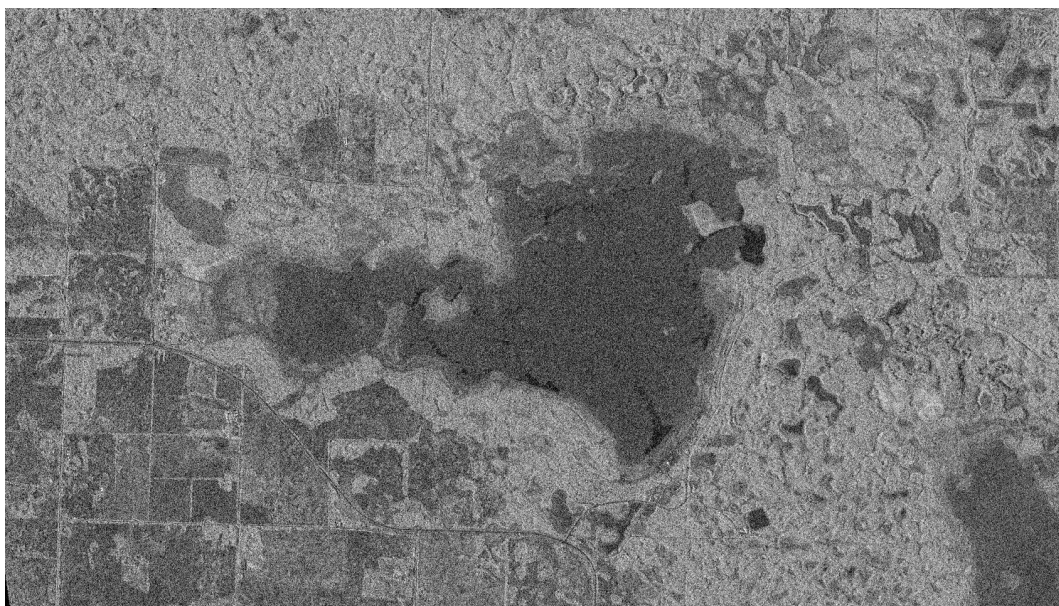
**February 22, 2009.©DLR 2009**



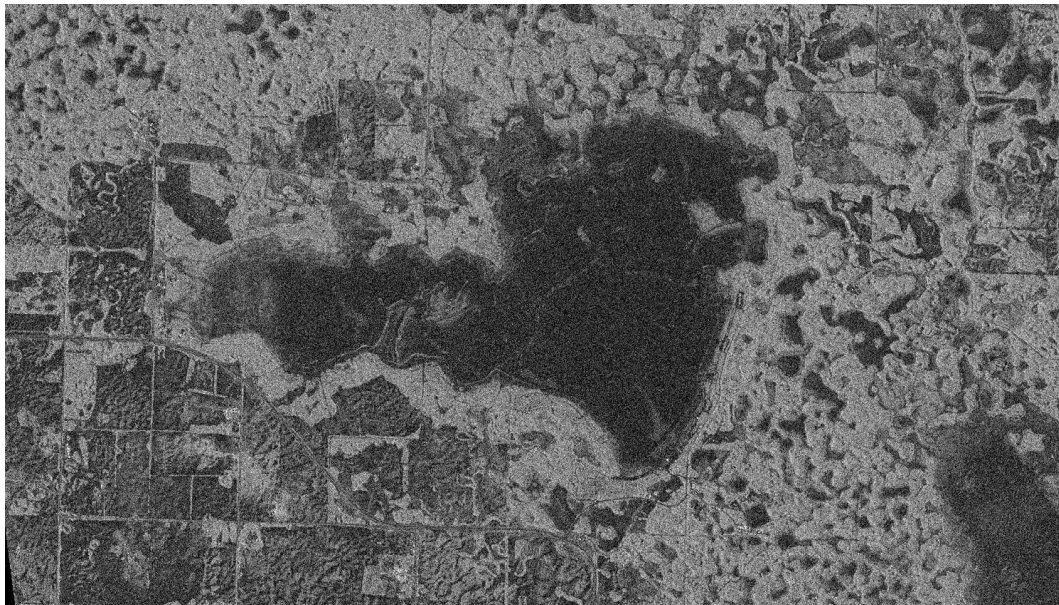
**March 05, 2009.©DLR 2009**



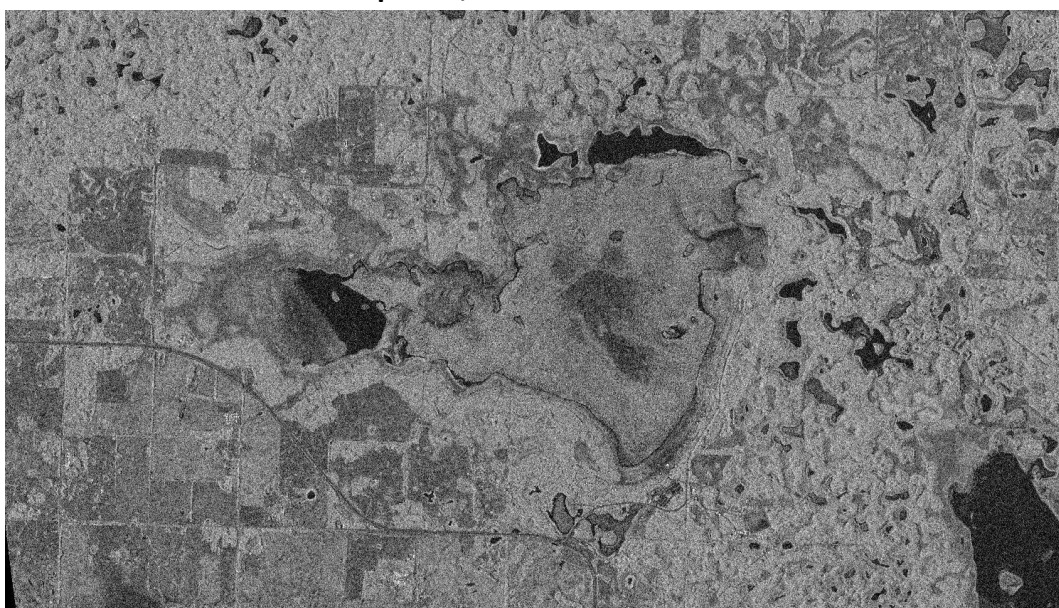
**March 16, 2009.©DLR 2009**



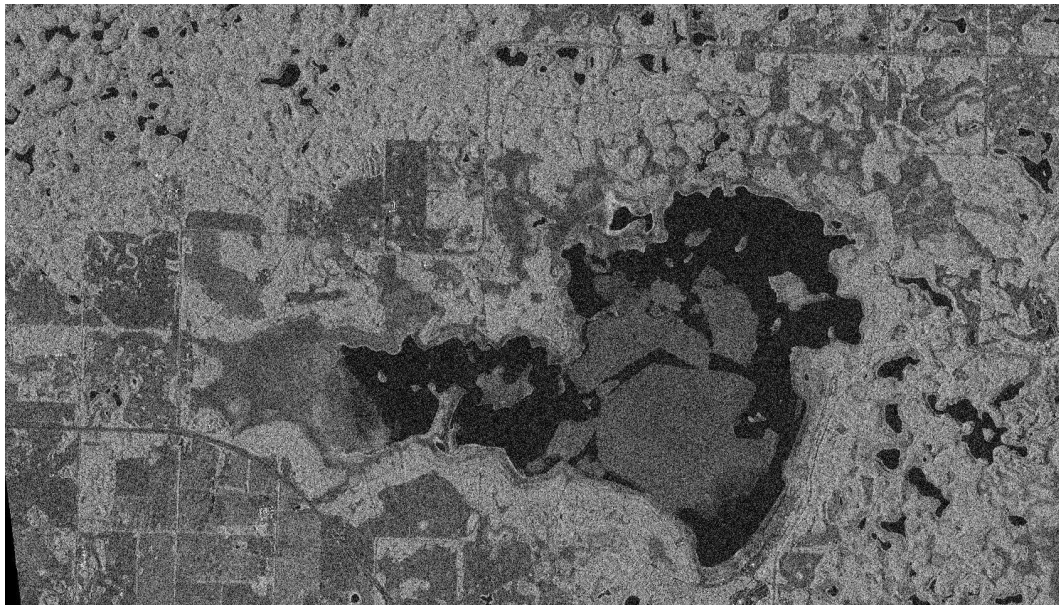
**March 27, 2009.©DLR 2009**



April 07, 2009.©DLR 2009



April 18, 2009.©DLR 2009



April 29, 2009. ©DLR 2009

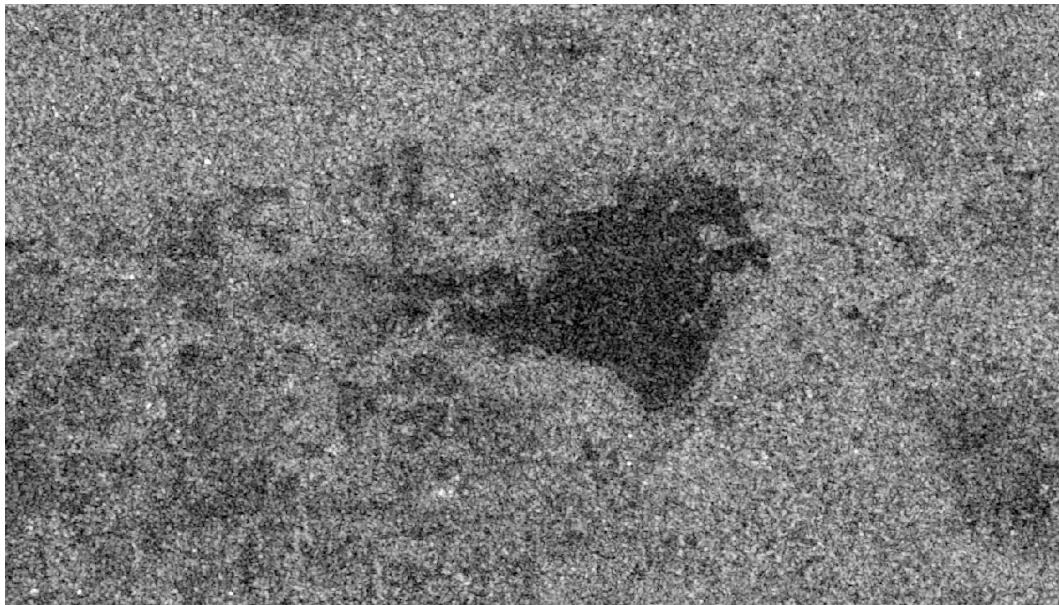
**Appendix B.4      Envisat ASAR APP VV Images 2009/10**



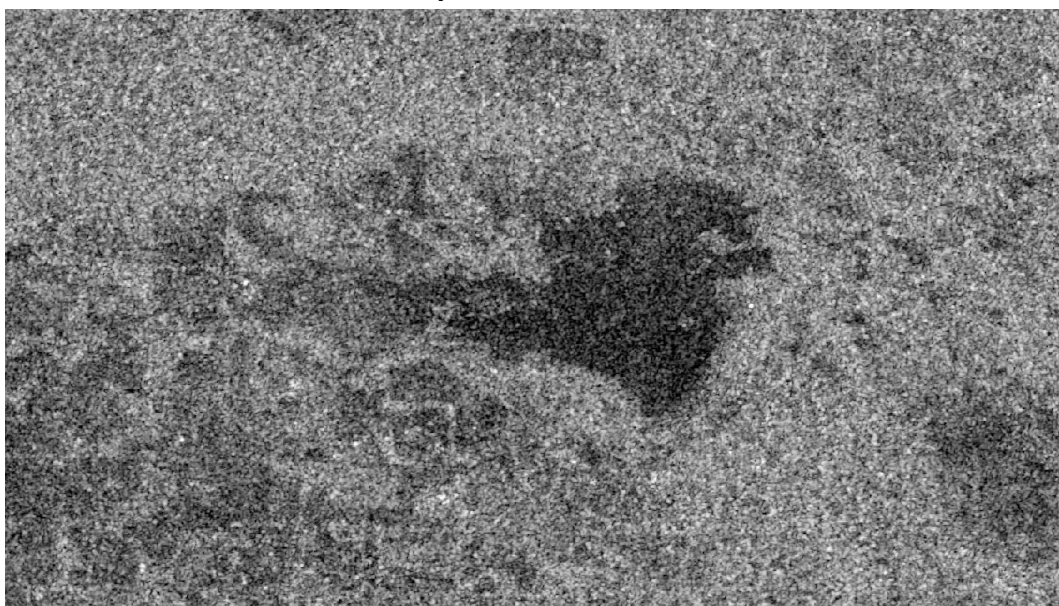
**December 29, 2009. ©ESA 2009**



**February 02, 2010. ©ESA 2010**



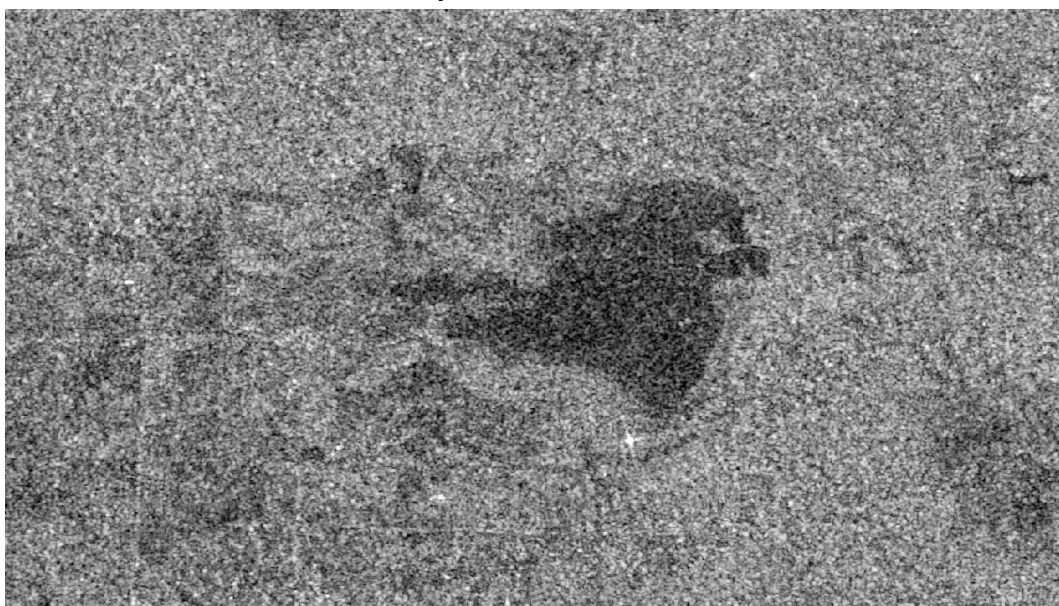
February 03, 2010. ©ESA 2010



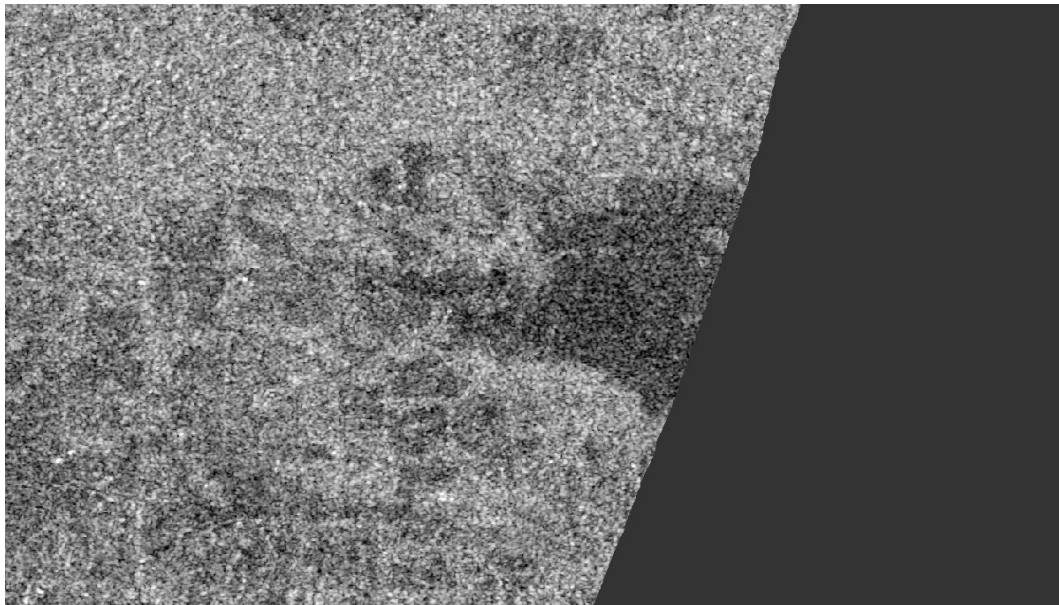
February 11, 2010. ©ESA 2010



February 12, 2010. ©ESA 2010



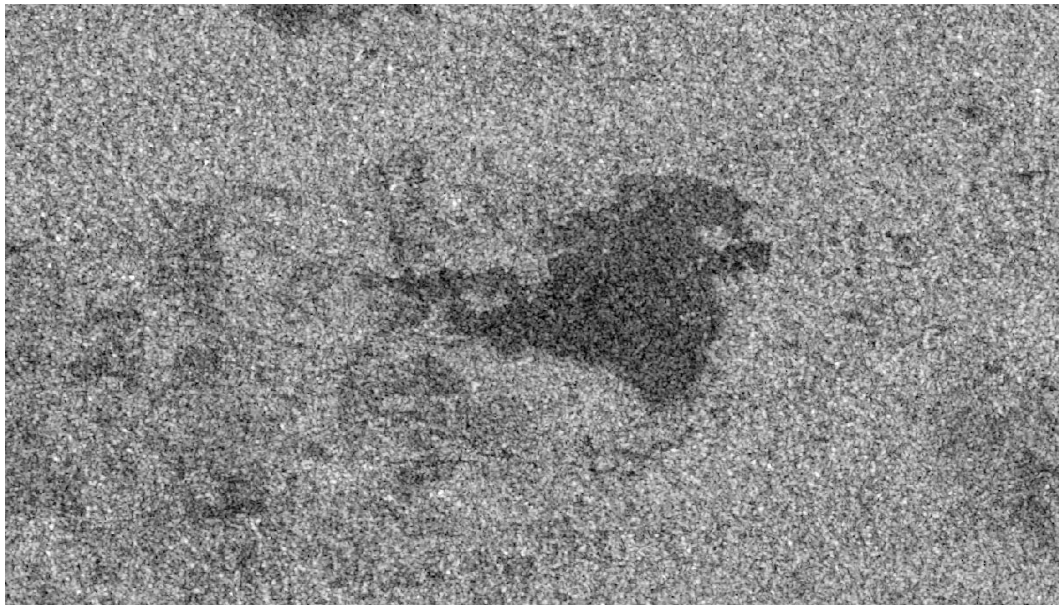
February 19, 2010. ©ESA 2010



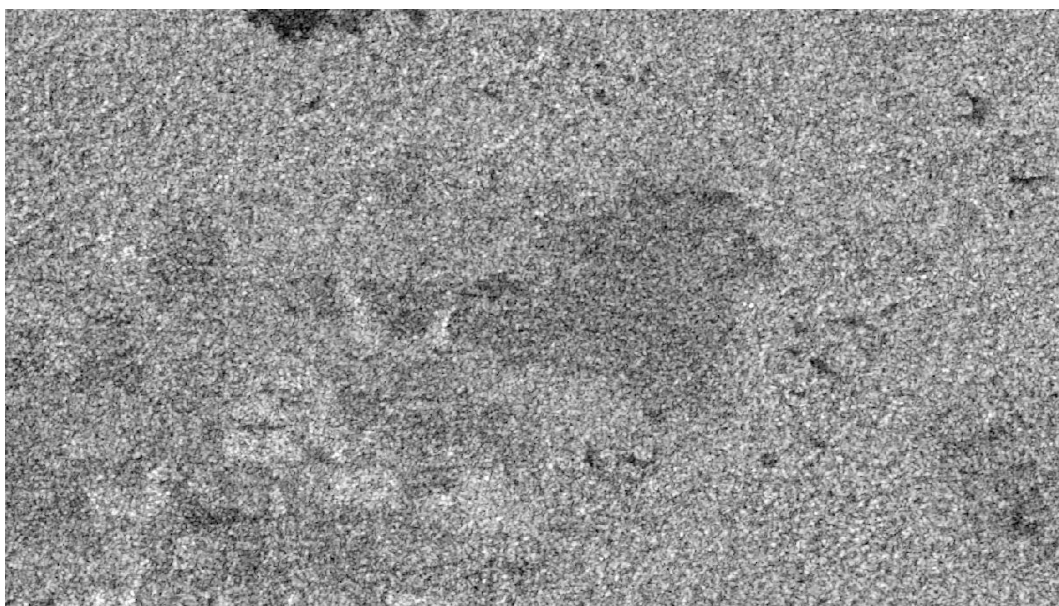
**March 02, 2010.©ESA 2010**



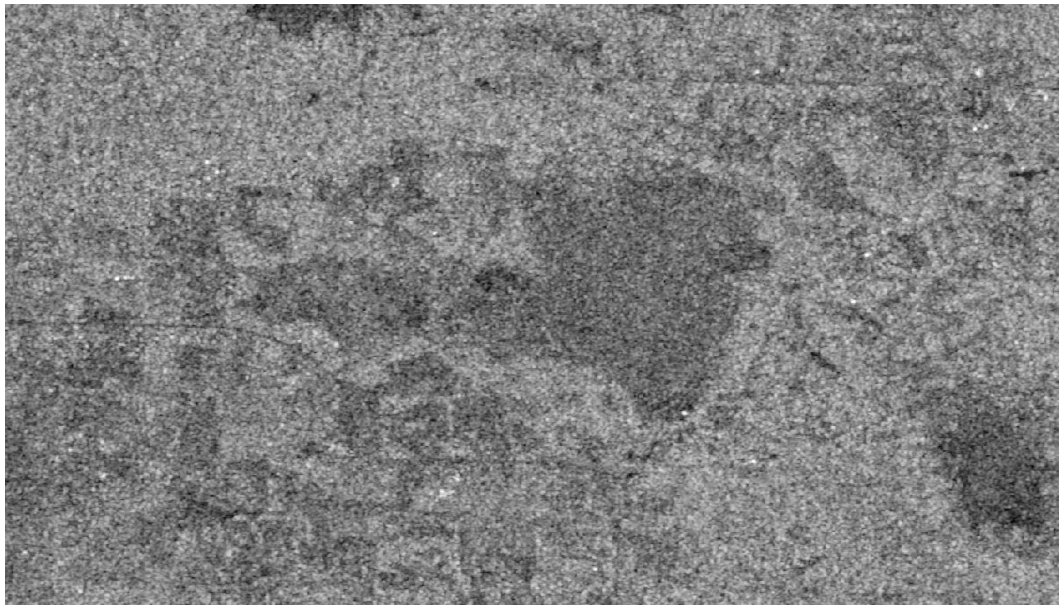
**March 9, 2010.©ESA 2010**



**March 10, 2010.©ESA 2010**



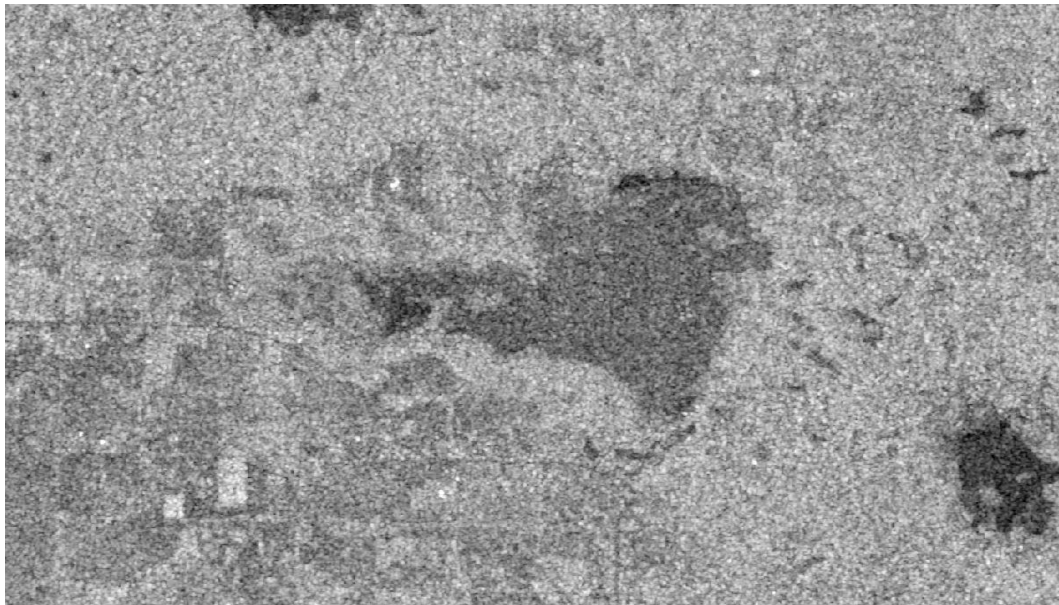
**March 18, 2010.©ESA 2010**



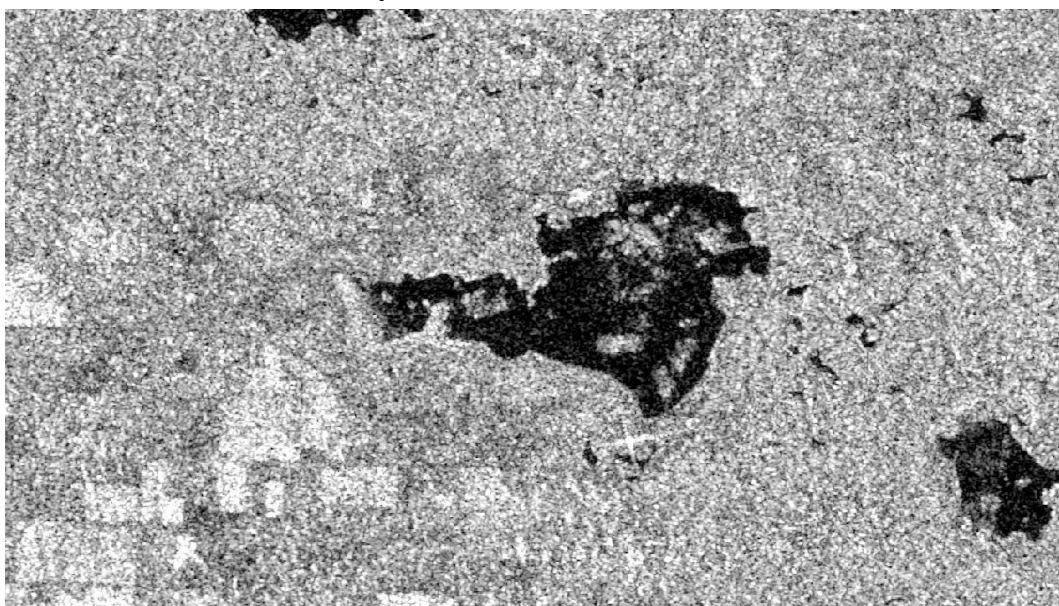
**March 19, 2010.©ESA 2010**



**April 22, 2010.©ESA 2010**



April 23, 2010. ©ESA 2010



April 30, 2010. ©ESA 2010

## **Appendix B.5 TerraSAR-X SM HH Images 2009/10**

This appendix presents the TerraSAR-X Stripmap Mode Complex images acquired over Miquelon Lake in 2009/10. The images presented are the HH polarization channel and are all presented with the same grayscale (-24dB and 0 dB).



**December 23, 2009. ©DLR 2009**



**December 29, 2009.©DLR 2009**



**January 03, 2010.©DLR 2010**



**January 09, 2010.©DLR 2010**



**January 14, 2010.©DLR 2010**



**January 20, 2010.©DLR 2010**



**January 31, 2010.©DLR 2010**



February 05, 2010.©DLR 2010



February 11, 2010.©DLR 2010



February 16, 2010.©DLR 2010



February 22, 2010.©DLR 2010



**February 27, 2010.©DLR 2010**



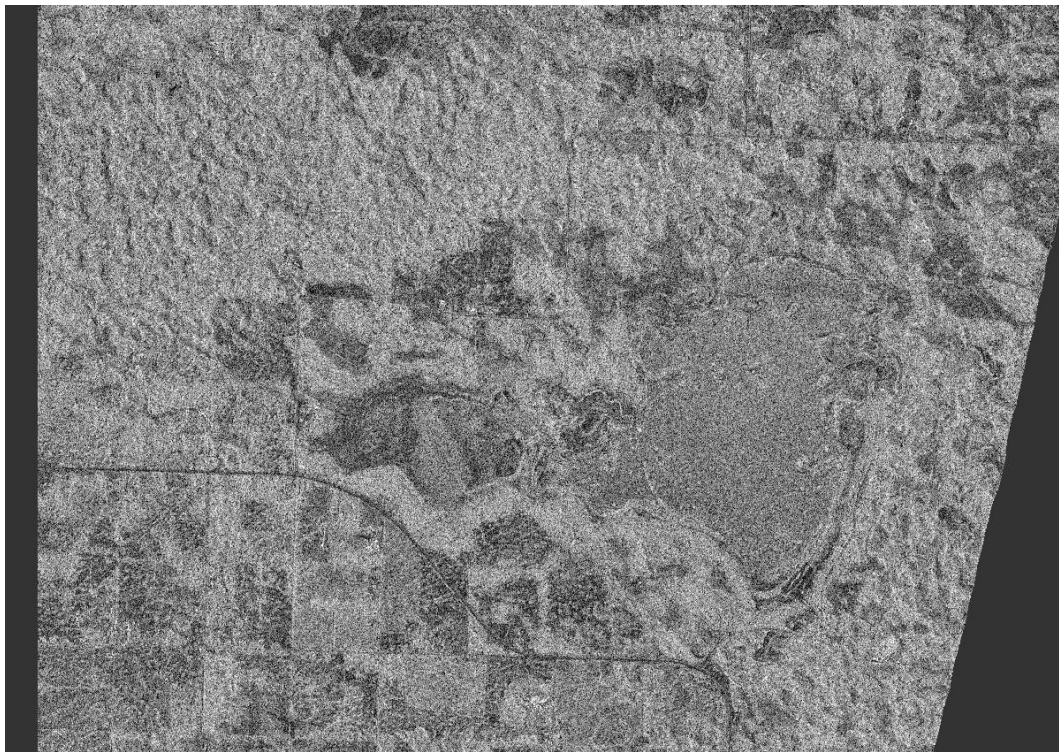
**March 05, 2010.©DLR 2010**



**March 10, 2010.©DLR 2010**



**March 16, 2010.©DLR 2010**



**March 21, 2010.©DLR 2010**



**March 27, 2010.©DLR 2010**